Regional structural geology of Earth and Mars

Thesis by

Daven P. Quinn

In partial fulfillment of the requirements for the degree of **PhD**

Caltech

California Institute of Technology
Pasadena, California

2018
Defended May 2, 2018

ORCID: 0000-0003-1895-3742

Acknowledgements

I have had the good fortune to work with several outstanding advisors over the course of my PhD at Caltech. First and foremost, I am thrilled to have worked with Bethany Ehlmann, all the more so as one of her first batch of students. Bethany's focus and clear-eyed vision allowed us to tackle some really big projects, and her commitment to getting it right encouraged careful and methodical work. I am glad that she turned my attention to Mars. John Grotzinger's trust and guidance helped mold me into a confident field geologist, and his willingness to embark on an exploratory project with a total sedimentary-rock neophyte led to a truly classic mapping study. Finally, Jason Saleeby helped me appreciate the true complexity of tectonics with his intersectional style in the field and in research. Having advisors in three different swathes of the geological sciences gave me a variety of models of scientific outlook and practice to draw from in my work, and I am the richer for it. Thanks for giving me the opportunity to do so much, and the tools to succeed.

Many others on the faculty and staff have contributed greatly to my PhD. From my thesis advisory committee, Paul Asimow was a great help with petrology, and John Eiler asked insightful and probing questions. Joann Stock kept me on academic track, and her field trips were amazing for their content and depth. The field classes taught by Caltech were one of the highlights of my graduate experience, and I especially thank Joe Kirshvink for his outsize role in organizing them. Several faculty and researchers, especially George Rossman, Chi Ma, Fenfang Wu, and Yunbin Guan lent their time and energy to my analytical work. Lisa Christiansen, Mike Black and Scott Dungan have diagnosed myriad GIS and computer problems over the years. Ajay Limaye taught me the SOCET Set tool that formed the basis of my Mars work, and Jay Dickson assisted with the compilation of satellite data. Financial support from NASA in the form of the Earth and Space Sciences

Fellowship was crucial to this work.

Janice Grancich was tireless in organizing the finances and logistics for my field seasons in the Naukluft Mountains, and Mark Garcia helped make sure everything was prepared. On the ground in Namibia, Roger Swart's hospitality was crucial to my success, and I am grateful for his friendship and that of the entire Swart family. More broadly, I must thank the entire staff of the Geologic Survey of Namibia and Namib-Naukluft National Park, who were extremely accommodating towards my fieldwork. Ted Present and Alice Michel donated months of their time to this project as my field assistants, and Ted additionally taught me how to log stratigraphic sections of carbonate rocks. Tina Seeger was instrumental in processing the enormous volume of stratigraphic logs and carbon isotope samples that we generated in the field.

Over the course of all of these projects, I have benefited from many amazing teachers and role models among the graduate students and postdocs at Caltech, who collectively modeled collegiality and competence. These forebears are too numerous to name, but a few rank as especially important: Frank Sousa, Jason Price, Jena Johnson, and Erica Swanson helped me to work carefully in the field and lab, and Abby Fraeman, Melissa Rice, Kirsten Siebach, and Rebecca Greenberger were crucial mentors in Mars science. Just as important were the numerous friends among the GPS community; among many, Joel Scheingross and Luca Malatesta kept me on my bike, and Jennifer Buz, Mathieu Lapotre, and Danielle Piskorz were simply amazing.

Outside of the department, I would like to thank those who put me on the path to this work. At UNC Chapel Hill, I am in debt to Drew Coleman for building my interest in geology, and to Kevin Stewart for conveying the richness of structural geology. Jeff Gillis-Davis at the University of Hawaii was also a wonderful mentor who steered me at crucial points. Thanks for the help!

Finally, I must thank my family — my parents, Robert and Smita Quinn, have been a huge source of support during this long process, as have my parents-in-law Jim and Teresa Sams. The rest of my family has been important to keeping me going too, especially the nascent West Coast branch headed by Chandra Patel, who has so often provided a home away from home. Most importantly, I must give the

final credit to Beth Sams: getting married to her was one of the superlative moments during this my time at Caltech. Beth has made these last six years amazing even as graduate school dominated my life. Beth, I know it's been a hard on you (due to my stress and long absences for fieldwork); I am lucky to have your love and support to lean on. It's been a series of adventures for both of us – I look forward to our next chapter!

Abstract

This thesis explores the geologic context around several key environmental transitions on Earth and Mars which are expressed at continental margins. Regional mapping techniques are applied to build links between methodologies used to explore rock samples and units — stratigraphy, structural geology, remote sensing, geochemistry, petrology, and geodynamic modeling. Four research projects are presented: Chapter 2 explores the tectonic context of xenoliths beneath the western margin of North America and illuminates the structural history of the lithospheric underpinnings of the California coast. In Chapter 3, we undertake a structural study of the southern Naukluft Mountains, Namibia, and re-interpret its tectonic context and age. Chapter 4 builds a new method for applying statistical errors to remotely measured planar orientations, and Chapter 5 applies this method to mapping the 3D structure of a globally significant stratigraphy on Mars. We find a long history of interaction with water at the margin of Isidis Basin. Together, these projects demonstrate the application of structural techniques to continental margins on Earth and Mars, and the creation of new techniques to support geological analysis from remotely-sensed data, where structural measurements may be poorly resolved.

Contents

Plates

Tables

Figures

1 Introduction

Reading environmental markers from the geologic record is key to understanding the evolution of the Earth through time. Packages of rock provide a window into the systems and processes that operated throughout the past. Their properties capture information about their formation environment, and these vignettes can be used to test the applicability of mechanistic and theoretical frameworks for global change.

There are two major aspects of this approach that must be unified. First, detailed observations of key features of the geologic system must be isolated and probed with the appropriate techniques for developing a detailed understanding of individual components. Second, observations must be contextualized with their surroundings, allowing disparate environmental markers to be integrated into a sequence that can illuminate global change.

1.1 Bridging scales of planetary observation

On Earth, operating over a range of scales has been fundamental to geology since its inception as a branch of science. Since their earliest scientific inspection, rocks have been investigated based on microscopic features, such as their fossil content, at human scale, using their outcrop geology and local structural geometry, and at regional scale with structural mapping and correlation. Global summary of regionally-observed trends has enabled the systematization of Earth history and understanding of its surface environment through time.

The methodology employed in small-scale studies has changed fundamentally over time, with the development of imaging and geochemical techniques that increase the amount of information that can be gleaned from a single sample. The techniques employed in global studies have dramatically shifted as well, with satellite imaging and modeling approaches fundamentally altering how problems are investigated, providing more powerful types of information that cannot be gained in other ways.

Our understanding of regional-scale geologic problems on Earth has been limited primarily by the ability to synthesize abundant data. Thus, regional geologic systems are still fundamentally characterized with geological mapping: technical development has served mostly to increase its efficiency and encourage revision based on new new interpretive frameworks (e.g *Atwater*, 1970; *Liu et al.*, 2010).

Technology-driven measurements in adjacent fields have motivated increasingly targeted assessment of regional structural relationships, rather than replacing the technique of regional mapping. A key case is the recent debate over the age of the Grand Canyon, which grapples with the reconciliation of geochemical ages constraining canyon incision with geologic cross-cutting relationships (e.g. *Wernicke*, 2011; *Flowers and Farley*, 2012; *Lucchitta*, 2013). The scale mismatch of localized geochemical data with regional and global interpretive frameworks means that detailed regional mapping studies retain their importance.

New branches of science that have been enabled by technical advances often find it hard to replicate this intermediate-scale component. For instance, global averaging by geochemical proxies is extremely powerful for understanding the large-scale evolution of the Earth, its composition, and its surface biogeochemical systems (e.g. *DePaolo and Wasserburg*, 1976; *Paytan et al.*, 2004; *Rohrbach et al.*, 2007; *Workman and Hart*, 2005; *Halverson et al.*, 2010), and small-scale geochemical systems have become increasingly well understood (e.g. *Gansecki et al.*, 1998; *Bindeman*, 2008), but regional contextualization of these results necessarily relies on inference from relatively limited sample sets (e.g. *Luffi et al.*, 2009) or, where possible, regional mapping studies (e.g. **?***Dibenedetto and Grotzinger*, 2005).

A similar dynamic is present in Mars science: generalized study of the planet's surface is enabled by remote-sensing data (e.g. *Malin and Edgett*, 2000; *Murchie et al.*, 2007; *McEwen et al.*, 2010), and modeling can drive understanding of the global environment through time (e.g. *Wordsworth et al.*, 2015; *Souček et al.*, 2015). Meanwhile, localized systems can be studied using rovers (e.g. *Squyres and Knoll*, 2005; *Grotzinger et al.*, 2012) or Mars meteorites, as permitted by sampling (e.g. *Rankenburg et al.*, 2006; *Agee et al.*, 2014). Cases where abundant data is available, such as landed rover campaigns, have made the most progress in understanding the evolution of integrated geologic systems (e.g. *Grotzinger et al.*, 2005; *Arvidson et al.*, 2014; *Grotzinger et al.*, 2015), but there remains a major scale gap, both in the lack of data at scales intermediate between orbital and rover imagery (*Stack et al.*, 2015) and in interpretive space — inferring planetary evolution from rover campaigns is difficult due to the lack of time constraints on geologic snapshots characterized during landed missions. Attempts to bridge this conceptual divide necessarily involve modeling (*Tosca and McLennan*, 2006; *Andrews-Hanna et al.*, 2007) or detailed geologic mapping (*Lichtenberg et al.*, 2010).

1.2 Differently scaled explorations of continental margins

This thesis consists of several projects that explore different parts of this conceptual space and try to bridge the scale gap through the application of new methodologies. Within this overarching framework, the investigations here are aligned by their examination of the structure of continental margins. On both Earth and Mars, continental edges are expressed as regions of high topographic gradients separating areas of fundamentally different crustal composition and structure. The topographic gradients of continental margins on both Earth and Mars provide a setting for the formation and preservation of stratigraphies that record the surface environment at key time periods in planetary evolution.

On Earth, continents are formed by tectonic processes, and continental edges are the locus of this construction. Chapter 2 of this thesis describes the process of construction of the continental margin terrane of coastal central California. This study uses investigation of mantle-sourced xenolith samples to estimate the structure and origin of a mantle domain beneath the Coast Ranges, linking the two scales using both a review of geologic context and modeling.

The latest Neoproterozoic Eon and its boundary with the Cambrian Period is a time of rapid global change culminating in origin of animal life (*Hoffman*, 1998; *Knoll*, 1999). Stratigraphies covering this period can yield information on the regional environment during this period of global change. In Chapter 3, we apply structural mapping techniques to the Naukluft Nappe Complex in Namibia, which dates from this time period but is tectonically displaced and deformed. We present the first detailed description of a thick, continuous passive-margin stratigraphy that records the Neoproterozoic paleoenvironment at the margin of the Kalahari Craton. This study is a straightforward application of geologic mapping and stratigraphy, eased by the introduction of new technology into the mapping process.

The remainder of this thesis deals with the structural assessment of paleoenvironmentally important stratigraphies on Mars. Reconstruction of depositional environments from Martian sedimentary rocks is limited by the accuracy of bedding orientation measurements. Chapter 4 explores the difficulty of making structural measurements from orbital data, and proposes general statistical and visualization tools to improve error reporting and data quality for remotely-sensed bedding orientations. Chapter 5 applies this method, along with regional mapping, to northeast Syrtis Major, a stratigraphy dating from early in Mars' history, in order to infer the surface environmental progression within the region. We find evidence for episodes of regional inundation and erosion spanning much of Mars history, from the Noachian to Early Amazonian.

Bibliography

Agee, C. B., N. V. Wilson, F. M. Mccubbin, K. Ziegler, V. J. Polyak, Z. D. Sharp, Y. Asmerom, M. H. Nunn, R. Shaheen, M. H. Thiemens, A. Steele, M. L. Fogel, R. Bowden, M. Glamoclija, Z. Zhang, and S. M. Elardo (2014), Unique Meteorite from Early Breccia Northwest Africa 7034, *780*(2013), doi:10.1126/science.1228858.

Andrews-Hanna, J. C., R. J. Phillips, and M. T. Zuber (2007), Meridiani Planum and the global hydrology of Mars, *Nature*, *446*(7132), 163–166, doi:10.1038/nature05594.

Arvidson, R. E., S. W. Squyres, J. F. Bell, J. G. Catalano, B. C. Clark, L. S. Crumpler, P. a de Souza, a. G. Fairén, W. H. Farrand, V. K. Fox, R. Gellert, a. Ghosh, M. P. Golombek, J. P. Grotzinger, E. a Guinness, K. E. Herkenhoff, B. L. Jolliff, a. H. Knoll, R. Li, S. M. McLennan, D. W. Ming, D. W. Mittlefehldt, J. M. Moore, R. V. Morris, S. L. Murchie, T. J. Parker, G. Paulsen, J. W. Rice, S. W. Ruff, M. D. Smith, and M. J. Wolff (2014), Ancient aqueous environments at Endeavour crater, Mars., *Science (New York, N.Y.)*, *343*(6169), 1248,097, doi:10.1126/science.1248097.

Atwater, T. (1970), Implications of plate tectonics for the Cenozoic tectonic evolution of western North America, *Geological Society of America Bulletin*, *81*(12), 3513–3536, doi:10.1130/0016-7606(1970)81.

Bindeman, I. (2008), Oxygen isotopes in mantle and crustal magmas as revealed by single crystal analysis, *Reviews in Mineralogy and Geochemistry*, *69*(1), 445–478.

DePaolo, D., and G. Wasserburg (1976), Inferences about magma sources and mantle structure from variations of 143Nd/144Nd, *Geophysical Research Letters*, *3*(12).

Dibenedetto, S., and J. Grotzinger (2005), Geomorphic evolution of a storm-dominated carbonate ramp (c. 549 Ma), Nama Group, Namibia, *Geological Magazine*, *142*(05), 583, doi:10.1017/S0016756805000890.

Flowers, R. M., and K. A. Farley (2012), Apatite 4He/3He and (U-Th)/He evidence for an ancient Grand Canyon., *Science (New York, N.Y.)*, *338*(6114), 1616–9, doi:10.1126/science.1229390.

Gansecki, C. A., G. A. Mahood, and M. McWilliams (1998), New ages for the climactic eruptions at Yellowstone: Single-crystal 40Ar/39Ar dating identifies contamination, *Geology*, *26*(4), 343–346.

Grotzinger, J. P., R. E. Arvidson, J. F. Bell, W. Calvin, B. C. Clark, D. A. Fike, M. Golombek, R. Greeley, A. Haldemann, K. E. Herkenhoff, B. L. Jolliff, A. H. Knoll, M. Malin, S. M. McLennan, T. Parker, L. Soderblom, J. N. Sohl-Dickstein, S. W. Squyres, N. J. Tosca, and W. A. Watters (2005), Stratigraphy and sedimentology of a dry to wet eolian depositional system, Burns formation, Meridiani Planum, Mars, *Earth and Planetary Science Letters*, *240*(1), 11–72, doi: 10.1016/j.epsl.2005.09.039.

Grotzinger, J. P., J. Crisp, A. R. Vasavada, R. C. Anderson, C. J. Baker, R. Barry, D. F. Blake, P. Conrad, K. S. Edgett, B. Ferdowski, R. Gellert, J. B. Gilbert, M. Golombek, J. Gómez-Elvira, D. M. Hassler, L. Jandura, M. Litvak, P. Mahaffy, J. Maki, M. Meyer, M. C. Malin, I. Mitrofanov, J. J. Simmonds, D. Vaniman, R. V. Welch, and R. C. Wiens (2012), *Mars Science Laboratory Mission and Science Investigation*, vol. 170, doi:10.1007/s11214-012-9892-2.

Grotzinger, J. P., S. Gupta, M. C. Malin, D. M. Rubin, J. Schieber, K. Siebach, D. Y. Sumner, K. M. Stack, A. R. Vasavada, R. E. Arvidson, F. Calef, L. Edgar, W. F. Fischer, J. A. Grant, J. Griffes, L. C. Kah, M. P. Lamb, K. W. Lewis, N. Mangold, M. E. Minitti, M. Palucis, M. Rice, R. M. E. Williams, R. A. Yingst, D. Blake, D. Blaney, P. Conrad, J. Crisp, W. E. Dietrich, G. Dromart, K. S. Edgett, R. C. Ewing, R. Gellert, J. A. Hurowitz, G. Kocurek, P. Mahaffy, M. J. McBride, S. M. McLennan, M. Mischna, D. Ming, R. Milliken, H. Newsom, D. Oehler, T. J. Parker, D. Vaniman, R. C. Wiens, and S. A. Wilson (2015), Deposition, exhumation, and paleoclimate of an ancient lake deposit, Gale crater, Mars, *Science*, *350*(6257), aac7575–aac7575, doi:10.1126/science.aac7575.

Halverson, G. P., B. P. Wade, M. T. Hurtgen, and K. M. Barovich (2010), Neoproterozoic chemostratigraphy, *Precambrian Research*, *182*(4), 337–350, doi:10.1016/j.precamres.2010.04.007.

Hoffman, P. F. (1998), A Neoproterozoic Snowball Earth, *Science*, *281*(5381), 1342–1346, doi:10.1126/science.281.5381.1342.

Knoll, A. H. (1999), Early Animal Evolution: Emerging Views from Comparative Biology and Geology, *Science*, *284*(5423), 2129–2137, doi:10.1126/science.284.5423.2129.

Lichtenberg, K. A., R. E. Arvidson, R. V. Morris, S. L. Murchie, J. L. Bishop, D. Fernandez Remolar, T. D. Glotch, E. Noe Dobrea, J. F. Mustard, J. Andrews-Hanna, and L. H. Roach (2010), Stratigraphy of hydrated sulfates in the sedimentary deposits of Aram Chaos, Mars, *Journal of Geophysical Research*, *115*, doi:10.1029/2009JE003353.

Liu, L., M. Gurnis, M. Seton, J. Saleeby, R. D. Müller, and J. M. Jackson (2010), The role of oceanic plateau subduction in the Laramide orogeny, *Nature Geoscience*, *3*(5), 353–357, doi:10.1038/ngeo829.

Lucchitta, I. (2013), Comment on "Apatite 4He/3He and (U-Th)/He evidence for an ancient Grand Canyon"., *Science (New York, N.Y.)*, *340*(6129), 143, doi:10.1126/science.1234567.

Luffi, P., J. B. Saleeby, C.-T. a. Lee, and M. N. Ducea (2009), Lithospheric mantle duplex beneath the central Mojave Desert revealed by xenoliths from Dish Hill, California, *Journal of Geophysical Research*, *114*(B3), B03,202, doi:10.1029/2008JB005906.

Malin, M. C., and K. S. Edgett (2000), Sedimentary Rocks of Early Mars, *Science*, *290*(5498), 1927–1937, doi:10.1126/science.290.5498.1927.

McEwen, A. S., M. E. Banks, N. Baugh, K. Becker, A. Boyd, J. W. Bergstrom, R. A. Beyer, E. Bortolini, N. T. Bridges, S. Byrne, B. Castalia, F. C. Chuang, L. S. Crumpler, I. Daubar, A. K. Davatzes, D. G. Deardorff, A. DeJong, W. Alan Delamere, E. N. Dobrea, C. M. Dundas, E. M. Eliason, Y. Espinoza, A. Fennema, K. E. Fishbaugh, T. Forrester, P. E. Geissler, J. A. Grant, J. L. Griffes, J. P. Grotzinger, V. C. Gulick, C. J. Hansen, K. E. Herkenhoff, R. Heyd, W. L. Jaeger, D. Jones, B. Kanefsky, L. Keszthelyi, R. King, R. L. Kirk, K. J. Kolb, J. Lasco, A. Lefort, R. Leis, K. W. Lewis, S. Martinez-Alonso, S. Mattson, G. McArthur, M. T. Mellon, J. M. Metz, M. P. Milazzo, R. E. Milliken, T. Motazedian, C. H. Okubo, A. Ortiz, A. J. Philippoff, J. Plassmann, A. Polit, P. S. Russell, C. Schaller, M. L. Searls, T. Spriggs, S. W. Squyres, S. Tarr, N. Thomas, B. J. Thomson, L. L. Tornabene, C. Van Houten, C. Verba, C. M. Weitz, and J. J. Wray (2010), The High Resolution Imaging Science Experiment (HiRISE) during MRO's Primary Science Phase (PSP), *Icarus*, *205*(1), 2–37, doi:10.1016/j.icarus.2009.04.023.

Murchie, S., R. Arvidson, P. Bedini, K. Beisser, J.-P. Bibring, J. Bishop, J. Boldt, P. Cavender, T. Choo, R. T. Clancy, E. H. Darlington, D. Des Marais, R. Espiritu, D. Fort, R. Green, E. Guinness, J. Hayes, C. Hash, K. Heffernan, J. Hemmler, G. Heyler, D. Humm, J. Hutcheson, N. Izenberg, R. Lee, J. Lees, D. Lohr, E. Malaret, T. Martin, J. A. McGovern, P. McGuire, R. Morris, J. Mustard, S. Pelkey, E. Rhodes, M. Robinson, T. Roush, E. Schaefer, G. Seagrave, F. Seelos, P. Silverglate, S. Slavney, M. Smith, W.-J. Shyong, K. Strohbehn, H. Taylor, P. Thompson, B. Tossman, M. Wirzburger, and M. Wolff (2007), Compact Reconnaissance Imaging Spectrometer for Mars (CRISM) on Mars Reconnaissance Orbiter (MRO), *Journal of Geophysical Research*, *112*(E5), doi: 10.1029/2006JE002682.

Paytan, A., M. Kastner, D. Campbell, and M. H. Thiemens (2004), Seawater sulfur isotope fluctuations in the Cretaceous., *Science (New York, N.Y.)*, *304*, 1663–1665, doi:10.1126/science.1095258.

Rankenburg, K., a. D. Brandon, and C. R. Neal (2006), Neodymium isotope evidence for a chondritic composition of the Moon., *Science (New York, N.Y.)*, *312*(5778), 1369–72, doi:10.1126/science.1126114.

Rohrbach, A., C. Ballhaus, U. Golla-Schindler, P. Ulmer, V. S. Kamenetsky, and D. V. Kuzmin (2007), Metal saturation in the upper mantle., *Nature*, *449*(7161), 456–8, doi:10.1038/nature06183.

Souček, O., O. Bourgeois, S. Pochat, and T. Guidat (2015), A 3 Ga old polythermal ice sheet in Isidis Planitia, Mars: Dynamics and thermal regime inferred from numerical modeling, *Earth and Planetary Science Letters*, *426*(August), 176–190, doi:10.1016/j.epsl.2015.06.038.

Squyres, S. W., and A. H. Knoll (2005), Sedimentary rocks at Meridiani Planum: Origin, diagenesis, and implications for life on Mars, *Earth and Planetary Science Letters*, *240*(1), 1–10, doi:10.1016/j.epsl.2005.09.038.

Stack, K. M., C. S. Edwards, J. P. Grotzinger, S. Gupta, D. Y. Sumner, F. J. Calef, L. A. Edgar, K. S. Edgett, A. A. Fraeman, S. R. Jacob, L. Le Deit, K. W. Lewis, M. S. Rice, D. Rubin, R. M. E. Williams, and K. H. Williford (2015), Comparing orbiter and rover image-based mapping of an ancient sedimentary environment, Aeolis Palus, Gale crater, Mars, *Icarus*, *280*, 3–21, doi: 10.1016/j.icarus.2016.02.024.

Tosca, N. J., and S. M. McLennan (2006), Chemical divides and evaporite assemblages on Mars, *Earth and Planetary Science Letters*, *241*(1-2), 21–31, doi:10.1016/j.epsl.2005.10.021.

Wernicke, B. (2011), The California River and its role in carving Grand Canyon, *Geological Society of America Bulletin*, *123*(7-8), 1288–1316, doi:10.1130/B30274.1.

Wordsworth, R. D., L. Kerber, R. T. Pierrehumbert, F. Forget, and J. W. Head (2015), Comparison of ”warm and wet” and ”cold and icy” scenarios for early Mars in a 3D climate model, *arXiv.org*, *astro-ph.E*, 1201–1219, doi:10.1002/2015JE004787.Received.

Workman, R. K., and S. R. Hart (2005), Major and trace element composition of the depleted MORB mantle (DMM), *Earth and Planetary Science Letters*, *231*(1-2), 53–72, doi:10.1016/j.epsl.2004.12.005.

2 Late-Cretaceous construction of the mantle lithosphere beneath the central California coast revealed by Crystal Knob xenoliths

Daven P. Quinn[1] J. Saleeby[1] M. Ducea[2,3] P. Luffi[4] P. Asimow[1]

1 Division of Geological and Planetary Sciences, California Institute of Technology, Pasadena, California, USA

2 Department of Geosciences, University of Arizona, Tuscon, Arizona, USA

3 Faculty of Geology and Geophysics, University of Bucharest, 010041, Bucharest, Romania

4 Institute of Geodynamics, Romanian Academy, 19-21 Jean-Luis Calderon St., Bucharest, Romania

Abstract

The Pleistocene (1.65 Ma) Crystal Knob volcanic neck in the California Coast Ranges is an olivine-plagioclase phyric basalt containing dunite and spinel peridotite xenoliths. Crystal Knob erupted through the Nacimiento belt of the Franciscan complex and adjacent to Salinian crystalline nappes. Its xenoliths sample the mantle lithosphere beneath the outboard exhumed remnants of the southern California Cretaceous subducting margin. This sample set augments previously-studied xenolith suites in the Mojave Desert and Sierra Nevada, which linked the mantle lithosphere architecture and crustal structure of the western Cordillera. We examine six peridotite samples ranging from fertile lherzolites to harzburgite residues. Time-corrected ϵ_{Nd} of 10.3-11.0 and $^{87}Sr/^{86}Sr$ of 0.702 are characteristic of underplated sub-oceanic mantle. Pyroxene-exchange geothermometry shows equilibration at 950-1060°C. Phase stability, Ca-in-olivine barometry, and 65-90 mW/m^2 regional geotherms suggest entrainment at 45-75 km depth. The samples were variably depleted by partial melting, and re-enrichment of the hottest samples suggests deep melt interaction. We test the Crystal Knob temperature-depth array against model geotherms matching potential sources for the mantle lithosphere beneath the Coast Ranges: (A) a shallow Mendocino slab window, (B) a young Monterey-plate "stalled slab", and (C) Farallon-plate mantle nappes, underplated during the Cretaceous and reheated at depth by the Miocene slab window. Models B and C fit xenolith thermobarometry, but only Model C fits the tectonic and geodynamic evolution of southern California. We conclude that the mantle lithosphere beneath the central California coast was emplaced after Cretaceous flat-slab subduction and records a thermal signature of Neogene subduction of the Pacific–

Farallon ridge.

The tectonic and petrogenetic processes by which Earth's continental mantle lithosphere develops through time are of fundamental importance to geodynamics and Earth history. The architecture of the mantle lithosphere, integrated with regional geophysical data and tectonic and petrogenetic studies of the overlying crust, offers critical insights into the geodynamic processes of continental assembly. Mantle xenoliths entrained in volcanic rock reveal compositions and textures in a vertical transect through the underlying deep lithosphere. Petrogenetic studies of xenolith suites can discern their thermal conditions, depth of entrainment, and geochemical evolution. These features can provide insight into tectonic processes affecting the entire lithosphere.

The Crystal Knob xenolith suite, in the Coast Ranges of central California, presents a rare opportunity to sample the mantle lithosphere directly beneath a region of long-lived subduction accretion. The complex Late Cretaceous and Neogene tectonic processes that built the present Coast Ranges suggest several possible sources for the underlying mantle lithosphere. When restored for Neogene dextral offset, the position of Crystal Knob suggests that its upper mantle underpinnings may have been emplaced as asthenospheric mantle upwelling into the Pacific-Farallon slab window (*Wilson et al.*, 2005). Other workers (e.g. *Pikser et al.*, 2012) propose a shallowly-dipping stalled slab beneath the Coast Ranges from the latest phase of subduction in the Neogene. We propose a third model, in which mantle lithosphere was underplated during the Cretaceous during extensional collapse after flat-slab subduction (*Luffi et al.*, 2009; *Chapman et al.*, 2012). Given its position near the edge of the continent, this underplated lithospheric mantle would have experienced a thermal pulse due to ridge subduction in the Neogene (*Wilson et al.*, 2005).

In this contribution, we present new petrologic, geochemical, and thermobarometric data on mantle xenoliths hosted in the Pleistocene Crystal Knob volcanic neck in coastal central California. These new datasets, plus derivative geochemical modeling and thermal modeling of the central California lithosphere, are used to decipher the petrogenesis of Crystal Knob xenoliths and host basaltic lavas. Constraints on the thermal structure of the mantle lithosphere are used to test the three models of the Late Cretaceous to present evolution of the lithospheric underpinnings of central California. The tectonic processes uncovered by this study can provide new insights into the relative role of Cretaceous and Neogene processes in building the margin of the North American continent.

2.1.1 Regional tectonic setting

The Crystal Knob xenolith locality samples an important lithospheric column through the Late Cretaceous convergent margin of the North American Cordillera. This regionally extensive belt includes a voluminous continental magmatic arc, generated as the Farallon oceanic plate subducted eastward beneath western North America (e.g. *Glazner*, 1991; *Ducea et al.*, 2015), and the Franciscan complex, the crustal-level accretionary complex of this subduction zone. The Franciscan includes tectonic slivers of Farallon plate oceanic basement and pelagic sedimentary rocks, as well as upper plate siliciclastic rocks derived from the magmatic arc (*Cowan*, 1978; *Murchey and Jones*, 1984; *Sliter*, 1984; *Blake et al.*, 1988; *Chapman*, 2016; *Chapman et al.*, 2016a). The crystalline basement blocks of the "Salinian terrane", or "Salinia" (*Page*, 1981), have recently been recognized as a series of nappes derived from the southern California segment of the Late Cretaceous magmatic arc, displaced westward to lie tectonically above the accretionary complex near the central California coast (*Hall*, 1991; *Barth et al.*, 2003; *Kidder and Ducea*, 2006; *Ducea et al.*, 2009; *Chapman et al.*, 2012; *Hall and Saleeby*, 2013). The Crystal Knob xenolith locality lies along the western margin of Salinia, adjacent to the Nacimiento fault [Figure 2.1], a polyphase shear zone which, in its original geometry, constituted the local structural base of the Salinian crystalline nappe sequence (*Hall and Saleeby*, 2013). The Crystal Knob xenolith suite samples the uppermost mantle beneath the Franciscan accretionary complex and its local veneer of Salinia crystalline nappes.

Restoring the central Coast Ranges to their position relative to North America prior to San Andreas transform offset places them outboard of the southern California batholith, the extended southern continuation of the Sierra Nevada batholith in the Mojave Desert [Figure 2.1]. In this restored position, the crystalline nappes that constitute Salinia correlate to deeply exhumed Cretaceous arc plutonic rocks of the southernmost Sierra Nevada batholith and northwestern southern California batholith (*Wood and Saleeby*, 1997; *Saleeby*, 2003; *Barbeau et al.*,

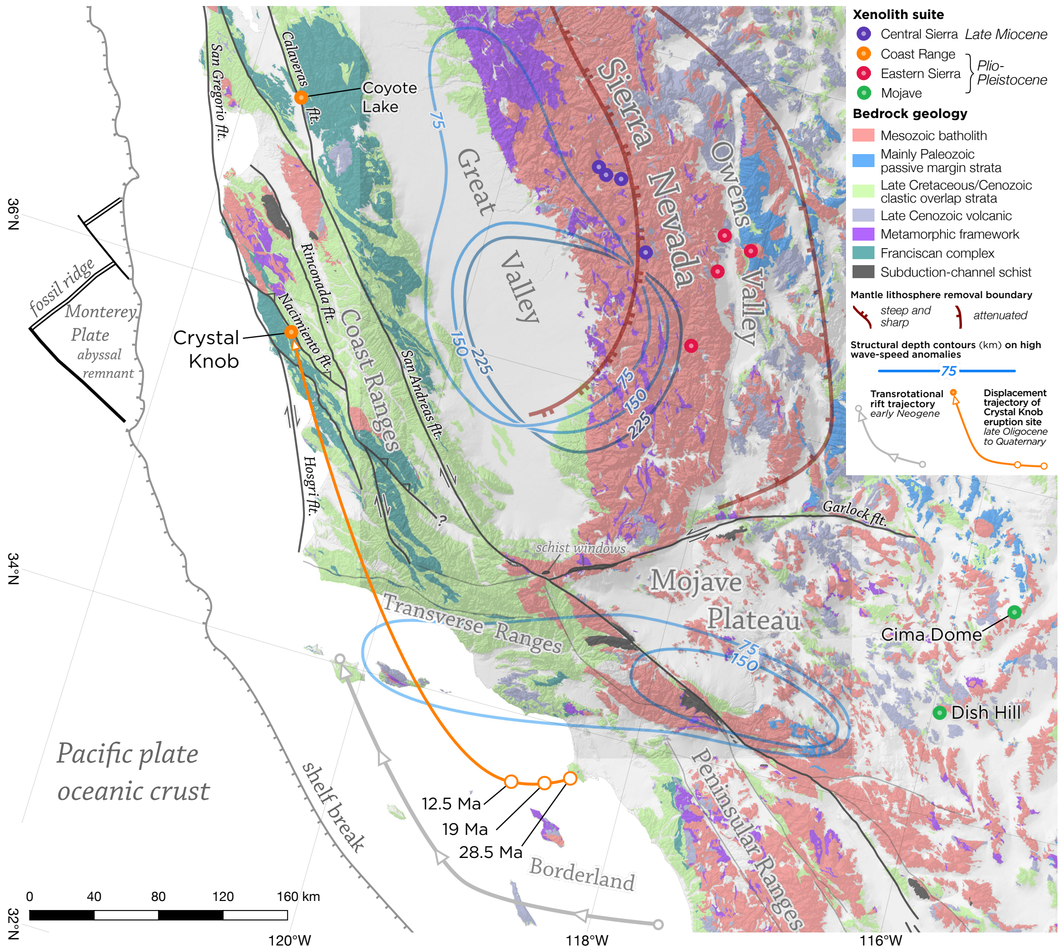

Figure 2.1: Map of southern California showing the tectonic setting of Crystal Knob and its placement relative to the dispersed Southern California batholith, Neogene dextral faults, and the stalled Monterey microplate. Sampling locations for previous xenolith studies are shown: the Central and Eastern Sierran suites show a record of delamination of a batholithic root (*Ducea and Saleeby*, 1996) and Mojave Plateau sites show underplating of Farallon-plate lithospheric nappes during the Cretaceous (*Luffi et al.*, 2009). The position of Crystal Knob is also shown, along with its North-America-relative position prior to dextral offset on the Neogene San Andreas transform system. Crystal Knob restores to ~350 km SE of its current location, with ~310 km displacement on the modern San Andreas Fault and ~40 km remainder on the Rinconada Fault. Independent reconstructions using the regional paleomagnetic framework of *Wilson et al.* (2005) and restoration of slip along San Andreas–system faults (*Dickinson et al.*, 2005) agree to within 5 km on the position of the Crystal Knob source locale at 19 Ma [see also Figure 2.17].

2005; *Chapman et al.*, 2012).

The southernmost Sierra Nevada batholith is exhumed, with granitic rocks at the surface originating at shallow to medial crustal depths (2 to 4 kb pressure) in the bulk of the batholith grading towards deep crustal levels (10 kb) at its southernmost reaches (*Ague and Brimhall*, 1988; *Nadin and Saleeby*, 2008). Seismic imaging shows a strong reflector which is effectively flat beneath the western Mojave plateau (*Yan et al.*, 2005) and dips ~30°N beneath the southernmost Sierra Nevada (*Malin et al.*, 1995). This inflection aligns with increasing exhumation of the batholith and is interpreted as the relict megathrust surface, with a lateral ramp towards a "flat slab" beneath the Mojave province, atop which the southern California batholith was dispersed and truncated (*Saleeby*, 2003; *Chapman et al.*, 2016b). The Garlock fault [Figure 2.1] nucleated along this inflection during the early Miocene (*Saleeby et al.*, 2016).

These exhumed batholithic rocks form the upper plate above a polyphase low-angle extensional fault system, remobilized along the former shallow subduction megathrust in the late Cretaceous. Franciscan-affinity, mainly metaclastic rocks were underplated beneath this tectonic surface (*Malin et al.*, 1995; *Barth et al.*, 2003; *Saleeby*, 2003; *Yan et al.*, 2005; *Ducea et al.*, 2009; *Chapman et al.*, 2010, 2012, 2016b). These subduction channel schists are exposed in a series of tectonic windows [Figure 2.1] and encase blocks and nappes of Farallon-plate oceanic basement and sedimentary rock. The schist protoliths were derived from the upper plate batholithic belt, which was rapidly exhumed above a shallow flat segment of the Franciscan subduction megathrust system (*Barth et al.*, 2003; *Saleeby et al.*, 2007; *Chapman et al.*, 2013, 2016a). The truncation of lower-crustal batholithic rocks and underplating of subduction-channel schists requires the tectonic erosion of the underlying mantle wedge lithosphere and deepest arc crust.

The southern California "flat slab" is attributed to the ephemeral buoyancy resulting from the subduction of the conjugate massif to the Shatsky Rise oceanic igneous province (*Livaccari et al.*, 1981; *Sliter*, 1984; *Saleeby*, 2003), which is currently resolved in deep seismic tomographic images beneath the interior of North America (*Liu et al.*, 2010; *Sun et al.*, 2017). As the Shatsky conjugate moved deeper into the mantle beneath the North American plate, the Salinia nappes and adjacent (restored for Neogene dextral faulting) deeply exhumed batholithic rocks were displaced and structurally attenuated by both the shallow subduction megathrust and subsequent trench-directed extensional faulting (*Saleeby*, 2003; *Liu et al.*, 2010; *Chapman et al.*, 2012).

In the Neogene, ridge subduction and the opening of the Pacific-Farallon slab window (*Atwater and Stock*, 1998) drove far-field effects including late Cenozoic regional volcanism in central and southern California (*Dodge*, 1988) and the convective ascent of asthenosphere in the southern Basin and Range province (*Le Pourhiet et al.*, 2006). Beginning in the Miocene, the crustal blocks through which Crystal Knob erupted were moved northwest along the San Andreas transform system to their present position (e.g. *Argus and Gordon*, 1991; *Wilson et al.*, 2005).

2.1.2 Previous mantle xenolith studies

The southwest North American Cordillera hosts many xenolith localities, at which upper mantle and lower crustal rock fragments were entrained in mainly late Cenozoic volcanic eruptions. Early studies of a number of these xenolith suites catalogued petrographic features and classified samples into textural groups (e.g. *Nixon*, 1987; *Wilshire et al.*, 1988). Subsequently, modern geochemical and petrogenetic techniques have revealed several regional mantle lithosphere domains: Precambrian crustal root, Cretaceous arc mantle wedge, underplated Farallon plate nappes, and late Cenozoic shallow convective asthenosphere (e.g. *Galer and O'Nions*, 1989; *Livaccari and Perry*, 1993; *Alibert*, 1994; *Beard and Glazner*, 1995; *Ducea and Saleeby*, 1998b; *Jové and Coleman*, 1998; *Lee et al.*, 2001a; *Usui et al.*, 2003; *Luffi et al.*, 2009).

The central Sierra Nevada xenolith suite [Figure 2.1] was entrained in late Miocene small-volume volcanic flows and plugs north of the zone of "flat slab" subduction. It samples the intact Sierra Nevada batholithic root and Cretaceous mantle wedge (*Ducea and Saleeby*, 1996, 1998b; *Lee et al.*, 2001a; *Saleeby*, 2003; *Lee et al.*, 2006; *Chin et al.*, 2015). In contrast, xenolith suites in the eastern Mojave Desert record the partial tectonic erosion of sub-continental mantle lithosphere (including Cretaceous mantle wedge) and underplating of Farallon-plate mantle lithosphere (*Shervais et al.*, 1973; *Luffi et al.*, 2009; *Armytage et al.*, 2015; *Shields and Chapman*, 2016). The Dish Hill locality [Figure 2.1] records an upper mantle duplex with imbricated nappes of Farallon-plate oceanic mantle lying structurally beneath a relatively thin roof of attenuated continental-lithosphere peridotite. The mantle duplex is interpreted to have formed as the Farallon plate retreated following low-angle subduction of the Shatsky conjugate (*Luffi et al.*, 2009).

Xenoliths of the eastern Sierra suite [Figure 2.1] occur in Pliocene-Quaternary mafic lava flows and record significantly steeper thermal gradients and more fertile compositions than the older xenoliths of the central Sierra, suggesting Neogene asthenospheric upwelling (*Ducea and Saleeby*, 1996, 1998a). Seismic studies show a corresponding domain of asthenospheric mantle that extends to the base of the crust (~30 km depth) in the eastern Sierra (*Jones and Phinney*, 1998; *Zandt et al.*, 2004; *Frassetto et al.*, 2011; *Jones et al.*, 2014). The eruption of xenolith-hosting lavas of the eastern Sierra suite within the <5 Ma Owens Valley rift system [Figure 2.1] was likely driven by upper mantle convection (*Le Pourhiet et al.*, 2006; *Jones et al.*, 2014).

The upper-mantle source of most xenolith suites in the Cordillera clearly corresponds to surface geology: sub-continental xenolith suites are generally erupted through cratonic and peri-cratonic crust, mantle wedge suites through the Cretaceous large-volume batholith, and asthenospheric suites through active rifts. However, xenoliths derived from underplated Farallon-plate material have thus far only been recovered from inboard crustal domains in the eastern Mojave province. These lithospheric underpinnings were underplated with large sub-horizontal displacements along a relatively shallow subduction megathrust system (*Helmstaedt and Doig*, 1975; *Lee et al.*, 2001b).

Restored for Neogene dextral faulting, the lithospheric block hosting Crystal Knob was directly outboard of the Dish Hill xenolith locality [Figure 2.1], where the mantle lithosphere is formed by Farallon nappes underplated during the Cretaceous (*Luffi et al.*, 2009). Accordingly, the mantle lithosphere beneath the Coast Ranges may be composed of outboard equivalents of these underplated nappes. However, the Coast Ranges are both proximal to a subduction zone that was active until the early Neogene and directly above the Pacific–Farallon slab window that developed at the end of this subduction. The Crystal Knob xenolith suite provides an opportunity to resolve the ambiguous mantle lithosphere architecture of coastal California and to understand the effects of flat-slab subduction, microplate rotation and capture, and ridge subduction on the deep structure of a subducting margin.

2.2 The Crystal Knob xenolith locality

The Crystal Knob volcanic neck (35.806° N, 121.174° W) is a Pleistocene olivine–plagioclase phyric basalt that erupted along the margin of the Franciscan assemblage 500 m west of the Nacimiento Fault in the Santa Lucia Mountains of central California (*Seiders*, 1989). It was described in *Wilshire et al.* (1988) but not studied in detail. The basaltic plug is ~80 m in diameter at the surface and has entrained abundant dunite and sparse spinel peridotite xenoliths [Figure 2.2]. The dunites have textural features typical of igneous cumulates, and olivine aggregates decrease in size to single grain xenocrysts, which are visually indistinguishable from phenocrysts in the basalt groundmass. Sparse spinel peridotites, lacking textures suggestive of cumulate origin, are also present. In conjunction with the compositional data presented below, we interpret the peridotites as entrained fragments of the mantle lithosphere.

Samples were collected from the Crystal Knob basalt with an emphasis on the polyphase peridotite xenoliths. Xenolith samples are 5-10 cm diameter friable peridotites with 200 μm – 1 mm grains. Additionally, samples of the host basalt and dunite cumulates were collected to establish context for the xenoliths.

2.2.1 Petrographic and analytical methods

Polished thin sections of 30 μm thickness were prepared for six peridotite xenolith samples (CK-2 through CK-7) and the basalt host lava (CK-1). The xenolith samples were bound with epoxy prior to sectioning. 1$×$2 inch rectangular thin sections were prepared for two dunite cumulate samples hosted in basalt (CK-D1 and CK-D2). The samples were evaluated under a petrographic microscope to determine their textural and mineralogic features. Characteristic textures of the xenolith samples and basaltic host are shown in Figure 2.3, and their textural characteristics are summarized in Table 2.1.

Electron backscatter intensity images of each thin section were collected using a ZEISS 1550 VP field emission SEM at the California Institute of Technology.

Figure 2.2: Cobble of Crystal Knob alkali basalt containing peridotite xenoliths.

Table 2.1: Summary of petrographic data

Sample	Type	Notes
CK-1	basalt	Host lava containing phenocrysts, xenocrysts, and < 1 cm xenolith fragments [Figure 2.3a]
CK-2	lhz	Fertile lherzolite with pristine textural features
CK-3	hzb	Depleted harzburgite with the largest crystals in the sample set and small equant spinels
CK-4	hzb	Most affected by post-formation melting, with grain-boundary melt veins containing 10-50 μm aggregates of equant amphibole and other phases
CK-5	hzb	Relatively depleted sample, but with more clinopyroxene than CK-3
CK-6	lhz	Fertile, with abundant spinel, large intergrown crystals, and recrystallized aggregates of orthopyroxene and clinopyroxene. Small-scale, vermicular intergrowth of clinopyroxene within orthopyroxene.
CK-7	lhz	Somewhat altered, with small-volume melt veins, but without growth of microcrystalline aggregates (as in CK-4).
CK-D1	dun	Host lava containing dunite and peridotite xenolith fragments. Peridotite fragments contain graphic exsolution lamellae of clinopyroxene within orthopyroxene [Figure 2.3c]
CK-D2	dun	Host lava containing dunite and peridotite xenolith fragments

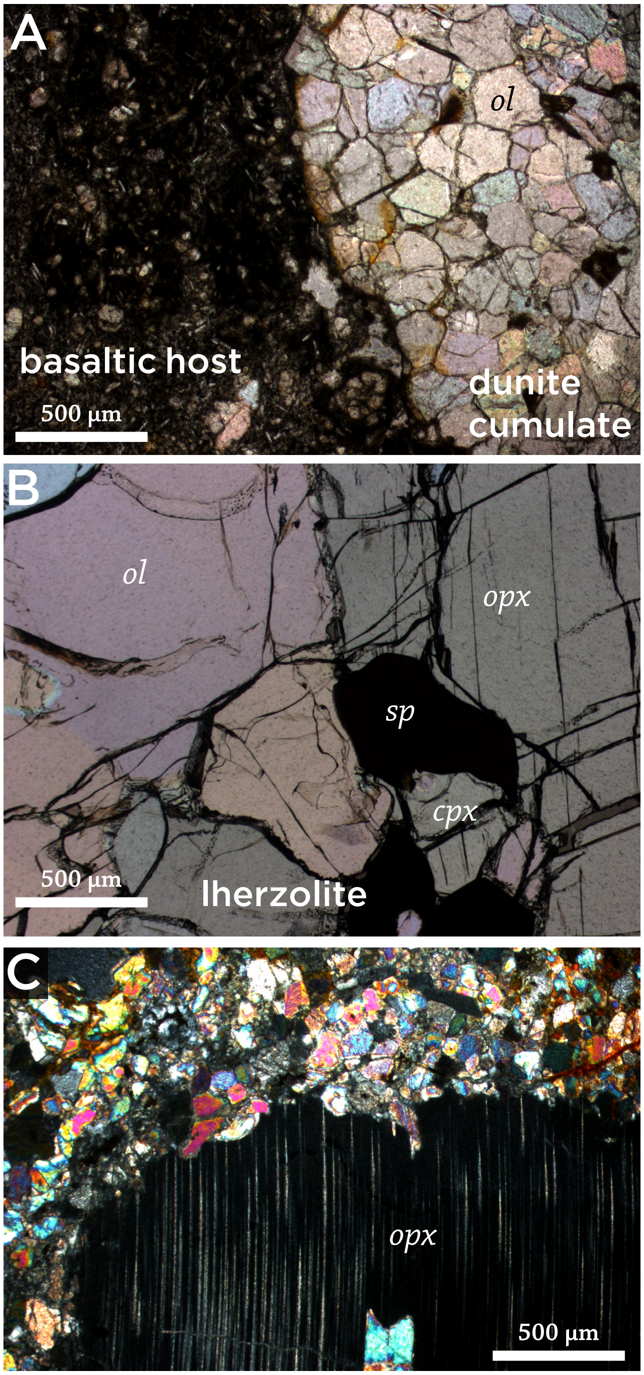

Figure 2.3: Optical petrographic images (2.5 mm wide field of view) showing characteristic textures of the xenolith samples and basaltic host. **(a)** Sample CK-D2, with the edge of a cumulate xenolith composed of equant olivine (ol) grains (~200 μm characteristic scale) set against a host lava groundmass containing <100 μm phenocrysts of olivine, pyroxene, and plagioclase feldspar. **(b)** The spinel lherzolite sample CK-4 with >2 mm olivine, orthopyroxene (opx), clinopyroxene (cpx), and spinel (sp). **(c)** Sample CK-D2, with a single large orthopyroxene crystal with augite exsolution lamellae and containing an olivine inclusion juxtaposed against dunite cumulate material consisting of mosaic-textured olivine grains.

These were coregistered with optical scans and electron-microprobe analysis points using an affine transformation between fixed stage coordinates. Modal mineralogy was mapped on a grid atop these aligned datasets [Figure 2.4].

Major-element compositions were measured on polished thin sections with a five-spectrometer JEOL JXA-8200 electron-probe microanalyzer at the California Institute of Technology. Abundances were counted in wavelength-dispersive mode using a 15 kV accelerating potential, a focused 25 nA beam, and counting times of 20 seconds on-peak and 10 seconds off-peak. The instrument was calibrated using natural and synthetic standards; matrix corrections were made using the CITZAF (*Armstrong*, 1988) algorithm. We performed 1714 measurements across the six peridotite samples, concentrated in 3-4 locations of interest per sample emphasizing areas with orthopyroxene and clinopyroxene in contact to aid in thermometry. We also took 403 measurements of the basaltic host and entrained dunites [Table 2.2].

Minerals were automatically assigned for microprobe measurements using a nearest-neighbor fitting algorithm between pure endmember phases. These analyses were aligned with optical and backscatter imagery and checked for consistency: poor-quality measurements with low totals were automatically flagged for removal (*Taylor*, 1998), and mixed phases along grain boundaries were discarded on a case-by-case basis.

Additional isotope and trace-element geochemical techniques applied to the harzburgite and lherzolite samples are discussed throughout Section 2.2.4.

2.2.2 The basaltic host

The Crystal Knob host rock (sample CK-1) is an alkali basalt with sparse vesicles and abundant plagioclase feldspar, potassium feldspar, clinopyroxene, and olivine phenocrysts. The sample also contains dunite and multiphase peridotite fragments ranging from aggregates of a few grains to ~5 cm xenoliths.

The groundmass is dominated by altered glass and abundant microphenocrysts of potassium and plagioclase feldspar. Though dominantly black, it is mottled with greenish-grey alteration color domains at ~500 μm scale. These domains are crosscut by elongate narrow (~1 mm) shear bands of finer-grained material with sparse

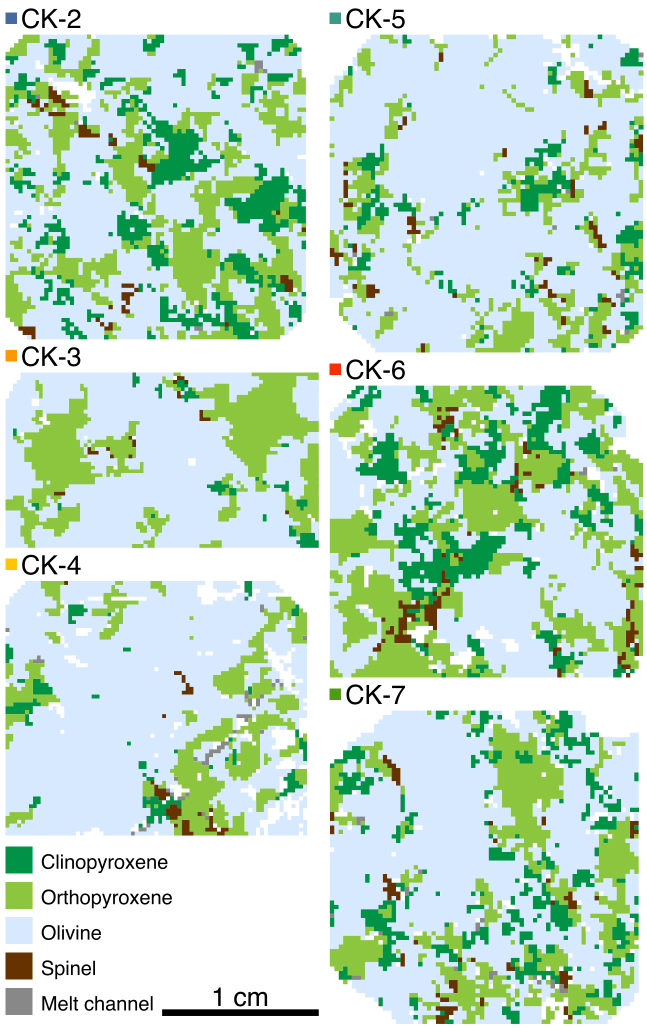

Figure 2.4: Mineral classification images of each sample (1" round thin section) created manually atop coregistered electron backscatter and optical imagery, showing the textural variation within Crystal Knob spinel peridotites. The variable clinopyroxene abundances correspond to fertility. A melt channel cutting diagonally across the bottom-right quadrant of CK-4 (dark gray line) is the most significant textural signature of late-stage melt-interaction in the sample set. These classifications form the basis of recalculated modal abundances [Figure 2.8].

Table 2.2: Xenolith and host lava major-element compositional data

Sample	SiO_2	FeO	MgO	TiO_2	Al_2O_3	Na_2O	CaO	MnO	Cr_2O_3	NiO	K_2O	Total	*n*	Mg#	Cr#
A. Xenolith mineral composition															average of *n* measurements, oxide $\%_{wt}$
Olivine															
CK-2	40.78	9.90	49.08	0.01	0.01	0.01	0.07	0.14	0.01	0.35	–	100.36	48	89.84	–
CK-3	41.00	9.45	49.77	0.02	0.02	0.01	0.10	0.13	0.03	0.35	–	100.88	52	90.37	–
CK-4	40.86	9.06	49.75	0.03	0.03	0.01	0.11	0.13	0.02	0.35	–	100.35	84	90.73	–
CK-5	41.35	10.04	49.41	0.02	0.01	0.00	0.07	0.14	0.01	0.34	–	101.39	28	89.76	–
CK-6	40.72	11.61	48.04	0.02	0.02	0.01	0.11	0.15	0.02	0.30	–	100.99	33	88.06	–
CK-7	40.98	10.47	48.85	0.01	0.01	0.00	0.08	0.15	0.01	0.35	–	100.92	44	89.26	–
Orthopyroxene															
CK-2	54.62	6.42	32.45	0.12	4.65	0.10	0.82	0.14	0.35	0.08	–	99.73	97	90.02	4.79
CK-3	54.97	6.17	32.83	0.12	4.30	0.12	1.11	0.13	0.63	0.09	–	100.45	105	90.46	8.90
CK-4	55.08	5.86	32.90	0.09	3.98	0.11	1.14	0.13	0.67	0.09	–	100.05	134	90.92	10.20
CK-5	55.67	6.49	32.84	0.13	4.63	0.11	0.89	0.14	0.34	0.08	–	101.32	66	90.02	4.69
CK-6	54.43	7.54	31.52	0.12	4.83	0.12	1.11	0.15	0.51	0.08	–	100.41	63	88.17	6.60
CK-7	54.97	6.85	32.54	0.11	4.74	0.11	0.90	0.15	0.36	0.09	–	100.83	68	89.43	4.83
Clinopyroxene															
CK-2	51.41	3.23	15.10	0.51	6.83	1.60	19.95	0.09	0.74	0.04	–	99.51	102	89.27	6.81
CK-3	52.09	3.35	16.34	0.29	5.77	1.33	19.73	0.09	1.19	0.04	–	100.23	115	89.68	12.12
CK-4	51.88	3.19	16.51	0.36	5.37	1.16	19.99	0.09	1.20	0.04	–	99.78	86	90.22	13.23
CK-5	52.39	3.21	15.14	0.60	7.03	1.70	20.08	0.09	0.74	0.04	–	101.02	70	89.38	6.62
CK-6	51.81	4.14	15.83	0.39	6.45	1.35	19.32	0.10	0.96	0.04	–	100.39	53	87.21	9.07
CK-7	51.93	3.55	15.40	0.45	6.81	1.58	19.87	0.09	0.74	0.05	–	100.47	69	88.55	6.83
Spinel															
CK-2	0.04	11.54	20.42	0.09	56.26	0.01	0.00	0.11	9.23	0.36	–	98.06	23	75.92	9.92
CK-3	0.04	13.49	18.89	0.16	45.03	0.01	0.00	0.16	20.22	0.28	–	98.29	28	71.40	23.15
CK-4	0.05	13.53	17.66	0.39	42.48	0.00	0.00	0.16	22.05	0.28	–	96.62	26	69.94	25.84
CK-5	0.03	11.58	20.59	0.12	57.74	0.00	0.00	0.12	9.21	0.34	–	99.74	11	76.02	9.67
CK-6	0.06	15.85	18.38	0.20	49.63	0.01	0.00	0.15	14.70	0.29	–	99.27	14	67.40	16.57
CK-7	0.04	12.61	20.24	0.10	55.82	0.00	0.00	0.13	9.97	0.35	–	99.26	8	74.10	10.70
B. Host lava (CK-1) mineral composition															representative measurement, oxide $\%_{wt}$
Potassium feldspar															
groundmass	64.09	0.47	0.00	0.25	21.26	6.50	1.50	0.01	0.00	–	6.29	100.37	–	1.37	–
Plagioclase feldspar															
groundmass	54.71	0.82	0.01	0.26	27.79	5.27	10.41	0.02	0.01	–	0.30	99.60	–	2.47	–
Olivine															
xenocryst	41.63	9.20	48.94	0.01	0.00	0.01	0.09	0.13	0.01	–	0.00	100.02	–	90.46	–
phenocryst	37.64	28.29	32.67	0.01	0.00	0.01	0.32	0.80	0.00	–	0.00	99.73	–	67.31	–
Clinopyroxene															
xenocryst	47.81	9.04	11.84	2.57	5.31	0.64	22.42	0.23	0.00	–	0.00	99.88	–	70.01	–
phenocryst	51.03	6.85	14.63	1.07	5.59	0.72	19.94	0.20	0.17	–	0.00	100.20	–	79.19	–
C. Xenolith whole-rock composition *recalculated from mineral modes*															normalized oxide $\%_{wt}$
CK-2	45.04	8.26	40.84	0.10	2.19	0.23	2.73	0.13	0.22	0.25	–	100	–	89.73	–
CK-3	44.28	8.50	44.77	0.04	1.20	0.05	0.54	0.13	0.21	0.28	–	100	–	90.37	–
CK-4	43.80	8.23	45.15	0.05	1.12	0.05	0.72	0.13	0.26	0.28	–	100	–	90.50	–
CK-5	43.01	9.13	44.83	0.06	1.25	0.09	1.04	0.13	0.13	0.29	–	100	–	89.68	–
CK-6	45.54	9.46	38.59	0.09	2.79	0.19	2.56	0.15	0.44	0.20	–	100	–	87.78	–
CK-7	43.94	9.06	41.98	0.07	1.93	0.18	2.15	0.14	0.21	0.27	–	100	–	89.05	–

vesicles and phenocrysts.

Petrographic study of dunite fragments within the Crystal Knob basalt reveals residues from multiple stages of melt fractionation. Thin sections CK-D1 and CK-D2 contain dunite and peridotite fragments up to 2 cm in diameter within a basaltic groundmass. The peridotite fragments show textures similar to the polyphase peridotite samples (CK-2 to CK-7). The dunite fragments have textures typical of cumulate residues: finer-grained than the peridotites, they contain similar-sized (typically 50–200 μm), closely-packed olivine grains with melt filling intergrain spaces. Some dunite encases peridotite fragments containing large (up to 2 mm) grains of olivine, pyroxene, and spinel. CK-D1 notably contains a large, pitted, spinel grain embedded in dunite. These dunite cumulates are texturally representative of the majority of xenoliths in the Crystal Knob basalt.

Clinopyroxene in the lava groundmass is separated into two compositional groups: some phenocrysts show an average Mg# of ~76 (Mg# defined as molar Mg/(Mg+Fe) $\cdot$ 100). A separate group of high-Mg# clinopyroxenes (up to Mg# 91) are hosted in xenolith fragments and cores of zoned single grains. Concentrically-zoned clinopyroxene grains with high-Mg# cores up to 300 μm in diameter [Figure 2.5] record multistage crystallization in a progressively evolving magma, and thin, low-Mg# rims suggest that the last phase of fractionation likely occurred during magma ascent and cooling.

Olivine grains in the host lava sample a range from fertile major-element compositions (Mg# $\approx$ 89) through progressively lower Mg#, with cumulate aggregates clustered at Mg#=68 [Figure 2.6a]. We suspect the olivine grains in the basalt represent both fragments of the mantle source (xenocrysts, possibly mechanically separated from entrained peridotites) and cumulates that crystallized at various stages of melt evolution.

2.2.3 Eruptive age

The age of lavas hosting mantle xenolith suites is required to link their petrogenesis to tectonic and geodynamic processes (e.g. *Ducea and Saleeby*, 1998a). The age of the Crystal Knob host lava was determined using the $^{40}Ar/^{39}Ar$ technique on phenocryst plagioclase. A billet of the host lava (sample CK-1) containing visible

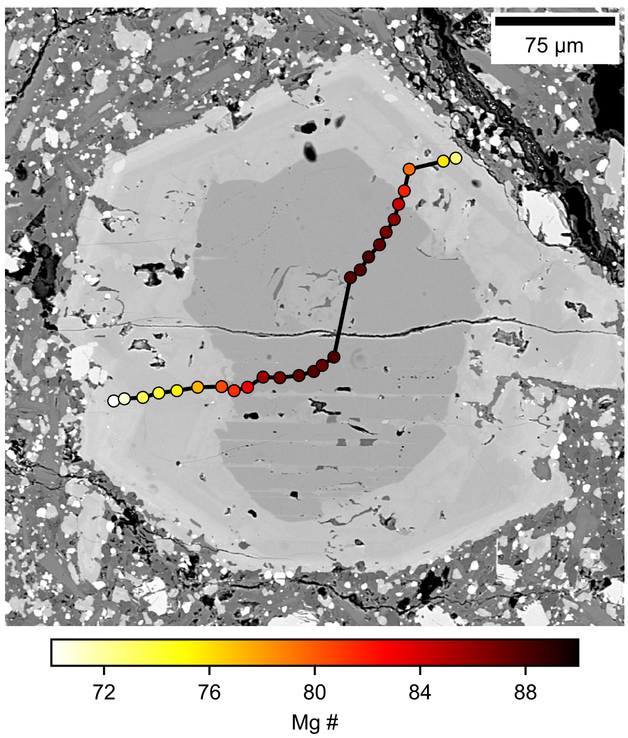

Figure 2.5: Profile of Mg# measured across clinopyroxene phenocryst in the host lava sample CK-1. The grain has a partially cannibalized and fractured xenocryst core with a Mg# of ~90, surrounded by successive layers with lower Mg#, with Mg# 75 material in the outermost 30 µm of the grain.

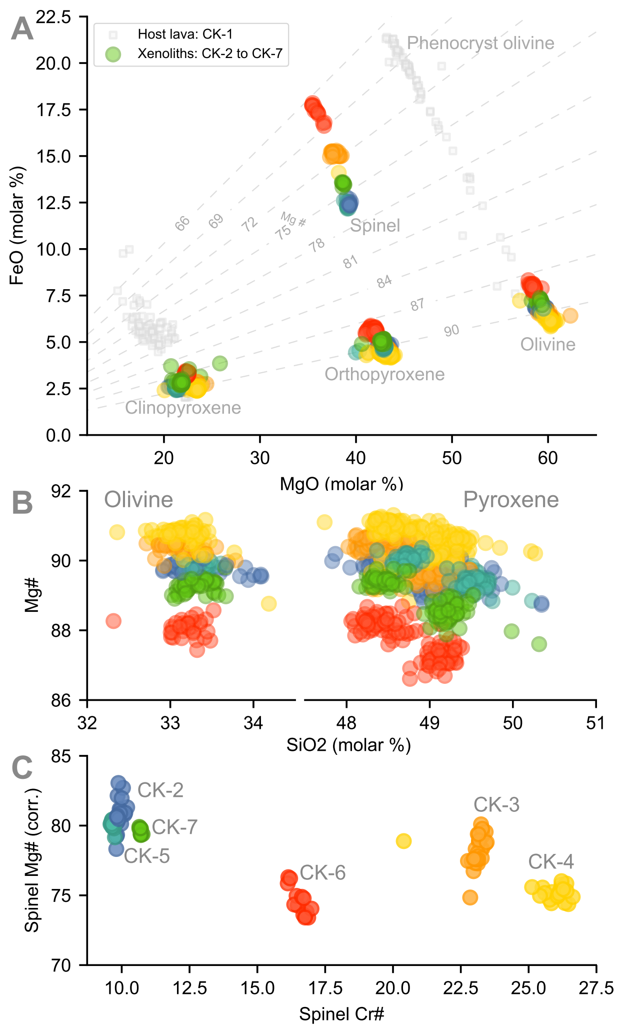

Figure 2.6: Major-element compositional data for the Crystal Knob spinel peridotites and host lavas. The data is colorized by sample in a consistent scheme used until Figure 2.15. **(a)** FeO vs. MgO measured by electron microprobe for grain cores, showing range in major-element depletion between samples. Dotted lines show Mg# levels. **(b)** Mg# (total iron basis) vs. SiO_2 for the silicate phases in the Crystal Knob peridotite xenoliths. This shows the range in major-element depletion between samples, including the low Mg# of CK-6, the most fertile sample. **(c)** Spinel Cr# vs. Mg# (corrected based on cation charge balance) showing grouping of samples by Cr content, corresponding to different levels of depletion. The highest-Cr samples (CK-3 and CK-4) are harzburgite residues. Colors are by sample as labeled in *(c)*.

Table 2.3: Step-heating data for Ar geochronology

Step	Power W	$\frac{^{36}Ar}{^{39}Ar}\times10^3$	$\frac{^{37}Ar}{^{39}Ar}$	$\frac{^{38}Ar}{^{39}Ar}\times10^2$	$\frac{^{40}Ar}{^{39}Ar}$	^{39}Ar mol $\times10^{-12}$	^{39}Ar %	$\frac{Ca}{K}$	$\frac{^{40}Ar^*}{^{39}Ar}$	$^{40}Ar^*$ %	Age Ma
1	1.25	13.54 (42)	0.397 (22)	3.9 (2.9)	4.97 (13)	1.07	0.471	2.87 (16)	1.041 (79)	20.93	2.00
2	1.5	5.116 (52)	0.3354 (27)	2.60 (39)	2.4085 (85)	8.21	3.624	2.429 (20)	0.976 (15)	40.52	1.88
3	1.75	0.927 (21)	0.2368 (16)	2.28 (25)	1.0901 (25)	13.36	5.898	1.716 (12)	0.8805 (66)	80.77	1.69
4	2	0.871 (19)	0.2218 (17)	2.56 (23)	1.0966 (27)	14.36	6.339	1.608 (12)	0.8995 (61)	82.03	1.73
5	2.25	1.284 (17)	0.2037 (12)	2.17 (20)	1.1963 (24)	16.82	7.427	1.4770 (90)	0.8707 (54)	72.79	1.67
6	2.5	1.668 (20)	0.2052 (13)	1.50 (20)	1.2988 (26)	16.22	7.161	1.4882 (94)	0.8586 (61)	66.11	1.65
7	2.75	1.167 (20)	0.2297 (16)	1.28 (24)	1.1311 (27)	13.48	5.952	1.666 (12)	0.8474 (64)	74.92	1.63
8	3	1.124 (22)	0.2570 (22)	0.84 (27)	1.0963 (33)	11.84	5.228	1.865 (16)	0.8331 (72)	75.98	1.60
9	3.5	1.252 (23)	0.3368 (22)	0.98 (28)	1.1016 (31)	11.25	4.968	2.445 (16)	0.8228 (73)	74.67	1.58
10	4	1.905 (33)	0.4860 (34)	0.70 (40)	1.2635 (49)	8.01	3.537	3.529 (25)	0.832 (10)	65.82	1.60
11	4.5	2.020 (42)	0.6755 (46)	0.57 (51)	1.2690 (50)	6.23	2.749	4.906 (33)	0.857 (13)	67.46	1.65
12	5	3.274 (33)	0.7668 (28)	1.04 (28)	1.5669 (40)	11.49	5.073	5.571 (20)	0.806 (10)	51.41	1.55
13	6	3.288 (27)	0.8220 (22)	1.04 (20)	1.6034 (33)	16.30	7.199	5.974 (16)	0.8549 (82)	53.25	1.64
14	8	4.072 (17)	0.89534 (91)	1.306 (82)	1.8180 (15)	42.65	18.831	6.5083 (66)	0.8563 (53)	47.04	1.65
15	10	4.701 (36)	1.1287 (31)	1.28 (24)	2.1567 (51)	13.23	5.844	8.207 (23)	1.074 (11)	49.70	2.06
16	15	6.048 (30)	1.2869 (21)	1.53 (15)	2.4689 (35)	21.97	9.701	9.360 (15)	1.0291 (90)	41.59	1.98

plagioclase lathes was provided to the USGS Geochronology Laboratory in Denver, Colorado. The sample was irradiated in the USGS TRIGA reactor, and plagioclase feldspar grains were step-heated *in situ* using an infrared laser. Loss of ^{39}Ar was measured simultaneously on a Thermo Scientific Argus VI using 4 Faraday detectors (m/e 40-37) and ion counting (m/e 36). The detectors were intercalibrated using standard gas and air pipettes. The measurements are corrected for blanks above baselines, radioactive decay, and nucleogenic interferences, and standardized against a Fish Canyon sanidine with an age of 28.20 Ma. Non-radiogenic argon is assumed to have an atmospheric composition of ^{40}Ar/^{39}Ar = 298.56 (*Cosca et al.*, 2011).

Step-heating data are presented in Table 2.3 and shown graphically in Figure 2.7. Our preferred age of 1.65$\pm$0.06 Ma (2σ) is defined by the twelve intermediate of fifteen heating steps. The entire spectrum defines a similar age, within error, of 1.71 Ma. We infer that the xenoliths were entrained from the upper mantle directly beneath the Crystal Knob volcanic pipe during the mid-Pleistocene.

2.2.4 Spinel peridotite xenoliths

Petrography The spinel peridotite xenoliths (CK-2 through CK-7) are texturally classified using the scheme of *Pike and Schwarzman* (1977). All samples display a xenomorphic texture with anisotropy largely absent. Most samples have minor plastic deformation features, including slight kink bands in some olivine crystals. However, small (~1°) axial rotations between large subgrain crystal domains suggest little to no strain. Samples CK-2 and CK-5 exhibit a weak shape-preferred

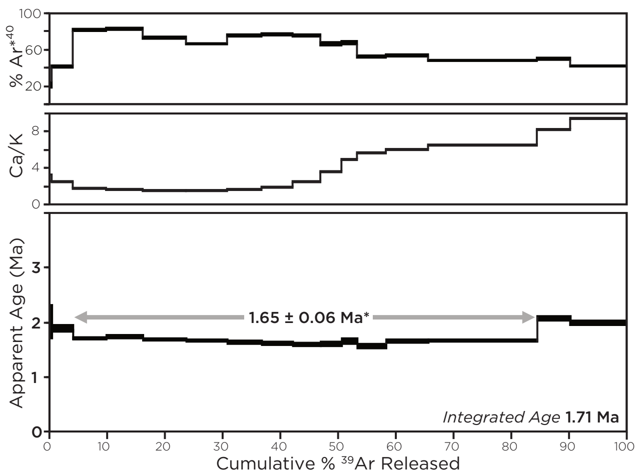

Figure 2.7: Step-heating results for $^{40}Ar/^{39}Ar$ dating of the Crystal Knob host basalt, with a broad plateau for 1.65 Ma and an average of 1.71 Ma.

alignment in elongate spinels [Figure 2.4].

Minor late-stage alteration is seen in all peridotite samples. This includes variably Fe-rich grain boundaries of major phases and Ti enrichment in pyroxene rims (<10 μm from the grain edge). Sample CK-4 contains a thin melt channel that cuts linearly across the thin section [Figure 2.4]. This channel is bounded by resorbed edges of the major phases (olivine and orthopyroxene) and hosts microcrystalline clinopyroxene, 10 μm-scale euhedral spinels, and minor amphibole. Near this melt channel, thin intergranular streamers are enriched in Na and Ti. This grain-boundary melt infiltration is less extensive in sample CK-3 and not present in other samples.

Clinopyroxene and orthopyroxene grains form interlocking crystal domains in all samples. This is most apparent in CK-3 and CK-4, where sparse clinopyroxene is always adjacent to orthopyroxene. Sample CK-7 shows minor exsolution lamellae of orthopyroxene and clinopyroxene. Peridotite fragments in CK-D1 show abundant pyroxene exsolution lamellae [Figure 2.3c], and sample CK-6 shows similar vermicular pyroxene exsolution. CK-6 also contains unique composite pyroxenes, with fused domains marked by substantially different crystal-axis orientations.

Compositions of dominant phases Major-element abundances for the peridotite xenoliths were measured by electron microprobe using methods discussed in Section 4.3. Results are summarized in Table 2.2a and Figure 2.6. Generally, phase

Table 2.4: Spinel ferric iron content[a]

Sample	Fe^{2+}	Fe^{3+}	Fe^{3+}/Σ Fe	Mg#[b]	Mg#[c]	n
CK-2	0.19	0.06	0.25	75.9	80.8	23
CK-3	0.22	0.10	0.31	71.4	78.3	28
CK-4	0.24	0.08	0.24	69.9	75.3	26
CK-5	0.20	0.05	0.21	76.0	80.0	11
CK-6	0.25	0.10	0.29	67.4	74.5	14
CK-7	0.20	0.07	0.27	74.1	79.6	8

[a] estimated from cation site balance
[b] using $Fe^{2+} = \Sigma$ Fe
[c] corrected

compositions show tight per-sample groupings, which suggest equilibrium within each sample. The major silicate phases show Mg# > 87, consistent with fertile or residual mantle compositions. Variations in Mg# between samples indicate differences in melt-extraction and refertilization history between the samples.

Samples CK-2, CK-5, and CK-7 cluster tightly in Fe-Mg space, with relatively low Mg#s indicative of fertile compositions similar to average depleted mantle (*Workman and Hart*, 2005). Silicate phases in CK-3 and CK-4 have Mg# > 90, suggesting a residual composition. Sample CK-6 has low Mg#s for all major phases, with values as low as 87 for clinopyroxenes. All phases in this sample show higher iron abundance than expected for fertile peridotites.

Based on measured phase composition, we correct spinel Mg# from total iron to ferrous iron basis using charge balance on a 4-oxygen basis. This correction results in spinel Mg# between 75 and 81, slightly higher than the uncorrected value [Table 2.4]. Some samples, particularly CK-2, have scatter in corrected Mg# due to unmeasured transition metals (e.g. Zn, Co, V) that are common in oxide minerals. A range of spinel Cr# (molar Cr/(Cr+Al) $\cdot$ 100) from 10 for the fertile samples to 22-27 for CK-3 and CK-4 implies variation in degree of partial melting. Sample CK-6 has an intermediate spinel Cr# [Figure 2.6c].

Modal mineralogy The spinel peridotite samples are dominated by olivine and orthopyroxene, and quantitative modal abundances were measured by mapping phases on a 5000-point grid atop coregistered optical scans and electron backscatter mosaics [Figure 2.4]. Volumetric modes were converted to wt. % using rep-

Table 2.5: Recalculated modal mineralogy[a]

Sample	Olivine	Orthopyroxene	Clinopyroxene	Spinel	Alteration
CK-2	64.29	22.79	12.45	0.46	0.02
CK-3	73.61	25.33	0.97	0.09	0.00
CK-4	76.10	21.44	1.93	0.31	0.22
CK-5	81.13	13.99	4.32	0.53	0.04
CK-6	56.11	31.67	11.14	1.07	0.00
CK-7	71.02	18.45	9.74	0.71	0.07

[a] %wt based on *Nesse* (2000) phase densities

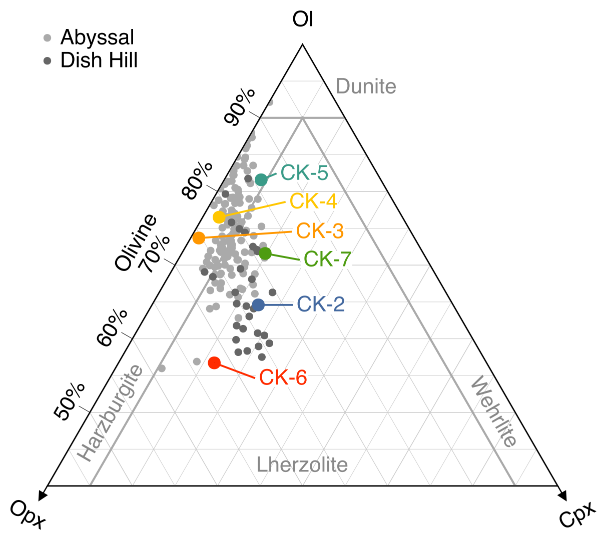

Figure 2.8: Modal composition of Crystal Knob peridotites. Abyssal (*Asimow*, 1999; *Baker and Beckett*, 1999) and Dish Hill (*Luffi et al.*, 2009) peridotite compositions are shown for comparison.

resentative densities for spinel-facies peridotite phases given in *Nesse* (2000) [Table 2.5].

Modal abundance data shows a range in lithology from lherzolites to clinopyroxene harzburgites [Figure 2.8]. All samples contain minor (<1%) spinel. The samples span a range of clinopyroxene content from 12.2% for the fertile lherzolite CK-2 to 0.91%wt for the depleted harzburgite CK-3. The harzburgites have larger grains (500 μm characteristic scale) than the lherzolites (~200 μm), and CK-3 contains 2 mm orthopyroxene crystals. All samples are Type I peridotites in the *Frey and Prinz* (1978) classification system.

Whole-rock composition Whole-rock major-element abundances are reconstructed from averaged mineral composition and estimated modes. Representative mineral compositions are given in Table 2.2a, and recalculated whole-rock compositions in Table 2.2c. Whole-rock Mg# ranges from 87 to 91. Within each sample, a consistent Mg# for all silicate phases [Figure 2.6] is indicative of Fe-Mg equilibrium. All samples contain <1%wt spinel, with Mg# variation mirroring that of the silicate phases.

Samples CK-2, CK-5, and CK-7 have Mg# between 89 and 90 (both for individual silicate phases and reconstructed whole-rock measurements). CK-3 and CK-4 have a whole-rock Mg# > 90. CK-6 has a whole-rock Mg# < 88 and contains substantially more Cr, Al, and Fe than the other samples. Though CK-6 is generally the most enriched in incompatible elements, sample CK-2 contains somewhat more Ca and Na. Both of these samples have fertile major element compositions.

Discussion of peridotite composition The coincident low Mg# and spinel Cr# of the lherzolite samples CK-2, CK-5, and CK-7 implies that they are fertile to partially depleted peridotites, with low melt volumes extracted (assuming no refertilization). These samples contain consistently fertile phases (Mg# of ~89), with variation in whole-rock composition coupled primarily to changing phase abundances: the samples show a range in olivine abundance from 65 to 75%wt [Figure 2.8] without adjustment in equilibrium phase compositions, suggesting low to moderate levels of depletion.

The harzburgite samples CK-3 and CK-4 contain high-Cr# spinels and high Mg# (>90) silicate phases. These features, along with low (<2%) clinopyroxene modes, are typical of residues of high-degree partial melting. The depleted phase compositions and abundance of refractory Cr in spinel indicate almost-complete removal of incompatible lithophile elements (*Dick and Bullen*, 1984).

CK-6 is a clear anomaly: high-iron phase compositions [Figure 2.6b], low whole-rock Mg#, and high clinopyroxene modal abundances [Figure 2.8] are markers of fertility, but intermediate spinel Cr# and abundant orthopyroxene are typical of depleted residues. We propose a two-stage history, where the highly fertile major-element composition of CK-6 was gained by assimilation of a fractionated, Fe-rich melt into a partially depleted residue. In this case, excess pyroxene would have

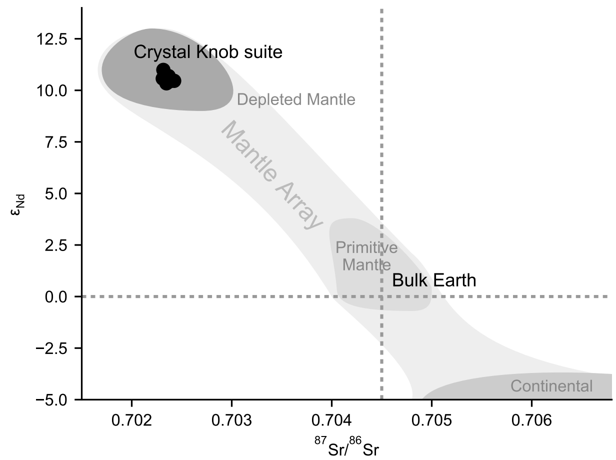

Figure 2.9: Paired Sm-Nd and Rb-Sr isotope data for the Crystal Knob sample set contextualized relative to major Earth reservoirs. The position of Crystal Knob within the "depleted mantle" field suggests that the mantle lithosphere underlying coastal California was sourced directly from shallow mantle material with no continental component, either beneath a mid-ocean ridge or by direct underplating.

formed due to the addition of silica to an olivine-rich residual assemblage, and the relatively chromian spinels represent a pre-refertilization vestige. We explore the potential depletion and re-enrichment of these samples further in Section 2.2.6.

2.2.5 Rb-Sr and Sm-Nd isotopes

Portions of each spinel peridotite sample were crushed using a disk mill at the California Institute of Technology. Clinopyroxene grains (150–300 µm, 35-45 mg per sample and free of visible inclusions and alteration) were picked by hand under a binocular microscope. These clinopyroxene separates were analyzed for strontium and neodymium isotopes at the University of Arizona, Tuscon following the procedures described in *Otamendi et al.* (2009) and *Drew et al.* (2009). The samples were spiked with mixed ^{147}Sm-^{150}Nd tracers (*Wasserburg et al.*, 1981; *Ducea and Saleeby*, 1998b). Rb was measured on a quadrupole ICP-MS, while Sr was measured in static multicollector mode on a VG 54 instrument. Sm was analyzed using a static routine on a VG Sector 54 multicollector thermal-ionization mass spectrometer, and Nd was measured as an oxide on a multicollector VG 354 instrument. Results are presented in Table 2.6.

All samples are enriched in radiogenic ^{143}Nd (time-corrected ϵ_{Nd} from 10.3 to

Table 2.6: Radiogenic isotope measurements

Sample	Sm	Nd	$\frac{^{147}Sm}{^{144}Nd}$	$\frac{^{143}Nd}{^{144}Nd[0]}$	$\Delta t \times 10^6$	ϵ_{Nd}	T_{CHUR}	Rb	Sr	$\frac{^{87}Rb}{^{86}Sr}$	$\frac{^{87}Sr}{^{86}Sr[0]}$	$\Delta t \times 10^7$
CK-2	1.388	2.994	0.28041	0.51319	-3.03	10.69	1.00	0.055	42.704	0.00370	0.70237	-0.85
CK-3	1.783	3.988	0.27031	0.51317	-2.92	10.34	1.10	0.342	49.802	0.01976	0.70235	-4.53
CK-4	1.087	2.539	0.25877	0.51320	-2.79	10.99	1.38	0.058	41.610	0.00403	0.70232	-0.92
CK-5	1.313	3.335	0.23799	0.51318	-2.57	10.57	1.99	0.354	52.082	0.01956	0.70231	-4.49
CK-6	1.470	3.285	0.27053	0.51317	-2.92	10.46	1.10	0.135	38.320	0.01009	0.70242	-2.31
CK-7	0.482	1.105	0.26379	0.51317	-2.85	10.42	1.21	0.092	13.665	0.01934	0.70237	-4.44

Δt is a time correction of the preceding measured isotope ratio to eruptive conditions ($t = 1.65$ Ma).

11.0) and depleted in ^{87}Sr (time-corrected ^{87}Sr/^{86}Sr of .702). These values are well below those of 0.708 recorded by Salinian granites (*Kistler and Champion*, 2001; *Chapman et al.*, 2014), suggesting that the mantle lithosphere sampled by Crystal Knob is sourced from a different mantle reservoir than the overlying crust of the central California coast. More broadly, this pattern of strong depletion in large-ion-lithophile elements is characteristic of the depleted convecting mantle. This signature rules out an origin in the sub-cratonic mantle lithosphere or Mesozoic mantle wedge beneath western North America (*Ducea and Saleeby*, 1998a; *Wilshire et al.*, 1988; *Luffi et al.*, 2009) and suggests an origin in the asthenospheric or underplated oceanic mantle (*DePaolo and Wasserburg*, 1976; *McCulloch and Wasserburg*, 1978).

2.2.6 Trace Elements

Trace element concentrations were acquired for pyroxene grains in each xenolith sample, using a Cameca IMS-7f-GEO magnetic-sector secondary ion mass spectrometer (SIMS) at the California Institute of Technology. Two to three each of orthopyroxene and clinopyroxene grains were targeted per xenolith sample. Measurements were acquired with 9 kV beam flux and a 100 μm spot size. The USGS glass standard NIST 610 was used as an external standard for all elements (*Gao et al.*, 2002). Minimal variation in measured concentration was observed at grain and sample scale, though clinopyroxene in CK-6 and orthopyroxene in CK-7 show differences outside of analytical error in Ba, La, and Ce (potentially attributable to concentrations near SIMS detection limits). Other measurements are largely concordant and results are presented as within-sample averages in Table 2.7 and Figure 2.10. Whole-rock trace element abundances [Table 2.7 and Figure 2.11a] are estimated by scaling measured concentrations in clinopyroxene and orthopyrox-

Table 2.7: Trace element abundances (ppm)

Sample	La	Ce	Pr	Nd	Sm	Eu	Gd	Tb	Dy	Ho	Er	Tm	Yb	Lu	n
Clinopyroxene															
CK-2	1.09	2.70	4.47	7.18	10.98	11.33	12.21	13.79	14.18	14.25	14.33	12.45	14.27	13.29	3
CK-3	9.05	8.03	6.46	6.09	6.57	4.80	8.07	8.04	8.52	8.49	8.40	6.61	8.43	4.96	3
CK-4	15.89	11.10	8.69	7.39	5.14	5.05	4.85	3.97	5.17	6.10	5.53	5.72	6.56	5.56	2
CK-5	12.18	12.23	11.73	12.35	12.84	13.66	14.24	15.51	15.43	16.38	14.97	14.62	15.78	11.94	2
CK-6	6.60	6.72	6.41	7.78	9.35	10.77	11.17	12.08	11.81	12.02	10.83	10.67	11.44	9.31	3
CK-7	5.24	5.76	7.33	9.02	12.38	17.48	13.15	16.08	14.25	14.68	13.49	13.44	14.99	11.20	2
Orthopyroxene															
CK-2	0.00	0.01	0.02	0.03	0.10	0.48	0.21	0.31	0.50	0.58	0.78	1.07	1.55	1.87	3
CK-3	0.04	0.03	0.04	0.04	0.10	0.20	0.15	0.22	0.38	0.53	0.67	0.74	0.95	1.11	4
CK-4	0.10	0.13	0.19	0.19	0.23	0.27	0.26	0.26	0.38	0.44	0.64	0.66	1.08	1.00	2
CK-5	0.02	0.03	0.05	0.07	0.11	0.08	0.21	0.38	0.46	0.66	0.83	0.96	1.59	1.90	2
CK-6	0.03	0.03	0.05	0.07	0.14	0.25	0.28	0.46	0.57	0.78	0.88	1.20	1.53	1.68	3
CK-7	0.02	0.03	0.04	0.04	0.12	0.16	0.22	0.38	0.51	0.64	0.87	1.03	1.50	1.71	3
Whole-rock (recalculated from modal mineralogy)															
CK-2	0.14	0.34	0.56	0.90	1.39	1.52	1.57	1.79	1.88	1.91	1.96	1.79	2.13	2.08	–
CK-3	0.10	0.09	0.07	0.07	0.09	0.10	0.12	0.13	0.18	0.22	0.25	0.25	0.32	0.33	–
CK-4	0.33	0.24	0.21	0.18	0.15	0.16	0.15	0.13	0.18	0.21	0.24	0.25	0.36	0.32	–
CK-5	0.53	0.53	0.51	0.54	0.57	0.60	0.64	0.72	0.73	0.80	0.76	0.77	0.90	0.78	–
CK-6	0.74	0.76	0.73	0.89	1.09	1.28	1.33	1.49	1.50	1.59	1.48	1.57	1.76	1.57	–
CK-7	0.51	0.57	0.72	0.89	1.23	1.73	1.32	1.64	1.48	1.55	1.47	1.50	1.74	1.41	–

ene to mineral modes. Olivine is excluded from calculations, which is of minimal impact as rare-earth elements (REEs) are 2-3 orders of magnitude less compatible in olivine than in clinopyroxene (*Witt-Eickschen and O'Neill*, 2005; *Luffi et al.*, 2009). The resulting whole-rock trace element compositions correct for decreasing modal pyroxene abundances during depletion.

Clinopyroxene, orthopyroxene, and recalculated whole-rock rare-earth elements show the effects of both depletion and refertilization. The samples show a range of depletion in rare-earth elements relative to depleted mantle, and clinopyroxene HREEs (heavy REEs) follow patterns seen in abyssal peridotites (*Warren*, 2016) and consistent with single-stage depletion. Elevated LREEs (light REEs) suggest later refertilization. Whole-rock trace elements also record this pattern, but the incorporation of modal abundances highlights the range in REE depletion: sample CK-5 in particular has much lower REE concentrations than its clinopyroxene abundances would suggest, due to low clinopyroxene modes.

Modeling depletion and re-enrichment The partial correspondence of the trace-element dataset to abyssal peridotites suggests that enrichment can be compared to a typical mantle fractional melting history. We construct a melt-partitioning model to determine the degree of depletion of the Crystal Knob xenolith samples and distinguish between potential enriching agents [Figure 2.11a].

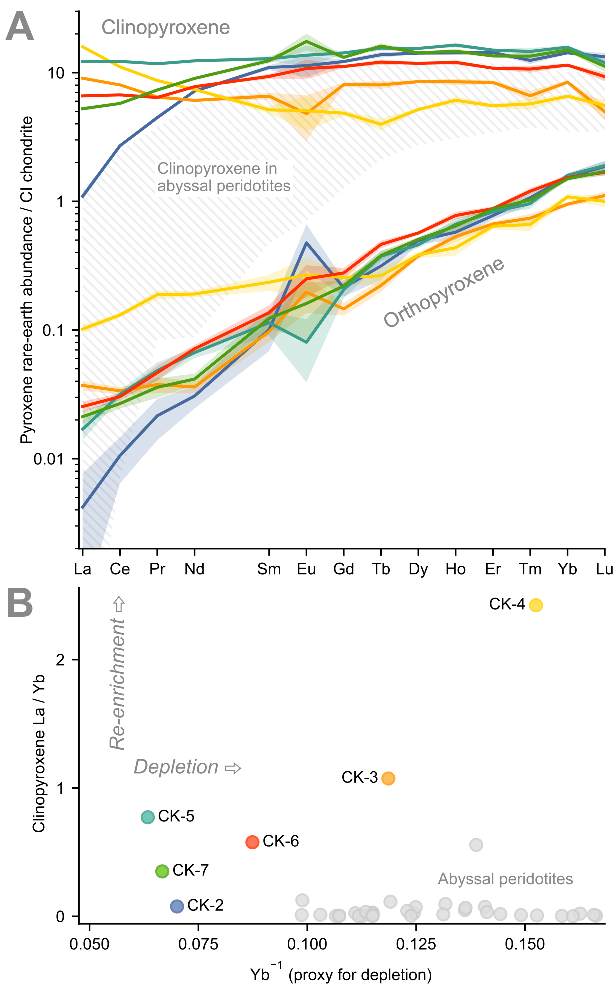

Figure 2.10: (a) Chondrite-normalized pyroxene rare-earth element abundances showing the range in depletion and re-enrichment in the Crystal Knob sample set. **(b)** Element-ratio proxies for depletion and re-enrichment of clinopyroxene rare-earth elements, showing that samples have a range of depletion characteristics and levels of re-enrichment. Colors are by sample as labeled in *(b)*.

A generic model of peridotite depletion is constructed in *alphaMELTS* (*Smith and Asimow*, 2005), using the pMELTS family of algorithms. A parcel of material is tracked along an isentropic fractional melting path (1% melt porosity) starting at a mantle potential temperature of 1350°C, 3.0 GPa, and a depleted MORB mantle (DMM) composition (*Workman and Hart*, 2005). Trace-element partition coefficients from *Lee et al.* (2007) are used to track these components, and we confirm that garnet is removed from the evolving system at ~2.0 GPa. These starting parameters were chosen to provide the best correspondence with the overall experimental dataset. A wide range of initial conditions (up to 1500°C at 3.0 GPa) provides similar results for the shape of depleted trace-element profiles, and the mapping of predicted composition to temperature depends on starting conditions.

The samples are fit to model steps along this adiabatic path using minimization of the squared deviations of measured values from model HREE (Er–Lu) compositions. HREE concentrations can reasonably be assumed to be a proxy for depletion, since HREEs are highly compatible, have low diffusion rates, and are not easily modified by late re-enrichment. Thus, the best-fitting decompression step gives a model composition for the samples after single-stage depletion. The measured composition of sample CK-2 matches this modeled composition across the REEs, while other samples have much higher LREE concentrations than is reasonable for residues of decompression melting.

In a second arithmetic step, the best-fit depleted profile is subtracted from measured REE. Excess REE in the sample (typically LREE) is interpreted as the contribution from batch addition of an enriching melt. To improve comparability of the trace-element pattern with that of potential enriching agents, the model is normalized to an average HREE of 6$\times$primitive mantle, a typical HREE concentration for both normal MORB (*Sun and McDonough*, 1989) and alkali basalt (*Farmer et al.*, 1995). The slope of the resulting normalized profile is diagnostic of the relative abundance of trace elements in the re-enriching agent. The normalization factor employed to shift the composition of enriching fluids to this value [Figure 2.11b] is proportional to the amount of material added during re-enrichment (assuming a consistent composition).

The model results show that partial melting, followed by re-enrichment by al-

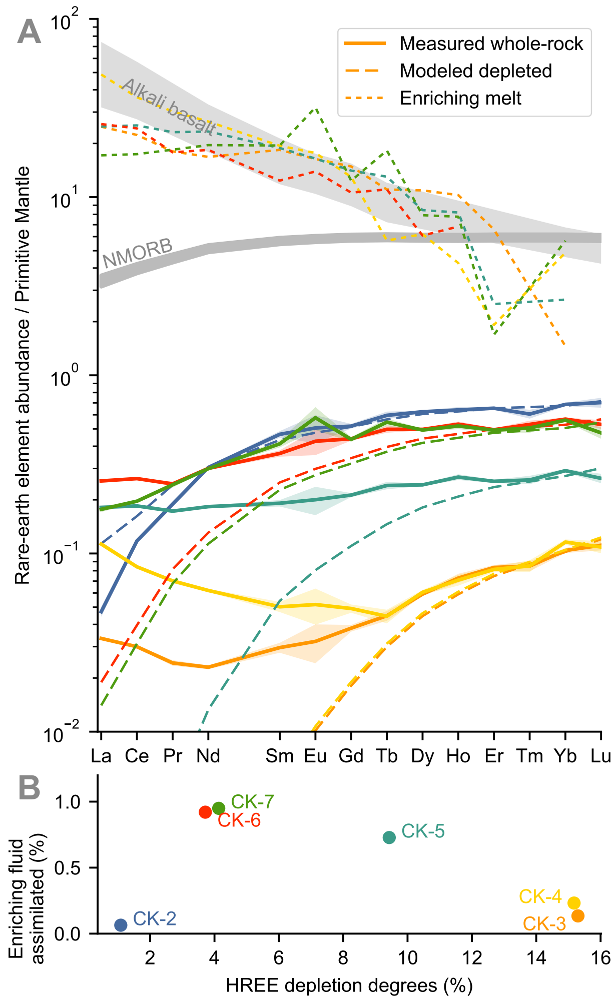

Figure 2.11: (a) Recalculated whole-rock trace elements for xenolith samples [Table 2.7] presented with best-fitting modeled compositions for depleted peridotite and enriching fluid, using the model discussed in text. The rare-earth compositions of normal mid-ocean ridge basalt (NMORB) (*Sun and McDonough*, 1989) and alkali basalt (*Farmer et al.*, 1995) are presented for comparison with the modeled composition of the enriching fluids, which closely resemble alkali basalt for all samples. Sample CK-2 shows no excess enrichment, and a hypothetical re-enriching fluid composition is not calculated. **(b)** REE depletion and re-enrichment trends for xenolith samples derived from modeling shown in *(a)*. For all samples, <1% assimilation of alkali-basalt-like melt is required to explain the observed trends of REE re-enrichment.

Table 2.8: Melting degrees estimated using MgO, Al_2O_3, and HREE content.

Sample	$F_{HREE}(\%)$	$F_{MgO(\%)}$	$F_{Al_2O_3(\%)}$
CK-2	1.1	7.0	11.6
CK-3	15.3	17.4	17.2
CK-4	15.2	18.3	17.6
CK-5	9.4	17.5	16.9
CK-6	3.7	0.3	7.9
CK-7	4.1	10.3	13.1

kali basalt, can explain the trace-element variability within the Crystal Knob sample set. REEs in the fertile lherzolite CK-2 follow the modeled trend for nearly undepleted peridotite [Figure 2.11]. Enrichment by the assimilation of small amounts (<1%) of a melt with a trace-element pattern similar to alkali basalt is reasonable for all samples [Figure 2.11b]. The low pyroxene modes in samples CK-3 and CK-4 lead to pronounced LREE enrichment, with the assimilation of small masses of enriching melt greatly increasing normalized abundances. However, if HREEs have been substantially enriched (as may be the case for sample CK-6), excess LREE is a minimum constraint on re-enrichment.

Primary depletion degrees are estimated by finding the pMELTS model compositions that best fit the whole-rock HREE, MgO, and Al_2O_3 composition of each xenolith sample [Table 2.8]. Results show trends superficially similar to those in modal abundance [Figure 2.8] and trace element [Figure 2.10] data.

Discussion of trace elements The HREE compositions and modeled depleted REE profiles of the Crystal Knob xenoliths are similar to those found in abyssal peridotites (*Johnson et al.*, 1990), suggesting that the xenoliths are residues of progressive fractional melting of primitive mantle at the mid-ocean ridge. Trace element patterns, and their alignment with phase composition and modal abundance, suggest that HREE depletion within the Crystal Knob samples is primary, without significant HREE re-enrichment. These trends are a proxy for fertility, and the lherzolite CK-2 is essentially undepleted and apparently has not been fractionally melted.

The variably elevated LREE content of all samples except CK-2 is not present in abyssal peridotites [Figure 2.10] and suggests secondary re-enrichment by LREE-

Table 2.9: Results of two-pyroxene thermometers

Sample		TA98 [°C]	BKN [°C]	Ca-Opx [°C]	n_{opx}	n_{cpx}	REE [°C]
CK-2	core	949 (12)	1010 (10)	992 (4)	52	23	973 (9)
	rim	953 (21)	1012 (20)	1001 (8)	26	72	
CK-5	core	962 (22)	1030 (23)	980 (4)	49	44	956 (13)
	rim	953 (19)	1018 (20)	1020 (114)	65	22	
CK-7	core	976 (8)	1029 (8)	1008 (5)	31	45	961 (10)
	rim	1002 (15)	1060 (22)	1026 (50)	33	28	
CK-4	core	1037 (15)	1075 (19)	1085 (4)	75	44	1071 (24)
	rim	1049 (9)	1093 (12)	1089 (14)	43	50	
CK-3	core	1042 (4)	1088 (4)	1069 (4)	44	65	1025 (17)
	rim	1043 (9)	1091 (10)	1083 (27)	67	60	
CK-6	core	1057 (14)	1093 (15)	1078 (4)	35	33	1087 (10)
	rim	1075 (5)	1110 (6)	1084 (11)	34	21	

For major-element thermometers, σ (in parentheses) represents errors between individual measurements. For REE thermometer, it is regression error.

rich material at depth. Our modeling of whole-rock depletion and re-enrichment suggests a similar degree of LREE refertilization for all samples except CK-2, corresponding to a volumetrically minor <1% bulk assimilation of fractionated basaltic melt. The most pronounced LREE enrichments occur in infrequent clinopyroxene grains in depleted harzburgites (CK-3 and CK-4), and may arise from the preferential assimilation of REEs in sparse clinopyroxene. Sample CK-6 contains high LREEs in excess of those formed at any stage of fractional melting. This suggests that CK-6 assimilated a significant amount of more-evolved melt and has a trace-element profile (including HREE composition) formed by refertilization.

2.2.7 Major-element thermometry

Electron-microprobe major-element data is used as the basis for pyroxene Ca–exchange geothermometry. Several complementary formulations are used: BKN (*Brey and Köhler*, 1990) and TA98 (*Taylor*, 1998) are two slightly different formulations based on empirical calibration of the two-pyroxene Ca exchange reaction in simple and natural systems. TA98 is explicitly calibrated to account for errors arising from high Na content. The Ca-in-orthopyroxene thermometer (*Brey and Köhler*, 1990) is formulated for use in the absence of clinopyroxene. Results are shown in Table 2.9 and Figure 2.12.

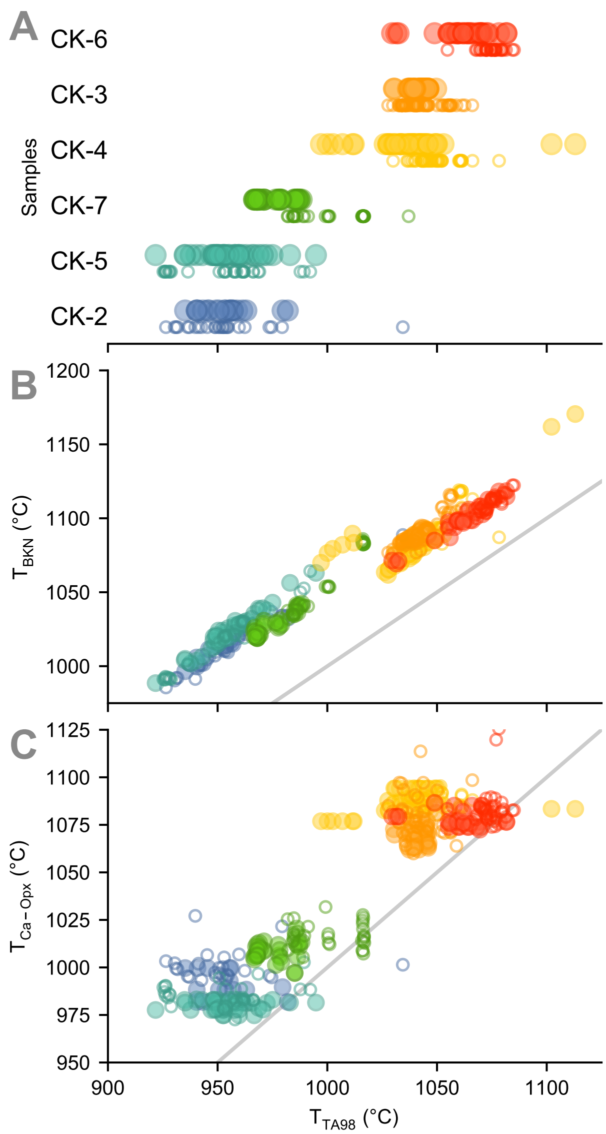

Figure 2.12: Comparison of results from pyroxene major-element thermometers. **(a)** TA98 core and rim measurements (filled and open circles, respectively) categorized by sample. Samples CK-3, CK-4, and CK-7 show elevated grain rim temperatures, and core temperatures largely fall within a 25-50 °C range for each sample. **(b)** TA98 and BKN temperatures showing a strong linear relationship, with BKN estimates higher by 30-70 °C. **(c)** Ca-in-orthopyroxene and TA98 temperatures, showing the reproduction of two temperature cohorts around 980 and 1080°C by the Ca-in-orthopyroxene thermometer. Colors are by sample as labeled in *(a)*. Grey lines show 1:1 relationship.

Core and rim compositions are separated to assess within-sample temperature disequilibrium and late-stage (e.g. eruptive) heating. Analytical errors (caused by uncertainty in microprobe data) are small, on the order of 5°C (1σ). Other sources of error include the calibration of the thermometer and potential bias from within-sample disequilibrium. *Taylor* (1998) reports residuals of calibration of the thermometer to experimental data, which yield total errors of 50-60°C (1σ). Unreported calibration errors for the BKN and Ca-OPX thermometers are likely similar in scale (*Taylor*, 1998). In practice, error distributions based on calibration with heterogeneous experimental samples likely form an upper bound on relative errors.

Within-sample variation in temperatures is a proxy for the relative error of recovered temperatures. Measured pyroxene compositions are grouped by location, and separate temperatures are calculated for each nearest-neighbor pair of orthopyroxene and clinopyroxene. Analytical errors are propagated through the calculation. The resulting distribution of temperatures for grain cores and rims for each sample (with n ranging from 19 to 74 pairs per group) accounts for within-sample variation and provides an approximation of measurement precision.

Thermometer results Average TA98 temperatures range from 957 to 1063°C for cores and 955 to 1054°C for rims [Table 2.9]. CK-2 core temperatures indicate more complete equilibration, with a standard deviation of only 2.3°C (compared with 8.2-12.4°C for all other samples). Core temperatures for individual grain pairs are distributed roughly normally, and clustered temperatures in a ~25-50°C range for each sample suggest that aggregated grain-pair temperatures model errors around true sample equilibrium temperatures. Outlying core temperatures in samples CK-4 and CK-6 may indicate two-pyroxene major element disequilibrium at millimeter scale. In CK-4, a few core TA98 temperatures of 1100°C are likely related to late-stage diffusion during entrainment and eruption.

Rim temperatures (measured ~10 μm from grain edges) are generally higher than core temperatures, although the level of disparity varies widely between samples. CK-2 shows only modestly elevated rim temperatures, while CK-3 and CK-6 show significant scatter to temperatures ~180°C higher than grain cores (CK-5 and CK-7 contain a few measurements of this type as well). High and variable rim compositions may be related to melt infiltration during entrainment and eruption, but with significant mobilization of cations limited to grain rims. CK-4, which shows high core temperatures and the most significant petrographic evidence of melt infiltration, lacks high-temperature rim compositions, suggesting equilibration at high temperature, possibly in the Crystal Knob melt.

Discussion of two-pyroxene thermometry Different two-pyroxene thermometers produce similar results, suggesting that temperature measurements are robust estimates of sample equilibrium temperatures [Figure 2.12]. The Ca-in-OPX thermometer shares its calibration with BKN (*Brey and Köhler*, 1990) and sensibly yields coincident results. The low within-sample scatter of Ca-in-OPX temperatures likely results from fast diffusion and re-equilibration of small amounts of Ca in orthopyroxene. TA98 and BKN temperatures have a strong linear relationship, with BKN temperature estimates higher by up to 50°C. This relationship mirrors the findings of *Nimis and Grütter* (2010) and can be expressed as $T_{\mathrm{BKN}} = 0.9T_{\mathrm{TA98}} + 145$ [°C]. *Nimis and Grütter* (2010) advise the preferred use of TA98 based on experimental validation. Given the largely predictable results of two-pyroxene thermometers, we accept their preference for further analysis.

The samples can be divided into two cohorts based on equilibration temperature. A cooler group (samples CK-2, CK-5, and CK-7) has grain core temperatures clustered at ~970°C (TA98). A hotter group (samples CK-3, CK-4, and CK-6) has a mean temperature of ~1050°C (TA98). The division between these two groups is robust, apparent in all thermometers, and aligned with geochemical differences within the sample set. The hotter samples have higher spinel Cr# and greater HREE depletion, and the range of temperatures likely records the sourcing of two sets of xenoliths from different depths within a magmatic ascent system. Throughout this paper, the samples are color-coded, with blue-green corresponding to the low-temperature array, and red-yellow representing the high-temperature samples [Figure 2.6-2.15].

2.2.8 REE-in-pyroxene thermometry

We use the *Liang et al.* (2013) REE-in-two-pyroxene thermometer to estimate sample equilibration temperatures using an independent system. The relative immo-

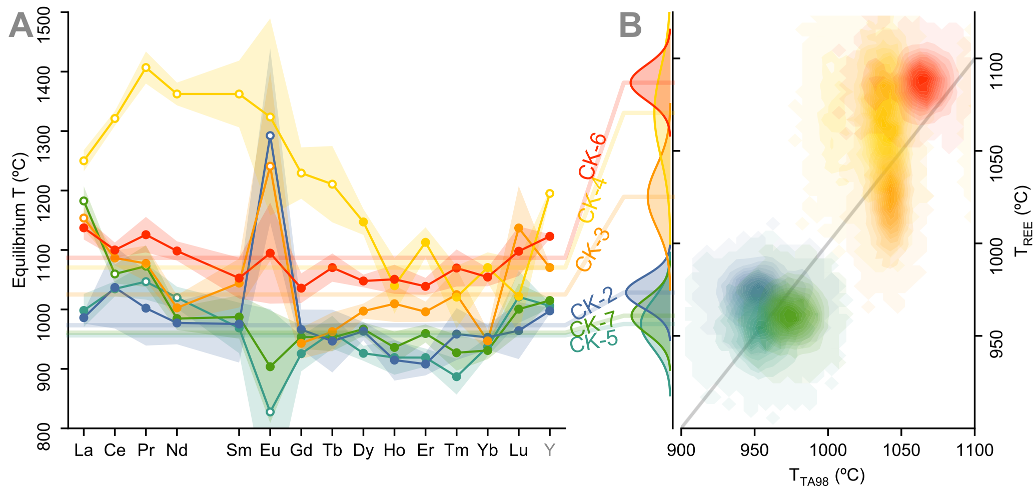

Figure 2.13: REE thermometry of xenolith samples. **(a)** Per-element equilibrium temperatures with projection of best-fitting sample temperature as horizontal lines for each sample. Data points far from the horizontal line signify disequilibrium between pyroxene phases, and those outliers plotted with open circles are excluded from the fit. **(b)** Best-fitting REE temperatures for each sample with Gaussian error bounds, plotted against a kernel density distribution of TA98 major-element temperatures. Joint error distributions are created using a Monte Carlo approach for both error distributions. This approach shows significant disequilibrium in Eu and across LREE for sample CK-4. The samples can be grouped into two temperature cohorts, with all samples, especially the low-temperature group, agreeing well with the TA98 thermometer. Colors are by sample.

bility of REEs allows assessment of equilibrium temperatures over longer timescales than those queried with two-pyroxene cation exchange thermometry.

Rare-earth abundances are compiled for SIMS measurements of pyroxene phases in contact (2–3 pairs) for each xenolith sample. A two-pyroxene equilibrium is calculated for each REE and Y, and is shown in Figure 2.13a. A robust regression with a Tukey biweight norm is used to find the equilibrium temperature for each sample. Significant outliers from the fit are excluded from thermometry and discussed below. Measured temperatures are between ~950 and 1100 °C for the sample set [Table 2.9] and broadly correspond to TA98 temperatures for each sample [Figure 2.13b and Figure 2.14], although some differences may be diagnostic of preserved fossil heating events.

Pyroxene rare-earth disequilibrium CK-3 shows misfit in La, while CK-5 and CK-7 have disequilibrium in several LREEs. Sample CK-4 shows major disequilibrium in the light and medium REEs, with only elements heavier than Ho retaining a linear relationship.

The pattern of disequilibrium in sample CK-4 could force assimilation of REEs into orthopyroxene, effectively raising the LREE mineral-melt partition coefficient $D^{\mathrm{opx/cpx}}$ relative to HREEs. The shape of this disequilibrium may be due to the parabolic nature of the partition curves for both pyroxene phases, which are incompletely modeled by a linear relationship when offset (*Blundy and Wood*, 2003; *Sun and Liang*, 2012). The incorporation of more LREEs into orthopyroxene due to low clinopyroxene modes [Figure 2.10] could also magnify any miscalibration of the thermometer. Regardless, since measured LREEs are consistently enriched, with low analytical errors for both orthopyroxene and clinopyroxene, we conclude that anomalies in LREE temperature do not signal disequilibrium compositions.

All samples except CK-6 and CK-7 show results off the linear trendline for Eu. This disequilibrium, discussed in *Sun and Liang* (2012), is dependent on the oxygen fugacity (and Eu^{2+}/Eu^{3+} ratio) of the host magma. In normal magmas, this pattern could also arise from the effect of "ghost" plagioclase, which can create local Eu enrichments and depletions in the neighborhood of resorbed plagioclase grains. This would suggest that the xenoliths originated in the shallow mantle lithosphere and were transported deeper, causing plagioclase breakdown. Discerning between these scenarios is difficult due to Eu abundances near ion microprobe detection limits.

Two-pyroxene REE disequilibrium can be explained by a fossil heating event that was retained only in REEs due to their slow diffusion rates. This must have happened prior to subsolidus major-element re-equilibration, and is thus unrelated to the Crystal Knob eruption. Potential causes include focused heating of sample CK-4, poorly understood equilibrium partition coefficients (for instance, due to reducing mantle conditions), and incomplete linearizing assumptions in the *Liang et al.* (2013) thermometer. Untangling these effects is beyond the scope of this work but presents several opportunities for further study.

Comparison with major-element thermometry Rare-earth exchange thermometry confirms the temperature groupings found by major-element thermometry [Figure 2.14]. REE temperatures of 950-970 °C for the low-temperature cohort

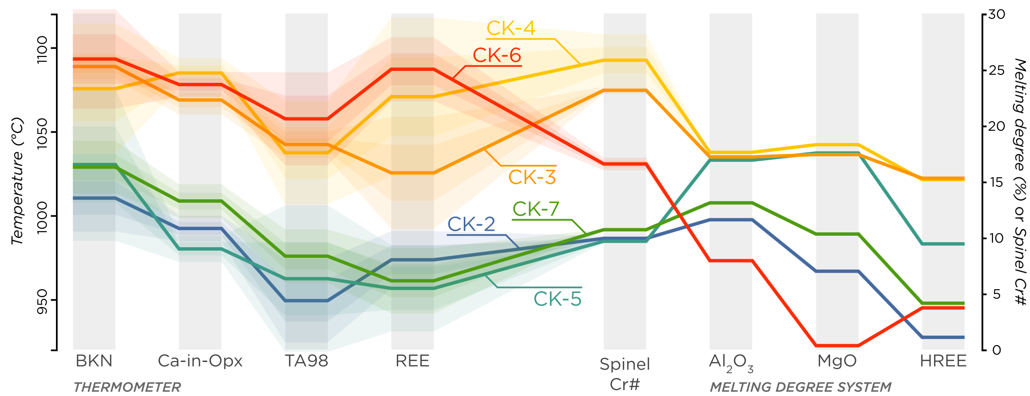

Figure 2.14: Summary of temperature and depletion-degree data for the peridotite xenoliths showing the two temperature cohorts of the dataset, which remain separable for all thermometers and are centered roughly 80°C apart. Estimates for all thermometers track together except for the higher temperature estimates for the REE thermometer for samples CK-4 and CK-6, which may reflect a fossil heating event. Spinel Cr# and several melt-extraction proxies are used to assess the level of depletion of the samples. The lower-temperature samples are generally less depleted in all systems, with variable MgO and Al_2O_3 depletion reflecting low modal abundances of pyroxene. Sample CK-6 has moderately high spinel Cr# but low levels of whole-rock depletion, suggesting bulk assimilation of an enriching fluid.

are most comparable to TA98. For these samples, the TA98 and REE temperatures together record long-term equilibrium with no significant thermal perturbations. In the high-temperature cohort, samples CK-4 and CK-6 record REE temperatures significantly higher than TA98 (~1080 °C vs. ~1040 °C). CK-3 records a lower temperature in line with major-element thermometry. Trivalent REEs in pyroxene diffuse several orders of magnitude slower than bivalent major elements (*Liang et al.*, 2013), so high-temperature events can set the distribution of REEs despite subsequent major-element re-equilibration at lower temperature. Higher temperatures recorded by REE thermometry for CK-4 and CK-6 are likely due to a fossil heating event that primarily affects the deepest samples.

CK-4 may have experienced a unique transient heating event, with individual LREE cations recording high temperatures (>1200 °C) in disequilibrium with the ~1070 °C HREE temperature [Figure 2.13a]. This event could result from metasomatic processes, which possibly correspond to the melt-infiltration textures (intergranular melt channels) unique to this sample [Figure 2.4].

2.3 Geothermal constraints on the deep lithosphere

2.3.1 Extrapolation from surface heat flow

Previous studies have used surface heat flows to estimate the thermal structure and evolution of the mantle lithosphere beneath the central California coast ranges. *Blackwell and Richards* (2004) compiled a heat flow database across the western U.S. based on borehole measurements in wells > 100 m deep. *Erkan and Blackwell* (2009) reports a "Coast Range Thermal Anomaly" of high surface heat flux (70-90 mW/m^2) which spans the entire Coast Range belt, on both sides of the San Andreas fault zone. The Mojave Plateau has similarly high heat flows, but lower heat flows of 20-40 mW/m^2 are found in the adjacent Central Valley and Sierra Nevada. Coast Range heat flows are high in the global distribution of regionally averaged continental heat flows, which ranges from lows of 20 mW/m^2 in cratonic cores to 120 mW/m^2 in focused areas of active mantle upwelling (e.g. the southern Salton Trough) (*Pollack and Chapman*, 1977; *Erkan and Blackwell*, 2009).

Erkan and Blackwell (2009) attributed high surface heat flows in the Coast Ranges to non-conductive processes such as shear heating, rapid surface uplift, and fluid circulation along faults. Shear heating does not cause significant additions to heat flow (e.g *Lachenbruch and Sass*, 1980; *Kidder et al.*, 2013). However, sustained rock uplift and erosion, such as that documented since 2 Ma in the Santa Lucia Range (*Ducea et al.*, 2003), can raise the crustal geothermal gradient through advection of material. More significantly, regional thermal conductivity can be enhanced by hydrothermal circulation in the presence of fractures. The crust of the Coast Ranges and the Mojave Plateau underwent extensive crustal detachment faulting during the late Cretaceous (*Wood and Saleeby*, 1997; *Chapman et al.*, 2012), and the Coast Ranges underwent additional transform faulting in the Neogene. Mantle fluids in the San Andreas fault zone (*Kennedy*, 1997) suggest fluid upwelling along these fractures, and high surface heat flows may be due to increased permeability, fracture-following fluid transport, and heat advection. In contrast, the intact batholithic domains underlying the Sierra Nevada, Central Valley, and Peninsular Ranges have relatively low heat flows (*Erkan and Blackwell*, 2009).

Non-conductive heat transport can significantly impact the extrapolation of lithospheric geotherms from surface heat flows, and conductive geotherms anchored at the surface may overestimate mantle lithosphere temperatures. Accordingly, mantle lithosphere temperatures modeled by seismic tomography are cooler than those extrapolated from surface heat flows. *Goes and van der Lee* (2002) predicts temperatures of 700–1100°C at 50–100 km depth beneath coastal California, suggesting < 60 mW/m^2 steady-state heat flows. *Li et al.* (2007) estimates the lithosphere-asthenosphere boundary to be at ~70 km depth in the southern Coast Ranges. With a 1200-1300°C lithosphere-asthenosphere boundary (e.g. *O'Reilly and Griffin*, 2010; *Fischer et al.*, 2010), this corresponds to steady-state heat flows of 70-80 mW/m^2.

Steady-state geotherms extrapolated from surface heat flows generalize the heat-transfer properties of the entire lithospheric column, and thus provide only first-order constraints on mantle lithosphere thermal state. Measurements of temperature and depth of xenolith equilibration can allow more direct reconstruction the deep lithospheric geotherm.

2.3.2 Depth constraints from Crystal Knob xenoliths

The depths of the xenolith samples in the mantle lithosphere, coupled with equilibration temperatures, provide a direct constraint on the geotherm beneath Crystal Knob at the time of eruption. Pyroxene-exchange geothermometry shows that the peridotite samples form two temperature groups with centroids separated by roughly 60°C. This temperature range likely corresponds to an array of sample sources along a depth gradient. For spinel peridotites, equilibration depths can only be analytically determined within broad boundaries. With no reliable geobarometers for spinel peridotites, several less robust metrics are used to evaluate the depth of the xenolith source. We present several lines of reasoning suggesting that the samples were entrained from relatively deep in the spinel stability field (~45-75 km). Several of the techniques below produce estimates of pressure, rather than depth. We convert these to depths using a hydrostatic gradient of ~0.03 GPa/km, integrating crust and mantle densities given in Table 2.10.

Limits of spinel stability Entrainment depths of all peridotite xenoliths must be greater than ~30 km, the depth of the Moho near the Crystal Knob eruption site

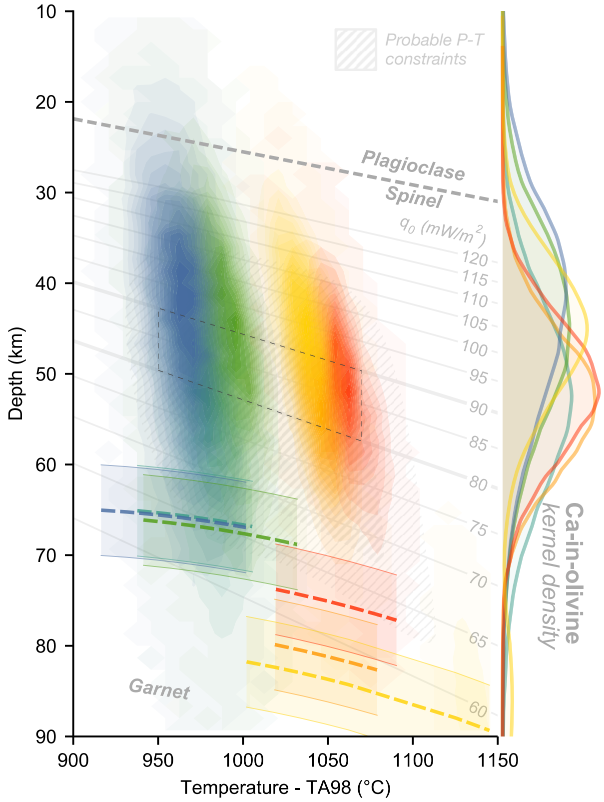

Figure 2.15: Summary of depth constraints for the xenolith samples. Colored fields represent density contours of Monte Carlo error distributions of Ca-in-olivine pressure/TA98 temperature pairs for each sample, accounting for analytical errors and within-sample scatter. Plots on the right margin project these distributions along the depth axis. Colored, dashed lines show estimates of the maximum spinel stability depth for spinel Cr content matching each sample (*O'Neill*, 1981), with imposed error bars of 0.15 GPa. The hatched background represents P-T bounds of the potential xenolith source region based on thermobarometry and phase stability. Steady-state conductive geotherms for values of surface heat flow q_0 are plotted beneath the data, with 80-90 mW/m^2 highlighted as maximum reasonable geotherms for the mantle. A dashed box shows the extent of sample temperatures along these geotherms. The synthesis of this data suggests that the samples were sourced from ~45–75 km depth.

(*Tréhu*, 1991), which will be discussed in more detail in Section 2.4. The plagioclase–spinel peridotite facies transition (typically at 20-30 km) is another minimum depth constraint, but it is highly composition-dependent (*Green and Ringwood*, 1970), with high-Cr harzburgites stable to the surface (*Borghini et al.*, 2009).

The high-pressure boundary of spinel stability limits maximum possible entrainment depths. The spinel–garnet peridotite facies transition is composition-dependent and poorly constrained for natural systems, but thought to lie over the 50-80 km depth interval (*O'Neill*, 1981; *Kinzler*, 1997; *Gasparik*, 2000; *Klemme*, 2004). The breakdown depth of spinel is strongly dependent on temperature and composition, particularly the amount of refractory Cr hosted by spinel. Several experimental and thermodynamic studies have estimated the magnitude of this effect. *O'Neill* (1981) presented experiments both with and without Cr and described a simple empirical relationship of spinel-out depth with Cr content and temperature. *Robinson and Wood* (1998) suggests that, given fertile "pyrolite" compositions with little Cr, garnet is unstable at depths less than 80 km at the peridotite solidus (~1470°C at this depth). Subsolidus experimental results show that the maximum depth of the spinel stability field in the absence of Cr ranges from 1.8-2.0 GPa (55-60 km) at 1000-1200°C (*Klemme and O'Neill*, 2000). Chromian spinels are stable to much greater depth: thermodynamic modeling by *Klemme* (2004) suggests a broad garnet-spinel co-stability field (up to a spinel-out reaction at 5 GPa for Cr# of ~30), but a spinel-weighted metastable assemblage is possible even at higher pressures.

Samples in the high-temperature cohort (CK-3, CK-4, and CK-6) have high spinel Cr# due to their history of depletion by partial melting [Figure 2.6c]. This enrichment in refractory Cr expands the stability field of spinel against garnet to deeper depths. Though *Robinson and Wood* (1998), *Klemme and O'Neill* (2000), and *Klemme* (2004) show a high-pressure phase transition with a complex compositional dependence, the rough estimate of the garnet-in pressure given by *O'Neill* (1981) performs sufficiently well at $T < 1200$ °C. This empirical relationship is used in Figure 2.15 to graphically illustrate the predicted depth of the spinel-garnet phase-transition based on the Cr# of each sample. This simple treatment provides a high-pressure constraint on the Crystal Knob xenolith source. The maximum possible entrainment depth of the highest-Cr residual samples is ~80 km, versus

~65 km for the low-Cr samples.

Ca-in-olivine barometer Equilibration pressure measurements are attempted for the peridotite xenoliths using the *Köhler and Brey* (1990) Ca-in-olivine barometer, which is based on the decreasing abundance of Ca in olivine with pressure. This barometer is calibrated for spinel peridotites but its accuracy is limited by poor resolution, high temperature dependence, vulnerability to late-stage diffusion, and dependence on low Ca concentrations in olivine near analytical thresholds for electron microprobe analysis (*Medaris et al.*, 1999; *O'Reilly*, 1997).

Within each sample, pressures are calculated separately for nearest-neighbor pyroxene and olivine measurements, and analytical errors are propagated through the calculation. Measured olivine Ca concentrations of ~200-400 ppm are scattered within each sample but separable [Figure 2.16]. To correct for the mild pressure dependence of the two-pyroxene thermometer and coupled temperature dependence of the olivine barometer, we jointly solve temperature and pressure by iterative optimization. This yields internally consistent pressure and temperature measurements for each set of analytical points. For each pressure estimate, sensitivity to analytical errors is explored using Monte Carlo random sampling ($n = 100,000$). The density of the resulting error space yields a probable depth range for each sample [Figure 2.15].

The Ca-in-olivine barometer yields model depths with modes between 40 and 53 km, largely coincident with the spinel stability field [Figure 2.15]. Within the Crystal Knob sample set, the low and high-temperature cohorts remain separable, with high-temperature samples showing deeper equilibrium depths. The scale of errors within a single sample reflects the barometer's strong covariance with major-element thermometers, as well as its sensitivity to small variations in Ca concentrations. Much of the spread in the data reflects the poor calibration of the barometer: the low-temperature samples in particular have significant scatter towards depths above the spinel-in isograd. The large Ca cation diffuses rapidly during transient heating (*Köhler and Brey*, 1990), producing a shallowing bias on the depth distribution. This may explain why CK-4, which apparently experienced a unique transient heating event, has a depth mode ~10 km shallower than samples with similar equilibration temperatures (CK-3 and CK-6). Likewise, higher REE

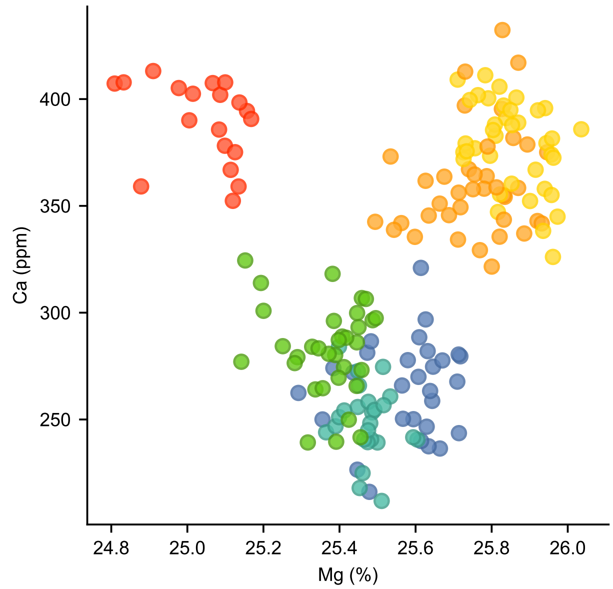

Figure 2.16: Ca abundance in olivine for peridotite samples, showing elevated Ca in samples CK-3, CK-4, and CK-6. The significant scatter in microprobe analyses (colored by sample) is due to low measured abundances.

temperatures for samples CK-4 and CK-6 may indicate a slightly deeper source. Despite the imprecision of the method, Ca-in-olivine barometry suggests that the samples were sourced from >40 km, relatively deep within the spinel stability field.

Comparisons with steady-state heat flow Estimates of xenolith depth can be constructed by pinning the equilibrium temperatures of the Crystal Knob samples to a conductive geotherm constrained by surface heat flux. On Figure 2.15, we show a range of geothermal gradients corresponding to surface heat fluxes of 60-120 mW/m^2. These are calculated using values for thermal conductivity and diffusivity given in Table 2.10 for the crust to a depth of 30 km, and mantle lithosphere below this level. The empirical factor of 0.6 proposed by *Pollack and Chapman* (1977) is used to reduce surface heat flux to a presumed mantle contribution, with the remainder being taken up by radiogenic heat production near the surface. Radiogenic heating is modeled to decrease exponentially with depth, with an e-folding length scale of 10 km. Mantle heat flux and lithospheric thermal conductivity are the main controls on the slope of the modeled geothermal gradient. This methodology is developed in *Turcotte and Schubert* (2002) and is identical to that used by *Luffi et al.* (2009), except that crustal thermal conductivity is reduced to match the conditions used in dynamic thermal modeling [Section 2.5]. This yields a slightly "hotter" geotherm throughout the mantle lithosphere.

Depths of entrainment can be estimated by projecting the TA98 temperatures for each sample onto these model geotherms. Geotherms corresponding to all reasonable surface heat flows suggest entrainment over a depth range of 5-10 km within the mantle lithosphere, with the hotter samples more deeply sourced. Steady-state geotherms anchored to surface heat flows of 65-120 mW/m^2 place the Crystal Knob sample set within the spinel stability field, and 70-110 mW/m^2 surface heat flows limit depths to the range modeled by Ca-in-olivine barometry. Measured surface heat flows of 80-90 mW/m^2 for the central California coast (*Erkan and Blackwell*, 2009) suggest depths of ~45-55 km for the Crystal Knob sample set.

2.3.3 Discussion of xenolith geothermal constraints

The Crystal Knob xenoliths are sourced within the mantle lithosphere, deeper than 30 km (the Moho) and shallower than the 60-90 km lower boundary of the spinel stability field. Ca-in-olivine barometry suggests tighter constraints near the center of the spinel stability field. Model depths of 45-55 km from steady-state geotherms agree with xenolith thermobarometry but may be underestimates due to potential non-conductive heat transfer through the crust [Section 2.3.1]. Given the bias of both Ca-in-olivine and heat-flow measurements towards shallower depths, we suggest that the xenoliths were likely entrained at 45-75 km depth. This implies that the thermal structure of the mantle lithosphere can be modeled by conductive geotherms with ~65-90 mW/m^2 steady-state heat flow. Relatively deep entrainment of the Crystal Knob xenoliths along a fairly "cool" lithospheric geotherm conforms to constraints from independent studies.

2.3.4 Geochemical variation with depth and temperature

The Crystal Knob peridotite xenoliths vary in composition with temperature, with two separable cohorts that sample mantle material with somewhat different major- and trace-element characteristics. Major-element and REE depletion track together and generally increase with the equilibration temperature of the sample, with the notable exception of sample CK-6. These differences in temperature are implicitly linked to a gradient in entrainment depth.

The low-temperature and shallower cohort includes phases with relatively fertile compositions in both major and trace elements. The samples have phase compositions similar to depleted MORB mantle (*Workman and Hart*, 2005), and clinopyroxene trace elements range from essentially undepleted to low levels of depletion characteristic of the least-depleted abyssal peridotites [Figure 2.10].

The higher-temperature, deeper samples CK-3 and CK-4 contain phases with high Mg#s, which suggests that all phases lost incompatible elements during high-degree depletion. These features, along with high levels of REE depletion, extremely low clinopyroxene modes, and chromian spinels, indicate significant melt extraction. Distinct enrichments in LREE likely correspond to assimilation of a fractionated melt, though this is modeled to be volumetrically insignificant.

Sample CK-6, the hottest and deepest sample, has a highly enriched major-element composition, and is only moderately depleted in HREEs. However, high modal abundance of pyroxenes and spinel, and simultaneously elevated Cr, Al, and LREE suggest both significant depletion and re-enrichment. This is bolstered by petrographic evidence of substantial intergrowth and aggregation of pyroxene grains, unique in the sample set. Elevated REE-in-two-pyroxene temperatures for samples CK-4 and CK-6 suggest a fossil heating event not shown in major-element thermometry. This event may have been more completely felt by sample CK-6, which has a fully equilibrated REE temperature measurement [Figure 2.13] and appears to have assimilated a sizable amount of enriched material.

The increasing depletion with depth of the Crystal Knob samples suggests increased melt extraction deeper in the lithospheric column. This pattern does not match the decrease in melting degrees with depth expected for decompression melting. Also, the geochemical variation between undepleted and depleted/re-enriched samples within a <10 km depth range suggests potential lateral heterogeneity to melting. *Luffi et al.* (2009) found a similar inverted pattern within mantle lithosphere packages beneath Dish Hill, ascribing fertile lherzolites at the top of the package to refertilization of suboceanic mantle lithosphere. With the exception of sample CK-6, HREE refertilization of the Crystal Knob samples is unlikely due to consistent major- and trace-element chemistry.

The low-temperature samples are petrologically similar to abyssal peridotites

[Figure 2.8 and Figure 2.10], suggesting an origin as fertile to moderately-depleted suboceanic mantle lithosphere. The depleted harzburgites CK-3 and CK-4 could be tectonically juxtaposed to deeper levels by duplexing (as in *Luffi et al.*, 2009) or depleted after emplacement by deeply-sourced melting. Along these lines, the obvious refertilization of CK-6 at the base of the column shows melt-rock interactions that were most intense at deep levels. This spatial pattern of melt generation is commonly associated with flux melting in subarc settings (e.g. *Jean et al.*, 2010) but could also arise from intense heating from below (*Thorkelson and Breitsprecher*, 2005). In this context, depletion of the deeper samples at Crystal Knob would correspond to melt generation deep within the mantle lithosphere.

2.4 Origin of the mantle lithosphere beneath the Coast Ranges

The Crystal Knob spinel peridotite xenoliths are uniformly isotopically depleted, with an ϵ_{Nd} of 10.3-11.0, and $^{87}Sr/^{86}Sr$ of 0.7023-0.7024. These values are typical for the depleted upper mantle (e.g. *Hofmann*, 1997) and require a mantle source that has not been recycled from the western North American subcontinental mantle or continental lithosphere more generally. Potential origins include underplated suboceanic or upwelling asthenospheric mantle material.

The lack of radiogenically enriched arc residues in the Crystal Knob xenolith suite confirms the unrooted nature of Salinia arc rocks (e.g. *Hall and Saleeby*, 2013) that lie slivered above the Franciscan accretionary complex that dominates the crust of the Coast Ranges. This suggests the existence of a major structural discontinuity below the crust, with underplated, depleted peridotite forming the framework of the mantle lithosphere. The Crystal Knob xenolith suite is the only known direct sampling of this underplated mantle beneath coastal California. Several tectonic events since Cretaceous time could have replaced the mantle lithosphere beneath the Coast Ranges.

The Franciscan complex of the region was assembled by sustained subduction of the Farallon plate during the Cretaceous and early Cenozoic periods (*Cowan*, 1978; *Saleeby et al.*, 1986; *Seton et al.*, 2012; *Chapman et al.*, 2016a). The mantle lithosphere beneath the eastern Mojave Plateau was constructed from partly subducted Farallon-plate upper mantle late in this Franciscan accretionary history

(*Luffi et al.*, 2009), and an outboard equivalent of this mechanism could have built the mantle lithosphere beneath Crystal Knob.

In Oligocene to early Miocene time, the Pacific-Farallon spreading ridge obliquely intersected the Cordilleran subduction zone at the coast of southern California, leading to the development of the San Andreas transform system (*Atwater*, 1970). Progressive impingement of large-offset ridge-ridge transforms resulted in the opening of a geometrically and kinematically complex slab window (*Atwater and Stock*, 1998; *Wilson et al.*, 2005). Late Cenozoic volcanism of the coastal region of central California has been attributed to partial melting of asthenosphere as it ascended into the slab window (*Wilson et al.*, 2005).

The Monterey microplate [Figure 2.17] nucleated as an oblique intra-oceanic rift along an ~250 km long segment of the Pacific-Farallon ridge (*Thorkelson and Taylor*, 1989; *Bohannon and Parsons*, 1995) during slab window formation (*Wilson et al.*, 2005). Microplates may have stalled beneath coastal central California as the coherent main part of the Farallon plate continued to subduct deeper into the mantle (*Bohannon and Parsons*, 1995; *Brocher et al.*, 1999; *Van Wijk et al.*, 2001). In this scenario, late Cenozoic volcanism in the region is linked to the youthfulness of the subducted microplate(s), implying a partial melting mechanism within and directly below the lithospheric lid. Both the slab window (or gap) and stalled microplate hypotheses are based on plate kinematic relationships which require a combination of slab window and stalled oceanic microplate segments (*Bohannon and Parsons*, 1995; *Atwater and Stock*, 1998; *ten Brink et al.*, 1999; *Wilson et al.*, 2005).

The cross-sections presented in Figure 2.18 show the first-order crustal relations implied by three potential origins for the sub-Crystal Knob mantle lithosphere: **A**. shallowly ascended asthenosphere within the Pacific-Farallon slab window (*Atwater and Stock*, 1998); **B**. subduction of an underplated, or stalled, Monterey oceanic microplate (*Bohannon and Parsons*, 1995); or **C**. underplated Farallon plate mantle lithosphere nappe(s) that lie in structural sequence with the upper mantle duplex resolved beneath the Dish Hill xenolith location in the Mojave region (*Luffi et al.*, 2009). Scenarios **A** and **B** have been proposed in previous models of the lithospheric structure of the California coast (*Erkan and Blackwell*,

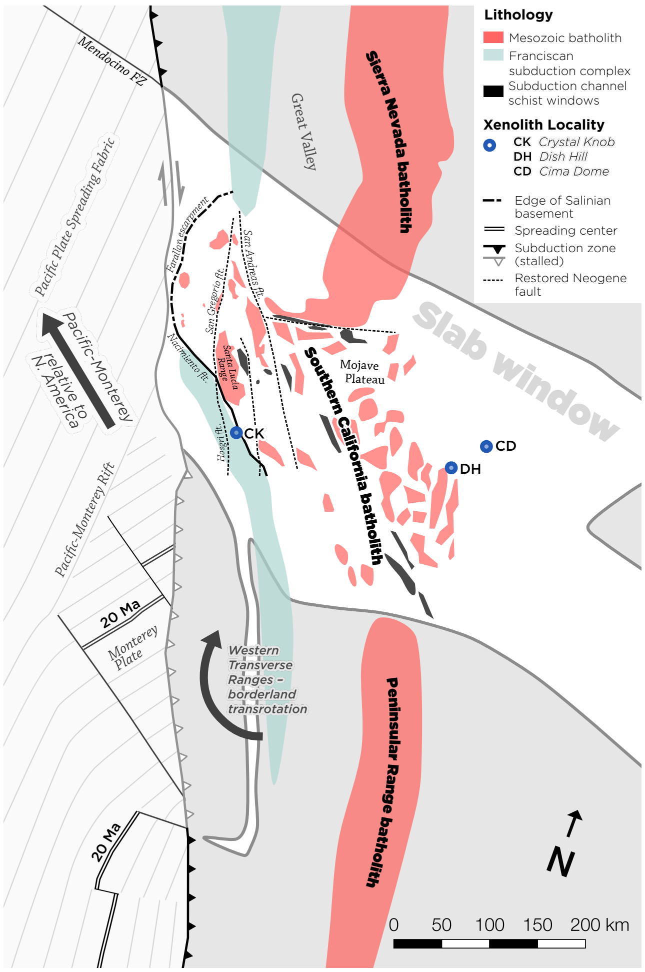

Figure 2.17: Tectonic reconstruction of the California margin at 19 Ma showing the early evolution of the San Andreas transform system, the evolving slab window and microplate detachment (after *Wilson et al.*, 2005), and the reconstructed location of modern exposures of the Cretaceous batholithic belt, the disaggregated Mojave–Salinia batholith, and surface outcrops of subduction channel schists in the Mojave province (after *Schott and Johnson*, 1998, 2001; *Chapman et al.*, 2012; *Dickinson et al.*, 2005).

2008), while scenario **C** is constructed from a large body of literature on crustal and mantle-lithosphere tectonics since the Cretaceous.

2.4.1 The Neogene slab window

Figure 2.17 shows a hypothetical surface projection of the Pacific-Farallon slab window and partially subducted Monterey plate at ca. 19 Ma (*Wilson et al.*, 2005). The slab window formed by subduction of the trailing edge of the Farallon plate and cessation of seafloor spreading along the former spreading axis with the Pacific plate. According to the *Wilson et al.* (2005) reconstruction of the Pacific-Farallon slab window and adjacent Monterey plate [Figure 2.17], the Crystal Knob eruption site was located above a slab window in the early Neogene, ~50-100 km northeast of the northeastern boundary transform fault of the Monterey plate. Diffuse volcanism, some clearly derived from decompression partial melting of convecting mantle, is widespread at this time period across the region of the reconstructed slab window (*Hurst*, 1982; *Sharma et al.*, 1991; *Cole and Basu*, 1995; *Wilson et al.*, 2005). However, this phase of slab window opening and related volcanism cannot account for the eruption of the ca. 1.7 Ma Crystal Knob volcanic neck itself [see Section 2.6.3].

2.4.2 The Monterey plate stalled slab

When the East Pacific Rise first reached the North American plate at 28.5 Ma, the Monterey microplate broke from the Farallon slab and subducted independently until 19.5 Ma, while rotating clockwise with respect to the Pacific plate (*Wilson et al.*, 2005). Partial subduction and stalling of the Monterey plate occurred along the outer edge of the Franciscan complex to the south of the evolving slab window, and Figure 2.17 shows the incipient tear between the rotating microplate and the bulk of the downgoing Farallon slab. The relict Monterey Plate slab was integrated into the Pacific plate and translated ~250 km north to outboard of Crystal Knob by slip on the subduction megathrust and the San Gregorio-Hosgri fault (*Dickinson et al.*, 2005; *Wilson et al.*, 2005). The remnant microplate still forms part of the abyssal seafloor in the proximal offshore region [Figure 2.1].

The eastward extent of the partially subducted Monterey Plate slab is unknown, and it is likely truncated by the San Gregorio-Hosgri fault system [see Section 2.6.1].

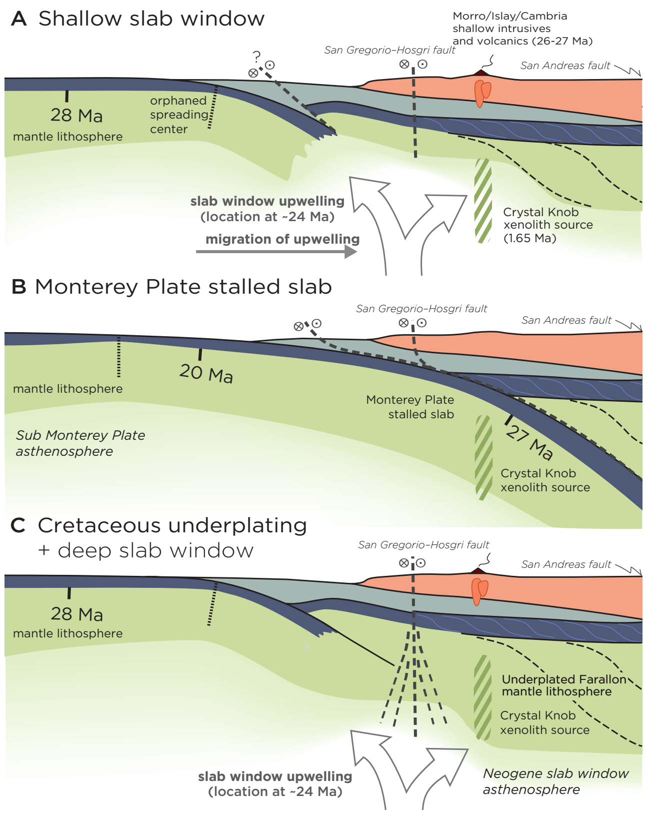

Figure 2.18: Schematic cross-sections showing potential scenarios for modification of the marginal mantle lithosphere at the end of subduction in the early Miocene. Forearc crust (orange) is generalized for late-Cretaceous inherited structure [see Figure 2.19], including Salina nappes and associated Franciscan-complex fragments. **(a)** Migration of the East Pacific mantle upwelling beneath the continental margin, forming a slab window and causing wholesale replacement of sub-Salinia mantle lithosphere with ascended asthenosphere. **(b)** Translation of the Monterey plate stalled slab along the former subduction megathrust to a current position beneath the California Coast Ranges (after *Bohannon and Parsons*, 1995) **(c)** Mantle lithosphere beneath the Crystal Knob eruption site composed of underplated Farallon plate mantle nappes reheated at their base by the Neogene slab window. The Monterey plate fragment is translated along the Hosgri fault from the Transverse Ranges region, to have its lithospheric column juxtaposed with previously underplated Farallon-plate mantle lithosphere.

However, if the Monterey plate extended further eastward and was translated northward beneath a reactivated subduction megathrust [Figure 2.18b], it would make up the mantle lithosphere beneath Crystal Knob. In its most recent iterations, the stalled slab hypothesis suggests that the Monterey plate extends eastward of the San Andreas fault as a horizontally translated stalled slab, potentially reaching ~300 km depth beneath the eastern Central Valley (*ten Brink et al.*, 1999; *Pikser et al.*, 2012; *Wang et al.*, 2013). Although geodynamically suspect, this model has been presented as a candidate for construction of the mantle lithosphere in previous modeling efforts (*Erkan and Blackwell*, 2008) and is commonly invoked in the seismology literature (e.g. *Wang et al.*, 2013). We include the model in our consideration of thermal history, but return to its viability in Section 2.6.1.

2.4.3 Underplated Farallon Plate mantle nappes

The reconstruction of the Crystal Knob eruption site to its pre-San Andreas position [Figure 2.17] places it outboard of the Mojave province, where much of the mantle lithosphere was replaced by Farallon-plate nappes during the Cretaceous. An outboard extension of this underplating, prior to Neogene transform faulting, is a highly viable alternative for the development of the mantle lithosphere beneath the Coast Ranges.

The pre-Neogene tectonic setting of the Crystal Knob eruption site is shown in Figure 2.17 by restoration of the San Andreas dextral transform system relative to North America (*Matthews*, 1976; *Dickinson et al.*, 2005; *Chapman et al.*, 2012; *Hall and Saleeby*, 2013; *Sharman et al.*, 2013). The Crystal Knob eruption site restores to a position outboard of the southern California batholith. The principal windows into shallowly underplated subduction channel schists are shown in Figure 2.17 along with the principal upper plate batholithic exposures. The current western extent of the Salinia crystalline nappes is shown as the Nacimiento fault and the offshore Farallon escarpment. Crystalline rocks of the Salinia nappes extended an unknown distance westwards across the Nacimiento belt Franciscan (*Hall and Saleeby*, 2013), but were eroded off the lower plate complex as the coastal region rose in the Pliocene (*Ducea et al.*, 2003).

The Crystal Knob neck erupted through the Nacimiento belt of the Franciscan complex, immediately adjacent to the current western limit of Salinia crystalline nappes [Figure 2.1]. Accretion of the Nacimiento belt occurred in the Late Cretaceous beneath the outer reaches of the Salinia nappe sequence (*Hall and Saleeby*, 2013; *Chapman et al.*, 2016a). In their core area, the Salinia nappes rode westwards on slightly older, higher metamorphic grade, Franciscan rocks that are shown in Figure 2.1 and Figure 2.17 as windows into subduction channel schists (*Barth et al.*, 2003; *Kidder and Ducea*, 2006; *Ducea et al.*, 2009). The southernmost Sierra Nevada-western Mojave "autochthon" for the Salinia nappes is likewise detached from its original mantle wedge underpinnings, and shingled into crystalline nappes that lie on underplated high-grade subduction channel schists (*Saleeby*, 2003; *Chapman et al.*, 2010, 2012; *Chapman*, 2016). Tectonic erosion of the mantle wedge followed by shallow subduction underplating of Franciscan rocks requires wholesale replacement of the mantle lithosphere beneath the Mojave province. *Luffi et al.* (2009) and *Armytage et al.* (2015) present petrologic studies on the Dish Hill and Cima mantle xenolith suites [Figure 2.1] that suggest the presence of a mantle lithosphere duplex with multiple Farallon plate upper mantle nappes in structural sequence beneath an eastern residual roof of continental mantle lithosphere. Since the crustal structural sequence of the western Mojave region is closely spatially and temporally correlated to that of the Salinia nappes (*Chapman et al.*, 2010, 2012, 2016a), it stands to reason that upper mantle duplex accretion progressed westwards from the Mojave region to beneath the Salinia nappes as well as the Nacimiento belt of the Franciscan Complex.

Mantle underplating after flat subduction In Figure 2.19, we present a model for the tectonic underplating of the Farallon plate mantle lithosphere beneath the Mojave-Salinia-Nacimiento segment of the Late Cretaceous convergent margin (after *Saleeby*, 2003; *Luffi et al.*, 2009), which occurred in conjunction with shallow flat subduction of the Shatsky Rise conjugate Large Igneous Province (*Saleeby*, 2003; *Liu et al.*, 2010; *Sun et al.*, 2017). The approximate age of Farallon plate entering the trench is shown on each frame (after *Seton et al.*, 2012). Crustal deformation, timing, and thermal conditions are integrated from *Kidder and Ducea* (2006), *Chapman et al.* (2010), *Chapman et al.* (2012), and *Chapman et al.* (2016a). Figure 2.19a and b show the arrival of the oceanic plateau into the subducting

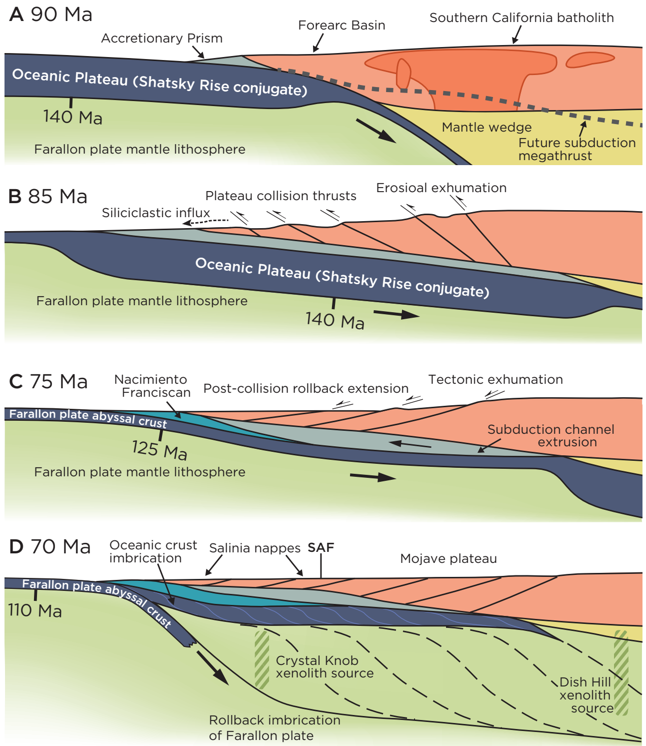

Figure 2.19: Cross sections showing the evolution of southern California during the subduction of a large oceanic plateau during the late Cretaceous, and underplating of Farallon-plate mantle nappes during slab rollback (after *Saleeby*, 2003; *Luffi et al.*, 2009; *Chapman et al.*, 2010).

trench, and plateau buoyancy-driven shallowing of the subduction megathrust, which drove tectonic erosion of the mantle wedge. During this episode, deep arc rocks cooled rapidly from ~900 °C, and temperatures along the flat megathrust were near the ~715 °C peak recorded in subduction-channel metaclastic rocks of the Sierra de Salinas schist (*Kidder and Ducea*, 2006).

In Figure 2.19c and d we adopt the focused slab rollback and mantle lithosphere underplating models of *Saleeby* (2003) and *Luffi et al.* (2009) for the dynamic response of the forearc to the end of LIP subduction. Gravitational collapse and/or suction by the retreating slab drove crustal responses including large-magnitude, trench-directed extension coupled to regional extrusion of the underplated subduction channel schists. In the Figure 2.19c to d transition, accelerated rollback corresponds to the formation of Farallon-plate mantle duplexes. Buoyancy-driven resistance to LIP subduction could have driven the transient imbrication of Farallon plate mantle lithosphere and establishment of successive basal megathrust surfaces, leading to forearc overthickening. Alternatively, duplex formation could have occurred due to negative buoyancy during retreating subduction, with tensile stresses in the slab promoting nappe detachment. Observational data and laboratory experiments showing profound co-seismic dilation transients along subduction megathrusts (*Gabuchian et al.*, 2017) underscore the ability of tensile stresses to cause dislocations in subducting slabs. We suspect that mantle nappe detachment was mediated by the temperature of the brittle-plastic transition in olivine: for ~40-50 Myr oceanic lithosphere entering a subduction zone [Figure 2.19c and d], this ~700-800 °C transition (*Warren and Hirth*, 2006; *Mei et al.*, 2010) occurs at ~25-40 km depth in the slab (*Doin and Fleitout*, 1996).

The lack of high-pressure mafic schists in both the Crystal Knob and Dish Hill xenolith suites further suggests that an intact subduction channel is not preserved in the mantle lithosphere. The seismically imaged, thickened lower crust of the region (*Tréhu*, 1991; *Brocher et al.*, 1999) may instead originate as underplated slivers of oceanic crust detached along with mantle lithosphere nappes. On the basis of both the regional structural evolution of the central to southern California basement and the petrogenetic history recorded in the region's mantle xenolith suites, we suspect the Figure 2.19d section most accurately represents the construction of the mantle domain sampled by Crystal Knob. This section is idealized for Late Cretaceous time, and we now layer the complexity of late Cenozoic tectonics onto this framework.

A deep slab window beneath relict lithosphere Kinematic reconstructions of the impingement of the Pacific-Farallon spreading center on the SW Cordilleran subduction zone require a slab window beneath the Crystal Knob eruption site in the early Neogene (*Atwater and Stock*, 1998; *Wilson et al.*, 2005). Previous modeling of thermal effects of the slab window (*Erkan and Blackwell*, 2008) only investigated the resulting emplacement of asthenosphere at immediate subcrustal levels. However, the depth of asthenospheric underplating related to slab window opening is poorly constrained and likely varies geographically as a function of thickness and thermal variations in the pre-existing lithospheric lid, as well as its state of stress and structural coherence. Volcanism in the central California Coast Ranges tied to slab window opening (e.g *Ernst and Hall*, 1974) has been volumetrically insignificant when compared to that generated by other coeval examples of shallow asthenospheric upwelling in the Cordillera, such as Eocene–Miocene high-flux volcanism in the Basin and Range province (e.g. *Humphreys*, 1995).

An apparent lack of shallow asthenopheric upwelling in the Miocene is readily explained if the slab window opened beneath pre-existing mantle lithosphere underplated in the late Cretaceous. This would consist of a tiered duplex of underplated Farallon-plate oceanic crust and mantle lithosphere nappes, roofed by the Nacimiento belt of Franciscan and Salinia nappes. Our estimate of a 45-75 km depth interval over which the Crystal Knob lavas sampled the underlying mantle lithosphere, coupled with a general lack of significant late Cenozoic extensional faulting in the immediate region, implies a strong thermo-mechanical lid that likely suppressed the ascent of voluminous asthenosphere–derived magmas that were hypothetically sourced from a deep underlying slab window.

Figure 2.18c shows the early Neogene architecture of the mantle lithosphere beneath the Coast Ranges in this scenario. The partially subducted terminus of the Monterey plate is bounded to the east by the San Gregorio-Hosgri fault. East of the fault, the Nacimiento-belt Franciscan complex and its tectonic veneer of Salinia nappes and associated oceanic crustal duplex lie tectonically above underplated Farallon-plate mantle nappes. The structural profile shown on Figure 2.18c closely aligns with offshore seismic lines in the region (*Tréhu*, 1991), and the part between the San Andreas and San Gregorio-Hosgri faults restores to southern California latitudes, adjacent to the Mojave Plateau and extended southern California batholith.

2.5 Thermal modeling of tectonic scenarios

The Crystal Knob mantle xenoliths have a peridotite composition with a depleted (convecting-mantle) isotopic and trace-element signature. Petrographic and geochemical variations provide information on the depletion history but cannot discriminate between slab window, Monterey Plate, and Cretaceous mantle duplexing origins of the mantle lithosphere. However, these emplacement scenarios present potentially distinct thermal structures due to large differences in timescales of cooling. Tectonic models for the emplacement of depleted mantle lithosphere un-

Table 2.10: Material properties used in modeling

Material properties		CC	ML	
Thermal conductivity	k	2.7	3.138	W/m/K
Specific heat capacity	C_p	1000	1171	J/kg/K
Density	ρ	2700	3300	kg/m^3
Radiogenic heat generation	α	2.5	0.006	μW/m^3
Mantle potential temperature	T$_p$		1450	$^\circ$C
Kinematic properties (*Royden*, 1993, subduction model)				
Rate of subduction	v		100	mm/yr
Backarc distance of emplacement	x		100	km
Depth of subduction interface	z		30	km
Frictional heating	q_{fric}		0	mW/m^2
Subduction accretion	a		0	m/s
Subduction erosion	e		0	m/s

CC: continental crust; ML: mantle lithosphere

der the central California coast can be tested by comparing their implied geothermal structure with xenolith geothermometry.

2.5.1 Model setup

To distinguish between potential emplacement mechanisms for the mantle lithosphere sampled by Crystal Knob, we construct a forward model of the geotherm implied by each of the tectonic scenarios discussed in Section 2.4. A model based on the one-dimensional heat-flow equation

$$\frac{\partial T}{\partial t} = \frac{k}{\rho C_p}\frac{\partial^2 T}{\partial z^2} + \frac{\alpha}{\rho C_p} \tag{2.1}$$

(e.g. *Turcotte and Schubert* (2002), with T: temperature, t: time, and standard values for oceanic and continental material properties shown in Table 2.10) is used to track the evolution of the lithospheric geotherm predicted by the three tectonic scenarios presented above.

The model is implemented in Python using the FiPy software package (*Guyer et al.*, 2009), combining explicit and implicit finite difference approaches using a two-sweep technique (*Crank and Nicolson*, 1947) to ensure a stable result. To simulate both subduction and slab-window driven mantle underplating, the forearc geotherm is stacked atop a modeled sub-oceanic or asthenospheric geotherm and relaxed towards the present. The model is run to a depth of 500 km to remove the effects of unknown mantle heat flux.

A mantle adiabat held at the base of the crust provides a static initial thermal structure for models of scenario **A**, while analytical models for the thermal evolution of oceanic crust (*Stein and Stein*, 1992) and a forearc geotherm under continuing subduction (*Royden*, 1993) provide time-dependent boundary conditions for scenarios **B** and **C**. More information about model setup and integration is given in Section 2.A.

2.5.2 Model results

Model results are presented as temperature–time tracers in Figure 2.20 and as geotherms corresponding to specific model steps in Figure 2.21.

Shallow slab window The geologic context of the shallow slab window scenario (model group **A**) is shown in Figure 2.18a, and thermal modeling results are shown in Figure 2.20a and Figure 2.21a. The model begins at 24 Ma, corresponding to the opening of the Mendocino slab window under southern California (*Wilson et al.*, 2005). A steady-state profile through the crust is truncated by a mantle adiabat to simulate direct contact with the ascended asthenosphere (for 0-6 Myr), after which the domain relaxes conductively to the conclusion of the model. Previous modeling by *Erkan and Blackwell* (2008) suggests that this scenario yields temperatures too hot to correspond to the modern regional geotherm. We confirm this assessment, finding that this scenario produces extremely steep geotherms at the upper boundary of spinel lherzolite stability for much of the temperature domain of interest [Figure 2.22], reproducing neither the xenolith pressure–temperature array observed in this study nor the seismically-inferred depth of the lithosphere-asthenosphere boundary (e.g. *Li et al.*, 2007).

Neogene stalled slab The geologic context of the stalled slab scenario (model group **B**) is shown in Figure 2.18b, and modeling results are displayed in Figure 2.20b and Figure 2.21b. This scenario tracks the potential thermal structure of oceanic plates stalled under the forearc at a range of times. Each run begins with the subduction of oceanic lithosphere assigned an initial thermal structure corresponding to oceanic lithosphere of a given age.

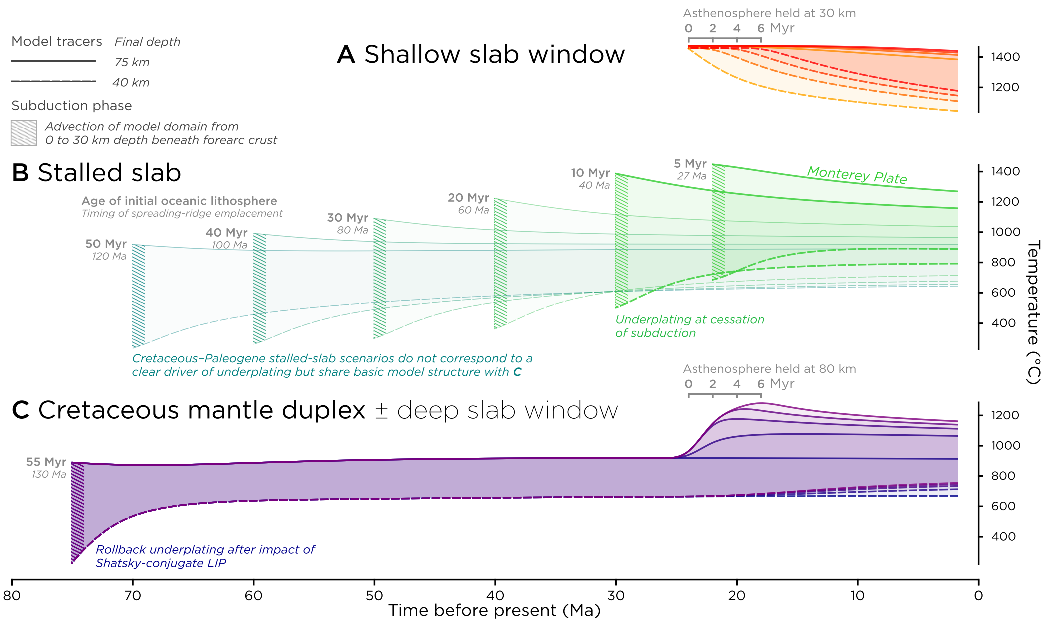

Figure 2.20: Temperature-time tracers for each modeled scenario, following the evolution of particles at final depths of 40 and 75 km in the model domain (dashed and solid lines, respectively), bracketing the boundary conditions of the Crystal Knob xenolith suite. All models conclude at 1.65 Ma, the eruptive age of the Crystal Knob xenoliths. **(a)** Upwelling-driven mantle lithosphere replacement to the base of the crust during the Mendocino slab window episode beginning at 24 Ma (*Wilson et al.*, 2005). Asthenospheric mantle is held at the base of the crust for a period of time between 0 and 6 Myr to represent potential durations of active convection. **(b)** Oceanic lithosphere slices underplated at different times until the cessation of Farallon-plate subduction in the Neogene. The youngest of these scenarios corresponds to the likely thermal evolution of a Monterey Plate stalled slab. The models with subduction times >30 Ma are included for completeness, though they do not correspond to specific events recorded by geologic features in coastal California. Model tracers begin at 10 and 45 km beneath the seafloor and are advected to depths of 40 and 75 km during subduction over the first 1.04 Myr of the model run. **(c)** A Farallon-plate slab subducted and underplated during the late Cretaceous [Figure 2.19]. While similar to the older stalled-slab models, it is tuned for key thermobarometric constraints on subduction channel schists (*Kidder et al.*, 2003). The effect of Mendocino slab window upwelling at the base of this section is shown, with timing equivalent to the replacement of the entire mantle lithosphere represented in *(a)*.

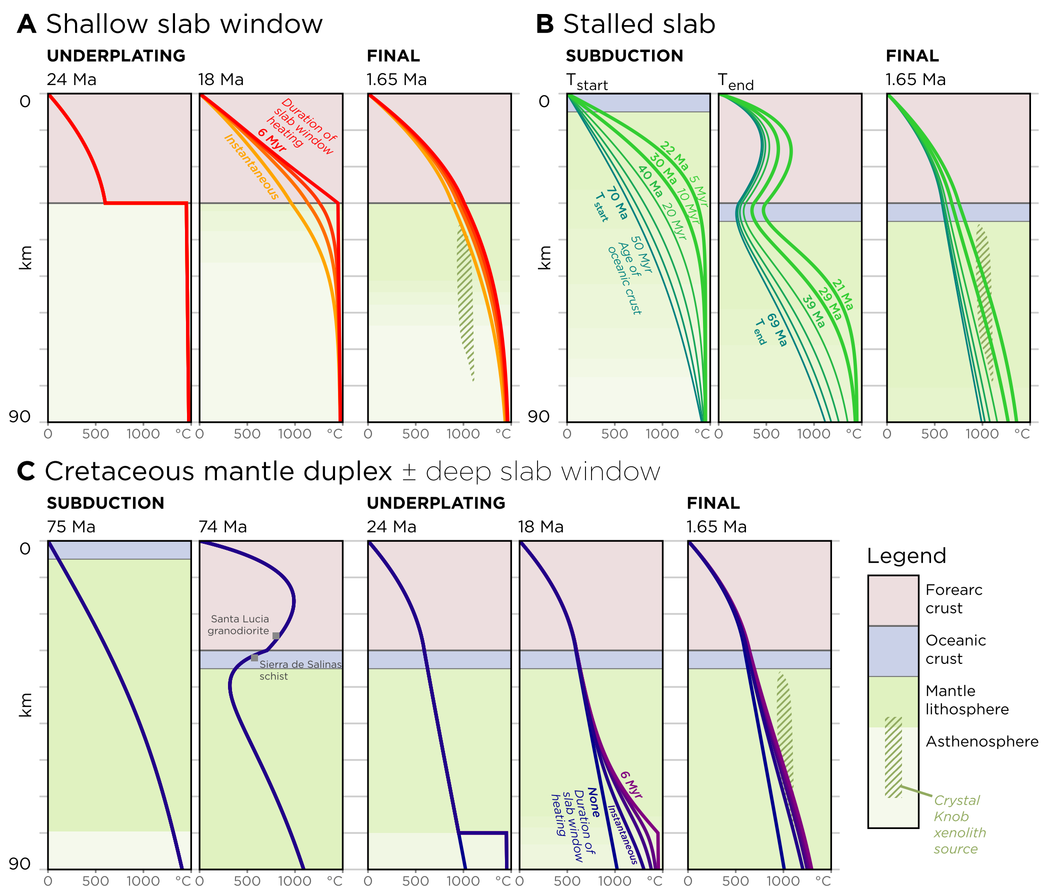

Figure 2.21: Temperature-depth profiles through the crust and upper mantle at key timesteps during the evolution of the three tectonic scenarios shown in Figure 2.20. Each profile represents a different model run based on the same scenario. **(a)** A shallow slab window scenario, with underplating of upwelling asthenosphere truncating a forearc geotherm at 24 Ma. This asthenosphere is held against the base of the crust from 0–6 Myr, accounting for the spread of models in the second panel. The final panel tracks all models to the present. **(b)** Stalled slabs of different ages, with panels corresponding to shared tectonic events, modeled at different times based on the timing of subduction and age of oceanic crust. Subduction is bracketed by T_{start} and T_{end}, with $T_{start} = T_{end} - 1.04$ Myr for all cases. The youngest and hottest of these runs corresponds to the “Monterey plate” tectonic scenario. **(c)** Farallon Plate mantle lithosphere emplaced beneath the central California coast by mantle duplexing during the late Cretaceous [Figure 2.19] and reheated by a pulse of heat from below during the Miocene slab window [Figure 2.18]. The second panel, at the end of subduction, shows the geologic temperature constraints used to tune the model to subduction conditions on the late-Cretaceous megathrust (e.g. *Ducea*, 2003; *Kidder and Ducea*, 2006) In this scenario, oceanic lithosphere is 55 Myr old at the time of subduction.

We model cooling scenarios for a wide range of underplating times, with the start of subduction ranging from 80 to 22 Ma. This reflects the long subduction history of the Farallon plate beneath the central California coast through the Cretaceous and Paleogene. These subduction times, T_{start}, set the initial conditions shown in Figure 2.20b and the first panel of Figure 2.21b. Each model operates on oceanic crust of the appropriate age for the time of subduction, given the geometry of Farallon plate subduction over the Cretaceous and Paleogene (*Liu et al.*, 2010; *Seton et al.*, 2012). As T_{start} approaches the present, the age of subducted oceanic crust generally decreases, reflecting the approach of the Pacific–Farallon spreading ridge to the western margin of North America.

Stalled slab scenarios with subduction ages older than 30 Ma simulate rollback during sustained Farallon-plate subduction. While backstepping of the subduction megathrust and underplating of a slice of mantle lithosphere could, in principle, occur at any time, these older stalled-slab models do not correspond to geodynamic and geological evidence of a specific episode of subduction instability. Though improbable, these models are included to fully explore the model space between model groups **B** and **C**, and are represented with a reduced opacity on Figure 2.20b. In the oldest model with a subduction time of 70 Ma, the oceanic lithosphere is 50 Myr old at the time of subduction. At this time, the Shatsky conjugate had already subducted to beneath the Cordilleran interior (*Liu et al.*, 2010) and the Nacimiento belt of the Franciscan was in its later stages of subduction accretion (*Chapman et al.*, 2016a). This is the earliest time a stalled slab could have developed outside of the specific scenario treated in model group **C**.

The youngest model run in Figure 2.20b corresponds to the "Monterey plate" hypothesis (*Pikser et al.*, 2012; *Van Wijk et al.*, 2001), which entails hypothetical northward lateral translation on a shallowly-dipping remobilized subduction megathrust. The potential thermal effects of the required anhydrous shearing of the underplated oceanic lithosphere along a ~300 km flat displacement trajectory [see Section 2.6.1] are not accounted for in model **B**. Instead, this scenario is modeled simply as a young endmember stalled-slab scenario, with generation of mantle lithosphere beneath the oceanic spreading ridge at 27 Ma (corresponding to the chron 7 magnetic anomaly) and subduction shortly thereafter (*Atwater and Stock*, 1998; *Wilson et al.*, 2005).

Overall, the stalled-slab underplating scenarios represented in **B** result in cooler geotherms than shallow slab window underplating, matching the broad thermobarometric constraints placing Crystal Knob xenolith entrainment relatively deep within the spinel stability field [Figure 2.22]. The Monterey plate subduction scenario likewise predicts a modern geotherm that matches the entrainment constraints on the Crystal Knob xenoliths. Without consideration of potential bias towards colder measurements in the modeled geotherms, this appears to match our xenolith data. Accounting for possible external effects [Section 2.3.1 and Section 2.A], it suggests a hotter geotherm marginally conforming to thermobarometric constraints.

Late-Cretaceous mantle nappe underplating The geologic context of the Late Cretaceous mantle nappe underplating scenario (model group **C**) is shown in Figure 2.18c, and model results are displayed in Figure 2.20c and Figure 2.21c. The initiation of this scenario is similar to the older stalled slab scenarios [Figure 2.20b]. In both cases, the oceanic mantle forms under the Pacific–Farallon spreading ridge during the early Cretaceous, thermally matures to form a mantle lithosphere lid during oceanic plate transport, and subducts beneath the southwest Cordilleran margin later in the Cretaceous. Thus, the initial conditions and thermal evolution of scenario **C** are qualitatively similar to the older runs of **B**, except that this scenario incorporates more crustal geological constraints that pertain to its subduction history. In model **C**, the *Royden* (1993) forearc geotherm is tied to temperature constraint of 715°C at 25 km depth based on garnet-biotite thermometry of Salinia granites that lie tectonically above the subduction complex, and ~575°C at 30 km depth based on garnet-biotite thermobarometry on the proximally underplated schist of Sierra de Salinas (*Ducea*, 2003; *Kidder and Ducea*, 2006). The subduction conditions and mantle lithosphere structure implied by this scenario are shown in Figure 2.19.

In model group **C**, the age of subduction and underplating is taken as 70 Ma, based on the youngest mica Ar/Ar ages for the Sierra de Salinas/Nacimiento Franciscan subduction complex (*Barth et al.*, 2003; *Grove et al.*, 2003; *Saleeby et al.*, 2007; *Chapman et al.*, 2010; *Chapman*, 2016; *Chapman et al.*, 2016a). Seafloor being subducted at that time was 40 Myr old (*Seton et al.*, 2012; *Liu et al.*, 2010). In this tectonic scenario [Figure 2.18c and Figure 2.19], Farallon oceanic lithosphere continued to subduct after mantle nappe detachment until the Pacific–Farallon spreading ridge encountered the trench in the Neogene.

In model runs for this scenario [Figure 2.21], the underplated mantle nappe(s) cool beneath the forearc for 50 Myr, after which the geotherm is perturbed by the underplating of asthenosphere at ~80 km depth, corresponding to a deep slab window. This interaction is modeled by holding an adiabatic temperature gradient with a mantle potential temperature of 1450°C against the base of the lithosphere for 0-6 Myr. The model for 0 Myr entails instantaneous contact followed immediately by conductive relaxation, while 6 Myr of sustained upwelling produces the "kinked" geotherm seen in panel 4 of Figure 2.21c at the 18 Ma time step, due to continuing imposition of a mantle adiabat below 80 km depth. A single model without slab window heating predicts much cooler geotherms than allowed by xenolith constraints [Figure 2.22].

Figure 2.21c, panel 2 shows the thermobarometric constraints and inverted metamorphic gradient recorded by subduction-channel schists for this episode of subduction (*Kidder and Ducea*, 2006; *Kidder et al.*, 2013) and used to tune the *Royden* (1993) forearc geotherm model. These high subduction temperatures constrained by crustal geothemometry make little difference to the final thermal structure of the mantle lithosphere [Figure 2.20c]. Without reheating by a deep slab window, the Cretaceous underplating scenario has a similar final thermal structure to the longest-running stalled slab scenarios in **B** [Figure 2.22], suggesting that high subduction-channel temperatures experienced during late-Cretaceous flat slab subduction and schist metamorphism did not have a long-lasting impact on the thermal structure of the margin. Thus, heating by a Miocene deep slab window is required for Cretaceous mantle nappe underplating scenarios to produce the mantle lithosphere temperatures sampled by the Crystal Knob xenoliths.

2.5.3 Summary of model results

An assessment of model sensitivity presented in Section 2.A includes biases that may influence the model results. The largest potential bias is a potential underesti-

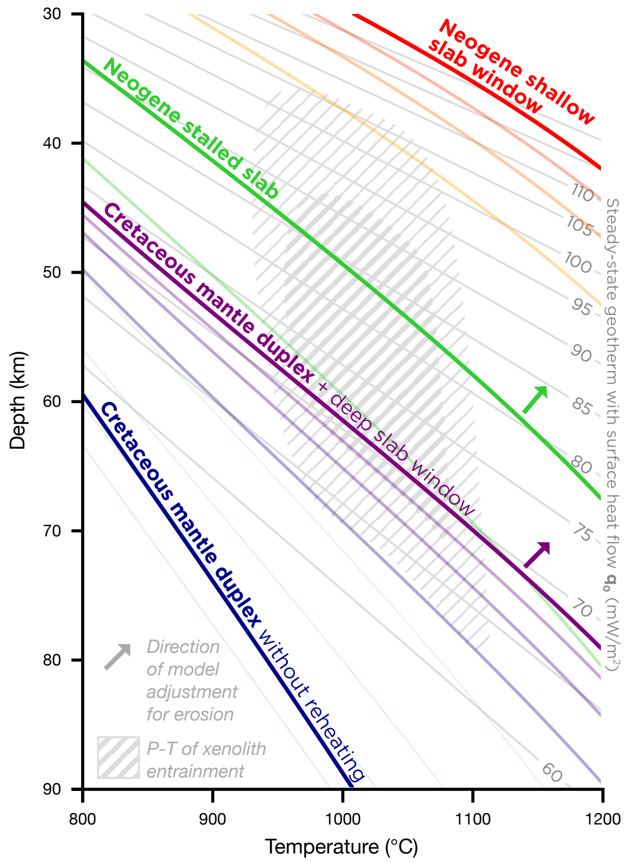

Figure 2.22: Comparisons of Crystal Knob eruptive (1.65 Ma) sub-Salinia geotherms for each of the modeled scenarios. The hottest model run of each group is highlighted, with cooler models of the same family shown with lower opacity. The model predicts purely conductive geotherms, and arrows show potential response to erosion [see Section 2.A]. The background of the plot shows a range of steady-state geotherms anchored to surface heat flows and the likely field of xenolith entrainment [Figure 2.15].

mation of true geothermal gradients due to lack of accounting for exhumation during the progression of the model. A correction for this bias would (1) push model results for the slab window scenario further out of the field of acceptable mantle lithosphere geotherms derived from xenolith constraints; (2) push the stalled slab scenario (**B**) to the upper margin of the field; and (3) push the reheated mantle nappe (**C**) towards the centroid of the field. The direction of these adjustments is summarized in Figure 2.22.

Our thermal modeling predicts much higher temperatures within the mantle lithosphere, and much higher geothermal gradients, for the shallow slab window (scenario **A**) than for either of the other modeled scenarios. Predicted geotherms for the slab window are much higher than mantle lithosphere temperatures measured by xenolith thermobarometry or extrapolated from surface heat flows [Figure 2.22]. We can thus reject a shallow slab-window source for the mantle lithosphere sampled by Crystal Knob.

The stalled slab (scenario **B**) and Cretaceous mantle nappes reheated by a deep slab window (scenario **C**) suggest mantle lithosphere temperatures similar to those measured by xenolith thermobarometry and inferred from surface heat flows and seismic tomography. Both scenarios **B** and **C** are acceptable given the thermal modeling. However, the geotherm predicted for the stalled slab occupies the higher-temperature part of the acceptable field, and its viability could be impacted by potential erosion in the Coast Ranges, which would elevate geotherms for all scenarios [Figure 2.22].

2.6 Discussion of lithospheric history

Both the Monterey plate stalled slab (scenario **B**) and Cretaceous underplating of mantle lithosphere followed by heating at depth by the Neogene slab window (scenario **C**) predict plausible mantle lithosphere geotherms beneath the Coast Ranges that match surface heat-flow measurements and xenolith thermobarometry.

We strongly prefer scenario **C**, which is informed by the architecture of the lithospheric mantle in the Mojave region (*Luffi et al.*, 2009) and the crustal geologic structure of southern California inherited from Cretaceous tectonics (e.g. *Liu et al.*, 2010; *Chapman et al.*, 2012). The Neogene thermal pulse in scenario **C** also incorporates the geodynamic response of coastal California to ridge subduction in the Neogene (*Atwater and Stock*, 1998; *Wilson et al.*, 2005), suggesting an explanation for the lack of large-volume magmatism associated with the Pacific–Farallon slab window.

The plausibility of mantle lithosphere temperatures produced by scenario **B** reproduces the results of previous modeling (*Erkan and Blackwell*, 2008). However, these workers did not consider a mechanism equivalent to our scenario **C**, which provides a viable alternative. Although we cannot reject the stalled slab model based on thermal modeling alone, there are many geologic and geodynamic reasons to discount its feasibility, which we detail below.

2.6.1 Geodynamic implausibility of the Neogene stalled slab

The Monterey plate nucleated along a ~250 km segment of the Pacific-Farallon ridge as an oblique rift that was rotated ~25° clockwise from the Pacific-Farallon rift axis (*Atwater and Severinghaus*, 1989). Its generation was synchronous with the early stages of Pacific-Farallon plate convergence into the Cordilleran subduction zone along the southern California coastal region, and coincided with transrotational rifting of the continental borderland region and displacement of the western Transverse Ranges bedrock (*Bohannon and Parsons*, 1995; *Atwater and Stock*, 1998).

The current position of the Monterey plate offshore of the Crystal Knob eruption site is a result of dextral displacements linked to borderland transrotational rifting, subsequent ~155 km-scale dextral offsets along the San Gregorio-Hosgri fault system, and ~100 km of additional dextral offsets in the offshore region [Figure 2.1] as modeled both by geologic reconstruction of fault offsets (*Dickinson et al.*, 2005) and plate kinematic reconstructions (*Wilson et al.*, 2005). Continuation of the Monterey plate east of the San Gregorio-Hosgri fault requires the lateral translation of its downdip extension along the former subduction interface beneath the Coast Ranges. Its hypothetical extension east of the San Andreas fault requires that this reactivated subduction interface likewise extended east of the San Andreas fault (e.g. *Brocher et al.*, 1999; *ten Brink et al.*, 1999; *Pikser et al.*, 2012). Seismological, geodynamic, and surface geological evidence presented here argues against models invoking horizontal translation of the Monterey plate "remnant slab" beneath both the Coast Ranges and Central Valley.

The Monterey microplate separated from the Farallon Plate at ca. 22 Ma, forming a widening slab window segment east of the Peninsular Ranges [Figure 2.17]. From ca. 22 to 10 Ma, the Monterey plate, already coupled to the Pacific plate, diverged from North America (*Atwater and Stock*, 1998; *Wilson et al.*, 2005). This likely caused extensional attenuation of its subducted extension (*Bohannon and Parsons*, 1995). Coupling of Monterey plate rotation across the stalled subduction megathrust may have driven dextral transrotational rifting of the southern California borderland (*Nicholson et al.*, 1994; *Bohannon and Parsons*, 1995).

As western Transverse Range crustal panels rotated to their current position at the end of borderland transrotation (ca. 10 Ma), the Monterey plate was displaced northward along the San Gregorio-Hosgri fault system [Figure 2.1], which is aligned with the outer edge of the Farallon-Monterey slab window [Figure 2.17]. The abyssal fragment of the Monterey Plate likely separated from its underthrust extension in conjunction with the sudden cessation of crustal transrotation. If the subducted portion of the Monterey Plate instead maintained its structural integrity, it would be translated northward beneath the Coast Ranges on a shallowly dipping fault surface (presumably, the remobilized subduction megathrust) along with its Pacific-plate abyssal fragment [Figure 2.18c] to its current position outboard of Crystal Knob. This geometry has been proposed to extend beneath the entire Coast Ranges and east of the San Andreas fault (e.g. *ten Brink et al.*, 1999; *Pikser et al.*, 2012). Although kinematically plausible, this is unlikely based on dynamic factors: a large mantle mass at the base of the crust should cause transients in dynamic topography and brittle crustal deformation in response to coupling across the shallow fault. Such surface deformation patterns are not expressed north of the Transverse Ranges during the Neogene.

Seismic tomography of central California (*Tréhu and Wheeler*, 1987) suggests a 8-15 km thick, shallowly east-dipping mafic lower crustal layer that extends from the offshore region towards the San Andreas fault, thickening eastwards over Moho depths of ~12-30 km. This layer could represents the continuous surface of the stalled Monterey plate beneath coastal central California (*Brocher et al.*, 1999).

However, strong internal reflectivity within this mafic layer (*Tréhu and Wheeler*, 1987; *Brocher et al.*, 1999) and sharp inflections in its upper surface (*Tréhu*, 1991) indicate that it is internally deformed and imbricated. It is accordingly two to three times as thick as typical mafic oceanic crust. Such imbrication and underplating require a basal detachment, which is most logically located at the underlying Moho. In this context, the regions's lower-crustal mafic layer is more plausibly interpreted as a regional underplated duplex of Farallon plate oceanic crustal nappes that accreted during Franciscan subduction [Figure 2.18c].

Distinct steps and inflections in lower-crustal velocity structure across the San Gregorio-Hosgri fault system (*Brocher et al.*, 1999) indicate that it cuts the entire crust, likely forming the eastern boundary of the underplated Monterey plate. Additionally, offshore seismic observations show a ~16° eastward-dipping Monterey plate, with a typical abyssal crustal thickness, juxtaposed against a nearly flat thickened lower crustal layer beneath the adjacent Franciscan complex (*Tréhu*, 1991; *Nicholson et al.*, 1992). These observations directly conflict with the idea that a structurally continuous Monterey Plate constitutes the lower crust beneath central coastal California and the adjacent offshore region.

Studies proposing a deep Monterey plate stalled slab (e.g. *Furlong et al.*, 1989; *Pikser et al.*, 2012) have suggested its translation on significant sub-horizontal fault segments beneath the San Andreas system that accommodated dextral displacements. As of yet, however, all seismically imaged segments of the transform system have been shown to be steeply oriented (*Dietz and Ellsworth*, 1990; *Brocher et al.*, 1999; *Yan et al.*, 2005; *Titus et al.*, 2007; *Yan and Clayton*, 2007; *Ozacar and Zandt*, 2009). These studies typically propose a steeply dipping eastward extension corresponding to the high-wave speed anomaly of the southern Sierra Nevada-Great Valley region [Figure 2.1], commonly called the “Isabella anomaly”.

Seismological and geodynamic studies show that the Isabella anomaly is derived primarily from the convectively mobilized mantle wedge, or mantle lithosphere, of the southern Sierra Nevada batholith (*Zandt et al.*, 2004; *Frassetto et al.*, 2011; *Gilbert et al.*, 2012; *Saleeby et al.*, 2012; *Jones et al.*, 2014; *Levandowski and Jones*, 2015). These studies show structural continuity between the seismic anomaly and the residual mantle lithosphere that is still in place beneath the Central Valley and Sierra Nevada [Figure 2.1] and suggest that the 200 km–deep by 100 km–wide Isabella anomaly far exceeds the reasonable size of an attenuated terminus of the Monterey Plate. These studies also provide mechanisms for lower crustal plastic deformation, observable surface faulting, upper mantle–lower crustal partial melting and dynamic topographic effects that are ignored in the stalled-slab hypothesis.

First-order geological effects such as volcanism and topographic transients are closely correlated to the convective mobilization of the sub-Sierran mantle lithosphere and its current expression as the Isabella anomaly (*Ducea and Saleeby*, 1998a; *Farmer et al.*, 2002; *Saleeby et al.*, 2013; *Cecil et al.*, 2014; *Levandowski and Jones*, 2015). The surface effects of Monterey plate partial subduction, followed by transtensional coupling to the Pacific plate, are closely correlated to transrotational rifting in the southern California Borderland and the linked clockwise rotation of the western Transverse Ranges (*Bohannon and Parsons*, 1995; *Wilson et al.*, 2005). This supports a Monterey slab with a limited down-dip extent, bounded by the Monterey-Farallon slab window segment [Figure 2.17]. If the hypothetical Monterey "relict slab" extended far enough inland to form the Isabella anomaly, its effects on surface geology should not be restricted to the Borderland and Transverse Ranges. Epeirogenic transients that correlate to the convective mobilization of the sub-Sierran mantle lithosphere as the Isabella anomaly are highly out of phase with the predicted translation pattern for a deep Monterey slab (*Saleeby et al.*, 2013; *Cecil et al.*, 2014). Possible remnants of necked-off, partially subducted Monterey plate are more plausibly correlated to the Transverse Ranges high-wave speed anomaly in terms of position and volume [Figure 2.1], and also have a firm geodynamic basis as such (*Burkett and Billen*, 2009).

The stalled slab hypothesis has provided an explanation for the limited Neogene volcanism and low modern crustal heat flow observed in the Coast Ranges, neither of which can correspond the shallow emplacement of asthenosphere within a slab window (*Brocher et al.*, 1999; *Erkan and Blackwell*, 2008). These observations can also be explained by the interaction of the slab window with the base of a preexisting mantle lithosphere domain attached to the continental margin, such as the Cretaceous-underplated lithospheric duplexes envisioned in Scenario **C**. Based on the geologic and geodynamic factors discussed above, we reject the stalled slab as a potential mechanism for underplating the mantle lithosphere beneath the central Coast Ranges.

2.6.2 Thermal events recorded by xenolith petrology

The Crystal Knob xenolith suite shows petrologic variation consistent with reheating from below, possibly due to interaction of a deep slab window with a thick pre-existing lithospheric lid from which the xenoliths were sourced. Increasing depletion with depth in the Crystal Knob sample set does not match the signature of simple decompression melting [Section 2.3.4], and sample CK-6 experienced polyphase major-element refertilization by fractionated melt presumably generated below its entrainment depth. At the same time, low levels of re-enrichment by alkali-basalt-like melt are evident across the sample set. Deep partial melting and alkalic melt generation are common features of slab window volcanism (*Hole et al.*, 1991) and may contribute to the signature of depletion and re-enrichment recorded by the Crystal Knob xenoliths.

The highly fractionated, alkalic magma of the Crystal Knob pipe and its entrainment of both dunite cumulates and spinel peridotite xenoliths suggest that it was sourced from a multi-tiered network within the mantle lithosphere at depths > 45 km. The fractally-scaled melt migration channels investigated by *Kelemen et al.* (2000) provide a good potential model, in which cumulates are sometimes re-entrained by small-volume volcanism during progressive upwards percolation of melt from a deep mantle source. A deep, slowly-cooling body of slab window material, locally mobilized as melt and rising through a thick lid of relict mantle lithosphere, provides a mechanism for both mid-Miocene hypabyssal intrusives (*Stanley et al.*, 2000; *Ernst and Hall*, 1974) and later deeply-sourced, small-volume eruptions such as Crystal Knob.

2.6.3 The timing of the Crystal Knob eruption

Although potentially sourced from slowly-rising slab window melts, the ca. 1.65 Ma eruption of Crystal Knob (and other Plio-Pleistocene volcanic eruptions in the Coast Ranges) was likely proximally triggered by recent tectonism. Rapid uplift of the central California coastal region at ca. 2 Ma (*Ducea et al.*, 2003) could have caused decompression melting in the lower lithosphere. Additionally, Neogene dextral faulting provides a localized mechanism for transient decompression leading to mobilization of small volumes of mantle lithosphere melt. Crystal Knob is located ~15 km east of the Hosgri fault, and its host Franciscan complex is pervasively cut by faults and shear zones (*Cowan*, 1978; *Seiders*, 1989). The Hosgri fault was likely active during the eruption of the Crystal Knob neck (*Dickinson et al.*, 2005; *Hardebeck*, 2010), and theoretical and observational data on intracontinental transform faults (*Platt and Behr*, 2011; *Titus et al.*, 2007) indicate that Hosgri fault shear could be distributed across 10s of kilometers laterally in the lower crust and upper mantle [Figure 2.18c].

Elsewhere in the Coast Ranges, Plio-Pleistocene eruptions of small-volume basalts are associated with the traces of active faults. This includes the Coyote Lake pipe [Figure 2.1], which occurred ~150 km north of Crystal Knob along the San Andreas-Calaveras fault bifurcation zone and entrained lower crust and upper mantle xenoliths (*Jové and Coleman*, 1998; *Titus et al.*, 2007). As at Crystal Knob, xenoliths recovered from these flows record partial melting of the mantle markedly post-dating any possible slab window opening. The interplay of localized extensional transients with deep, low-volume melts is consistent with infrequent but energetic recent volcanism in the Coast Ranges.

2.7 Conclusion

The lithospheric structure of southern California, to first order created by Cretaceous convergent margin tectonics, was severely overprinted by two subsequent tectonic episodes: the impact and subduction of the Shatsky Rise large igneous province conjugate during the Late Cretaceous, and the progressive evolution of a transform boundary in the Neogene. These episodes have remade the crustal architecture of southern California and the central California Coast Ranges outboard of the San Andreas Fault. Using constraints from the Crystal Knob xenolith suite along with thermal modeling of tectonic scenarios, we show that the mantle lithosphere beneath the central California coast was created during the late Cretaceous and heated by an asthenospheric pulse in the Neogene.

The Crystal Knob xenolith suite was entrained along a depth gradient from

~45-75 km and erupted at 1.65 Ma. It has the isotopic signature of the depleted convecting mantle, which is typical of mid-ocean ridges or shallowly-ascended asthenosphere. Samples are variably depleted by partial melting, and trace-element re-enrichment (and a single example of likely major-element assimilation) suggests interaction with low-volume melts after the formation and initial thermal equilibration of this mantle lithosphere material.

Major element, trace element, and radiogenic isotope data for the Crystal Knob xenolith suite equally satisfy the first-order geochemical features of the shallow slab window, stalled slab, and Late Cretaceous mantle duplex tectonic scenarios. Xenolith pressure-temperature constraints, thermal modeling, and geochemical signatures of depletion and re-enrichment together allow some discrimination between these scenarios. Thermal modeling of a shallowly underplated slab window predicts extremely hot geotherms that are untenable for the xenolith constraints of this study, while the stalled slab and mantle nappe scenarios are both reasonable. When the effects of potential exhumation/erosion are qualitatively considered, the Monterey plate stalled slab endmember scenario corresponds less well to constraints on the upper-mantle geotherm. This, along with the poor correspondence of a stalled slab to crustal geology and geodynamic constraints, leads us to strongly favor the Late Cretaceous mantle duplex underplating scenario, with reheating by a deep slab window in the Neogene.

A late-Cretaceous origin of the mantle lithosphere beneath the Coast Ranges (our scenario **C**) matches crustal geologic evidence of slab rollback and regional extension during the Late Cretaceous, as the Shatsky Rise conjugate subducted deeper into the mantle following its initial collision and shallow subduction beneath the southern California convergent margin. This episode built the mantle lithosphere beneath the Mojave province by duplexing during the retreat of the Farallon Plate subducting slab (*Luffi et al.*, 2009), and appears to have subsequently built the outboard mantle lithosphere beneath the Crystal Knob eruption site. The presence of underplated Cretaceous mantle lithosphere beneath the Coast Ranges confirm that the entire lithospheric column, including the Salinia nappes and Nacimiento belt of the Franciscan complex, were formed in a single episode of extension during the Late Cretaceous. The outer toe of this extensionallycollapsed accretionary belt was subsequently displaced along the San Andreas transform system to its current location beneath the central California Coast Ranges.

In the Neogene, the underplated mantle lithosphere was reheated by the Mendocino slab window, which opened as the Pacific–Farallon ridge encountered the California convergent margin. The deep mantle lithosphere appended to southern California during the Cretaceous shielded the crust from intense slab window heating and volcanism. Peridotite major- and trace-element re-enrichment and abundant dunite cumulate xenoliths and xenocrysts within the Crystal Knob basalt record the percolation of fluids and melts through the lithosphere. This percolation, the highly fractionated Crystal Knob basaltic pipe, and the modeled thermal pulse at the base of the lithosphere can be attributed to the ca. 24 Ma opening of an asthenospheric slab window at 70-90 km depth. This interaction of the slab window with the base of an integrated lithospheric column could explain the relatively subdued response of coastal California to Neogene ridge subduction.

Acknowledgements

We would like to thank M. Cosca and the USGS Argon geochronology laboratory for their assistance with dating the Crystal Knob basalt flow. J. Blundy and M. Gurnis were valuable resources on REE thermometry and geodynamic modeling, respectively. F. Sousa and J. Price encouraged consideration of the wider tectonic context. We would also like to thank A. Chapman, E. Nadin, and one anonymous reviewer for their excellent feedback, which greatly improved this contribution. This work was supported by the Caltech Tectonics Observatory and funded by the Gordon and Betty Moore Foundation through Grant GBMF423.01. A PostgreSQL database containing analytical data and modeling results is archived with CaltechDATA at DOI 10.22002/D1.320. Data-reduction, modeling, and graphics-compilation code is at 10.22002/D1.321.

Bibliography

Ague, J. J., and G. H. Brimhall (1988), Magmatic arc asymmetry and distribution of anomalous plutonic belts in the batholiths of California: Effects of assimilation, crustal thickness, and depth of crystallization, *Bulletin of the Geological Society of America*, *100*(6), 912–927, doi: 10.1130/0016-7606(1988)100<0912:MAAADO>2.3.CO;2.

Alibert, C. (1994), Peridotite xenoliths from western Grand Canyon and The Thumb: A probe into the subcontinental mantle of the Colorado Plateau, *Journal of Geophysical Research: Solid Earth*, *99*(B11), 21,605–21,620, doi:10.1029/94jb01555.

Argus, D. F., and R. G. Gordon (1991), Current Sierra Nevada-North America motion from very long baseline interferometry: Implications for the kinematics of the western United States, *Geology*, *19*(11), 1085, doi:10.1130/0091-7613(1991)019<1085:csnnam>2.3.co;2.

Armstrong, J. T. (1988), Quantitative analysis of silicate and oxide materials: Comparison of Monte Carlo, ZAF, and Phi-Rho-Z Procedures, in *Microbeam Analysis*, pp. 239–246, San Francisco Press, San Francisco.

Armytage, R. M. G., A. D. Brandon, R. Andreasen, and T. J. Lapen (2015), Evolution of Mojavian mantle lithosphere influenced by Farallon plate subduction: Evidence from Hf and Nd isotopes in peridotite xenoliths from Dish Hill, CA, *Geochimica et Cosmochimica Acta*, *159*, 264–284.

Asimow, P. (1999), A model that reconciles major-and trace-element data from abyssal peridotites, *Earth and Planetary Science Letters*, *169*, 303–319.

Atwater, T. (1970), Implications of plate tectonics for the Cenozoic tectonic evolution of western North America, *Geological Society of America Bulletin*, *81*(12), 3513–3536, doi:10.1130/0016-7606(1970)81.

Atwater, T., and J. Severinghaus (1989), Tectonic maps of the northeast Pacific, in *The Geology of North America, Vol. N, The Eastern Pacific Ocean and Hawaii*, edited by E. Winterer, D. Hussong, and R. Decker, pp. 15–20, Geological Society of America, Boulder, Colorado, doi:10.1130/dnag-gna-n.15.

Atwater, T., and J. Stock (1998), Pacific-North America plate tectonics of the Neogene southwestern United States: An update, *International Geology Review*, *40*(5), 375–402, doi:10.1080/00206819809465216.

Baker, M. B., and J. R. Beckett (1999), The origin of abyssal peridotites: A reinterpretation of constraints based on primary bulk compositions, *Earth and Planetary Science Letters*, *171*(1), 49–61, doi:10.1016/S0012-821X(99)00130-2.

Barbeau, D. L., M. N. Ducea, G. E. Gehrels, S. Kidder, P. H. Wetmore, and J. B. Saleeby (2005), U-Pb detrital-zircon geochronology of northern Salinian basement and cover rocks, *Geological Society of America Bulletin*, *117*(3), 466, doi:10.1130/b25496.1.

Barth, A. P., J. L. Wooden, M. Grove, C. E. Jacobson, and J. N. Pedrick (2003), U-Pb zircon geochronology of rocks in the Salinas Valley region of California: A reevaluation of the crustal structure and origin of the Salinian block, *Geology*, *31*(6), 517.

Beard, B. L., and A. F. Glazner (1995), Trace element and Sr and Nd isotopic composition of mantle xenoliths from the Big Pine Volcanic Field, California, *Journal of Geophysical Research: Solid Earth*, *100*(B3), 4169–4179, doi:10.1029/94jb02883.

Blackwell, D., and M. Richards (2004), Geothermal Map of North America.

Blake, M. C. J., A. S. Jayko, R. J. McLaughlin, and M. B. Underwood (1988), Metamorphic and tectonic evolution of the Franciscan Complex, northern California, in *Metamorphism and Crustal Evolution of the Western United States*, vol. 8, pp. 1035–1060, Prentice-Hall Englewood Cliffs, New Jersey.

Blundy, J., and B. Wood (2003), Partitioning of trace elements between crystals and melts, *Earth and Planetary Science Letters*, *210*(3-4), 383–397, doi:10.1016/S0012-821X(03)00129-8.

Bohannon, R. G., and T. Parsons (1995), Tectonic implications of post-30 Ma Pacific and North American relative plate motions, *Geological Society of America Bulletin*, *107*(8), 937–959, doi:10.1130/0016-7606(1995)107<0937:TIOPMP>2.3.CO;2.

Borghini, G., P. Fumagalli, and E. Rampone (2009), The stability of plagioclase in the upper mantle: Subsolidus experiments on fertile and depleted lherzolite, *Journal of Petrology*, *51*(1-2), 229–254, doi:10.1093/petrology/egp079.

Brady, R. J., M. N. Ducea, S. B. Kidder, and J. B. Saleeby (2006), The distribution of radiogenic heat production as a function of depth in the Sierra Nevada Batholith, California, *Lithos*, *86*(3-4), 229–244, doi:10.1016/j.lithos.2005.06.003.

Brey, G., and T. Köhler (1990), Geothermobarometry in four-phase lherzolites II. New thermobarometers, and practical assessment of existing thermobarometers, *Journal of Petrology*, *31*(c), 1353–1378.

Brocher, T. M., U. S. . T. B. Brink, and T. Abramovitz (1999), Synthesis of crustal seismic structure and implications for the concept of a slab gap beneath coastal California, *International Geology Review*, *41*(3), 263–274, doi:10.1080/00206819909465142.

Burkett, E. R., and M. I. Billen (2009), Dynamics and implications of slab detachment due to ridge-trench collision, *Journal of Geophysical Research: Solid Earth*, *114*(12), 1–16, doi:10.1029/2009JB006402.

Cecil, M. R., Z. Saleeby, J. Saleeby, and K. A. Farley (2014), Pliocene-Quaternary subsidence and exhumation of the southeastern San Joaquin Basin, California, in response to mantle lithosphere removal, *Geosphere*, *10*(1), 129–147, doi:10.1130/GES00882.1.

Chapman, A., J. Saleeby, D. Wood, A. Piasecki, S. Kidder, M. Ducea, and K. Farley (2012), Late Cretaceous gravitational collapse of the southern Sierra Nevada batholith, California, *Geosphere*, *8*(2), 314–341, doi:10.1130/GES00740.1.

Chapman, A. D. (2016), The Pelona – Orocopia – Rand and related schists of southern California : A review of the best-known archive of shallow subduction on the planet, *International Geology Review*.

Chapman, A. D., S. Kidder, J. B. Saleeby, and M. N. Ducea (2010), Role of extrusion of the Rand and Sierra de Salinas schists in Late Cretaceous extension and rotation of the southern Sierra Nevada and vicinity, *Tectonics*, *29*(5), 1–21, doi:10.1029/2009TC002597.

Chapman, A. D., J. B. Saleeby, and J. Eiler (2013), Slab flattening trigger for isotopic disturbance and magmatic flare-up in the southernmost Sierra Nevada batholith, California, *Geology*, *41*(9), 1007–1010, doi:10.1130/g34445.1.

Chapman, A. D., M. N. Ducea, S. Kidder, and L. Petrescu (2014), Geochemical constraints on the petrogenesis of the Salinian arc, central California: Implications for the origin of intermediate magmas, *Lithos*, *200-201*(1), 126–141, doi:10.1016/j.lithos.2014.04.011.

Chapman, A. D., C. E. Jacobson, W. Ernst, M. Grove, T. Dumitru, J. Hourigan, and M. N. Ducea (2016a), Assembling the world's type shallow subduction complex: Detrital zircon geochronologic constraints on the origin of the Nacimiento block, central California Coast Ranges, *Geosphere*, *12*(2), GES01,257.1, doi:10.1130/GES01257.1.

Chapman, A. D., D. Wood, J. B. Saleeby, and Z. Saleeby (2016b), Late Cretaceous to early Neogene tectonic development of the southern Sierra Nevada region, in *Geological Society of America Field-trip Guide*, vol. 7, Ontario, California.

Chin, E., C.-T. Lee, and J. Blichert-Toft (2015), Growth of upper plate lithosphere controls tempo of arc magmatism: Constraints from Al-diffusion kinetics and coupled Lu-Hf and Sm-Nd chronology, *Geochemical Perspectives Letters*, *1*(1), 20–32, doi:10.7185/geochemlet.1503.

Cole, R. B., and A. R. Basu (1995), Nd-Sr isotopic geochemistry and tectonics of ridge subduction and middle Cenozoic volcanism in western California, *Geological Society of America Bulletin*, *107*(2), 167–179, doi:10.1130/0016-7606(1995)107<0167:NSIGAT>2.3.CO;2.

Cosca, M., H. Stunitz, A.-L. Bourgeix, and J. P. Lee (2011), 40Ar⊠ loss in experimentally deformed muscovite and biotite with implications for 40Ar/39Ar geochronology of naturally deformed rocks, *Geochimica et Cosmochimica Acta*, *75*(24), 7759–7778, doi:10.1016/j.gca.2011.10.012.

Cowan, D. S. (1978), Origin of blueschist-bearing chaotic rocks in the Franciscan Complex, San Simeon, California, *Geological Society of America Bulletin*, *89*(9), 1415, doi:10.1130/0016-7606(1978)89<1415:oobcri>2.0.co;2.

Crank, J., and P. Nicolson (1947), A practical method for numerical evaluation of solutions of partial differential equations of the heat-conduction type, *Mathematical Proceedings of the Cambridge Philosophical Society*, *43*(01), 50–67.

DePaolo, D., and G. Wasserburg (1976), Inferences about magma sources and mantle structure from variations of 143Nd/144Nd, *Geophysical Research Letters*, *3*(12).

Dick, H., and T. Bullen (1984), Chromian spinel as a petrogenetic indicator in abyssal and alpine-type peridotites and spatially associated lavas, *Contributions to Mineralogy and Petrology*, *86*, 54–

76.

Dickinson, W., M. N. Ducea, L. I. Rosenberg, G. H. Greene, S. A. Graham, J. C. Clark, G. E. Weber, S. Kidder, W. G. Ernst, and E. E. Brabb (2005), Net dextral slip, Neogene San Gregorio-Hosgri fault zone, coastal California: Geologic evidence and tectonic implications, *Geological Society of America Special Papers*, *391*, 43, doi:10.1130/2005.2391.

Dietz, L. D., and W. L. Ellsworth (1990), The October 17, 1989, Loma Prieta, California, Earthquake and its aftershocks: Geometry of the sequence from high-resolution locations, *Geophysical Research Letters*, *17*(9), 1417–1420, doi:10.1029/gl017i009p01417.

Dodge, F. (1988), Fragments of the mantle and crust from beneath the Sierra Nevada batholith: Xenoliths in a volcanic pipe near Big Creek, California, *Geological Society of America Bulletin*, doi:10.1130/0016-7606(1988)100<0938.

Doin, M. P., and L. Fleitout (1996), Thermal evolution of the oceanic lithosphere: An alternative view, *Earth and Planetary Science Letters*, *142*(1-2), 121–136, doi:10.1016/0012-821x(96)00082-9.

Drew, S. T., M. N. Ducea, and L. M. Schoenbohm (2009), Mafic volcanism on the Puna Plateau, NW Argentina: Implications for lithospheric composition and evolution with an emphasis on lithospheric foundering, *Lithosphere*, *1*(5), 305–318.

Ducea, M., and J. Saleeby (1996), Buoyancy sources for a large, unrooted mountain range, the Sierra Nevada, California: Evidence from xenolith thermobarometry, *Journal of Geophysical Research*, *101*(B4), 8229–8244.

Ducea, M., and J. Saleeby (1998a), A case for delamination of the deep batholithic crust beneath the Sierra Nevada, California, *International Geology Review*, *40*(1), 78–93, doi:10.1080/00206819809465199.

Ducea, M., M. A. House, and S. Kidder (2003), Late Cenozoic denudation and uplift rates in the Santa Lucia Mountains, California, *Geology*, *31*(2), 139, doi:10.1130/0091-7613(2003)031<0139:lcdaur>2.0.co;2.

Ducea, M. N. (2003), Arc composition at mid-crustal depths: Insights from the Coast Ridge Belt, Santa Lucia Mountains, California, *Geophysical Research Letters*, *30*(13), 0–3.

Ducea, M. N., and J. B. Saleeby (1998b), The age and origin of a thick mafic-ultramafic keel from beneath the Sierra Nevada batholith, *Contributions in Mineralogy and Petrology*, *133*, 169–185.

Ducea, M. N., S. Kidder, J. T. Chesley, and J. B. Saleeby (2009), Tectonic underplating of trench sediments beneath magmatic arcs: The central California example, *International Geology Review*, *51*(1), 1–26, doi:10.1080/00206810802602767.

Ducea, M. N., J. B. Saleeby, and G. Bergantz (2015), The architecture, chemistry, and evolution of continental magmatic arcs, *Annual Review of Earth and Planetary Sciences*, *43*(1), 299–333, doi:10.1146/annurev-earth-060614-105049.

England, P., and P. Molnar (1990), Surface uplift, uplift of rocks, and exhumation of rocks, *Geology*, *18*(12), 1173–1177, doi:10.1130/0091-7613(1990)018<1173:SUUORA>2.3.CO.

Erkan, K., and D. Blackwell (2009), Transient thermal regimes in the Sierra Nevada and Baja California extinct outer arcs following the cessation of Farallon subduction, *Journal of Geophysical Research*, *114*(B2), B02,107, doi:10.1029/2007JB005498.

Erkan, K., and D. D. Blackwell (2008), A thermal test of the post-subduction tectonic evolution along the California transform margin, *Geophysical Research Letters*, *35*(7), n/a–n/a, doi:10.1029/2008GL033479.

Ernst, W. G., and C. A. Hall (1974), Geology and petrology of the Cambria Felsite, a new Oligocene formation, west-central California Coast Ranges, *Bulletin of the Geological Society of America*, *85*(4), 523–532, doi:10.1130/0016-7606(1974)85<523:GAPOTC>2.0.CO;2.

Farmer, G. L., A. F. Glazner, H. G. Wilshire, J. L. Wooden, W. J. Pickthorn, and M. Katz (1995), Origin of late Cenozoic basalts at the Cima volcanic field, Mojave Desert, California, *Journal of Geophysical Research*, *100*(B5), 8399, doi:10.1029/95JB00070.

Farmer, G. L., A. F. Glazner, and C. R. Manley (2002), Did lithospheric delamination trigger late

Cenozoic potassic volcanism in the southern Sierra Nevada, California?, *Geological Society of America Bulletin*, *114*(6), 754–768, doi:10.1130/0016-7606(2002)114<0754:dldtlc>2.0.co;2.

Fischer, K. M., H. A. Ford, D. L. Abt, and C. A. Rychert (2010), The lithosphere-asthenosphere boundary, *Annual Review of Earth and Planetary Sciences*, *38*(1), 551–575, doi:10.1146/annurev-earth-040809-152438.

Fowler, C. (2005), *The Solid Earth: An Introduction to Global Geophysics*, 1 ed., Cambridge University Press, Cambridge.

Frassetto, A. M., G. Zandt, H. Gilbert, T. J. Owens, and C. H. Jones (2011), Structure of the Sierra Nevada from receiver functions and implications for lithospheric foundering, *Geosphere*, *7*(4), 898–921, doi:10.1130/ges00570.1.

Frey, F. A., and M. Prinz (1978), Ultramafic inclusions from San Carlos, Arizona - Petrologic and geochemical data bearing on their petrogenesis, *Earth and Planetary Science Letters*, *38*, 129–176, doi:10.1016/0012-821X(78)90130-9.

Furlong, K. P., W. D. Hugo, and G. Zandt (1989), Geometry and evolution of the San Andreas Fault Zone in northern California, *J. Geophys. Res.*, *94*(B3), 3100–3110, doi:10.1029/jb094ib03p03100.

Gabuchian, V., A. J. Rosakis, H. S. Bhat, R. Madariaga, and H. Kanamori (2017), Experimental evidence that thrust earthquake ruptures might open faults, *Nature*, *545*(7654), 336–339.

Galer, S. J. G., and R. K. O'Nions (1989), Chemical and isotopic studies of ultramafic inclusions from the San Carlos Volcanic Field, Arizona: A bearing on their petrogenesis, *Journal of Petrology*, *30*(4), 1033–1064, doi:10.1093/petrology/30.4.1033.

Gao, S., X. Liu, H. Yuan, B. Hattendorf, D. Günther, L. Chen, and S. Hu (2002), Determination of forty two major and trace elements in USGS and NIST SRM glasses by laser ablation-inductively coupled plasma-mass spectrometry, *Geostandards and Geoanalytical Research*, *26*(2), 181–196, doi:10.1111/j.1751-908X.2002.tb00886.x.

Gasparik, T. (2000), An Internally Consistent Thermodynamic Model for the System CaO-MgO-Al2O3-SiO2 Derived Primarily from Phase Equilibrium Data, *The Journal of Geology*, *108*, 103–119.

Gilbert, H., Y. Yang, D. W. Forsyth, C. H. Jones, T. J. Owens, G. Zandt, and J. C. Stachnik (2012), Imaging lithospheric foundering in the structure of the Sierra Nevada, *Geosphere*, *8*(6), 1310–1330, doi:10.1130/GES00790.1.

Glazner, A. F. (1991), Plutonism, oblique subduction, and continental growth: An example from the Mesozoic of California, *Geology*, *19*, 784–786, doi:10.1130/0091-7613(1991)019<0784.

Goes, S., and S. van der Lee (2002), Thermal structure of the North American uppermost mantle inferred from seismic tomography, *Journal of Geophysical Research*, *107*.

Green, D., and A. Ringwood (1970), Mineralogy of peridotitic compositions under upper mantle conditions, *Physics of the Earth and Planetary Interiors*, *3*, 359–371, doi:10.1016/0031-9201(70)90076-2.

Grove, M., C. E. Jacobson, A. P. Barth, and A. Vucic (2003), Temporal and spatial trends of Late Cretaceous-early Tertiary underplating ofPelona and related schist beneath southern California and southwestern Arizona, *Tectonic evolution of northwestern Mexico and the southwestern USA*, *374*, 381.

Guyer, J. E., D. Wheeler, and J. A. Warren (2009), FiPy: Partial differential equations with python, *Computing in Science and Engineering*, *11*, 6–15, doi:10.1109/MCSE.2009.52.

Hall, C. A. (1991), Geology of the Point Sur-Lopez Point region, Coast Ranges, California: A part of the Southern California allochthon, *Geological Society of America Special Papers*, *266*, 1–41, doi:10.1130/SPE266-p1.

Hall, C. A., and J. B. Saleeby (2013), Salinia revisited: A crystalline nappe sequence lying above the Nacimiento fault and dispersed along the San Andreas fault system, central California, *International Geology Review*, *55*(13), 1575–1615, doi:10.1080/00206814.2013.825141.

Hardebeck, J. L. (2010), Seismotectonics and fault structure of the California Central Coast, *Bul-*

letin of the Seismological Society of America, *100*(3), 1031–1050, doi:10.1785/0120090307.

Helmstaedt, H., and R. Doig (1975), Eclogite nodules from kimberlite pipes of the Colorado Plateau—samples of subducted Franciscan-type oceanic lithosphere, *Physics and Chemistry of the Earth*, *9*, 95–111.

Hofmann, A. W. (1997), Mantle geochemistry: The message from oceanic volcanism, *Nature*, *385*, 219–229, doi:10.1038/385219a0.

Hole, M. J., G. Rogers, a. D. Saunders, and M. Storey (1991), Relation between alkalic volcanism and slab window formation, *Geology*, *19*(June), 657–660, doi:10.1130/0091-7613(1991)019<0657.

Humphreys, E. D. (1995), Post-Laramide removal of the Farallon slab,western United States, *Geology*, *23*, 987–990, doi:10.1130/0091-7613(1995)023<0987.

Hurst, R. W. (1982), Petrogenesis of the Conejo volcanic suite, southern California: Evidence for mid-ocean ridge–continental margin interactions, *Geology*, *10*(5), 267, doi:10.1130/0091-7613(1982)10<267:potcvs>2.0.co;2.

Jean, M. M., J. W. Shervais, S. H. Choi, and S. B. Mukasa (2010), Melt extraction and melt refertilization in mantle peridotite of the Coast Range ophiolite: An LA-ICP-MS study, *Contributions to Mineralogy and Petrology*, *159*(1), 113–136, doi:10.1007/s00410-009-0419-0.

Johnson, K., H. Dick, and N. Shimizu (1990), Melting in the oceanic upper mantle: An ion microprobe study of diopsides in abyssal peridotites, *Journal of Geophysical Research*, *95*(89), 2661–2678.

Jones, C. H., and R. A. Phinney (1998), Seismic structure of the lithosphere from teleseismic converted arrivals observed at small arrays in the southern Sierra Nevada and vicinity, California, *Journal of Geophysical Research: Solid Earth*, *103*(B5), 10,065–10,090, doi:10.1029/97jb03540.

Jones, C. H., H. Reeg, G. Zandt, H. Gilbert, T. J. Owens, and J. Stachnik (2014), P-wave tomography of potential convective downwellings and their source regions, Sierra Nevada, California, *Geosphere*, *10*(3), 505–533, doi:10.1130/ges00961.1.

Jové, C. F., and R. G. Coleman (1998), Extension and mantle upwelling within the San Andreas fault zone, San Francisco Bay area, California, *Tectonics*, *17*(6), 883–890, doi:10.1029/1998tc900012.

Kelemen, P. B., M. Braun, and G. Hirth (2000), Spatial distribution of melt conduits in the mantle beneath oceanic spreading ridges: Observations from the Ingalls and Oman ophiolites, *Geochemistry Geophysics Geosystems*, *1*(1), doi:10.1029/1999GC000012.

Kennedy, B. M. (1997), Mantle Fluids in the San Andreas Fault System, California, *Science*, *278*(June), 1278–1281, doi:10.1126/science.278.5341.1278.

Kidder, S., and M. N. Ducea (2006), High temperatures and inverted metamorphism in the schist of Sierra de Salinas, California, *Earth and Planetary Science Letters*, *241*(3-4), 422–437.

Kidder, S., M. Ducea, G. Gehrels, P. J. Patchett, and J. Vervoort (2003), Tectonic and magmatic development of the Salinian Coast Ridge Belt, California, *Tectonics*, *22*(5), 1058, doi:10.1029/2002TC001409.

Kidder, S. B., F. Herman, J. Saleeby, J.-P. Avouac, M. N. Ducea, and a. Chapman (2013), Shear heating not a cause of inverted metamorphism, *Geology*, *41*(8), 899–902, doi:10.1130/G34289.1.

Kinzler, R. J. (1997), Melting of mantle peridotite at pressures approaching the spinel to garnet transition: Application to mid-ocean ridge basalt petrogenesis, *Journal of Geophysical Research*, *102*(B1), 853, doi:10.1029/96JB00988.

Kistler, R. W., and D. E. Champion (2001), Rb-Sr whole-rock and mineral ages, K-Ar , Ar/Ar, and U-Pb mineral ages, and Strontium, Lead, Neodymium, and Oxygen Isotopic Compositions for granitic rocks from the Salinian Composite Terrane, California, *USGS Open File Report*, *01-453*, 1–80.

Klemme, S. (2004), The influence of Cr on the garnet–spinel transition in the Earth's mantle: Experiments in the system MgO–Cr2O3–SiO2 and thermodynamic modelling, *Lithos*, *77*(1-4), 639–646, doi:10.1016/j.lithos.2004.03.017.

Klemme, S., and H. S. C. O'Neill (2000), The near-solidus transition from garnet Iherzolite to spinel Iherzolite, *Contributions to Mineralogy and Petrology*, *138*(3), 237–248, doi:10.1007/

s004100050560.

Köhler, T., and G. Brey (1990), Calcium exchange between olivine and clinopyroxene calibrated as a geothermobarometer for natural peridotites from 2 to 60 kb with applications, *Geochimica et Cosmochimica Acta*, *54*(1988), 2375–2388.

Lachenbruch, A., and J. Sass (1980), Heat flow and energetics of the San Andreas Fault Zone, *Journal of Geophysical Research*, *85*, 6185–6222.

Le Pourhiet, L., M. Gurnis, and J. Saleeby (2006), Mantle instability beneath the Sierra Nevada Mountains in California and Death Valley extension, *Earth and Planetary Science Letters*, *251*, 104–119, doi:10.1016/j.epsl.2006.08.028.

Lee, C.-T., R. L. Rudnick, and G. H. Brimhall (2001a), Deep lithospheric dynamics beneath the Sierra Nevada during the Mesozoic and Cenozoic as inferred from xenolith petrology, *Geochemistry, Geophysics, Geosystems*, *2*(12), doi:10.1029/2001gc000152.

Lee, C.-T., Q. Yin, R. L. Rudnick, and S. B. Jacobsen (2001b), Preservation of ancient and fertile lithospheric mantle beneath the southwestern United States, *Nature*, *411*(6833), 69.

Lee, C.-T. A., X. Cheng, and U. Horodyskyj (2006), The development and refinement of continental arcs by primary basaltic magmatism, garnet pyroxenite accumulation, basaltic recharge and delamination: Insights from the Sierra Nevada, California, *Contributions to Mineralogy and Petrology*, *151*(2), 222–242, doi:10.1007/s00410-005-0056-1.

Lee, C.-T. T. A., A. Harbert, and W. P. Leeman (2007), Extension of lattice strain theory to mineral/mineral rare-earth element partitioning: An approach for assessing disequilibrium and developing internally consistent partition coefficients between olivine, orthopyroxene, clinopyroxene and basaltic melt, *Geochimica et Cosmochimica Acta*, *71*(2), 481–496, doi:http://dx.doi.org/10.1016/j.gca.2006.09.014.

Levandowski, W., and C. H. Jones (2015), Linking Sierra Nevada, California, uplift to subsidence of the Tulare basin using a seismically derived density model, *Tectonics*, *34*(11), 2349–2358, doi:10.1002/2015tc003824.

Li, X., X. Yuan, and R. Kind (2007), The lithosphere-asthenosphere boundary beneath the western United States, *Geophysical Journal International*, *170*(2), 700–710, doi:10.1111/j.1365-246x.2007.03428.x.

Liang, Y., C. Sun, and L. Yao (2013), A REE-in-two-pyroxene thermometer for mafic and ultramafic rocks, *Geochimica et Cosmochimica Acta*, *102*, 246–260, doi:10.1016/j.gca.2012.10.035.

Liu, L., M. Gurnis, M. Seton, J. Saleeby, R. D. Müller, and J. M. Jackson (2010), The role of oceanic plateau subduction in the Laramide orogeny, *Nature Geoscience*, *3*(5), 353–357, doi:10.1038/ngeo829.

Livaccari, R. F., and F. V. Perry (1993), Isotopic evidence for preservation of Cordilleran lithospheric mantle during the Sevier-Laramide orogeny, western United States, *Geology*, *21*(8), 719, doi:10.1130/0091-7613(1993)021<0719:iefpoc>2.3.co;2.

Livaccari, R. F., K. Burke, and A. M. C. Şengör (1981), Was the Laramide orogeny related to subduction of an oceanic plateau?, *Nature*, *289*(5795), 276–278, doi:10.1038/289276a0.

Luffi, P., J. B. Saleeby, C.-T. a. Lee, and M. N. Ducea (2009), Lithospheric mantle duplex beneath the central Mojave Desert revealed by xenoliths from Dish Hill, California, *Journal of Geophysical Research*, *114*(B3), B03,202, doi:10.1029/2008JB005906.

Malin, P. E., E. D. Goodman, T. L. Henyey, Y. G. Li, D. A. Okaya, and J. B. Saleeby (1995), Significance of seismic reflections beneath a tilted exposure of deep continental crust, Tehachapi Mountains, California, *Journal of Geophysical Research: Solid Earth*, *100*(B2), 2069–2087, doi:10.1029/94jb02127.

Mancktelow, N. S., and B. Grasemann (1997), Time-dependent effects of heat advection and topography on cooling histories during erosion, *Tectonophysics*, *270*(3-4), 167–195, doi:10.1016/S0040-1951(96)00279-X.

Matthews, V. (1976), Correlation of Pinnacles and Neenach Volcanic Formations and Their Bearing on San Andreas Fault Problem, *AAPG Bulletin*, *60*, doi:10.1306/

c1ea3a82-16c9-11d7-8645000102c1865d.

McCulloch, M., and G. Wasserburg (1978), Sm-Nd and Rb-Sr Chronology of Continental Crust Formation, *Science*, *200*(4345), 1003–1011.

Medaris, G., H. Wang, and J. Fournelle (1999), A cautionary tale of spinel peridotite thermobarometry: An example from xenoliths of Kozákov Volcano, Czech Republic, *Geolines*, *9*, 92.

Mei, S., A. M. Suzuki, D. L. Kohlstedt, N. A. Dixon, and W. B. Durham (2010), Experimental constraints on the strength of the lithospheric mantle, *Journal of Geophysical Research*, *115*(B8), doi:10.1029/2009jb006873.

Murchey, B. L., and D. L. Jones (1984), Age and significance of chert in the Franciscan Complex in the San Francisco Bay Region, *Franciscan Geology of Northern California*.

Nadin, E. S., and J. B. Saleeby (2008), Disruption of regional primary structure of the Sierra Nevada batholith by the Kern Canyon fault system, California, in *Ophiolites, Arcs, and Batholiths: Geological Society of America Special Paper*, vol. 438, edited by J. Wright and J. W. Shervais, chap. 15, pp. 429–454, The Geological Society of America, doi:10.1130/978-0-8137-2438-6.

Nesse, W. D. (2000), *Introduction to Mineralogy*, Oxford University Press, Oxford.

Nicholson, C., C. C. Sorlien, and B. P. Luyendyk (1992), Deep crustal structure and tectonics in the offshore southern Santa Maria Basin, California, *Geology*, *20*(3), 239–&, doi:10.1130/0091-7613(1992)020<0239.

Nicholson, C., C. C. Sorlien, T. Atwater, J. C. Crowell, and B. P. Luyendyk (1994), Microplate capture, rotation of the western Transverse Ranges, and initiation of the San Andreas transform as a low-angle fault system, *Geology*, *22*(6), 491–495, doi:10.1130/0091-7613(1994)022<0491:MCROTW>2.3.CO;2.

Nimis, P., and H. Grütter (2010), Internally consistent geothermometers for garnet peridotites and pyroxenites, *Contributions to Mineralogy and Petrology*, *159*(3), 411–427, doi:10.1007/s00410-009-0455-9.

Nixon, P. H. (1987), *Mantle Xenoliths*, John Wiley and Sons Inc., New York, NY.

O'Neill, H. (1981), The transition between spinel lherzolite and garnet lherzolite, and its use as a geobarometer, *Contributions to Mineralogy and Petrology*, 77, 185–194.

O'Reilly, S. Y. (1997), Minor elements in olivine from spinel lherzolite xenoliths: Implications for thermobarometry, *Mineralogical Magazine*, *61*(405), 257–269, doi:10.1180/minmag.1997.061.405.09.

O'Reilly, S. Y., and W. L. Griffin (2010), The continental lithosphere-asthenosphere boundary: Can we sample it?, *Lithos*, *120*(1-2), 1–13, doi:10.1016/j.lithos.2010.03.016.

Otamendi, J. E., M. N. Ducea, A. M. Tibaldi, G. W. Bergantz, J. D. de la Rosa, and G. I. Vujovich (2009), Generation of tonalitic and dioritic magmas by coupled partial melting of gabbroic and metasedimentary rocks within the deep crust of the Famatinian magmatic arc, Argentina, *Journal of Petrology*, *50*(5), 841–873, doi:10.1093/petrology/egp022.

Ozacar, A. A., and G. Zandt (2009), Crustal structure and seismic anisotropy near the San Andreas Fault at Parkfield, California, *Geophysical Journal International*, *178*(2), 1098–1104, doi:10.1111/j.1365-246x.2009.04198.x.

Page, B. M. (1981), The southern Coast Ranges, *The geotectonic development of California; Rubey Volume I*, *1*, 329–417.

Pike, J. E. N., and E. C. Schwarzman (1977), Classification of textures in ultramafic xenoliths, *The Journal of Geology*, *85*(1), 49–61, doi:10.2307/30068676.

Pikser, J. E., D. W. Forsyth, and G. Hirth (2012), Along-strike translation of a fossil slab, *Earth and Planetary Science Letters*, *331-332*, 315–321, doi:10.1016/j.epsl.2012.03.027.

Platt, J. P., and W. M. Behr (2011), Deep structure of lithospheric fault zones, *Geophysical Research Letters*, *38*(24), doi:10.1029/2011GL049719.

Pollack, H. N., and D. S. Chapman (1977), On the regional variation of heat flow, geotherms, and lithospheric thickness, *Tectonophysics*, *38*(3-4), 279–296, doi:10.1016/0040-1951(77)90215-3.

Robinson, J. A. C., and B. J. Wood (1998), The depth of the spinel to garnet transition at the peridotite solidus, *Earth and Planetary Science Letters*, *164*(1-2), 277–284, doi:10.1016/S0012-821X(98)00213-1.

Royden, L. (1993), The steady state thermal structure of eroding orogenic belts and accretionary prisms, *Journal of Geophysical Research: Solid Earth*, *98*, 4487–4507.

Saleeby, J. (2003), Production and loss of high-density batholithic root, southern Sierra Nevada, California, *Tectonics*, *22*(6), 1064, doi:10.1029/2002TC001374.

Saleeby, J., R. Speed, M. Blake, R. Allmendinger, P. B. Gans, R. W. Kistler, D. C. Ross, D. A. Stauber, M. L. Zobak, A. Griscom, D. S. McCulloch, A. Lachenbruch, R. Smith, and D. Hill (1986), Continent-Ocean Transect, Corridor C2, Monterey Bay offshore to the Colorado Plateau, in *Map and Chart Series TRA C2, 2 Sheets, Scale 1:500,000*, p. 87, Geologic Society of America.

Saleeby, J., K. A. Farley, R. W. Kistler, and R. J. Fleck (2007), Thermal evolution and exhumation of deep-level batholithic exposures, southernmost Sierra Nevada, California, in *Special Paper 419: Convergent Margin Terranes and Associated Regions: A Tribute to W.G. Ernst*, pp. 39–66, Geological Society of America, doi:10.1130/2007.2419(02).

Saleeby, J., L. Le Pourhiet, Z. Saleeby, M. Gurnis, L. L. Pourhiet, Z. Saleeby, and M. Gurnis (2012), Epeirogenic transients related to mantle lithosphere removal in the southern Sierra Nevada region, California, part I: Implications of thermomechanical modeling, *Geosphere*, *8*(6), 1286–1309, doi:10.1130/GES00746.1.

Saleeby, J., Z. Saleeby, and L. Le Pourhiet (2013), Epeirogenic transients related to mantle lithosphere removal in the southern Sierra Nevada region, California: Part II. Implications of rock uplift and basin subsidence relations, *Geosphere*, *9*(3), 394–425, doi:10.1130/GES00816.1.

Saleeby, J. B., Z. Saleeby, J. Robbins, and J. Gillespie (2016), Sediment provenance and dispersal of Neogene-Quaternary strata of the southeastern San Joaquin Basin and its transition into the southern Sierra Nevada, California, *Geosphere*.

Schott, R. C., and C. M. Johnson (1998), Sedimentary record of the Late Cretaceous thrusting and collapse of the Salinia-Mojave magmatic arc, *Geology*, *26*(4), 327, doi:10.1130/0091-7613(1998)026<0327:SROTLC>2.3.CO;2.

Schott, R. C., and C. M. Johnson (2001), Garnet-bearing trondhjemite and other conglomerate clasts from the Gualala basin, California: Sedimentary record of the missing western portion of the Salinian magmatic arc?, *Geological Society of America Bulletin*, *113*(7), 870–880.

Seiders, V. (1989), Geologic map of the Burnett Peak Quadrangle, Monterey and San Luis Obispo Counties, California, *U.S. Geological Survey Geologic Maps*.

Seton, M., R. Müller, S. Zahirovic, C. Gaina, T. Torsvik, G. Shephard, A. Talsma, M. Gurnis, M. Turner, S. Maus, and M. Chandler (2012), Global continental and ocean basin reconstructions since 200Ma, *Earth-Science Reviews*, *113*(3-4), 212–270, doi:10.1016/j.earscirev.2012.03.002.

Sharma, M., A. R. Basu, R. B. Cole, and P. G. DeCelles (1991), Basalt-rhyolite volcanism by {MORB}-continental crust interaction: Nd, Sr-isotopic and geochemical evidence from southern San Joaquin Basin, California, *Contributions to Mineralogy and Petrology*, *109*(2), 159–172, doi:10.1007/bf00306476.

Sharman, G. R., S. A. Graham, M. Grove, and J. K. Hourigan (2013), A reappraisal of the early slip history of the San Andreas fault, central California, {USA}, *Geology*, *41*(7), 727–730, doi:10.1130/g34214.1.

Shervais, J. W., H. G. Wilshire, and E. C. Schwarzman (1973), Garnet clinopyroxenite xenolith from Dish Hill, California, *Earth and Planetary Science Letters*, *19*(2), 120–130, doi:10.1016/0012-821x(73)90106-4.

Shields, J. E., and A. D. Chapman (2016), Late Cretaceous tectonic displacement of sub-continental mantle lithosphere beneath the SW U.S. Cordillera; mantle xenolith constraints from the Colorado Plateau transition zone (central Arizona)., *Abstracts with Programs - Geological Society of America*, *48*(7), @Abstractno.267–12.

Sliter, W. V. (1984), Foraminifers from Cretaceous limestone of the Franciscan Complex, northern California, in *Society of Economic Paleontologists and Mineralogists, Pacific Section*, edited by M. Blake, pp. 149–162, Los Angeles, California.

Smith, P. M., and P. D. Asimow (2005), Adiabat-1ph: A new public front-end to the MELTS, pMELTS, and pHMELTS models, *Geochemistry, Geophysics, Geosystems*, *6*(2), Q02,004, doi: 10.1029/2004GC000816.

Stanley, B. R. G., D. S. Wilson, and P. A. McCrory (2000), Locations and Ages of Middle Tertiary Volcanic Centers in Coastal California, *USGS Open File Reports*, *00*(154), 0–27.

Stein, C. A. (1995), Heat flow of the Earth, *AGU Reference Shelf*, pp. 144–158, doi:10.1112/S0024609301008396.

Stein, C. A., and S. Stein (1992), A model for the global variation in oceanic depth and heat flow with lithospheric age, *Nature*, *356*(6391), 133–135, doi:10.1038/359123a0.

Sun, C., and Y. Liang (2012), Distribution of REE between clinopyroxene and basaltic melt along a mantle adiabat: Effects of major element composition, water, and temperature, *Contributions to Mineralogy and Petrology*, *163*(5), 807–823, doi:10.1007/s00410-011-0700-x.

Sun, D., M. Gurnis, J. Saleeby, and D. Helmberger (2017), A dipping, thick segment of the Farallon Slab beneath Central US, *Journal of Geophysical Research: Solid Earth*, doi:10.1002/2016JB013915.

Sun, S.-s., and W. F. McDonough (1989), Chemical and isotopic systematics of oceanic basalts: Implications for mantle composition and processes, *Geological Society, London, Special Publications*, *42*(1), 313–345, doi:10.1144/GSL.SP.1989.042.01.19.

Taylor, W. (1998), An experimental test of some geothermometer and geobarometer formulations for upper mantle peridotites with application to the thermobarometry of fertile lherzolite and garnet websterite, *Neues Jahrbuch für Mineralogie Abhandlungen*, *172*(2), 381–408.

ten Brink, U., N. Shimizu, and P. Molzer (1999), Plate deformation at depth under northern California: Slab gap or stretched slab?, *Tectonics*, *18*(6), 1084–1098.

Thorkelson, D. J., and K. Breitsprecher (2005), Partial melting of slab window margins: Genesis of adakitic and non-adakitic magmas, *Lithos*, *79*(1-2 SPEC. ISS.), 25–41, doi:10.1016/j.lithos.2004.04.049.

Thorkelson, D. J., and R. P. Taylor (1989), Cordilleran slab windows, *Geology*, *17*(9), 833–836, doi: 10.1130/0091-7613(1989)017<0833:CSW>2.3.CO;2.

Titus, S. J., L. G. Medaris, H. F. Wang, and B. Tikoff (2007), Continuation of the San Andreas fault system into the upper mantle: Evidence from spinel peridotite xenoliths in the Coyote Lake basalt, central California, *Tectonophysics*, *429*(1-2), 1–20, doi:10.1016/j.tecto.2006.07.004.

Tréhu, A. (1991), Tracing the subducted oceanic crust beneath the central California continental margin: Results from ocean bottom seismometers deployed during the 1986 Pacific Gas and Electric EDGE experiment, *Journal of Geophysical Research*, *96*(90), 6493–6506.

Tréhu, A. M., and W. H. Wheeler (1987), Possible evidence for subducted sedimentary materials beneath central California., *Geology*, *15*(3), 254–258, doi:10.1130/0091-7613(1987)15<254:PEFSSM>2.0.CO;2.

Turcotte, D., and G. Schubert (2002), *Geodynamics*, 2 ed., Cambridge University Press, Cambridge.

Usui, T., E. Nakamura, K. Kobayashi, S. Maruyama, and H. Helmstaedt (2003), Fate of the subducted Farallon plate inferred from eclogite xenoliths in the Colorado Plateau, *Geology*, *31*(7), 589, doi:10.1130/0091-7613(2003)031<0589:fotsfp>2.0.co;2.

Van Wijk, J., R. Govers, and K. Furlong (2001), Three-dimensional thermal modeling of the California upper mantle: A slab window vs. stalled slab, *Earth and Planetary Science Letters*, *186*, 175–186.

Vilà, M., M. Fernández, and I. Jiménez-Munt (2010), Radiogenic heat production variability of some common lithological groups and its significance to lithospheric thermal modeling, *Tectonophysics*, *490*(3-4), 152–164, doi:10.1016/j.tecto.2010.05.003.

Wang, Y., D. W. Forsyth, C. J. Rau, N. Carriero, B. Schmandt, J. B. Gaherty, and B. Savage (2013), Fossil slabs attached to unsubducted fragments of the Farallon plate., *Proceedings of the National Academy of Sciences*, pp. 5342–6, doi:10.1073/pnas.1214880110.

Warren, J. (2016), Global variations in abyssal peridotite compositions, *Lithos*, *248-251*, 193–219, doi:10.1016/j.lithos.2015.12.023.

Warren, J. M., and G. Hirth (2006), Grain size sensitive deformation mechanisms in naturally deformed peridotites, *Earth and Planetary Science Letters*, *248*(1-2), 438–450, doi:10.1016/j.epsl.2006.06.006.

Wasserburg, G., S. Jacobsen, D. DePaolo, M. McCulloch, and T. Wen (1981), Precise determination of ratios, Sm and Nd isotopic abundances in standard solutions, *Geochimica et Cosmochimica Acta*, *45*(Table 1), 2311–2323, doi:10.1016/0016-7037(81)90085-5.

Wilshire, H., C. E. Meyer, J. K. Nakata, and L. C. Calk (1988), Mafic and ultramafic xenoliths from volcanic rocks of the western United States, *USGS Open File Report*, *1443*, 179.

Wilson, D. S., P. a. McCrory, and R. G. Stanley (2005), Implications of volcanism in coastal California for the Neogene deformation history of western North America, *Tectonics*, *24*, 1–22, doi:10.1029/2003TC001621.

Witt-Eickschen, G., and H. S. O'Neill (2005), The effect of temperature on the equilibrium distribution of trace elements between clinopyroxene, orthopyroxene, olivine and spinel in upper mantle peridotite, *Chemical Geology*, *221*(1-2), 65–101, doi:10.1016/j.chemgeo.2005.04.005.

Wood, D. J., and J. B. Saleeby (1997), Late Cretaceous-Paleocene extensional collapse and disaggregation of the southernmost Sierra Nevada batholith, *International Geology Review*, *39*(11), 973–1009, doi:10.1080/00206819709465314.

Workman, R. K., and S. R. Hart (2005), Major and trace element composition of the depleted MORB mantle (DMM), *Earth and Planetary Science Letters*, *231*(1-2), 53–72, doi:10.1016/j.epsl.2004.12.005.

Yan, Z., and R. W. Clayton (2007), A notch structure on the Moho beneath the Eastern San Gabriel Mountains, *Earth and Planetary Science Letters*, *260*(3-4), 570–581, doi:10.1016/j.epsl.2007.06.017.

Yan, Z., R. W. Clayton, and J. Saleeby (2005), Seismic refraction evidence for steep faults cutting highly attenuated continental basement in the central Transverse ranges, California, *Geophysical Journal International*, *160*(2), 651–666, doi:10.1111/j.1365-246x.2005.02506.x.

Zandt, G., H. Gilbert, T. J. Owens, M. Ducea, J. Saleeby, and C. H. Jones (2004), Active foundering of a continental arc root beneath the southern Sierra Nevada in California, *Nature*, *431*(7004), 41–46, doi:10.1038/nature02847.

2.A Thermal modeling approach and sensitivity

Thermal modeling setup

In this section, we discuss parameters and techniques used in modeling. Standard values for thermal conductivity from *Fowler* (2005) yield good results. Increasing the thermal conductivity of the model domain substantially depresses the modeled geotherms (lowering predicted temperatures at a given depth), but does not affect the relative temperatures predicted by the geotherms. Radiogenic heat flow for the continental marginal crust is estimated conservatively, and changes result in only minor changes to modeled geotherms across the board.

Slab window crustal replacement In model group **A**, we model shallow slab-window upwelling. The emplacement of slab-window asthenosphere directly under the coastal central California crust entails the truncation of a low-temperature forearc geotherm at the base of the crust and the substitution of an asthenospheric adiabat below this level. The model begins at 24 Ma, corresponding to the time of opening of the Mendocino slab window under southern California (*Wilson et al.*, 2005). The geotherm begins as a steady-state profile to 600 °C at 30 km, truncated by a mantle adiabat. The mantle is held at asthenospheric conditions for a set period which is varied between model runs (from 0 to 6 Myr) to simulate a period of active convection, after which it relaxes conductively to the conclusion of the model.

Subduction and underplating Thermal conditions during subduction are tracked using the *Royden* (1993) steady-state forearc model. The samples then relax to the present. After subduction and underplating, the cooled oceanic lithosphere re-equilibrates with an overlying 30 km of forearc crust until the present, or for our xenolith samples until the time of ca. 1.7 Ma entrainment and eruption.

Progressive subduction of the downgoing slab beneath the forearc wedge is modeled as stepwise advection beneath a linearly thickening forearc wedge conforming to the *Royden* (1993) thermal model using the parameters outlined above. For all cases, the final depth of the underplated subduction interface is taken to be 30 km, and the distance landward of the subduction zone is taken to be 100 km. No effort is made to differentiate 'flat-slab' and baseline subduction geometries.

Though increasing the slab dip angle will result in a cooler subduction interface at a given depth, the overall effect on the evolution of the thermal scenarios appears to be minimal.

Oceanic geotherm For the Neogene stalled Monterey plate and Late Cretaceous Farallon mantle nappe scenarios, the Global Depth and Heat (GDH) model (*Stein and Stein*, 1992) is used to trace the thermal evolution of the oceanic lithosphere from its emplacement at the spreading ridge until subduction. This model is a Taylor-polynomial fit of cooling parameters to global heat-flow and depth datasets. This fit yields higher geotherms than half-space cooling models that are directly based on Equation 2.1 (e.g., *Fowler* (2005)), and tends to produce higher geotherms for old oceanic lithosphere.

With the GDH model in conjunction with the *Royden* (1993) subduction model, we predict low temperatures (~235-245 $^{\circ}$C) at the subduction interface for the oldest stalled slabs modeled. For the Monterey Plate scenario (with young oceanic crust) the temperature at the subduction interface is predicted to be 980 $^{\circ}$C.

All oceanic-cooling models, including GDH and half-space cooling models, significantly overestimate heat flux from young oceanic plates, a fact that is likely attributable to vigorous hydrothermal circulation in young submarine lithosphere (*Stein and Stein*, 1992; *Stein*, 1995). This may result in overestimates of geothermal gradients for the scenarios with the youngest subducted oceanic crust, such as the Monterey Plate scenario at the left of Figure 2.20.

Supra-subduction geotherm The geotherm of the forearc wedge during subduction is calculated using the *Royden* (1993) analytical solution for the steady-state thermal structure of continuously-subducting systems. Shear heating on the subduction thrust is ignored, as recent studies suggest that it is not an important factor (*Kidder et al.*, 2013). Forearc rock uplift and erosion, as well as accretion and erosion on the subduction megathrust are ignored. In reality, megathrust accretion rates of 0.2-3.6 km/Myr are favored by *Kidder et al.* (2013) based on the Pelona schist, and some rock uplift is evident for the Coast Ranges.

The coastal California accretionary crust is represented homogenously as a material with a thermal conductivity of 2.71 W/m/K, specific heat capacity of 1000 J/kg/K, density of 2800 kg/m^3 and a radiogenic heat flux of 2 uW/m^3, values that are close to average for the continental crust (*Fowler*, 2005) and those used by *Kidder et al.* (2013) to model the thermal conditions along the Late Cretaceous shallow subduction megathrust segment. A radiogenic heat production in the crust of 2 uW/m^3 is actually a relatively conservative estimate given the fluxes shown for Sierra Nevada batholithic material by *Brady et al.* (2006), and the fact that much of the Franciscan material within the subduction channel is pelitic sediment rich in radiogenic elements (*Vilà et al.*, 2010). Still, lower radiogenic heat production in the crust yields only a slight decrease in modeled geotherms across the board, not impacting conclusions.

Thermal model sensitivity and bias

Generally, changes in model parameters such as radiogenic heat flux, thermal conductivity, and heat capacity do not impact the relative results for modeled scenarios, due to the consistent lithologic structure of the model domains.

Due to widely varying timescale of equilibration for modeled scenarios in groups **B** and **C**, the model is sensitive to assumptions about steady-state cooling of the oceanic mantle lithosphere. The choice of the "GDH" model to track the evolution of the suboceanic thermal structure is an important control on the scale of temperature variation in Figure 2.20b. Though GDH is well-calibrated, oceanic cooling models tend to overestimate the heat flow from young oceanic plates (*Stein*, 1995). Thus, the modeled geothermal gradients for the younger stalled slab model runs may be too high.

Another potential confounding factor affecting the older scenarios of **B** and **C** is the thermal effects of continued subduction beneath the underplated mantle nappes. After rollback and underplating of the modeled section of oceanic mantle lithosphere, a downgoing slab at depth could, depending on its age, cool the forearc lithosphere from below. However, this effect is considered minimal and diminishes over time due to the progressive subduction of younger, hotter oceanic lithosphere. Reconstruction of the Pacific–Farallon spreading ridge history show that, between ca. 70 and 30 Ma, oceanic lithosphere entering the southwest Cordilleran subduction zone got younger at a rate of ~1 Myr/Ma (*Atwater and Stock*, 1998; *Liu* *et al.*, 2010; *Seton et al.*, 2012) corresponding to the approach of the ridge to the subduction zone. This factor coupled with slab window emplacement starting at ca. 24 Ma leads to the interpretation that cooling from below by continued subduction was of second-order significance.

Surface erosion is not modeled, but may bias the results. Any erosion will yield higher apparent heat flows and increased geotherm convexity, as heat is advected from the top of the model domain by material removal (*Mancktelow and Grasemann*, 1997; *England and Molnar*, 1990). Geologic constraints suggest that 15-20 km of exhumation is likely to have occurred in a major pulse of unroofing coincident with flat-slab underplating and rollback in the Cretaceous (*Saleeby*, 2003; *Chapman et al.*, 2012), and is thus likely to disproportionately affect the older models. The lack of erosion in the model framework biases towards predicting lower geothermal gradient overall. For the slab window and underplated Monterey plate scenarios (model groups **A** and **B**) this effect would push the final geotherm to or beyond the limit of xenolith thermobarometry [Figure 2.21a and b]. In the underplated mantle nappe scenario (model **C**) this effect would push the final modeled geotherm towards the centroid of the xenolith thermobarometric array [Figure 2.21c and 2.22].

The uncertainties inherent in this model bias the results towards predicting lower-temperature, less-convex geotherms over the model domain. These potential biases affect comparisons comparisons with measured values of heat flux and xenolith thermobarometry, which are not subject to these biases [Figure 2.22]. Thus, geotherms predicted by this model might be underestimates for potential mantle temperature at a given depth, especially for the older tectonic scenarios modeled.

Factors not incorporated in the model

Several simplifications are made to create an internally consistent model framework. Subducted oceanic crust is not considered to have distinct thermal properties from the oceanic mantle. Additionally, though there are no reliable estimates of the mantle heat flux that cover the model domain, the model is run to great depth to avoid any influence of this uncertainty on the surface geotherm.

Subduction zone rollback The confounding factor of an active subduction zone just outboard of the scenarios for the older models is also not included within the model. When the trench interface jumps with the emplacement of an oceanic mantle nappe beneath the forearc, the new subduction interface will cool the detached nappe from below. This is not modeled because it would substantially increase model complexity (requiring a fully iterative approach to the forearc geotherm), and at this distance (~100 km) inboard of the final trench interface, there is limited scope for further episodic rollback after emplacement of the nappe(s) of presumed xenolith source [e.g. Figure 2.18c]. Further, although an active subduction interface at depth will cool the mantle lithosphere from below, the subduction of progressively younger crust until cessation at ~27 Ma will yield gradually increasing heat on the subduction interface (*Royden*, 1993). The models for scenarios **B** and **C** [Figure 2.22b and c] are already near the coolest permitted by our xenolith constraints. As these geotherms are already quite cold, introducing this added complexity will not significantly change the model results. However, late-Cretaceous underplating and other stalled-slab scenarios can be treated as maximum temperatures because of the influence of the subducting slab.

Change in convergence rate of rotating microplates Potential Monterey Plate mantle lithosphere beneath Crystal Knob would have been emplaced under the ridge at 27 Ma (corresponding to the chron 7 magnetic anomaly) and subducted shortly thereafter (*Atwater and Stock*, 1998; *Wilson et al.*, 2005). Due to slower margin-normal convergence during microplate fragmentation and rotation (*Wilson et al.*, 2005), the parcel would take ~3 Myr to reach its final stalled position (~100 km behind the trench) as shown in Figure 2.18b. This is responsible for the kink in the "Age of initial oceanic lithosphere" curve in Figure 2.20b. For model simplicity, we do not incorporate this disequilibrium shift into the starting parameters of the *Royden* (1993) subduction model.

Erosion of the forearc Surface erosion after underplating is taken to be zero. Any erosion will result in higher apparent heat flow values and increased geotherm convexity, as heat is advected from the top of the model domain by material removal. Geologic constraints suggest that the majority of erosion to the mid-crustal levels now at the surface in Salinia is likely to have occurred in a major pulse of unroofing coincident with flat-slab underplating and rollback (*Saleeby*, 2003; *Chapman et al.*, 2012), and is thus likely to disproportionately affect the older models. The 30 km of crust shown in the study area is based on modern estimates of the Moho depth, so recent erosion is unlikely to have biased the whole-lithosphere geotherm significantly. Still, the lack of erosion in the model framework will likely bias the results towards predicting a lower geothermal gradient overall, and lower temperatures in the mantle lithosphere, as upward advection of material by erosion increases the geothermal gradient (*Mancktelow and Grasemann*, 1997; *England and Molnar*, 1990). Thus, these values need to be biased to higher temperatures to accurately capture the relationship between xenolith constraints on the actual temperature and temperatures derived from this modeling.

3 The Zebra Nappe: a structurally displaced Neoproterozoic passive margin stratigraphy in the southern Naukluft Mountains, Namibia

Daven P. Quinn[1] J.P. Grotzinger[1] T.M. Present[1]

1 Division of Geological and Planetary Sciences, California Institute of Technology, Pasadena, California, USA

Abstract

The Zebra Nappe is the youngest allocthonous tectonic unit of the Naukluft Nappe Complex (NNC), an outlier of the 650-540 Ma Damara orogeny that consists of carbonate and clastic strata thrust south- and southwestward over the Nama foreland basin. The tectonic units of the NNC are Neoproterozoic in depositional age, while Damara orogenesis and foreland-basin deposition span the Precambrian-Cambrian boundary. We present a new geologic mapping, detailed stratigraphic characterization, and detrital zircon data of the southern Naukluft Mountains, focusing on the Zebra Nappe. The Zebra Nappe overlies the Dassie Nappe on a small-displacement roof thrust. We have provisionally (pending confirmation with mapping of the upper nappes) revised and simplified the multistage depositional model proposed by previous workers to two phases of south-directed and east-directed deformation that coincide with the overall tectonic context of the Kalahari craton margin: (1) southward blind thrusting of the Dassie nappe beneath the Zebra Nappe stratigraphy and (2) southwest thrusting of the entire NNC over the Nama on a major basal detachment. The Zebra Nappe contains three major stratigraphic sequence: (1) a peritidal sequence, (2) a deepening inner to outer shoreface sequence and (3) a monotonous carbonate shoal. This overall deepening environment may signify a tectonic forcing (e.g. the onset of foreland basin systematics) or isostatic adjustment after rapid sedimentation (e.g. after cap-carbonate deposition). Chemostratigraphy does not permit a clear age determination. Detrital zircon data for the Zebra Nappe show no Damara-orogen input, suggesting that the sequence does not correlate to the Nama Group. While the lithology of the upper nappes is characteristic of Marinoan cap carbonates, the Zebra Nappe apparently represents a Neoproterozoic passive margin sequence with no clear correlative in southern Namibia, which revises its previously-assumed correlation with the Nama Group foreland basin sequence.

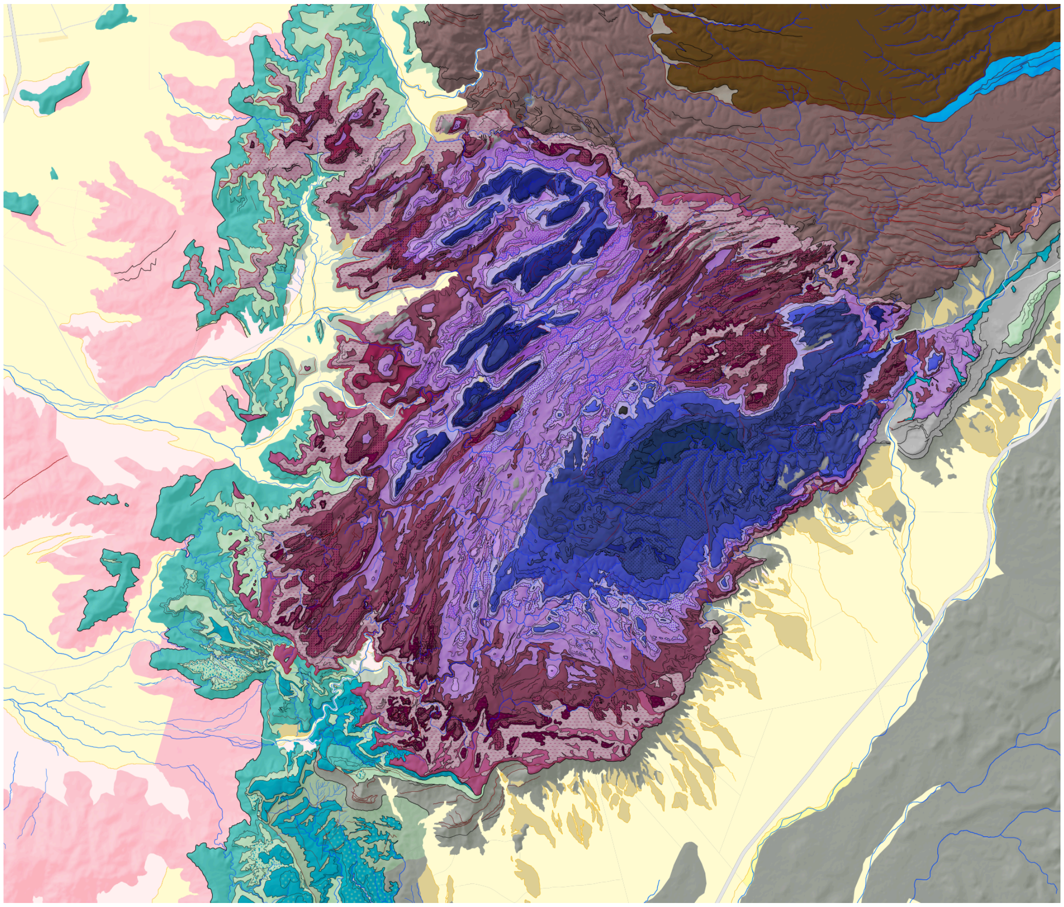

Plate 1: Interactive digital plate of the preliminary geologic map of the southern Naukluft mountains, archived with this dissertation at https://doi.org/10.7907/5exk-mr58 in the CaltechDATA repository.

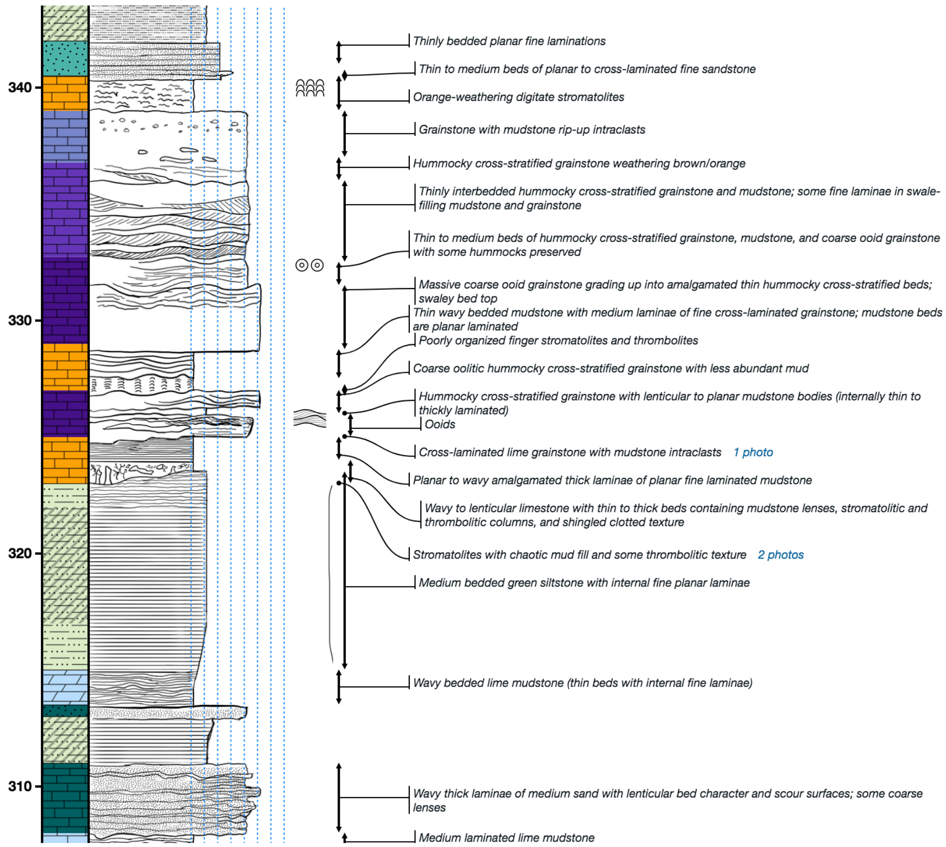

Plate 2: Interactive digital plate of full-resolution and generalized stratigraphic sections and correlations in the Zebra Nappe, archived with this dissertation at https://doi.org/10.7907/9kva-eq78 (current version works best in the Chrome or Firefox browsers).

The ca. 542 Ma Precambrian-Cambrian boundary marks a key environmental transition in Earth history, highlighted by the emergence of complex animal life. This important transition was preceded by an interval of rapid paleoenvironmental changes, including several snowball Earth glaciations during Cryogenian time (*Kirschvink*, 1992; *Hoffman*, 1998) and rapid environmental shifts preserved in the ocean's isotopic record (e.g. **?***Halverson et al.*, 2002, 2004; *Ohnemueller et al.*, 2014). During this time enigmatic Ediacaran fauna explored body plan morphologies and animals diversified and began to biomineralize, forever changing the ocean's chemical cycles, and dominance of the world's shallow marine ecosystems transitioned from microbes to animals (e.g. **?***Grotzinger et al.*, 2011; *Knoll*, 1999). Latest Neoproterozoic strata are the key record of these globally significant environmental shifts.

This period of Earth history is well preserved in several well-known and globally distributed locations, but there is still room to improve sampling to separate global and local environmental signals, especially as recorded via geochemical proxies. Different stratigraphic sections may not be complete records of geologic time, and may further show bias by sampling different sedimentary environments. Therefore, additional stratigraphic records covering Cryogenian to Ediacaran time are needed to fully understand the evolution of the Earth system across this crucial boundary (e.g. *Smith et al.*, 2016).

The Damara-Gariep orogenic belt of central to southern Namibia, a branch of the pan-African orogenic belt that formed during assembly of Gondwana and eventually Pangaea, dates to this time period. Orogenic activity led to the end of passive-margin sedimentation on the continental margin (*Stanistreet et al.*, 1991; *Blanco et al.*, 2011) but allowed the preservation of deposits from a variety of sedimentary environments. The northern externides of the Damara orogenic belt contain well-preserved glacial and cap carbonate sequences in passive-margin and foreland basin sequences atop the Congo Craton (*Prave*, 1996; *Hoffman et al.*, 1998; *Halverson et al.*, 2004). The foreland basin of the Damara-Gariep orogen in southern Namibia, developed atop the Kalahari Craton, contains globally superlative exposures of late Ediacaran to earliest Cambrian strata, preserving a shallow carbonate-siliciclastic ramp (*Dibenedetto and Grotzinger*, 2005) with thrombolite reefs containing late Ediacaran calcifying meazoans (**?***Grotzinger and Knoll*, 1999; **?**; *a. Watters et al.*, 2011). Previous work on these rocks provides a clear record of paleoenvironmetal conditions associated with this transition.

The Naukluft Nappe Complex (NNC) of southern Namibia is an isolated remnant of a shallow fold-and-thrust belt of the southern margin of the Damara Orogen, vergent onto the Kalahari Craton. Several distinct nappes preserve slices of dominantly carbonate sedimentary sequences, though clastic sediments including glacial diamictites are common. Some of the nappes have been discussed as glacial to cap-carbonate sequences, potentially correlating to other globally distributed glacial and cap strata, including those deposited atop the Congo craton in northern Namibia. Others are mixed carbonate-clastic successions that have been tentatively correlated to Nama Group foreland basin deposits (*Hartnady*, 1978; *Hoffmann*, 1989; *Miller*, 2008). The uncertain tectonic setting and internal stratigraphy and structure of these nappes has limited their usefulness in regional to global correlation. However, they clearly preserve records of Cryogenian to possibly Ediacaran Earth history that could aid understanding of this important period in time.

The well-established understanding of Neoproterozoic paleogeography and environmental history captured in northern Namibia (Congo craton), and new work on the mechanics of Damara orogenesis, allows renewed focus on the NNC to contextualize it and determine what it may record. Here we present new mapping of the southern NNC, focusing on the Zebra Nappe, the southernmost nappe, which is thought to most closely tie to the autochthonous Nama Group. This fresh mapping effort clarifies the structure and stratigraphy of the Zebra Nappe and simplifies its tectonic relationships with the other Naukluft nappes.

In addition to structural mapping, our work is accompanied by detailed stratigraphic analysis within the Zebra Nappe. We present a detailed lithostratigraphy and the first high-resolution chemostratigraphy of the nappe. The Zebra Nappe has heretofore been treated as a distal facies of the Nama Group foreland basin sequence. Instead, we suggest that the Zebra Nappe likely represents a passive margin sequence, and is thus older than the Nama Group which consists entirely of foreland basin fill. As such, these rocks provide an important new window into the sedimentary–tectonic history of the northern margin of the Kalahari Craton.

3.1.1 Geologic context

Neoproterozoic to Cambrian Pan-African orogenesis during the formation of Gondwana was the last major tectonic event to affect the cratonic core of Namibia. Three branches of this orogenesis operated in Namibia: First, the coastal Kaoko-belt suture in northern Namibia between the Sao Francisco (South America) and Congo cratons developed as the Adamastor Ocean began a diachronous closure from north to south at ca. 580 Ma (*Stanistreet et al.*, 1991; *Gresse and Germs*, 1993; *Gray et al.*, 2008). During this progressive suturing, the perpendicular inland branch of the Damara orogen fused the Kalahari and Congo cratons as the Khomas Ocean closed. Coastal suturing completed with the Gariep orogeny of southern Namibia, which welded the western margin of the Kalahari craton to the South American Rio de la Plata craton (*Frimmel*, 1998). The absence of subsequent tectonic overprinting resulted in preservation of significant volumes of Cryogenian to Cambrian strata; Cretaceous uplift associated with opening of the Atlantic Ocean basin produced superb exposures along the western African escarpment (e.g. *Gallagher and Brown*, 1999).

Northern Namibia preserves classic glacial to cap carbonate sequences along the Congo craton margin (*Hoffman*, 1998). The Swakop group, which was and metamorphosed and thrust atop the Congo Craton in the Damara Orogen, also preserves these facies, with accurate 630 Ma depositional dates (*Hoffmann et al.*, 2004).

The northern Kalahari craton margin also has autochthonous Cryogenian glacial and cap carbonate strata, but exposures generally are much less extensive and well exposed. The Witvlei Group of east-central Namibia is thin, deposited across a marginal structural arch of the Kalahari Craton. Its basal Court Formation has been correlated based on coarse stratigraphic relationships (*Hoffmann*, 1989) and carbon-isotope chemostratigraphy (*Prave et al.*, 2011) to the Sturtian glaciation, and the upper Buschmannsklippe Formation has been correlated to the Marinoan glaciation. The autochthonous Gariep Group along the coast of southern Namibia contains glacial strata potentially correlating to these sequences but is likewise thin, preserving relatively little stratigraphy (*Hoffmann*, 1989). Allocthonous equivalents are thicker but significantly strained. The allocthonous rocks of the NNC

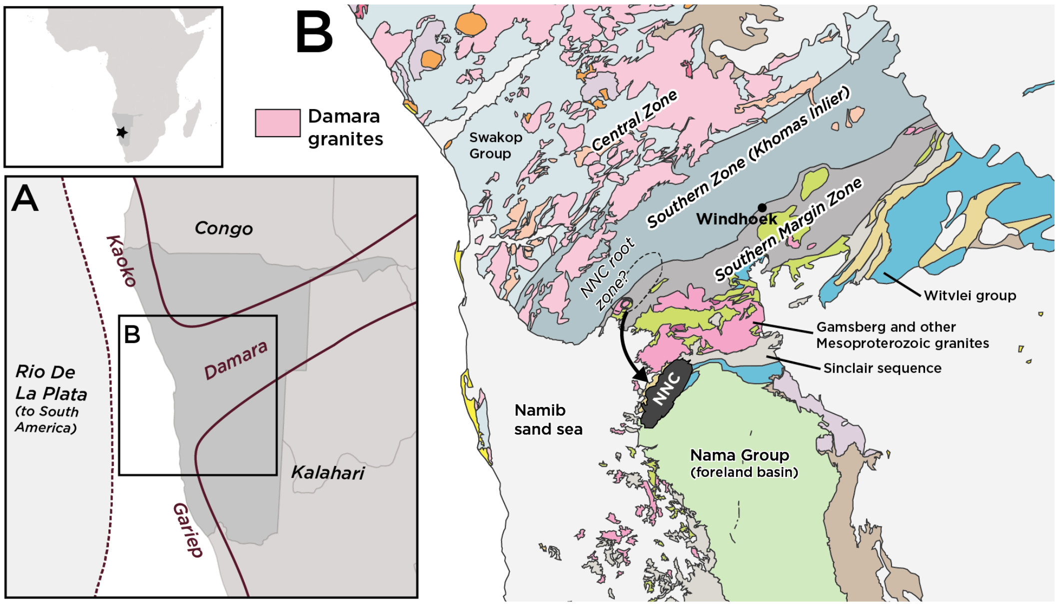

Figure 3.1: Tectonic context of the NNC within the Damara orogenic belt of central Namibia.

provide the best likelihood of sampling thick stratigraphic sequences representing the late Neoproterozoic margin of the Kalahari craton, if they can be placed in time. Though imbricated and folded, penetrative strain is minimal, allowing detailed analysis of sedimentary structures and paleoenvironmental history.

The Nama Group, an extensive and well-preserved foreland-basin sequence of the Damara-Gariep orogen (*Germs*, 1974; *Saylor et al.*, 1995, 1998) contains key environmental markers and fossil records of latest Ediacaran and early Cambrian time (*Grotzinger and Knoll*, 1999; **?**). Its completeness contrasts with the sparse stratigraphic record on the Kalahari Craton prior to latest Ediacaran time. If the Zebra Nappe of the NNC represents a distal facies of the Nama Group, as has been previously proposed (*Hartnady*, 1978; *Hoffmann*, 1989), it would provide a new sedimentary environment with different manifestations of the dynamic ecosystem of the Nama Group, and a temporally-constrained pin for evaluating relationships with the other nappes. If this correlation is incorrect, the Zebra Nappe represents a fundamentally different stratigraphy deposited earlier in the Neoproterozoic.

The Naukluft Nappe Complex (NNC) The NNC is a sequence of lithologically distinct, internally deformed nappes dominantly composed of carbonate sedimentary rocks and structurally separated by thrust faults. The NNC corresponds to the

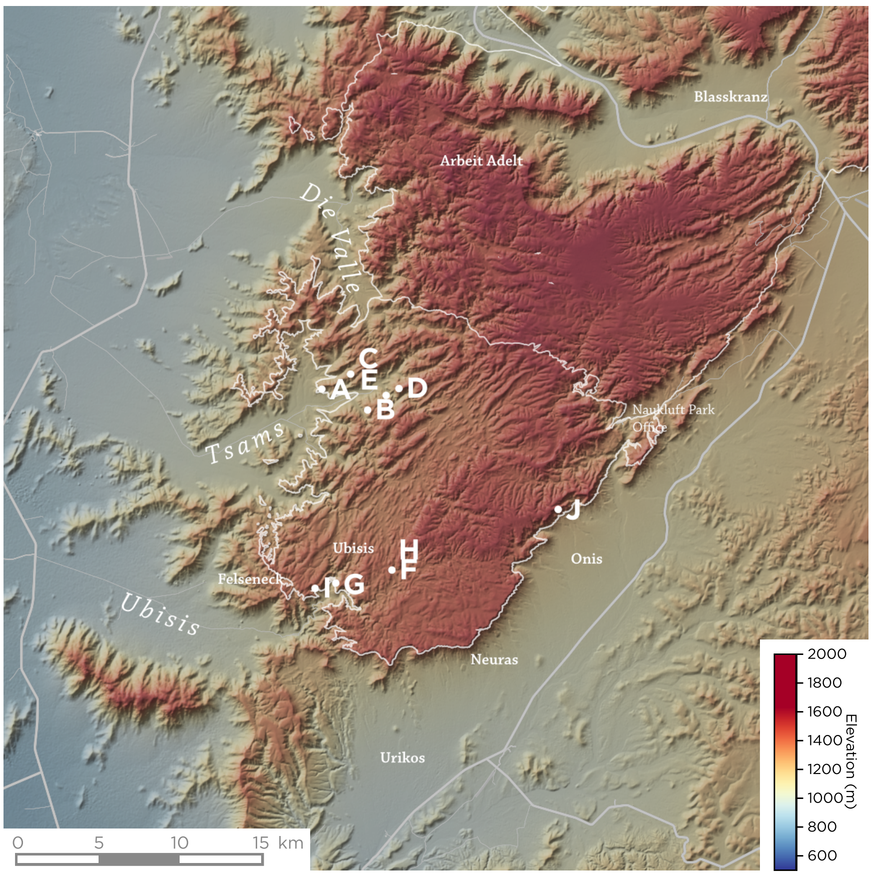

Figure 3.2: Physiographic elevation and shaded-relief map of the southern Naukluft Mountains, with the Zebra Nappe and NNC outlined in white. The locations of stratigraphic sections measured in this study (A-J) are also labeled. Farms and valleys within the study area labeled, and roads within the study area are shown in light gray.

Naukluft Mountains, a major physiographic feature on the African escarpment in west-central Namibia. The mountain range forms a plateau 300-800 m above the surrounding plains, which attains a maximum height of ~1850 m at its center and eastern edge [Figure 5.2]. The flat peneplain at the top of the Naukluft Mountains has been discussed as a "Pre-Karoo surface" likely dating to Ordovician beveling by the Dwyka ice sheet (*Martin*, 1953). This topographic relic is preserved by the long-lived arid climate of southwest Africa.

There has been a sustained interest in the basal décollement of the NNC, or "Sole thrust", a carbonate-hosted basal thrust fault (*Korn and Martin*, 1959; *Behr et al.*, 1983; *Weber and Ahrendt*, 1983; *Viola et al.*, 2006). The basal thrust forms a gently concave surface beneath the mountain range and dips the steepest at its eastern edge. Early work suggested that the nappes were emplaced atop this surface by "gravity tectonics" lubricated by carbonate brines (*Korn and Martin*, 1959; *Martin et al.*, 1983), while more recent work has focused on typical thin-skinned thrustbelt processes (*Viola et al.*, 2006; *Fagereng et al.*, 2014) focused on the eastern margin of the Zebra Nappe, where the "gritty dolomite" on the fault surface hosts in-situ mineral growth (*Rowe et al.*, 2012).

Hartnady (1978) proposed that the overall NNC was transported from a minimum of 78 km northwest of its current location from roughly overlying the Hakos Terrane, inside the southern margin zone of the Damara orogenic belt. *Martin et al.* (1983) suggest a slightly further displacement of 90 km from the same direction, proposing a correlation between the Corona Formation within the Damara Sequence and the Büllsport Formation.

The NNC has been mapped several times with different tectonic interpretations. *Korn and Martin* (1959) mapped the mountain range and recognized five "Series," rock units which correspond to the nappe units recognized today. *Hartnady* (1978) again mapped the mountain range, describing its lithostratigraphy in somewhat more detail. *Hoffmann* (1989) proposed stratigraphic correlations for the NNC, presumably based on unpublished mapping. In general, the nappe units are the Kudu, Pavian, Dassie, and Zebra nappes, ordered from oldest to youngest, with the older nappe units thrust over the younger (except apparently the Zebra Nappe). Several subdivisions of the nappe units have been proposed by previous workers to account for distinctions in lithology and deformational style, and nomenclature is summarized in Table 3.1. The rock units of the Zebra Nappe are referred to as the Zebra River Formation by *Hartnady* (1978) and elevated to the Zebra River Group in this study. The Dassie Nappe, adjacent to the Zebra Nappe, is primarily referred to as the Büllsport Formation.

The Zebra Nappe The Zebra Nappe is distinctive among the major nappe components of the NNC due to its thick and varied stratigraphy of carbonate and siliciclastic rocks. It is also clearly tectonically distinct from the rest of the nappe complex, with southeast-vergent structures contrasting with the southward imbrication pattern of the other nappes. The uniqueness of the Zebra Nappe has been recognized by previous workers, but its tectonic context and correlation cannot be easily assessed from existing studies.

Coarse structural relationships between the nappes suggest that the Zebra Nappe preserves a younger stratigraphy than the nappes further north in the complex, and the Zebra Nappe has been correlated with the basal stratigraphy of the Nama Group (*Hartnady*, 1978; *Hoffmann*, 1989). Correlations with the Nama group and older formations are poorly developed in the literature, and no rationale for tectonic assembly of the Zebra Nappe is advanced. Our more detailed mapping effort is targeted at gaining a fuller understanding the internal structure and possible stratigraphic correlations of the Zebra Nappe.

Hartnady (1978) discussed the Zebra Nappe as the Zebra River Formation of the Western Dassie Nappe, describing a conformable depositional contact separating the Zebra Nappe from the imbricated Dassie Nappe dolomite, with lithologically similar dolomites on either side of the contact. However, both *Korn and Martin* (1959) and *Hartnady* (1978) recognized the distinct structural styles and vergence directions of the two domains, suggesting that several deformation events were needed to explain these features regardless of the original nature of the contact. *Hartnady* (1978) proposed that the Zebra River Formation is the stratigraphically youngest unit of the NNC, and proposed that it a distal equivalent of the basal Nama Group foreland basin sequence, based its the mixed carbonate and siliciclastic stratigraphy.

Both *Hartnady* (1978) and *Hoffmann* (1989) describe a structural discordance

Table 3.1: Nomenclature and overview of NNC tectonic units

<table>
<tr><th colspan="4">Nappe tectonic units</th><th rowspan="2">Lithologic formations (Hartnady, 1980)</th></tr>
<tr><th>Korn and Martin (1959)</th><th>Hartnady (1978)</th><th>Hoffmann (1989)[a]</th><th>this work</th></tr>
<tr><td>Kudu</td><td></td><td rowspan="4"></td><td rowspan="2">not studied</td><td>Noab
Klipbokrivier</td></tr>
<tr><td rowspan="3">Pavian</td><td>Northern Pavian</td><td>Remhoogte
Blasskranz
Tsabisis</td></tr>
<tr><td rowspan="2">Southern Pavian</td><td>Büllsport[b]</td><td rowspan="2">Aubsluscht
Zebra River</td></tr>
<tr><td>Arbeit Adelt[b]</td></tr>
<tr><td rowspan="2">Dassie</td><td colspan="2">Eastern Dassie</td><td rowspan="2">Zebra Nappe overrides Dassie on a passive roof thrust</td><td rowspan="2">Büllsport</td></tr>
<tr><td rowspan="3">Western Dassie[c]</td><td rowspan="2"></td></tr>
<tr><td rowspan="2">Zebra</td><td rowspan="2">No internal discontinuities within Zebra Nappe</td><td rowspan="2">Zebra River</td></tr>
<tr><td>Leopard[d]</td></tr>
<tr><td>Rietoog</td><td colspan="4">parautochthonous Omkyk Formation of Nama Group</td></tr>
</table>

[a] completed with *Miller* (2008) summary of unpublished work by *Hoffmann*
[b] mapped as Zebra River Formation (ZRF) by *Hartnady* (1980)
[c] ZRF unconformably deposited above imbricated Dassie Nappe
[d] Onis Formation thrust atop lower ZRF

at the base of the Onis Formation within the Zebra Nappe. *Hartnady* (1978) envisions an erosional unconformity between the lower Zebra River Formation and the Onis Formation, with deposition of the lower Zebra River Formation atop the Dassie Nappe during its imbrication and the Onis Formation being deposited discordantly atop folded and eroded Lower Zebra River Formation rocks. *Hoffmann* (1989) suggested that the Onis Formation was instead the hanging wall of a major thrust fault, and proposed lithostratigraphic correlations linking the Onis Formation with the Court Formation of the Witvlei Group, based on lithologic similarity to the 'black limestones' of the Gobabis Member. The lower Zebra Nappe was correlated with the Kuibis subgroup of the Nama Group, which are the autochthonous–parautochthonous rocks structurally beneath the NNC. Such a correlation requires a major thrust contact within the Zebra Nappe to place Cryogenian Witvlei-equivalent strata atop the latest-Ediacaran lower Zebra Nappe. In *Miller* (2008), the putatively thrust-emplaced Onis Formation is named the Leopard Nappe and is envisioned to have been emplaced atop the lower Zebra Nappe prior to other tectonic events in the formation of the Naukluft Nappe Complex.

Hartnady (1978) additionally correlated several fragments of the Southern Pavian Nappe, exposed in the Tsondab River Valley, with the Zebra River Formation. These two domains, discussed here as the Arbeit Adelt and Büllsport facies of the Southern Pavian Nappe [Figure 2.1], were grouped based on lithologic features suggestive of units within the Zebra Nappe. However, their position at different levels of the nappe stack requires a complex tectonic model to explain the deformational history of the units from a coherent original source.

Hartnady (1978) proposed a five-stage deformational history for emplacement of the NNC, culminating with the eastward thrusting of the entire nappe complex over the Nama foreland basin to its current position. An alternative five-stage model is proposed by K.H. Hoffmann in unpublished work and described in *Miller* (2008), with several amendments. Much of the complexity in deformational episodes is due to different interpretations of the Zebra Nappe and its relationship with adjacent units.

These previous interpretations of Zebra Nappe kinematics have several issues. First, the unconformable deposition of similar rocks across an imbricated edge of the Dassie Nappe requires emergent thrusting and is not a common surface pattern in foreland thrust systems. Second, the position of the Zebra Nappe above the planar "Sole Thrust", and deformation within the nappe, suggests a far-traveled hanging wall. Lastly, thrust emplacement of the Onis Formation above the lower Zebra Nappe and dismemberment into outliers at different structural positions require complex out-of-sequence thrusting that is not demonstrated adequately with field relationships (*Hartnady*, 1978; *Hoffmann*, 1989). Consequently, a major goal of our study is to clarify the structural setting of the Zebra Nappe.

3.2 Methods

3.2.1 Geologic mapping and stratigraphic sections

Geologic mapping of the southern Naukluft Mountains was undertaken during two field seasons in 2015 and 2016. Mapping was based in the valleys at the margins of the nappe [Figure 5.2] and overnight backpacking trips into the center of the study area (limited in radius and duration by water availability). Mapping of the valley walls provided the most complete cut of the stratigraphy. Field mapping was supplemented by UAV imagery of key areas. Highly consistent exposure of bedrock allowed the interpolation of local relationships to more regional scale using Landsat and QuickBird basemaps. Airborne radiometric survey data compiled by the Geological Survey of Namibia (*Duffy et al.*, 1997) was used to augment imagery data.

A combination of field- and imagery-based mapping was used to map the Zebra Nappe at ~1:10000 scale, and reconnaissance mapping of its surroundings (including the Dassie Nappe, potential outliers of Zebra Nappe lithologies from *Hartnady* (1978), and imbricated foreland basin carbonates) at 1:20000 scale.

Contacts interpreted from field mapping and satellite imagery were digitized into a PostGIS spatial database using desktop GIS software and a iPad graphics tablet and stylus.

Ten stratigraphic sections totaling ~1800 m were measured in several areas of the nappe, which were determined to cover the stratigraphy and capture the maximum lateral variability within the Zebra Nappe. Partial sections with stratigraphic overlap were measured at the margins of Tsams and Ubisis valleys in the western part of the nappe, and a complete ~670 m section was measured at Onis at its eastern front [Figure 5.2]. Sections were sampled in stratigraphic height for carbon and oxygen isotopes, with 5 m sampling in carbonate rocks typical. Stratigraphic columns document lithology and bed features at an approximately 30 cm resolution, though this varies with stratigraphic interval.

Stratigraphic sections were correlated into a sequence-stratigraphic framework with the development of a facies model and recognition of key stratigraphic surfaces separating facies.

3.2.2 Carbon and oxygen isotopes

Stratigraphically-sampled bulk carbonates were analyzed at Caltech during December 2015 to May 2017. Samples for measurement were drilled from a cut slab using a dremel rotary drill with a 2 or 3 mm bit. Care was taken to avoid sparry recrystallized or weathered exterior faces. 100-200 mg of each sample (more for dolomite) was weighed on a microbalance into stoppered vials. The samples were measured on the GasBench instrument at Caltech, and were standardized to in-house CIT-CM and ETH-1 samples. Carbon isotopic measurements have ~0.2 permil standard reproducibility, while oxygen isotopes are somewhat less reproducible. Poor standardization of oxygen for Section J prevents us from reporting these values at this time.

3.2.3 Detrital zircons

Sandstone samples of the Zebra Nappe were collected for detrital zircon U-Pb dating. Samples were collected from the *coarse sandstone and pebble conglomerate* facies to maximize the recoverability of intact zircon grains. Two samples from within the Ubisis Formation and one from the Lemoenputs Formation were analyzed. A sample from the Nama Group (Niederhagen Member of the Nudaus Formation) was collected from the footwall of the Naukluft thrust at Onis Farm. The samples were measured at the Arizona Laserchron Center at the University of Arizona (Tucson, AZ) using analytical methods discussed in *Gehrels* (2012) and *Spencer et al.* (2014). ~300 analytical points were measured for each sample.

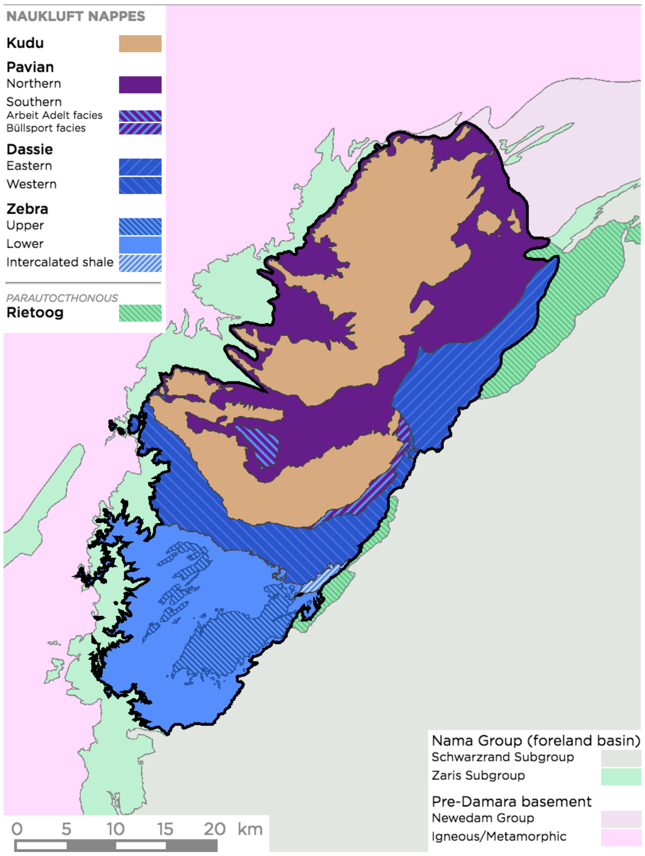

Figure 3.3: Generalized tectonic map of the NNC showing nappe units as defined by *Hartnady* (1978) and *Miller* (2008), with amendments by this study discussed in text.

3.3 Results

3.3.1 Geologic mapping

We have mapped the Zebra Nappe in detail, and the other nappes of the Naukluft context according to their definitions in previous work [Figure 3.3].

Our mapping broadly confirms the lithostratigraphic divisions advanced by *Hartnady* (1978) for the Zebra Nappe. The members of the "Zebra River Formation" discussed by *Hartnady* (1978) (the Neuras, Ubisis, Tsams, Lemoenputs, and Onis members) are elevated to formations in this work. Additionally, we add a Tafel Formation above the Onis Formation, covering lithologies that were not described in *Hartnady* (1978).

Table 3.2: Map units within the Zebra Nappe

Unit	Key facies	Lateral variation and other features
Tafel Formation		
Upper	Cross-stratified grainstone	
Lower	Wavy-bedded heterolithic	
Onis Formation		
Upper	Intraclast grainstone	At Tsams, thick-bedded intraclast breccia At Onis, intraclast grainstone
Middle	Wavy-bedded heterolithic	
Lower	Intraclast grainstone Intraclast breccia	
Lemoenputs Formation		
Upper	Graded-bed fine sandstone – mudstone	
Bed 2	Stromatolite-topped reworking surface Wavy-bedded heterolithic Cross-stratified ooid grainstone	Thickens towards Tsams Digitate stromatolite become more poorly organized downdip
Middle	Graded-bed fine sandstone – mudstone	
Bed 1	Stromatolites-topped reworking surface Wavy-bedded heterolithic Pebble conglomerate	Digitate stromatolites are replaced by thrombolitic grainstone downdip Pebble conglomerate and intraclast grainstone are lost downdip
Lower	Graded-bed fine sandstone – mudstone	
Tsams Formation		
Member C	Wavy-bedded carbonate mudstone Stromatolite-colonized surface at top	
Member B	Inner shoreface sandstone	
Member A	Wavy-bedded dolomite mudstone with chert nodules	
Ubisis Formation	Inner shoreface siltstone Coarse sandstone	Abrupt contact between Neuras and Ubisis Formation is lost downdip (Section A)
Neuras Formation	Wavy-bedded dolomite mudstone with domal stromatolites	Lithologically similar to Büllsport formation of Dassie Nappe

3.3.2 Lithostratigraphy of the Zebra Nappe

The Zebra Nappe of the NNC is a stratigraphic succession lacking angular discordances and composed of mixed carbonate and siliciclastic sedimentary rocks. Lithologic variability forms the basis for subdivision as members within what was originally designated the Zebra River Formation (*Hartnady*, 1978). However, the present study allows further subdivision and thus the Zebra River Formation is elevated to group status, and we define seven formations within the Zebra Nappe [Table 3.2].

The Neuras Formation, Ubisis Formation, Tsams Formation, Lemoenputs Formation, and Onis Formation were all previously regarded as members in *Hartnady* (1978). An additional Tafel Formation (named due to its exposure solely on top of the plateau), is proposed for the uppermost part of the Onis Formation. This formation is mapped by *Hartnady* (1978) as O2 in the eastern part of the nappe, but is not well-described. It is minimally present at the top of the plateau in the western part of the nappe.

All formations except the Neuras and Ubisis formations were divided into several separately mappable members. The Tsams Formation members A, B, and C form distinctive markers across the nappe. Beds A and B in the Lemoenputs Formation are laterally variable in thickness, with a maximum thickness at Tsams, and are not mappable separately in the eastern part of the nappe. They are generalized as part of the lower and middle Lemoenputs formation where not individually mapped.

3.3.3 Internal structure of the nappe

The conformable stratigraphy of the Zebra Nappe is heavily strained, with tectonic shortening along a SE-NW axis corresponding to transport direction. Within the Zebra Nappe, rheology controls deformation responses of stratigraphic units to tectonic stresses. There is imbrication of the basal dolomite, open folding in the middle stratigraphy, and alternating localized imbrication and long-wavelength, low-amplitude plunging folds in the upper stratigraphy [Figure 3.4].

The lower stratigraphy of the Zebra Nappe contains imbrications of the basal Neuras Formation dolomite

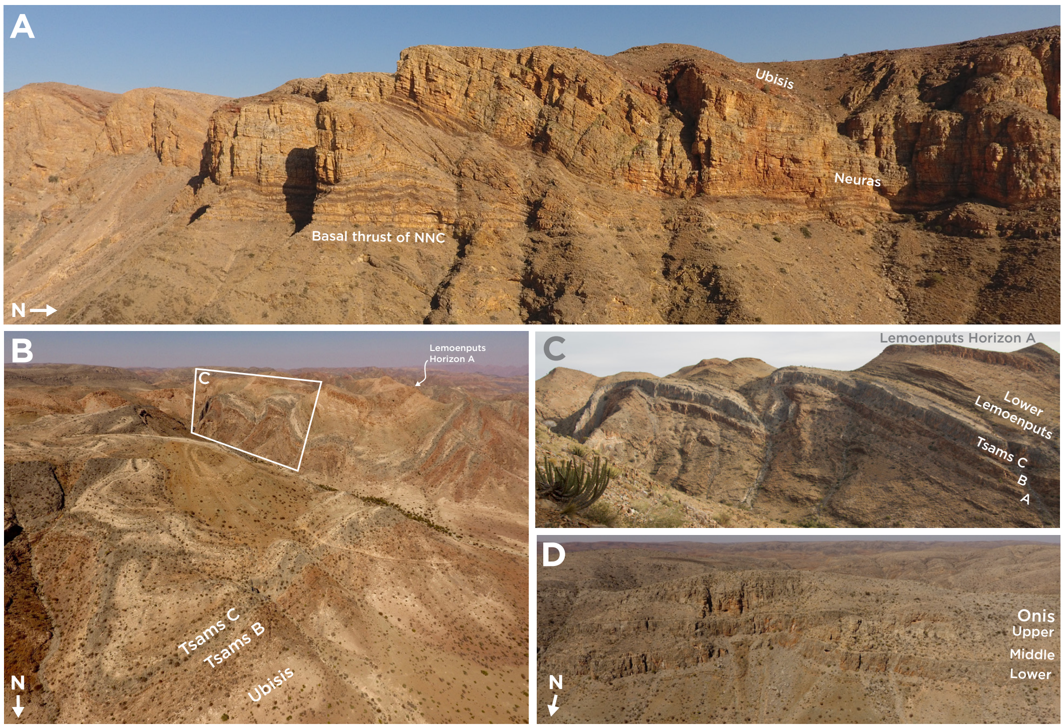

Figure 3.4: Rheology-dependent styles of internal deformation within the Zebra Nappe. **(a)** West-looking UAV image of the southeast margin of the Zebra Nappe on Neuras Farm, showing imbrication in the basal Neuras Formation of the nappe. **(b)** South-looking UAV view of the southeast side of Tsams valley, showing open folding in the middle stratigraphy of the Zebra Nappe (the Ubisis, Tsams, and lower Lemoenputs Formations). Bed 1 of the Lemoenputs formation is ~15 m thick and forms a resistant cap unit here. **(c)** South-looking view of kink folds in the Tsams Formation, with steep forelimbs dipping in the southeastward direction of tectonic vergence. **(d)** Southeast-looking UAV image (towards the direction of tectonic vergence) showing imbrication of the Onis Formation with several closely-spaced lateral ramps.

The middle stratigraphy of the Zebra Nappe is dominated by top-to-the-southeast Z- or S- folds (depending on view direction). These folds have long, northwest-dipping backlimbs and steep southeast-dipping or overturned forelimbs, in the direction of tectonic transport. In some areas of the nappe, Z folds give way to imbrication.

The upper stratigraphy of the nappe, composed of the Onis and Tafel formations, is gently folded in the southern part of the nappe and imbricated at its northern margin. An overprinted tectonic fabric of low-angle south-directed folding and imbrication is expressed in the Onis Formation

3.3.4 Nappe bounding contacts

Of particular interest for geologic mapping given inconsistencies in previous mapping (*Hartnady*, 1980) is the nature of the contact between the Zebra and Dassie Nappes. We find that the Zebra Nappe overrides the Dassie Nappe on a south-dipping tectonic contact everywhere the two adjoin, except where the contact is modified by propagating defects at the east and west margin of the nappe.

Over most of the contact, Dassie Nappe strata are imbricated directly below a south-dipping master surface separating it from the Zebra Nappe [Figure 3.5a]. Often, there is relatively little lithologic contrast over this contact between the Neuras formation within the Zebra Nappe and the Büllsport Formation dolomite within the Dassie Nappe.

On the western margin of the Zebra Nappe adjacent to Die Valle, the Dassie Nappe oversteps this contact, forming a local thrust relationship with the Zebra Nappe strata overturned on its southern margin [Figure 3.5b].

On the eastern margin of the Zebra Nappe, strata within the lower Zebra Nappe are tilted to vertical between the Dassie Nappe and the Onis Formation [Figure 3.5c]. This occurs above a "tear fault" in the Zebra Nappe originating at the Zebra–Dassie contact. The tip of this fault tore the Zebra Nappe where its stata steepen to override the Dassie Nappe [Figure 3.6b].

Beneath this fault, areas mapped as Lemoenputs Formation of the Zebra Nappe by *Hartnady* (1980) are composed of dominantly olive-green shales with stretched carbonate lenses and thin beds of orange-weathering dolomite mudstone. This

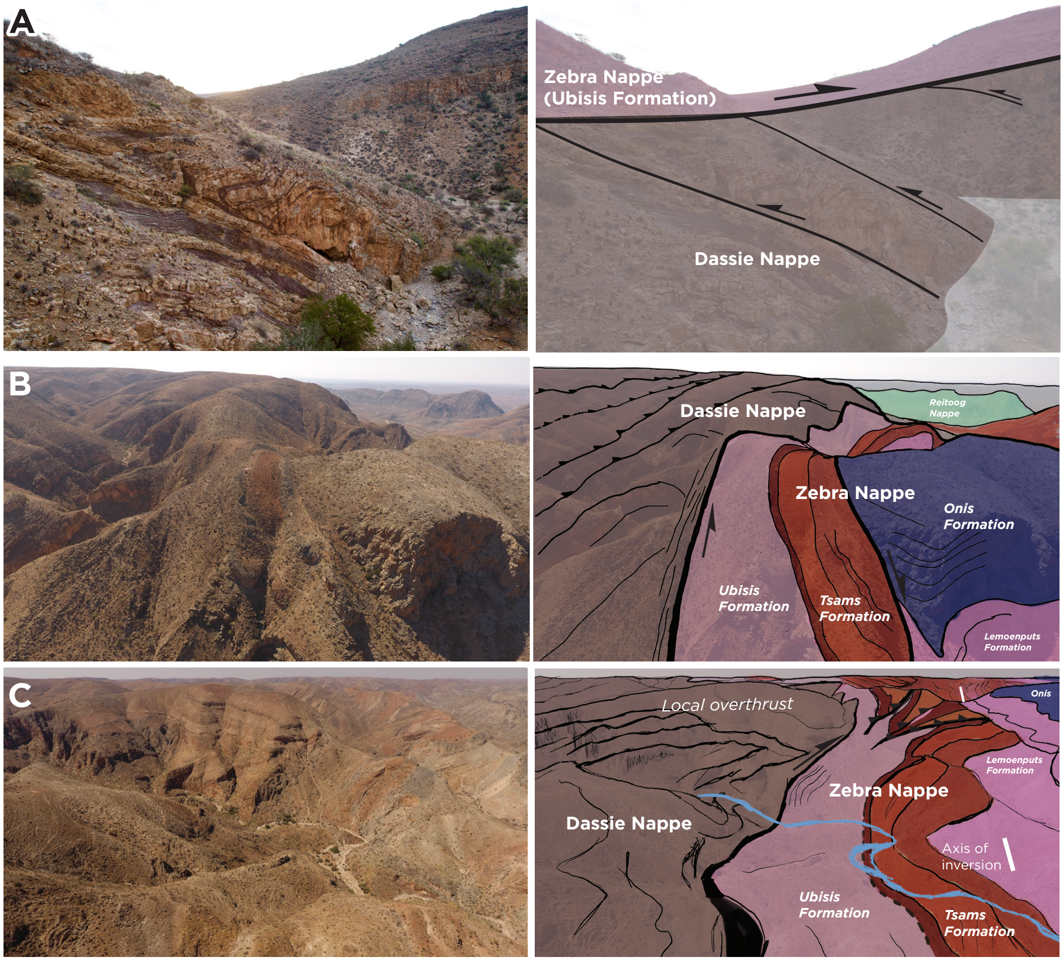

Figure 3.5: Interpreted field photos demonstrating key relationships at the Zebra–Dassie Nappe contact. **(a)** Tectonic contact between the Zebra Nappe and Dassie Nappe, showing truncation of a minor Dassie nappe thrust into an oppositely-dipping fault. This is the typical style of the passive roof thrust at the nappe contact. **(b)** East-looking UAV image of the Zebra-Dassie contact on the east side of the nappe near the Naukluft Park Office, showing the nappe contact tilted to vertical above the torn eastern margin of the Zebra Nappe [Figure 3.6b]. The Tsams Formation is locally juxtaposed against the Onis Formation by a high-angle antithetic fault. **(c)** East-looking UAV image of the Zebra–Dassie nappe contact on the west side of the Zebra Nappe at Die Valle. The Dassie Nappe is locally thrust over the Zebra Nappe, inverting the lower units of the Zebra Nappe [Figure 3.6c].

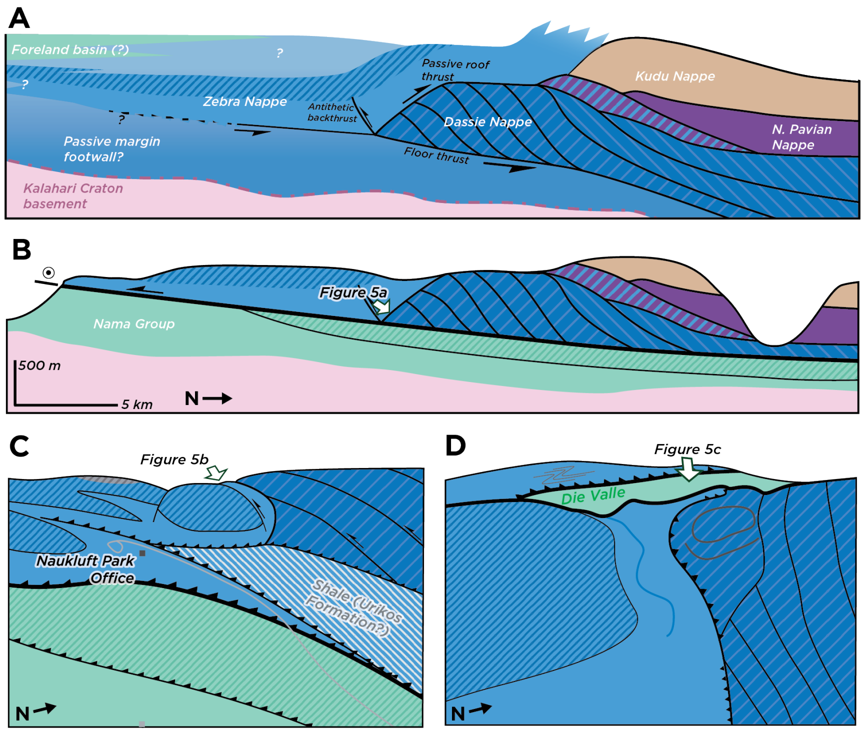

Figure 3.6: Schematic cross-sections of nappe relationships constructed during this study, colored by nappe tectonic unit as in Figure 3.3 and showing our preferred tectonic model for the evolution of the Zebra Nappe and NNC. **(a)** The first stage of our preferred model, with southward blind thrusting of the upper nappes of the NNC beneath the Zebra Nappe, which overrides the Dassie Nappe on a passive backthrust. **(b)** The second phase of southeastward thrusting of the entire NNC atop the basal thrust to its current position atop the Nama Group foreland basin sequence. **(c)** The structurally complex eastern frontal zone of Dassie–Zebra Nappe contact, with a tear fault propagating into the Zebra Nappe and inserting a wedge of footwall shale (likely Urikos Formation). **(d)** The western margin of the Dassie–Zebra contact, showing the overstepping of the backthrust by the Dassie Nappe.

package sits above a sliver of recognizable Zebra Nappe lithologies. We re-interpret this shale package as a tectonic sliver of shale interposed between the Zebra and Dassie Nappes. Brighter-colored green and purple shales within the Dassie Nappe are tectonically above this wedge at its western margin. This sliver only occurs near the eastern thrust front at the meeting of the Zebra and Dassie nappes and is closely associated with the Rietoog Nappe, a tectonic sliver of the Omkyk Formation of the Nama Group.

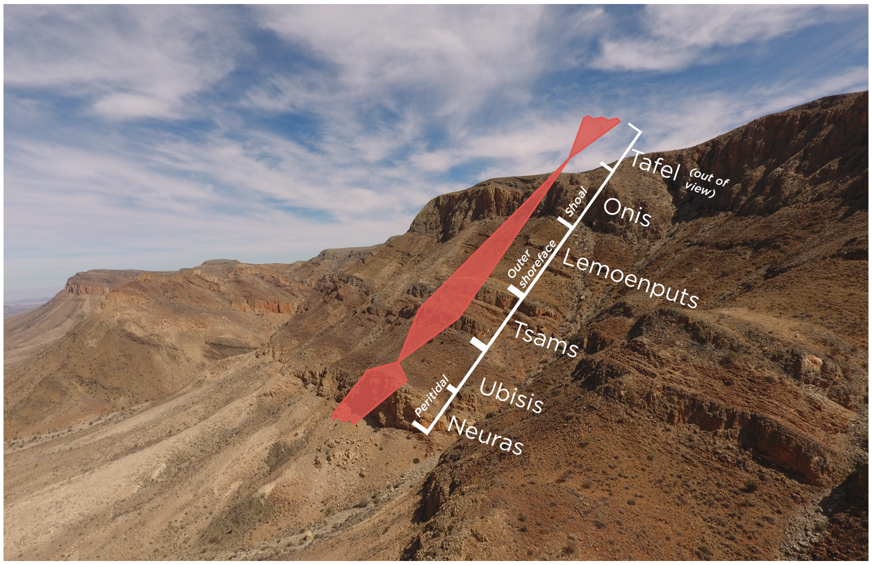

Figure 3.7: View southward of Onis Cliff exposing the entire ~700 m stratigraphy of the Zebra Nappe where Section J was measured. Large-scale variation in accomodation space is schematically rendered atop the image.

3.3.5 Stratigraphic context for facies analysis

Stratigraphic sections were measured in three primary locations within the Zebra Nappe [Figure 5.2]. The eastern cliff face of the nappe at Onis farm preserves a nearly complete section of the Zebra River Group stratigraphy with relatively little deformation, although small thrust faults do cut the Onis Formation [Figure 3.7]. A single ~700 m section (Section J) was measured up this cliff face. In the more northeast exposure area of the nappe, at Tsams, a relatively open valley allowed five partial sections (Sections A-E) covering the middle stratigraphy of the nappe to be measured. At the southern margin of the nappe, sections F-I were measured within or near Ubisis Canyon, a narrow canyon with the lower stratigraphy of the nappe exposed in its walls and discontinuous exposure of the upper stratigraphy on the nearby plateau.

Ten facies were identified which occur in particular intervals within the Zebra River Group, although some were deposited throughout. Siliciclastic facies include coarse sandstone and pebble conglomerate, inner shoreface sandstone–siltstone, and outer shoreface sandstone–mudstone. Carbonate facies include wavy-bedded mudstone, intraclast grainstone, cross-stratified grainstone, wavy-bedded heterolithic, intraclast breccia, and stromatolites.

3.3.6 Sedimentary facies

Table 3.3: Facies descriptions

Facies	Description	Sedimentary structures	Interpretation
Coarse sandstone and pebble conglomerate	Coarse-grained sandstone and pebbly conglomerate	0.2–0.5 m beds, massive to trough cross-stratified	Alluvial fan to upper shoreface
Rippled and mud-cracked siltstone–fine sandstone	Red to green-weathering siltstone to fine sandstone	Mud cracks, ripple cross-lamination, trough cross-stratification, flaser lamination	Low-energy intertidal Upper shoreface
Graded-bed mudstone–fine sandstone	Mudstones, siltstones, and fine sandstones	Graded beds, hummocky cross-stratification, occasional rafted intraclasts	Deepwater deposition by settling from turbidity currents Background settling of suspended fines
Wavy-laminated carbonate mudstone	Planar to wavy-bedded lime and dolomitic mudstone	Mud cracks, coarse sand wisps and gutters, mudstone partings, domal stromatolites Fine laminations, occasional 1 cm intraclasts, ripple cross-lamination	Peritidal to quiescent shallow subtidal
Intraclast grainstone	Medium to thick-bedded oolitic grainstone	Mudstone rip-up chips	Bedload transport on a shallow platform margin shoal
Cross-stratified grainstone	Amalgamated beds of sand-sized carbonate grains, few to no intraclasts	Trough and hummocky cross stratification	Bedform generation on inner ramp, above storm wave base
Wavy bedded heterolithic	Intraclast, cross-stratified, and massive oolitic grainstone Ribbony grainstone with sinuous mudstone partings	Scoured bed tops, cobble-sized intraclasts, hummocky cross-stratification, mudstone laminations	Storm-reworked tidal flats on inner ramp to low-energy middle ramp
Intraclast breccia	Rafted angular to tabular intraclast debris in a mudstone matrix	Matrix supported 0.5 – 2 m beds, 10-50 cm angular to tabular grainstone and mudstone intraclasts	Debris flows on platform margin
Stromatolite	Branching, columnar stromatolites with mudstone fill	Isolated columns 1-2 cm diameter, up to 10 cm high or laterally-linked arrays 2cm high	Shallow-water reefs

Coarse sandstone and pebble conglomerate

Description Coarse-grained sandstones are present throughout the Ubisis Member, and medium- to coarse-grained sandstones containing lenticular bodies of pebble conglomerate are found in the lower Lemoenputs Formation [Figure 3.8]. The Ubisis Formation contains laterally extensive coarse-grained sandstones, particularly at its base and top. Laterally extensive coarse-grained sandstones are observed at all localities within these formations and are found primarily in the Ubisis Formation, particularly at its base and within its uppermost portions. At Tsams, the coarse-grained sandstones are interleaved with laminated carbonate mudstone to a greater degree than seen at the Ubisis and Onis farms.

The Ubisis Formation is dominated by thin to thick-bedded coarse sandstone, both massive and with planar, wavy, and trough cross-stratification. Bedsets are 20 cm to 1 m thick and show tabular geometries with wavy to rippled bed tops. Occasional thinner (~20 cm) interbeds form lenses with ~50 m lateral extent, and some wedges of fine sandstone up to 1 m thick are present as well. Clast compositions range from feldspathic to quartz-normative , and grains are generally subangular to subrounded. Many of the coarse sandstone bodies, especially those stratigraphically near dolomite, are quartz-cemented, forming a highly indurated rock.

The basal sandstones of the Ubisis Member are poorly sorted, planar laminated thick beds with feldspathic compositions, weathering gray-red (Section J @ 90 m). Near the top of the Ubisis Member, bedsets are sometimes thinner, and trough cross-stratification is more common. The facies coarsens upwards within the Ubisis formation, and beds near the top are capped by pebbly lags. Grains in the upper Ubisis Member are subrounded to rounded, and the clast population is less feldspathic than in the lower part of the formation. The grainsize, texture, and composition of these coarse sandstones is similar to that present as thin lenses and bedding-parallel "wisps" in the dolomite mudstone of the Neuras Formation, and as sand-filled gutters in the Tsams A Member, suggesting a similar provenance.

In the lower Lemoenputs Formation, this facies is present as pebble conglomerate lenses hosted in fine to medium sandstone within a single ~15 m thick interval. This interval is present at Ubisis (Section F @ 90 m) and Onis (Section J

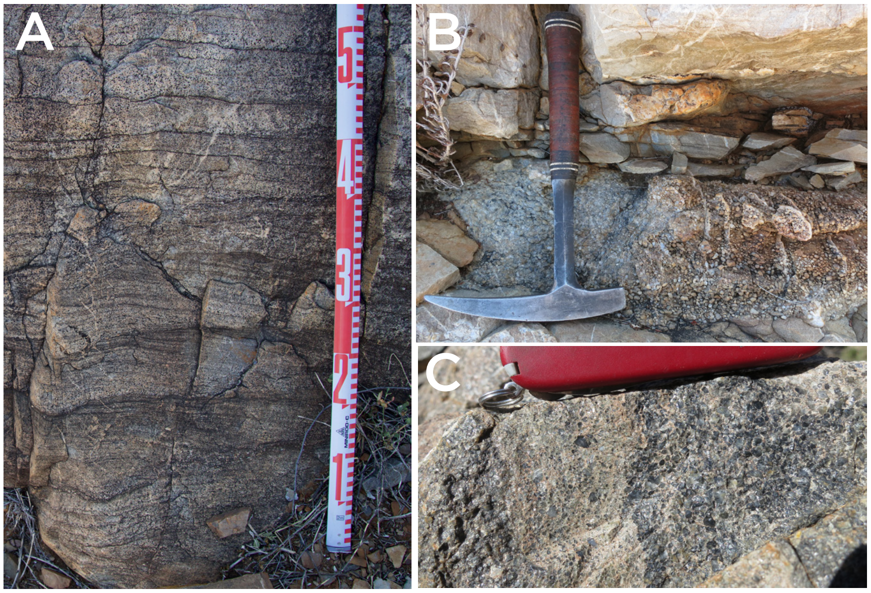

Figure 3.8: The *coarse sandstone and pebble conglomerate* facies. **(a)** Cross-bedded coarse sandstone, upper Ubisis Formation (Section J). **(b)** Lenticular pebble conglomerate, Lemoenputs Bed 1. **(c)** Close-up view of coarse sand and occasional pebble clasts.

@ 300 m) but absent at Tsams, where the equivalent horizon is occupied by *fractured/clotted grainstones*.

Sandstones occur in the lower Lemoenputs Formation as several tabular ~5 m sets of 10-20 cm thick lenticular beds with wavy laminations, scoured top surfaces, and occasional trough cross-stratification. Lenticular sand bodies have a lateral extent of ~50 m. These beds contain ~50 cm thick lenses of coarse sandstone to cobble conglomerate (most commonly pebble conglomerate) with well-rounded quartz clasts. Similar beds were observed at the top of the Tsams Formation near Ubisis, but were not measured.

Interpretation The expression of this facies differs between the Ubisis Member and the Lemoenputs Formation. In the Ubisis Formation, the coarse grain-size, thicker bedding of this facies suggest high energy transport in an active hydrodynamic regime. Massive beds (dominant at the base of the Ubisis Formation) are associated with wedge-shaped interbeds and poorly-sorted clasts, suggesting alluvial deposition. In the upper Ubisis Member, rippled bed tops suggest lower flow-regime transport, and bidirectional cross-stratification suggest tidal influence. The presence of lenticular beds suggests channelized flows, and pebbly lags show subaerial exposure and winnowing. The Ubisis Formation coarse sandstones occur in an upper-shoreface assemblage also containing peritidal and outer shoreface sandstones, and occasional carbonate mudstones, organized in coarsening-upwards parasequences.

The sandstones and pebbly conglomerates of the lower Lemoenputs Formation imply similar transport processes, but the limited thickness and lenticular nature of exposures in this interval likely preclude an extensive shoreface deposit. The segregation of quartz-pebble conglomerate and fine-medium sandstone lenses suggests clast concentration, winnowing, and local fluvial transport within incised channels. The limited thickness and lenticular bed geometries suggest lowstand deposition during a regressive phase.

Inner shoreface sandstone–siltstone

Description This facies is present in the Chain Formation (both Neuras and Ubisis members), and in the Tsams Formation (Tsams B member) at all locales. It consists of siltstone to fine sandstone (rarely, medium sandstone) with shallow-water sedimentary structures. Thin to medium beds (5-80 cm thick) are packaged together in 2-5 m sets [Figure 3.9a]. Some beds have decimeter-scale polygonal dessication cracks [Figure 3.9c], and sandstone beds are sometimes topped by dessication cracks with 90° angles. Beds are red to green-weathering and form well-cemented steps. Siltstone beds are massive or planar to wavy-laminated at mm scale, while sandstone beds are wavy to trough cross-stratified, often with flaser lamination, symmetric ripple cross-lamination, and rippled tops.

In the Ubisis Member, beds of this facies are thin (5-20 cm), forming tabular sheet-like beds. Individual beds may be packaged into 1-5 m-thick, coarsening upwards sets. This facies is typically interbedded with thin (~10 cm) intervals of wavy bedded carbonate, packages of coarse sandstone up to 5 m thick, and siliciclastic mudstones 0.5 to >20 m thick (depending on locale). The Tsams B member is composed of the fine sandstone variant of this facies, with medium beds (20-80 cm) amalgamated into packages 10-15 m thick Figure 3.9. Planar, wavy, and trough cross-stratification are common. Unlike in the Ubisis Member, beds are clearly lenticular, with a 20 m lateral scale. Gutter casts are commonly preserved at the

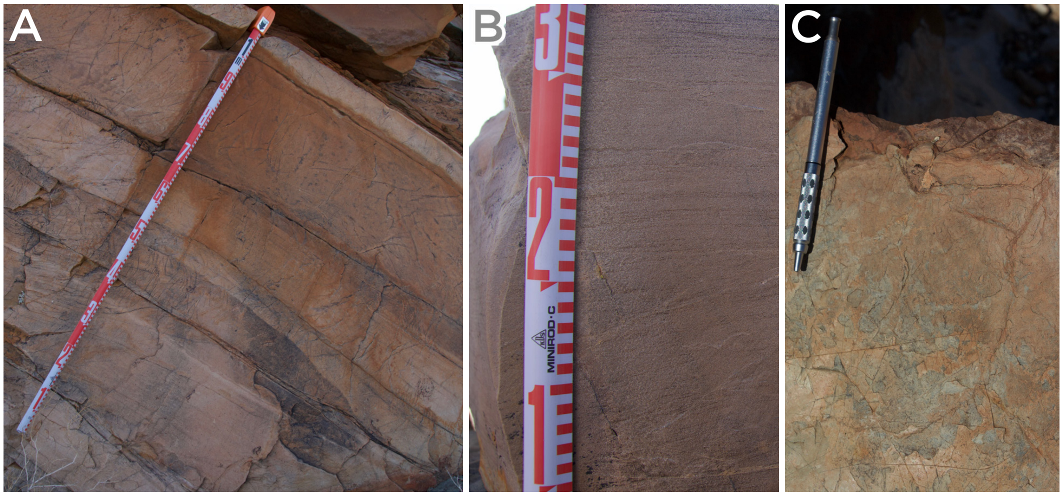

Figure 3.9: Inner shoreface fine sandstone. **(a)** amalgamated fine sandstone beds of the Tsams Formation, Member A. **(b)** Massive medium bed of the Tsams Formation, Member A. **(c)** Dessication cracks in siltstone, Ubisis Formation (Section B @ XX m).

edges of bed lenses, but hummocky cross-stratification is not found.

Interpretation The polygonal dessication cracks found in this facies are clear markers of subaerial exposure. In the Ubisis Member, its association with other upper shoreface and peritidal facies (coarse trough cross-stratified sandstone and wavy-laminated mudstone) suggest that it is part of a peritidal sequence, occurring within cycles often capped by coarse sand. The planar bed character and common unidirectional ripple cross-lamination suggest low-velocity, shallow flows, and trough cross-stratification occurred in somewhat deeper water. In the Tsams B member, the thicker, lenticular beds and gutter casts are features of migrating channel bodies, suggesting deposition by a fluvial system. The Tsams B member is a regional marker interval, distinctively present and consistent in thickness in all areas on the nappe. This is indicative of regionally extensive, siliciclastic-dominated inner-shoreface system. The Tsams B member is a regional marker interval, with two clear parasequences defined in all areas of the nappe.

Outer shoreface sandstone–mudstone

Description This facies features fine sandstones, siltstones, and mudstones. Mudstones commonly have grey, green, red, or variegated color, commonly with slaty cleavage imparted by tectonic strain. Some siltstone intervals contain trough and

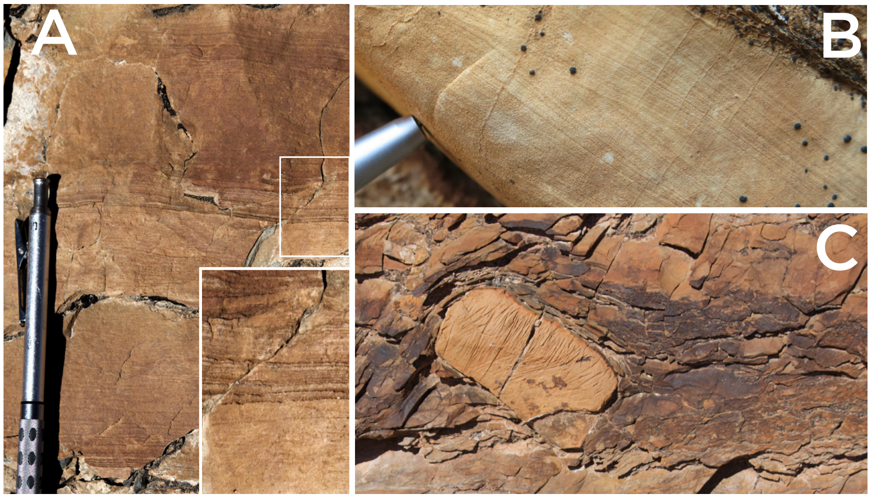

Figure 3.10: Outer shoreface mudstone–fine sandstone facies. **(a)** Graded beds in fine sandstone of the Lower Lemoenputs Formation. **(b)** Fine cross-laminations in siltstone. **(c)** Isolated rafted dolomite intraclast in medium-bedded fine sandstone. Lamina below the clast are planar, while those above the clast drape over it.

hummocky cross-stratification. The sandstone–mudstone facies is present in all localities, but thickens dramatically towards Tsams and Die Valle on the northwest margin of the nappe. It is most common in the Ubisis Formation and Lemoenputs Formation, but occurs at the base of cycles in other formations as well, especially towards Tsams and Die Valle on the northwest margin of the nappe.

Sandstones are commonly planar laminated to wavy laminated, ripple trough cross-stratified, and can show and hummocky cross-stratification in some intervals. This facies infrequently contains 1-10 cm thick interbeds of dolomitized carbonate mud, spaced 5-10 m apart. In the Lemoenputs Formation, fine sandstones are packaged into 10 cm graded beds [Figure 3.10a]. Infrequently, these fine sandstones contain 1-10 cm carbonate intraclasts [Figure 3.10c].

Interpretation Graded bedding in fine sandstones suggests outer shoreface deposition by settling from turbidity currents. The occasional presence of intraclast cobbles is puzzling, but it may suggest that more massive layers originate as mass flows. Trough and hummocky cross-stratification suggest that some of these intervals were above storm wave base. The siltstones and mudstones of this facies occur in association both with other outer-ramp lithologies and in peritidal settings. This suggests a source from background deposition by settling of dominantly siliciclastic suspended sediment.

Graded bedding in fine sandstones suggests outer shoreface deposition by settling from turbidity currents. The absence of wave-ripple cross stratification in sandstones indicates deposition below fairweather wavebase. However, hummocky cross-stratification indicates that some of these intervals were above storm wave base. The occasional presence of carbonate intraclasts suggests thin carbonate beds may have been reworked during sediment transport events. More massive sandstones suggest deposition from sandy debris flows (*Whipple*, 1997) The siltstones and mudstones of this facies are generally finely laminated [Figure 3.10b] to massive which indicates settling of dominantly siliciclastic sediment from suspension, both as distal storm/flood events and as background.

Wavy-laminated carbonate mudstone The wavy-laminated mudstone facies is typically dolomitized, and occurs as either grey-weathering or tan-weathering "sugary" dolomite. The facies contains a gradation from mudstone with mud cracks, detrital quartz sand wisps and gutter casts at bed bases [Figure 3.11a-e], to a somewhat deeper component with wavy-bedded mudstone grading into rippled carbonate grainstone [Figure 3.11f]. This facies is found dominantly in the basal part of the Zebra Nappe stratigraphy, in the Neuras Formation and Tsams Formation (members A and C). This facies is also found at the top of the Onis Formation high in the stratigraphy [Figure 3.17].

The shallower component of this facies consists of "sugary" dolomite mudstone, typically in decimeter beds with internal planar, wavy, and tufted laminations. Beds often have green shale, purple shale, or siltstone partings. Coarse, subrounded quartz grains are common, ranging from isolated-grain "wisps" to thicker lags along bedding planes. Tufted laminations and stromatolites are also common. In some cases, 10-30 cm diameter domal "dinner-plate" stromatolites, with quartz sand fill between the domes emphasising their 2-5 cm synoptic relief [Figure 3.11a-b].

At the base of the Neuras Formation in Section J, wavy-laminated carbonate mudstones contain interbeds of green and purple shale and dolomite-cemented siltstone and fine sandstone infilling the wavy, locally scoured top surfaces of 10-50 cm dolomite mudstone beds. There are occasional locally sourced rip-up intra-

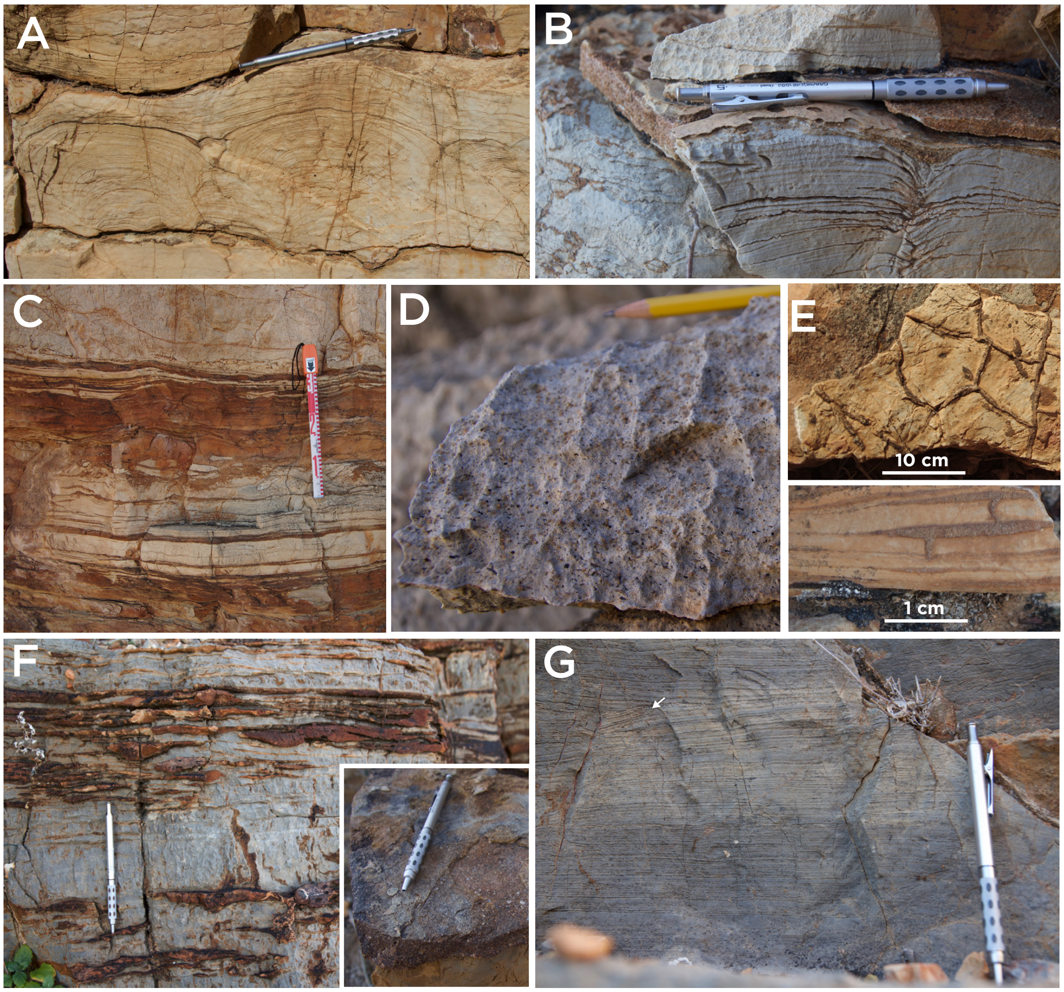

Figure 3.11: Carbonate mudstone facies. **(a)** Domal "dinner-plate" stromatolites in the Neuras Formation. **(b)** Close-up view of stromatolites showing coarse sand infilling and ~2 cm synoptic relief. **(c)** Fine sand interbedded with dolomitic mudstone, with locally-sourced rip-up intraclasts, Neuras Formation. **(d)** Rounded, coarse sand-sized quartz grains in dolomite mudstone, upper Onis Formation (Section J @ 560 m). **(e)** Dessication cracks in dolomite mudstone, filled with fine sand grains. **(f)** Coarse sand-filled lenses and gutters in the Tsams Formation, Member A. **(g)** Deeper-water component of this facies, with planar-laminated dolomite mudstone in the Tsams Formation, Member C. Arrow shows cross-bedding truncation indicating coarser grain size and gradational boundary with *cross-bedded grainstone* facies.

clasts in sandstone [Figure 3.11c]. Both siltstone and mudstone beds have mudcracks [Figure 3.11d]. The range of grainsizes and bedding features in these siliciclastic interlayers is somewhat finer than the siltstones of the inner-shoreface siltstone–sandstone facies, and the coarse sand lags are composed of grains similar to the *coarse sandstone* facies. Dolomite mudstone in the Neuras Fm. and uppermost Onis Fm. contains detrital sand "wisps" similar to those in the Neuras Member.

The Tsams A Member contains distinctive lenticular bedding-parallel chert bodies up to 5cm thick, which are silicified remnants of gutters filled with coarse to very coarse quartz sand, with clasts similar to those found in the Neuras Formation dolostone.

The deeper component of this facies, wavy bedded mudstones, consist of ~10-30 cm thick beds with internal planar to wavy laminations. Some parts have occasional ripples or low-amplitude cross-bedding truncations [Figure 3.11f], suggesting coarser grain sizes. Near the top of the Tsams C Member, the wavy-laminated mudstone contains stromatolites with up to 5 cm diameter and 1 cm synoptic relief. Tufted to crinkly laminations texturally grade into the stromatolites in some intervals. Some intervals (typically in the Onis formation) are fenestral, containing ~1 mm spar-filled voids. Also, infrequent intervals contain rip-up intraclasts.

Interpretation The *wavy-bedded carbonate mud* facies records a quiescent to low-energy environment with stromatolite growth and periodic input of fine clastic sediments. In its shallower version, the presence of coarse sand and mudcracks implies periodic exposure at the surface, with surface relief (e.g. cracks, stromatolite interstices) filled by wind-blown quartz sand. This suggests a sabkha or tidal-flat environment. The wavy-laminated mudstone component of this facies records a somewhat deeper-water environment with no direct signatures of subaerial exposure. Planar-laminated mudstone shows no evidence of interaction with currents. Occasional cross-bedding records a somewhat higher-energy environment with wavy to rippled bedding due to currents. Bedforms also potentially signifying a gradation with coarser-grained material such as the cross-bedded grainstone facies.

Intraclast grainstone

Description The intraclast grainstone facies is a major component of the carbonate-dominated upper Zebra Nappe. It forms the bulk of the Onis Formation at Onis Farm on the eastern side of the nappe, and is somewhat less common in the Onis Formation at Tsams, where it is replaced by a distinctive interclast breccia facies. This facies also occurs in < 10 m intervals within the Tsams and Lemoenputs Formations.

The intraclast grainstone facies consists of tabular to rounded clasts of carbonate mudstone within a carbonate grainstone matrix. Beds are 50 cm to 2 m thick and internally massive. In the Onis Formation, beds are typically amalgamated, with scoured bases. Intraclasts are typically 1-10 cm, subrounded to tabular carbonate mudstone, with 2 cm subrounded clasts typical. Tabular mudstone clasts are generally ~1 cm thick and sometimes imbricated to form edgewise conglomerates [Figure 3.12]. Beds are commonly amalgamated, with wavy interbeds and scoured bases. Some beds have internal planar to wavy lamination. The intraclast grainstone facies has grainstone clasts that are commonly oolitic, although some of the intervals in the Onis Formation appear to have smaller class sizes.

At the eastern margin of the nappe, this facies makes up the bulk of the lower and upper Onis Formation, expressed as amalgamated intraclast beds that locally comprise a thickness in excess of 100 m. In contrast, at Tsams, this facies is a minor component of the Onis Formation, which is instead dominated by intraclast breccia with much larger rafted chunks of debris.

Intraclast grainstone is also present lower in the stratigraphy for several <10 m intervals near the top of the Tsams C member and within the Lemoenputs formation. In these intervals, intraclast grainstone are commonly associated with hummocky-cross-stratified beds, and some thin intervals are grouped with the wavy-bedded heterolithic facies.

Interpretation The intraclast grainstone facies represents deposition and local reworking of carbonate intraclasts on a shoal. In the Onis Formation, thick beds of grainstone with rounded intraclasts show the aggradation of a sandy shoal.

In the upper Lemoenputs Formation, thick, matrix-supported beds containing

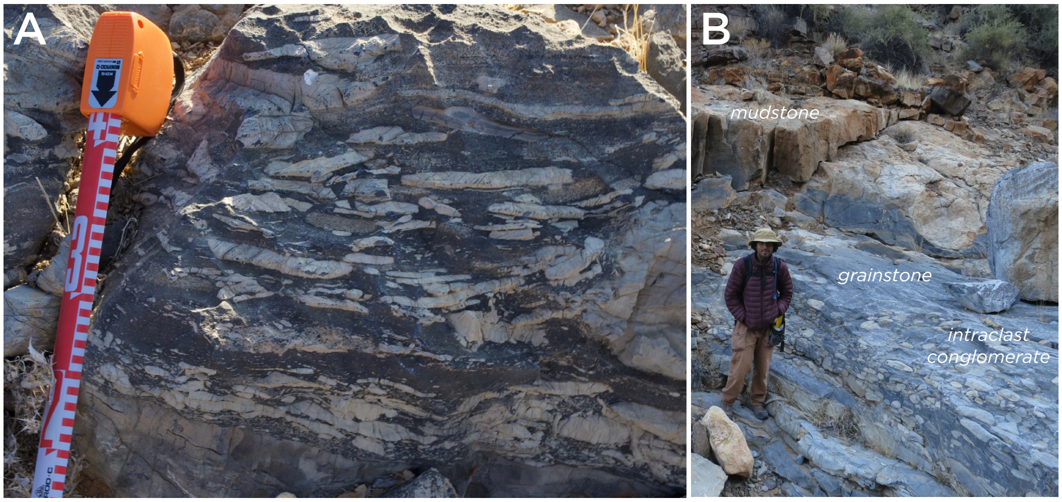

Figure 3.12: **(a)** Example of the intraclast grainstone facies, with mudstone rip-up intraclasts. **(b)** Intraclast grainstone in the middle Lemoenputs, grouped with *wavy-bedded heterolithic* facies, due to its coarse interbedding with massive grainstone and mudstone beds. The 10-20 cm rounded interclasts are much larger than is typical for intraclast grainstone in the Zebra Nappe.

tabular intraclasts suggest storm deposition, and the association with hummocky cross-stratified grainstones and the *wavy-bedded heterolithic* facies enhances this correlation.

Cross-stratified grainstone The cross-stratified grainstone facies consists of carbonate grainstones with tabular, trough, and hummocky cross-stratification [Figure 3.13]. Generally, cross-stratification is well-organized and continuous through 5-10 m of section. Trough cross-stratification consists of medium bidirectional laminae that are grouped into decimeter-scale bedsets [Figure 3.13a]. In some horizons, cross-stratified grainstone is interbedded at meter scale with intraclast grainstone and grainstones with less-organized wavy stratification. Hummocky cross-stratified intervals are generally finer-grained, with low-angle hummocks defined in ~5 mm thick laminae [Figure 3.13b]

This facies occurs in the Lemoenputs formation, typically forming basal packages that grade upward into the wavy-bedded heterolithic facies. A few instances of this facies occur in the middle Onis Formation, and the upper Tafel Formation is dominated by this facies, which is continuous for over 20 m at the top of Section J. In the Tafel formation, grain sizes are medium, and detrital coarse quartz sand

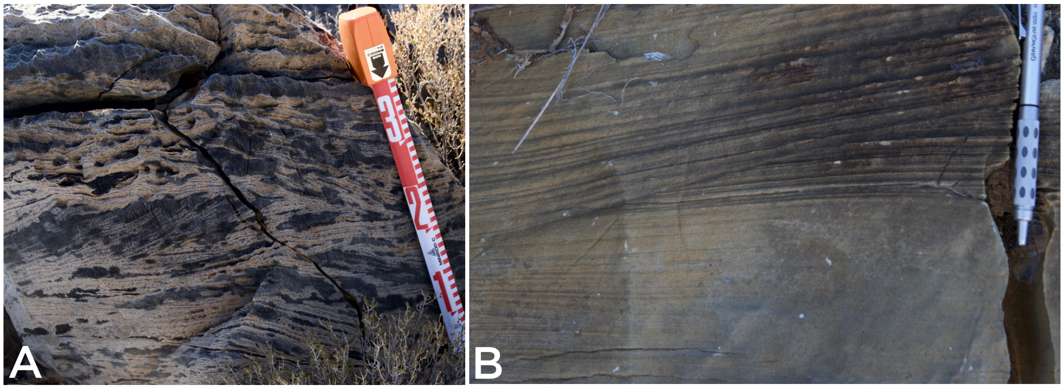

Figure 3.13: Cross-stratified carbonate grainstone facies. **(a)** Trough cross-stratified grainstone, Tafel Formation. Section J @ 659 m. **(b)** Hummocky cross-stratified grainstone, Lemoenputs Formation. Section J @ 335 m.

grains are incorporated into dominantly grainstone bedforms.

Wavy-bedded heterolithic

Description The wavy-bedded heterolithic facies includes wavy-bedded and heterolithic endmembers, with a gradation between them. Gradation between the ribbon-grainstone and heterolithic endmembers of this facies is typically expressed by increased organization towards the heterolithic endmember: more continuous mudstone bodies, tabular interbedding with grainstone beds, and the presence of scour and rip-up intraclasts.

The wavy to ribbon grainstone component of this facies [Figure 3.14a and b] is dominated by fine-medium carbonate grainstone, sometimes with identifiable ooids. Discontinuous, bedding-parallel lenticular mudstone bodies (up to 5cm thick) are common, filling swales and interstices in grainstones. Poorly organized wavy laminations are typical.

The heterolithic endmember consists of several discrete interstratified subfacies: wavy-bedded to ribbon grainstone; intraclast grainstone; fine, hummocky cross-stratified grainstone; and carbonate mudstone. Beds of different types are interstratified at decimeter scale or bundled together in 1-5 m thick packages. Beds are typically 5-50 cm thick, lenticular to tabular, with gutter casts and rip-up intraclasts.

The heterolithic endmember of this facies incorporates discrete beds of carbonate grainstone and mudstone [Figure 3.14c]. Grainstone bodies are massive, wavy laminated, trough cross-stratified, and hummocky cross-stratified [Figure 3.14e-f]. Medium to coarse-sand-sized ooids are present in grainstone beds and collected in mudstone-filled swales [Figure 3.14d]. Massive grainstones frequently scour underlying beds. Intraclast grainstones beds are present in these intervals as well, with commonly 2-10 cm locally-sourced, tabular mudstone intraclasts or small rounded pebble-sized mudstone bodies. At Onis and Ubisis, grainstone bodies in this facies contain instances of soft-sediment deformation and slumping. Slumped bodies are up to 1-2 m thick and continuous over ~50 m laterally. Carbonate mudstones are interbedded with the grainstones, forming lenticular to tabular beds, sometimes with wavy bedding and trough cross-lamination.

The lower Tafel Formation consists of ribbon to cross-stratified grainstones that grades upwards into more organized heterolithic beds. The Lemoenputs Formation contains several discrete 5-30 m packages of this facies, with more thickly interbedded grainstones and mudstones. The lithologic heterogeneity within the Lemoenputs Formation is significant: in the southeast part of the nappe (at Neu Onis farm), this facies contains thickly interbedded grainstones, mudstones, and intraclast breccias with rounded, cobble-sized mudstone intraclasts [Figure 3.12b].

Interpretation The wavy-bedded heterolithic facies represents deposition at a range of water depths on a grainstone-dominated shoal. The intimate alternation of grainstone and mudstone suggest deposition in a periodically high-energy setting, with mudstone deposition and reworking during quiescent intervals. The ribbon grainstone component of this facies suggests a more quiescent overall environment, but one in which currents were able to develop small scale ripples.

This mixed facies is commonly found in association with intraclast and cross-bedded grainstone facies. In the Onis and Tafel formation, it typically occurs as >20 m thick intervals grading into similarly thick, monotonous intervals of intraclast and cross-stratified grainstone. In the Lemoenputs formation, this facies occurs in several discrete intervals 5-20 m thick and typically surrounded by shale. These intervals are commonly topped by the *fractured/clotted to stromatolitic grainstone*, which could represent a reworking surface.

Overall, this facies likely represents a grainstone shoal environment. In the Onis and Tafel formation, these strata represent sustained environments due to

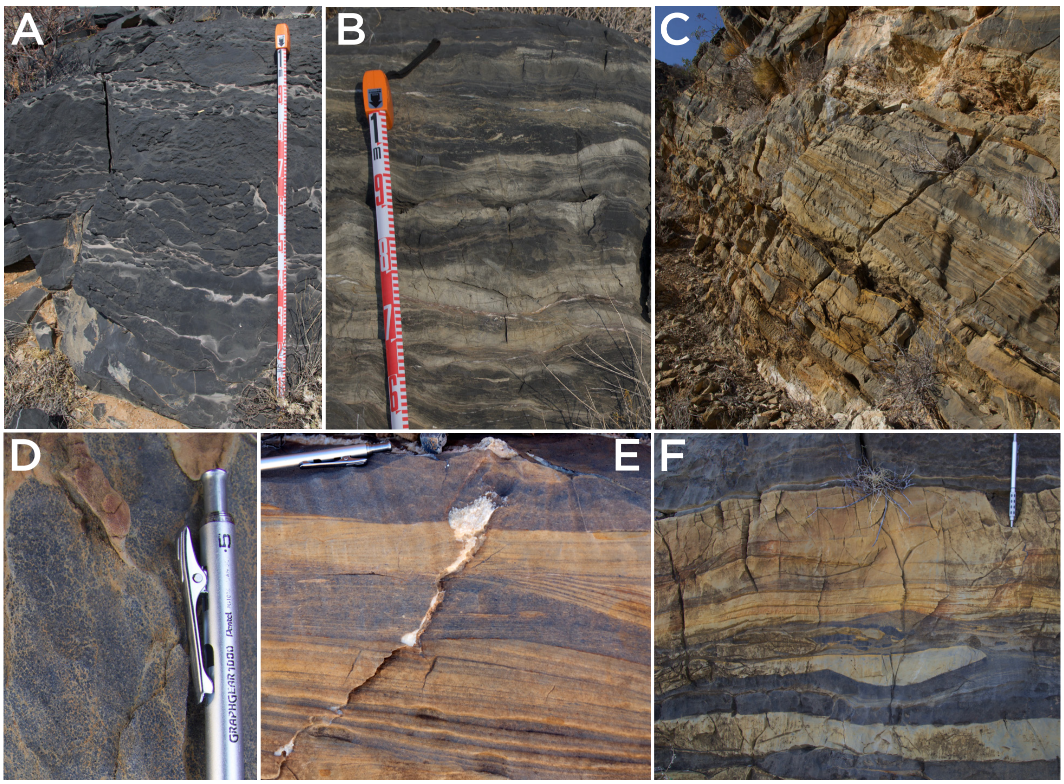

Figure 3.14: The range of lithologies making up the wavy-bedded heterolithic facies **(a)** Ribbon grainstone. **(b)** Wavy-bedded grainstone with mudstone partings. **(c)** Heterolithic grainstone/mudstone. **(d)** Ooids in heterolithic grainstone. **(e)** Low-angle cross-stratification in mudstone interlayers. **(f)** Lenticular mudstone bodies.

their substantial thickness. In contrast, in the Lemoenputs formation, they appear to form the tops of regressive sequences, where facies belts backstep rapidly due to deepening. This is bolstered by the presence of apparent exposure surfaces at the tops of *wavy-bedded heterolithic* sequences in the Onis Formation.

Fractured/clotted grainstone

Description The *fractured, clotted grainstone* facies occurs in several discrete intervals in the Lemoenputs Formation and at the top of the Tsams Formation, on the western side of the nappe at Tsams. It is gradational with the *heterolithic grainstone* facies and consists of 10-50 cm thick beds of massive, wavy-bedded, and intraclast ooid grainstone with scoured, irregular bed surfaces, occasional mudstone interbeds, and soft-sediment deformation. However, several additional features mark this as a separate facies: chaotic bedding, clotted thrombolitic laminations [Figure 3.15f], mudstone-hosted pustular features [Figure 3.15e], and poorly-developed stromatolites (similar to the *Stromatolite* facies discussed below) at the tops of beds. In some locations, two generations of overlapping filled polygonal fractures [Figure 3.15d] are identified: (1) gray dolomite to micrite limestone isopachous cemented fractures and (2) orange dolomite polygonal fractures with no apparent internal structure.

This facies is principally found at Tsams, as two distinct thick, orange-weathering beds that are relatively erosionally resistant. These beds correlate to much thinner intervals at Ubisis and Onis. The strong association with the *Stromatolite* facies allows the top of this facies to be used as a timeline within the Lemoenputs Formation. They are mapped as separate units (Lemoenputs Formation beds 1 and 2) in the western part of the nappe, and some parts of the unit were mistaken for the Onis Formation by *Hartnady* (1978) due to their thickness and resistant character.

Interpretation We interpret the clotted/fractured grainstone facies as representative of a similar overall environment to the *heterolithic grainstone* facies, recording the tops of shallowing-upwards sequences. Microbial laminite growth indicates shallow-water deposition during quiescent periods, and the filled fractures potentially record subaerial exposure and dessication. This implies that this facies could represent a grainstone-shoal to tidal-flat environment recording major

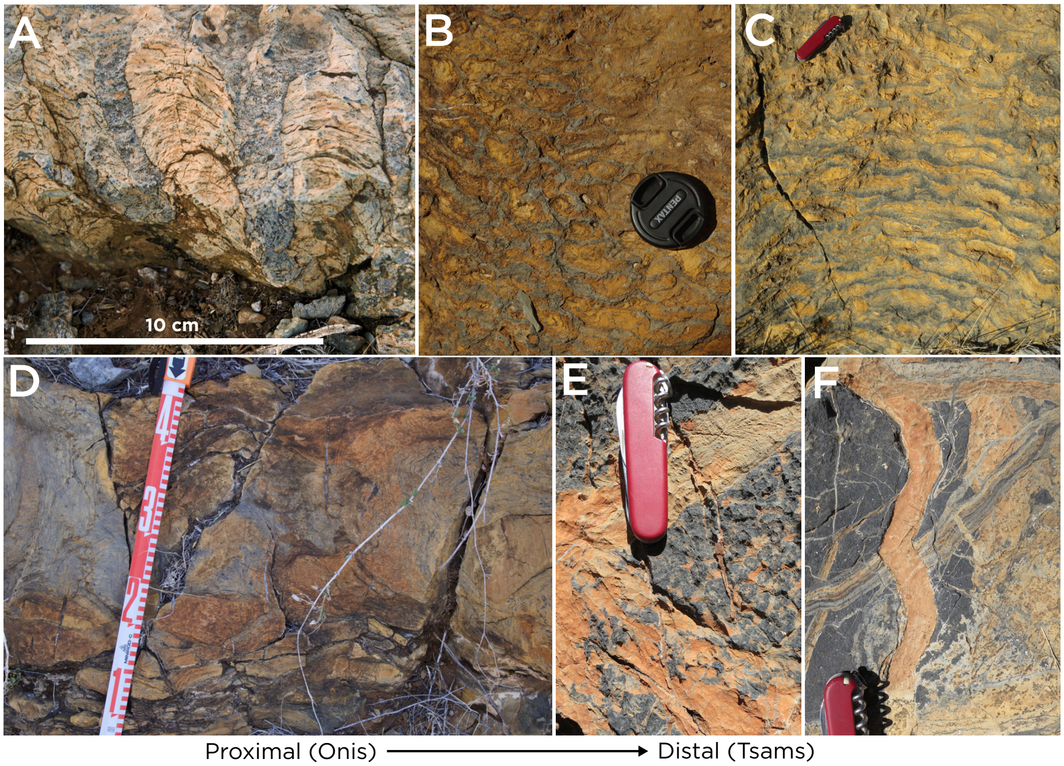

Figure 3.15: Microbial structures and diagenetic features found at the top of the Tsams Formation and Beds 1 and 2 of the Lemoenputs Formation. *(a-c)* show features of the *Stromatolites* facies, which forms the very top of cycles, and *(d-f)* show the fractured/clotted subtype of the heterolithic facies, which commonly occurs a few meters stratigraphically below cycle tops. **(a)** Digitate stromatolite columns. **(b)** Plan view of closely-packed array of slightly smaller digitate stromatolites. **(c)** Poorly organized, elongate digitate stromatolites. **(d)** Clotted thrombolitic texture in heterolithic mudstone/grainstone. **(e)** Pustular texture in lime mudstone. **(f)** Lime grainstone with cross-cutting dolomite-filled fractures.

regressions within the Lemoenputs formation.

Stromatolites

Description The stromatolite facies occurs as several distinct intervals at the top of the Tsams Fm. and within the Lemoenputs Fm. Intervals are up to 2 m thick and always below flooding surfaces switching to the *graded-bed sandstone* facies. This facies is found in all locales, commonly associated with the *heterolithic grainstone* and *fractured/clotted grainstone* facies.

This facies commonly consists of mm-scale laminated dolomitic mudstone, thrombolites, and stromatolites. In some areas, thrombolitic and stromatolitic mounds are laterally embayed at 10 m scale by mm-scale laminated mudstone. Other areas

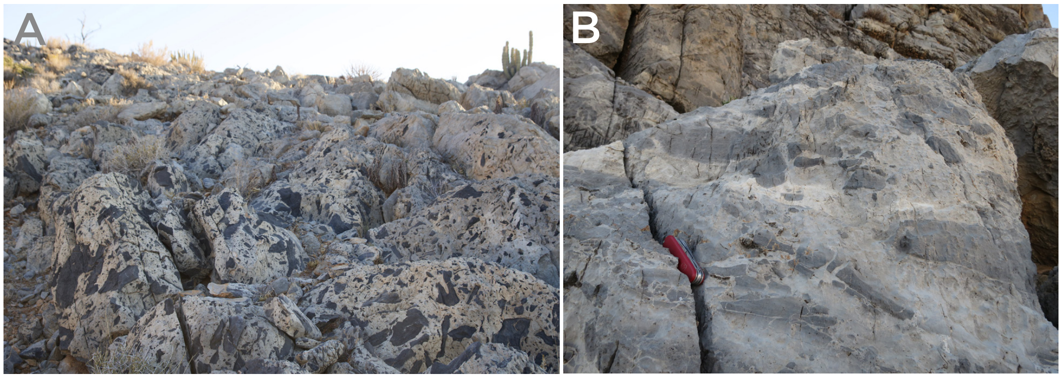

Figure 3.16: **(a)** Tabular mudstone blocks in mudstone matrix. **(b)** Lime grainstone boulders in dolomitic mudstone.

show thin (~20-50 cm thick), laterally continuous stromatolite-containing beds. Stromatolites range from closely-spaced "finger" stromatolites to somewhat larger (2cm diameter) stromatolites which branch upward from more thrombolitic core [Figure 3.15a-c]. These stromatolites tend to be orange-weathering, contrasting strongly with the surrounding rock.

Interpretation This facies repeatedly occurs above *heterolithic grainstone* intervals, marking regionally-correlative cycle boundaries beneath shale. At Tsams, the clotted-fractured grainstone facies is potentially an offshore equivalent of this facies.

Intraclast breccia

Description The matrix-supported intraclast breccia facies is found only in the Onis Formation, and is dominant at Tsams at the northeast margin of the nappe. This facies consists of matrix-supported intraclast breccia with a typically mudstone matrix [Figure 3.16]. The typical form of this facies is 1-2 m thick beds, with jumbled angular intraclasts from ~10 to 50 cm. Clasts are angular to tabular, sometimes meter-scale rafted fragments of beds. Clasts can be either mudstone and grainstone [Figure 3.16b].

Interpretation While this facies is similar to the *intraclast grainstone* facies, the fine-grained matrix, thick beds, and intraclast cobbles to boulders implies an origin from mass-flow deposits, which are potentially storm-triggered and gravity enhanced on an oversteepened platform margin.

3.3.7 Summary of stratigraphic sequences

Sections were correlated based on sequence boundaries and maximum flooding surfaces [Figure 3.17] and used to build a sequence-stratigraphic model of the Zebra Nappe.

The Zebra Nappe broadly consists of three depositional sequences. The first, represented by the Neuras Formation and Ubisis Formation, and the lower part of the Tsams Formation is dominantly composed of peritidal, upper-shoreface, and shallow subtidal facies. The second, beginning near the top of the Tsams Formation and continuing through the Lemoenputs Formation, is a deepening facies system that consists of west-thickening shale wedges interspersed with compressed regressive intervals of shallower facies belts, culminating in reworking surfaces. The final sequence is a relatively monotonous interval of grainstones.

The facies recorded here show a range of depositional environments from shoreface and potentially supratidal to outer ramp, potentially corresponding to a peritidal to shoreface setting with a carbonate platform offshore.

Moving up through the section, there is a general trend from facies with clear shallow-water characteristics (fine sand and mud-cracked dolomite, for instance), towards deeper-water facies (mixed grainstones, wavy-bedded limestones). The upper stratigraphy contains high-energy grainstones and debris-flows facies that suggest the development of a grainstone-dominated ramp.

Lateral facies variation

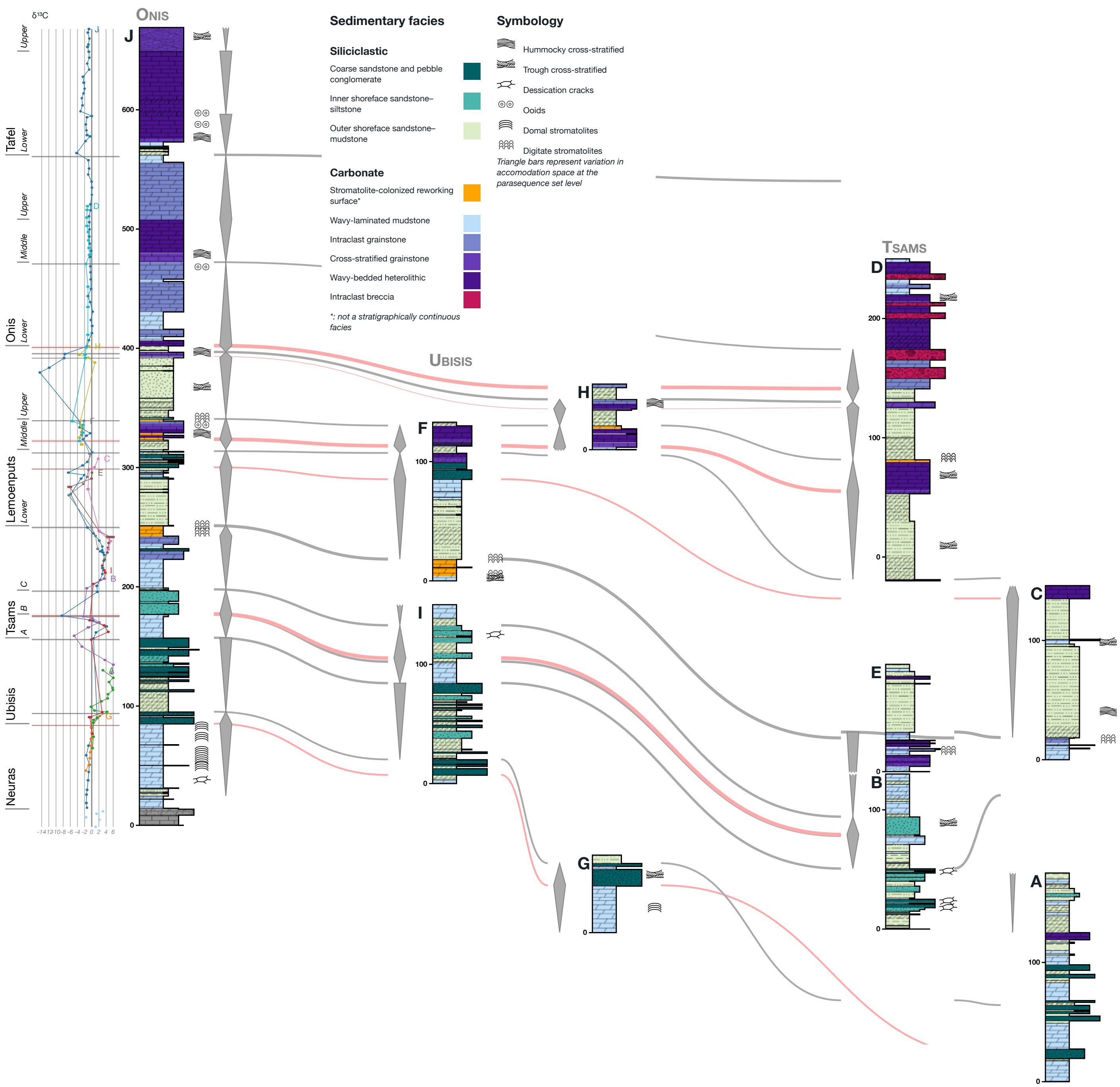

Figure 3.17: Correlated stratigraphic sections for the Zebra Nappe, showing facies model, sequence stratigraphic correlations, major sequence boundaries and flooding surfaces, and lithostratigraphic naming scheme.

Lateral facies variation is most pronounced on a NE-SW trend, with the Tsams locality generally presenting significant differences in facies composition from Onis and Ubisis (which are relatively similar in many respects). The outer-shoreface fine sandstone facies thicken substantially within both the Ubisis Formation and Lemoenputs Formation towards Tsams in the northeast of the nappe. In the Onis Formation, trough and HCS grainstone intervals are generally lost westward into Tsams and are replaced by interclast breccia facies. The Tafel Formation (above the Onis) records a retrograding sequence of grainstone facies over a substantial stratigraphic interval.

Marker intervals in the Lemoenputs Formation In the Lemoenputs Formation, two distinct stratigraphic intervals of heterolithic facies are mapped separately as "Lemoenputs Bed 1" and "Lemoenputs Bed 2". When they cannot be mapped separately, these beds are grouped with the Middle and Upper Member of the Lemoenputs Formation, respectively. At Onis and Ubisis, the lower of these units contains pebbly conglomerates inboard, and cracked, slumped (potentially dessicated) grainstone outboard [Figure 3.15c-e]. Both of these intervals are topped by digitate stromatolites and clotted thrombolites. They thicken considerably from the east (Onis) to west (Tsams). At Tsams and Ubisis, and across much of the center of the plateau, these intervals nearly abut each other, but at Tsams they are separated by a thick clastic wedge.

The grainstone and Onis maps into a > 20 m sequence at Tsams. In some cases, the Lemoenputs Bed A was mismapped by *Hartnady* (1980) as the Onis Formation, potentially due to its imposing character and resistant erosional style within Tsams Valley.

3.3.8 Chemostratigraphy

Chemostratigraphy is generally seen as a reasonably globally representative marker of ocean chemistry over time, and chemostratigraphic markers can be used to correlate stratigraphies regionally and globally (e.g. *Halverson et al.*, 2005). Of key interest is whether the stratigraphy matches the carbon isotope signature of the Shuram Excursion (*Grotzinger et al.*, 2011), a latest-Cryogenian carbon isotope excursion that should be present globally.

The chemostratigraphic data collected for sections of the Zebra Nappe was coregistered in stratigraphic height using the sequence-stratigraphic framework developed here [Figure 3.17]. Chemostratigraphic results for δ^{13}C (VPDB) are shown in the context of the correlated sections that are the basis for their stratigraphic normalization in Figure 3.17. They are also shown separately in Figure 3.18. In the Neuras Formation, values of –2 increase to 2. Values jump to +5 in the Ubisis Formation, with a sharp negative excursion in the Tsams Formation and a return to +5 in Member C of the Tsams Formation. The Lemoenputs Formation records a falling limb from +5 to -5, and a poorly sampled negative excursion to -15 at its top. These low δ^{13}C values are sampled only in a few isolated limestone beds at the top of the Lemoenputs Formation in Section J and are not repeated in sections D or H which also capture this interval, suggesting that these are the result of localized conditions or diagenesis. The Onis and Tafel formations record consistent values of 0 through several hundred meters of stratigraphy, and a slight decrease to -2-3 in the lower Tafel Formation is accompanied by a decrease in δ^{18}O to approximately -10. These values might be due to prolonged diagenesis and meteoric effects, which these limestones at the top of the plateau would be particularly susceptible to.

3.3.9 Detrital zircons

To help establish correlations and tectonic-stratigraphic setting, detrital zircons were analyzed for their U-Pb age information. Detrital zircon age spectra show a clear difference in the provenance ages of sedimentary materials between the Zebra Nappe and the structurally underlying Nama Group foreland basin [Figure 3.19]. The Zebra Nappe samples show no ages younger than 1 Ga, except for a single 539 Ma zircon found in sample J-89. Due to the lack of statistical power, we suspect that this measurement is the result of sample contamination or a misplaced standard grain on the grain mount (the SL-Mix standard used at University of Arizona has an overlapping age spectrum).

The Nama Group contains much younger material: Sample SL-1, collected in the Nudaus formation ~300 m below the basal NNC thrust fault on Onis Farm, shows a prominent 500-600 Ma peak corresponding to the Damara Orogen, which

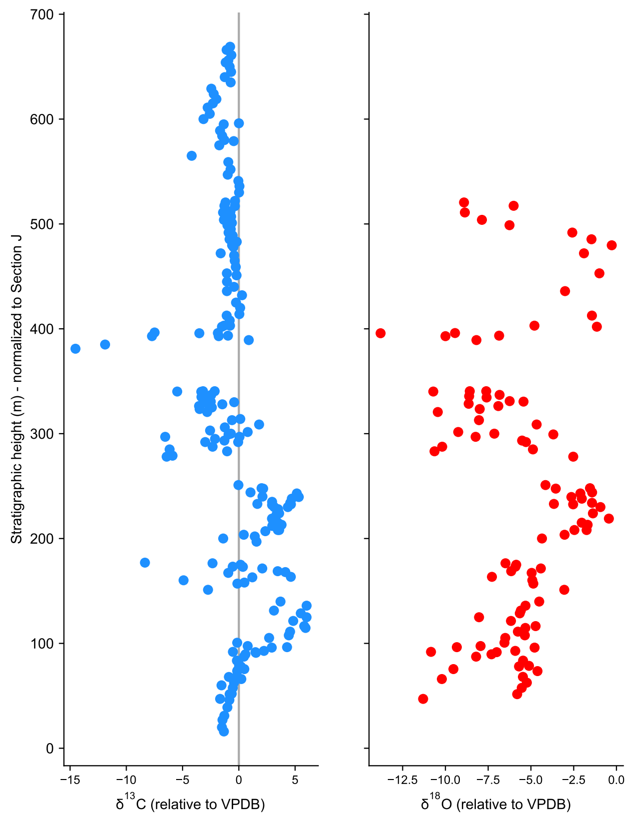

Figure 3.18: **(a)** δ^{13}C(VPDB) for the Zebra Nappe organized by stratigraphic height and normalized to Section J using the sequence-stratigraphic model developed in Section **??**. **(b)** δ^{18}O(VPDB) measurements excluding Section J, which must be remeasured due to an instrument failure.

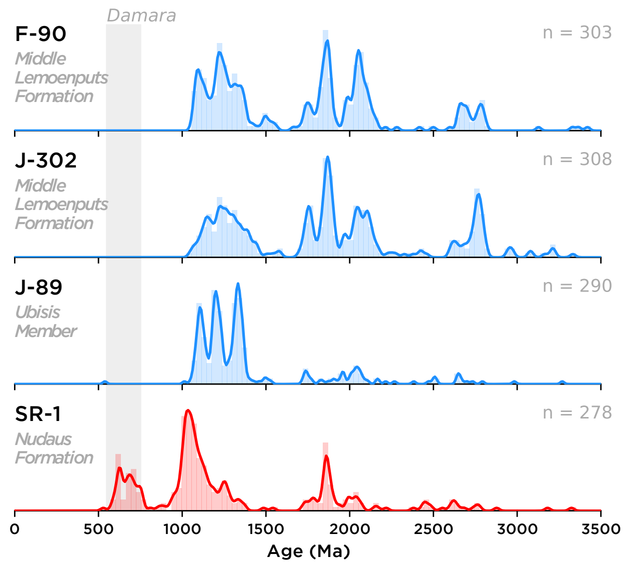

Figure 3.19: Detrital zircon age spectra for the Zebra Nappe (blue) and Nama Group (red) showing the lack of Damara Orogen material within the NNC.

is broadly bracketed between 580 and 500 Ma (*Gray et al.*, 2006).

3.4 Discussion

3.4.1 Tectonic interpretations

We find that there is no internal tectonic discontinuity or unconformity within the Zebra Nappe, as proposed by *Hartnady* (1978) and *Hoffmann* (1989) respectively. Instead, the Onis Formation sits conformably atop the lower units of the Zebra Nappe. The local relationships that *Hartnady* (1978) interpreted as the local non-deposition of the Lemoenputs Formation at the northeast corner of the nappe are more plausibly attributable to high-angle reverse faulting at the interface between the nappes, where the basal strata of the Zebra Nappe is kinked above the propagating tip of the fold and thrust belt to form antithetic high-angle reverse faults [Figure 3.6c and Figure 3.5c].

The nappe is adjacent to the Dassie Nappe, but the nature of the boundary between the two has been uncertain in the literature. We find that the Zebra Nappe overtops the Dassie Nappe as a passive backthrust [Figure 3.6]. On the western margin of the Zebra Nappe, the imbricated Dassie Nappe oversteps this south-dipping contact, locally inverting the Zebra Nappe strata south of this contact [Figure 3.5c and Figure 3.6c] On the eastern margin, a tear fault occurred when the Dassie Nappe began to ramp over a thick shale wedge and eventually incorporated it into the nappe complex. The identity and correlation of this shale wedge is uncertain, but we anticipate that it correlates with the Urikos Formation, which forms the footwall of the Naukluft complex locally.

It is unclear whether this is a sliver of the parautochtonous Rietoog Nappe or, since it sits across the major tectonic discontinuity of the sole thrust, something more akin to a shale in the Dassie Nappe. Either way, it is not a recognizable component of the typical Zebra Nappe sequence of lithologies.

We speculate that this tectonic slivering and incorporation of the Nama occurred because lateral differences in nappe rheology between the Zebra and Dassie Nappe favored defect propagation and disaggregation of the thrust ramp from the single "sole thrust" as the thrust ramped towards the surface on the eastern margin of the thrust belt.

The presence of tectonic discontinuities at the western and eastern margin of the Zebra Nappe suggests that N-S shortening began to involve the Zebra Nappe after the production of a E-W flexural syncline in front of the propagating thrust front at the Dassie-Zebra contact. This effectively juxtaposed the Onis formation with the Dassie Nappe, "locking" the passive backthrust at the margins of the nappe [Figure 3.5b and c].

The similarity of the Dassie Nappe dolomite and the Neuras Formation at the base of the Zebra Nappe is consistent with a passive backthrust at the Dassie–Zebra contact. This geometry implies that neither side of the tectonic interface is far-traveled, consistent with similar lithologic units and depositional environments on each side of the contact. Stratigraphic analysis of the Dassie Nappe may allow extension of the stratigraphic framework developed for the Zebra Nappe here.

3.4.2 Outliers formerly mapped as Zebra Nappe

Several tectonic units exposed within the Tsondab River Valley were mapped as Zebra Nappe by *Hartnady* (1978). Our more detailed lithologic understanding of the Zebra Nappe allows us to take a more detailed look at these correlations. The Arbeit Adelt outlier consists entirely of imbricated dolomite, with at least 50 m of

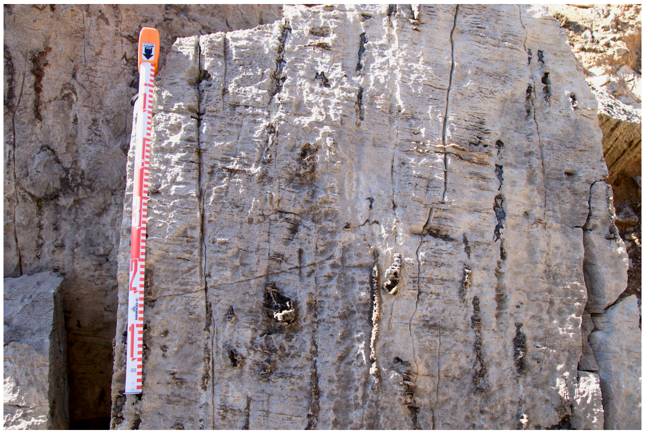

Figure 3.20: Tubestone dolomite in the Arbeit Adelt outlier mapped by *Hartnady* (1978) as a Zebra Nappe outlier. The lithologic features shown here do not correspond to any features within the Zebra Nappe.

stratigraphy in each sliver. This dolomite contains distinctive sedimentary structures such as tubestone [Figure 3.20] which are not present in the Zebra Nappe.

The intraclast breccias in the Onis formation are, to first order, similar to the "limestone-dolomite mass flow breccias" described in the Remhoogte and Klipbokrivier formations in the northern NNC (*Korn and Martin*, 1959; *Martin et al.*, 1983). *Martin et al.* (1983) suggest that the Remhoogte Formation was originally stratigraphically above the Büllsport formation, and became part of a different nappe due to differing rheological properties. If the Kudu and Dassie Nappes were originally linked, it is possible that the both the Klipbokrivier and Remhoogte formations can be correlated to the Zebra Nappe.

3.4.3 Simplification of NNC deformational sequence

The tectonic framework proposed here allows substantial simplification of the tectonic model proposed for the NNC. *Hartnady* (1978) defined five separate episodes of deformation: D1 eastward emplacement of the Pavian Nappe, D2 southward emplacement of a combined Kudu-Dassie Nappe, D3 dismembering of this Kudu-Dassie Nappe, D4 NW-SE folding of the Zebra Nappe (followed by unconformable deposition of the Onis Formation), and D5 emplacement of the entire NNC atop the Sole Dolomite. Given our simplification of the tectonic contacts and assessment of an internal lack of disconformities in the Zebra Nappe, we find that the stages of deformation affecting the Zebra Nappe can be modeled more simply.

We can collapse from five deformational episodes to two. The first episode of southward thrusting built the entire nappe stack. The second, eastward thrusting, built the southeastward-vergent structures within the Zebra Nappe during eastward thrusting over the Nama group.

If the thrust contact between the Pavian and Kudu nappes (proposed by *Hartnady* (1978)) is not a major structural surface, as advanced by K.H. Hoffmann (unpublished; described in *Miller* (2008)), then no out-of-sequence thrusting is required for the Dassie and Kudu Nappes to be part of a single original unit, as envisioned by *Hartnady* (1978) and *Miller* (2008).

The roof-thrust geometry proposed here for the Zebra Nappe still allows for the Büllsport outlier to be correlative the Zebra Nappe, if it was intercalated between the Kudu and Dassie nappes during stage-two eastward thrusting. The speculative correlation of the Klipbokrivier Formation with the Zebra Nappe discussed by *Hartnady* (1978) is also reasonably given relative structural positions. The Arbeit Adelt outlier cannot reasonably retain its correlation with the Zebra Nappe, but we have established that its lithology is substantially different.

This tectonic framework can be evaluated in future work by assessing the potential links between the Kudu and Dassie nappes, as well as the relationship of the Büllsport outlier to the Zebra Nappe.

3.4.4 Stratigraphic interpretations

Based on these factors, we reject the correlation with Nama Group advanced by *Hartnady* (1979) and *Hoffmann* (1989). The Zebra Nappe could represent a passive margin system or an early foreland basin. It records repeated backstepping of sedimentary facies and deeper environments upwards.

This is very different than the Nama Group, in which there are no prograding clastic sediments indicative of major regressions. We also underscore that intervals of prograding sandstone would not be seen in a classic evolving foreland basin (although such reworking surfaces could be expected during the passage of a flexural bulge at the continental margin).

Prave (1996) proposes that the Otavi group of Northern Namibia is a foreland basin system (oriented towards the Rio de la Plata craton) despite the lack of key features such as clastic sedimentation sourced from the orogen. One of the key critera used to make this argument is the presence of backstepping facies belts signifying deepening deposition. The broad sequence outlined in this paper, of coarse siliciclastic sediments followed by carbonate-platform deposition, is suggestive of an initial foreland-basin pattern.

Detrital zircon age constraints The lack of Damara-age zircons the coarse siliciclastic sediments of the ZN suggests the ZN is significantly older and deposited in a fundamentally different tectonic environment than the Nama foreland basin rocks. Although the youngest zircon peaks in the ZN samples are older than 1 Ga, this is not a particularly useful minimum age constraint – the youngest pre-Damara rocks on the Kalahari craton are the Sinclair group and Namaqua Metamorphic belts *van Schijndel et al.* (2014), which are of similar 1 Ga ages. Detrital zircon data show that ZN sediments predate the beginning of Damara continental suturing, when significant clastic input was directed southward from the eroding orogenic belt. However, most of the magmatism of the Damara orogen occurred on the Kalahari craton, towards which subduction was oriented prior to cratonic collision, so an early foreland basin system associated with Damara orogenesis is not precluded by this dataset. In this case, Damara zircons from airfall ash would have been diluted out by sediment sorting.

Variation in the detrital zircon data within the nappe records a potential tectonic signal corresponding to our stratigraphic results. The coarse sandstones and pebbly conglomerates of the Lemoenputs formations show a substantially higher abundance of Archean clasts. These clasts likely originate from the Kaapvaal Craton, an Archean (3.1 Ga) craton underlying eastern South Africa and Botswana, although the Rehoboth Basement Inlier to the north has been identified as the source of some similarly-aged grains (*Van Schijndel et al.*, 2011; *van Schijndel et al.*, 2014). The younger component of the detrital zircons shows substantially the same peaks for all ZN samples, although the youngest Mesoproterozoic peak is much more enhanced in the stratigraphically lower Ubisis Formation samples.

Carbon isotope age constraints Chemostratigraphy is not like the lower Nama group (as previously correlated) at all. Comparison of the chemostratigraphic variation within the Zebra Nappe with the broader context of Neoproterozoic chemostratigraphy yield no obvious correlations with specific time periods that could be represented by this section.

3.5 Future work

More understanding of lateral variation in the Onis upper ramp. Should the Tafel Formation be taken as a distinct stratigraphic unit? The change in environment between Onis and Tsams has not been fully characterized, and there is more work to do (at Tsams, particularly) to understand the sedimentary environment at the top of the nappe.

Bibliography

a. Watters, W., J. P. Grotzinger, J. Bell, J. Grant, A. G. Hayes, R. Li, S. W. Squyres, and M. T. Zuber (2011), Origin of the structure and planform of small impact craters in fractured targets: Endurance Crater at Meridiani Planum, Mars, *Icarus*, *211*(1), 472–497, doi:10.1016/j.icarus.2010.08.030.

Behr, H., H. Ahrendt, H. Porada, and K. Weber (1983), The Sole Dolmite at the Base of the Naukluft Nappe Complex, *Special Publications of the Geological Society of South Africa*, pp. 185–197.

Blanco, G., G. J. B. Germs, H. M. Rajesh, F. Chemale, I. a. Dussin, and D. Justino (2011), Provenance and paleogeography of the Nama Group (Ediacaran to early Palaeozoic, Namibia): Petrography, geochemistry and U-Pb detrital zircon geochronology, *Precambrian Research*, *187*(1-2), 15–32, doi:10.1016/j.precamres.2011.02.002.

Dibenedetto, S., and J. Grotzinger (2005), Geomorphic evolution of a storm-dominated carbonate ramp (c. 549 Ma), Nama Group, Namibia, *Geological Magazine*, *142*(05), 583, doi:10.1017/S0016756805000890.

Duffy, A., D. G. Eberle, R. L. Grasty, D. G. Hutchins, and W. E. S. Urquhart (1997), Compilation, back-calibration and standardization of aeroradiometric surveys from Namibia, Southern Africa.

Fagereng, ⊠., Z. Smith, C. D. Rowe, B. Makhubu, and F. Y. G. Sylvester (2014), Stress, strain, and fault behavior at a thrust ramp: Insights from the Naukluft thrust, Namibia, *Journal of Structural Geology*, *58*, 95–107, doi:10.1016/j.jsg.2013.11.002.

Frimmel, H. (1998), Neoproterozoic tectono-thermal evolution of the Gariep Belt and its basement, Namibia and South Africa, *Precambrian Research*, *90*(1-2), 1–28, doi:10.1016/S0301-9268(98)00029-1.

Gallagher, K., and R. Brown (1999), Denudation and uplift at passive margins: The record on the Atlantic Margin of southern Africa, *Philosophical Transactions of the Royal Society A: Mathematical, Physical and Engineering Sciences*, *357*(1753), 835–859, doi:10.1098/rsta.1999.0354.

Gehrels, G. (2012), Detrital Zircon U-Pb Geochronology: Current Methods and New Opportunities, in *Tectonics of Sedimentary Basins*, pp. 45–62, Wiley-Blackwell, doi:10.1002/9781444347166.ch2.

Germs, G. J. B. (1974), The Nama Group in South West Africa and Its Relationship to the Pan-African Geosyncline, *The Journal of Geology*, *82*(3), 301–317, doi:10.1086/627966.

Gray, D. R., D. a. Foster, B. Goscombe, C. W. Passchier, and R. a. J. Trouw (2006), 40Ar/39Ar thermochronology of the Pan-African Damara Orogen, Namibia, with implications for tectonothermal and geodynamic evolution, *Precambrian Research*, *150*(1-2), 49–72, doi:10.1016/j.precamres.2006.07.003.

Gray, W., a. F. Glazner, D. S. Coleman, and J. M. Bartley (2008), Long-term geochemical variability of the Late Cretaceous Tuolumne Intrusive Suite, central Sierra Nevada, California, *Geological Society, London, Special Publications*, *304*, 183–201, doi:10.1144/SP304.10.

Gresse, P., and G. Germs (1993), The Nama foreland basin: Sedimentation, major unconformity bounded sequences and multisided active margin advance, *Precambrian Research*, *63*(3-4), 247–272, doi:10.1016/0301-9268(93)90036-2.

Grotzinger, J. P., and a. H. Knoll (1999), Stromatolites in Precambrian carbonates: Evolutionary mileposts or environmental dipsticks?, *Annual review of earth and planetary sciences*, *27*, 313–358, doi:10.1146/annurev.earth.27.1.313.

Grotzinger, J. P., D. a. Fike, and W. W. Fischer (2011), Enigmatic origin of the largest-known carbon isotope excursion in Earth's history, *Nature Geoscience*, *4*(5), 285–292, doi:10.1038/ngeo1138.

Halverson, G. P., P. F. Hoffman, D. P. Schrag, and A. J. Kaufman (2002), A major perturbation of the carbon cycle before the Ghaub glaciation (Neoproterozoic) in Namibia: Prelude to snowball Earth?, *Geochemistry, Geophysics, Geosystems*, *3*(6), 1–24.

Halverson, G. P., A. C. Maloof, and P. F. Hoffman (2004), The Marinoan glaciation (Neoproterozoic) in northeast Svalbard, *Basin Research*, *16*(3), 297–324.

Halverson, G. P., P. F. Hoffman, D. P. Schrag, A. C. Maloof, and A. H. N. Rice (2005), Toward a Neoproterozoic composite carbon-isotope record, *Geological Society of America Bulletin*, *117*(9), 1181, doi:10.1130/B25630.1.

Hartnady, C. (1978), The Structural Geology of the Naukluft Nappe Complex and its relationship to the Damara Orogenic Belt, South West Africa/Namibia, Ph.D. thesis.

Hartnady, C. J. (1980), Geological map of the Naukluft area, *Precambrian Research Unit, University of Cape Town*.

Hartnady, C. J. H. (1979), Overthrust tectonics, stratigraphic problems and metallogenesis in the Khomas Ridge Province, Damara orogenic belt, *Precambrian Research Unit of the University of Cape Town Annual report*, *16*, 73–89.

Hoffman, P. F. (1998), A Neoproterozoic Snowball Earth, *Science*, *281*(5381), 1342–1346, doi:10.1126/science.281.5381.1342.

Hoffman, P. F., A. J. Kaufman, G. P. Halverson, and D. P. Schrag (1998), Comings and goings of global glaciations on a Neoproterozoic tropical platform in Namibia, *GSA today*, *8*(5), 1–9.

Hoffmann, K. H. (1989), New aspects of lithostratigraphic subdivision and correlation of late Proterozoic to early Cambrian rocks of the southern Damara Belt and their correlation with the central and northern Damara Belt and Gariep Belt, *Communications of the Geological Society of Namibia*, *5*, 59–67.

Hoffmann, K.-H., D. Condon, S. Bowring, and J. Crowley (2004), U-Pb zircon date from the Neoproterozoic Ghaub Formation, Namibia: Constraints on Marinoan glaciation, *Geology*, *32*(9), 817, doi:10.1130/G20519.1.

Kirschvink, J. L. (1992), Late Proterozoic low-latitude global glaciation: The snowball Earth.

Knoll, A. H. (1999), Early Animal Evolution: Emerging Views from Comparative Biology and Geology, *Science*, *284*(5423), 2129–2137, doi:10.1126/science.284.5423.2129.

Korn, H., and H. Martin (1959), Gravity tectonics in the Naukluft Mountains of South West Africa, *Geological Society of America Bulletin*, *70*(8), 1047, doi:10.1130/0016-7606(1959)70[1047:GTITNM]2.0.CO;2.

Martin, H. (1953), Notes on the Dwyka succession and on some pre-Dwyka valleys in South West Africa, *Transactions of the Geological Society of South Africa*, *46*, 7.

Martin, H., H. Porada, and R. Wittig (1983), Where lies the root zone of the naukluft nappe complex?, *Special Publications of the Geological Society of South Africa*, pp. 199–207.

Miller, R. M. (2008), Neoproterozoic and early Palaeozoic rocks of the Damara Orogen, *The geology of Namibia*, *3*.

Ohnemueller, F., A. R. Prave, A. E. Fallick, and S. A. Kasemann (2014), Ocean acidification in the aftermath of the Marinoan glaciation, *Geology*, *42*(12), 1103–1106, doi:10.1130/G35937.1.

Prave, A., K.-H. Hoffmann, W. Hegenberger, and A. Fallick (2011), The Witvlei Group of east-central Namibia, *The Geological Record of Neoproterozoic Glaciations*, pp. 211–216, doi:10.1144/M36.15.

Prave, A. R. (1996), Tale of three cratons: Tectonostratigraphic anatomy of the Damara orogen in northwestern Namibia and the assembly of Gondwana, *Geology*, *24*(12), 1115, doi:10.1130/0091-7613(1996)024<1115:TOTCTA>2.3.CO;2.

Rowe, C. D., ⊠. Fagereng, J. a. Miller, and B. Mapani (2012), Signature of coseismic decarbonation in dolomitic fault rocks of the Naukluft Thrust, Namibia, *Earth and Planetary Science Letters*, *333-334*, 200–210, doi:10.1016/j.epsl.2012.04.030.

Saylor, B. Z., J. P. Grotzinger, and G. J. B. Germs (1995), Sequence stratigraphy and sedimentology of the Neoproterozoic Kuibis and Schwarzrand Subgroups (Nama Group), southwestern Namibia, *Precambrian Research*, *73*(1-4), 153–171, doi:10.1016/0301-9268(94)00076-4.

Saylor, B. Z., a. J. Kaufman, J. P. Grotzinger, and F. Urban (1998), A composite reference section for terminal proterozoic strata of southern Namibia., *Journal of sedimentary research. Section A, Sedimentary petrology and processes : an international journal of SEPM (Society for Sedimentary Geology)*, *68*(6), 1223–1235, doi:10.2110/jsr.68.1223.

Smith, E. F., F. A. Macdonald, T. A. Petach, U. Bold, and D. P. Schrag (2016), Integrated stratigraphic, geochemical, and paleontological late Ediacaran to early Cambrian records from southwestern Mongolias, *Bulletin of the Geological Society of America*, *128*(3-4), 442–468, doi:10.1130/B31248.1.

Spencer, C. J., A. R. Prave, P. A. Cawood, and N. M. W. Roberts (2014), Detrital zircon geochronology of the Grenville/Llano foreland and basal Sauk Sequence in west Texas, USA, *Bulletin of the Geological Society of America*, *126*(7-8), 1117–1128, doi:10.1130/B30884.1.

Stanistreet, I. G., P. A. Kukla, and G. Henry (1991), Sedimentary basinal responses to a Late Precambrian Wilson Cycle: The Damara Orogen and Nama Foreland, Namibia, *Journal of African Earth Sciences*, *13*(1), 141–156, doi:10.1016/0899-5362(91)90048-4.

Van Schijndel, V., D. H. Cornell, K.-H. Hoffmann, and D. Frei (2011), Three episodes of crustal development in the Rehoboth Province, Namibia, *Geological Society, London, Special Publications*, *357*(1), 27–47, doi:10.1144/SP357.3.

van Schijndel, V., D. H. Cornell, D. Frei, S. L. Simonsen, and M. J. Whitehouse (2014), Crustal evolution of the Rehoboth Province from Archaean to Mesoproterozoic times: Insights from the Rehoboth Basement Inlier, *Precambrian Research*, *240*, 22–36, doi:10.1016/j.precamres.2013.10.014.

Viola, G., N. S. Mancktelow, and J. A. Miller (2006), Cyclic frictional-viscous slip oscillations along the base of an advancing nappe complex : Insights into brittle-ductile nappe emplacement mechanisms from the Naukluft Nappe Complex , central Namibia, *25*, 1–20, doi:10.1029/2005TC001939.

Weber, K., and H. Ahrendt (1983), Mechanisms of nappe emplacement at the southern margin of the Damara Orogen (Namibia), *Tectonophysics*, *92*(1-3), 253–274, doi:10.1016/0040-1951(83)90093-8.

Whipple, K. X. (1997), Open-channel flow of Bingham fluids: Applications in debris-flow research, *The Journal of Geology*, *105*(2), 243–262.

4 A PCA-based framework for determining remotely-sensed geological surface orientations and their statistical quality

Daven P. Quinn[1] B.L. Ehlmann[1,2]

1 Division of Geological and Planetary Sciences, California Institute of Technology, Pasadena, California, USA

2 Jet Propulsion Laboratory, California Institute of Technology, Pasadena, California, USA

Abstract

The orientations of planar rock layers are fundamental to our understanding of structural geology and stratigraphy. Remote-sensing platforms including satellites, unmanned aerial vehicles (UAVs), and LIDAR scanners are increasingly used to build three-dimensional models of structural features on Earth and other planets. Remotely-gathered orientation measurements are straightforward to calculate but are subject to uncertainty inherited from input data, differences in viewing geometry, and the regression process, complicating geological interpretation. Here, we improve upon the present state of the art by developing a generalized means for computing and reporting errors in strike-dip measurements from remotely sensed data. We outline a general framework for representing the error space of uncertain orientations in Cartesian and spherical coordinates and develop a principal-component analysis (PCA) regression method which captures statistical errors independent of viewing geometry and input data structure. We also build graphical techniques to visualize the uniqueness and quality of orientation measurements, and a process to increase statistical power by jointly fitting bedding planes under the assumption of parallel stratigraphy. These new techniques are validated by comparison of field-gathered orientations with minimally-processed satellite imagery of the San Rafael Swell, Utah and UAV imagery from the Naukluft Mountains, Namibia. We provide software packages supporting planar fitting and the visualization of error distributions. This method provides a means to increase the precision and comparability of structural measurements gathered using a new generation of remote-sensing techniques.

The orientations of geological features such as faults, dikes, lava flows, and sedimentary beds record characteristics of deposition or emplacement, episodes of deformation, and relationships between bodies of rock. Idealized planes describing these features are common units of geological analysis. Planar orientations have most often been collected directly, using a field structural compass or surveying equipment. The increasing viability of high-resolution remote-sensing techniques has allowed three-dimensional imaging of geological features at sub-meter scale.

In field mapping by a structural geologist, directly-measured orientations (e.g. using a pocket transit on outcrops) have been considered sufficiently accurate that errors are not reported. Orientations measured using remotely-gathered data are a powerful new tool for geological analysis, especially when outcrops are inaccessible to direct measurement. However, poorly-modeled and hard-to-visualize errors complicate the process of arriving at the true orientation of a geological structure. Remote-sensing datasets can spatially vary in resolution and quality, and measurements are potentially biased by terrain effects, sensor-dependent noise, measurement geometry, and operator error in defining relevant features, among other sources of error.

One major motivation of this work is the orbital mapping of layered rocks on Mars, which are key indicators of Mars' geological history (e.g. **??????**). For example, sedimentary deposits are mapped from orbit and with rovers, but detailed evaluation of their depositional mechanisms requires understanding bedding orientations, particularly bedding dip (e.g. **??????????**, submitted). Detailed accounting for errors is also important in large-scale regional studies, where variable data resolution and outcrop quality affect the dataset (e.g **?**).

At present, some Mars mapping studies report no error ranges (e.g. **?**) while others report bedding orientations with error ranges output from commercial regression packages (e.g. **?**). Other studies use "dip error" (**??**), "pole error" (**?**), or bootstrap resampling statistics (**??**) to evaluate measurement quality. The varying approaches used to generate orientation errors, along with different degrees of reporting rigor, complicate understanding of the accuracy and precision of specific strike-dip measurements and consequent implications for the geologic structure.

Even carefully-planned structural studies with consistent error analysis procedures cannot be easily interpreted using current visualization tools. For instance, map symbols for nominal strike and dip do not provide a means of understanding commonly unpredictable, nonlinear errors inherent in orientation measurements in varied terrain, and individual orientation measurements often only coarsely correspond to the overall structural pattern (e.g. **???**, submitted). Without methods to visualize orientation certainty, reported bedding orientations do not fully communicate information used in study interpretations.

The use of remotely-sensed orientation measurements in terrestrial geology is also a key driver of this work. High-resolution satellite imagery and DEMs are now available for much of the Earth's surface (e.g. **?**), supporting regional photogeologic mapping. The advent of field-portable Light Detection and Ranging (LIDAR) instruments (**?**) and the improving accuracy of structure-from-motion (SfM) photogrammetry support the increasing remote measurement of geological surface orientations. Numerous recent studies use orientation measurements from unmanned aerial vehicle (UAV) photogrammetry (e.g. **?**), often using three-point analytical approximations (**?**) or commercial regression packages.

Terrestrial datasets are often hindered by the same factors complicating analyses on Mars. For example, in a recent study of the accuracies of remotely derived data, **?** extract bedding planes and fold axes from LIDAR and SfM photogrammetric digital surface models of weathered beds of the Stackpole syncline that are comparable with high accuracy to direct measurements in most cases. However, significant difference in fit were found between LIDAR, ground-, and UAV-based photogrammetry that were related to the orientation of the outcrop and viewing geometry as well as the scale of facet construction and point fitting.

Improvements on the state-of-the-art in computing and visualizing error methods must include several factors. Bedding orientation measurements depend not only on the internal errors of the remote-sensing dataset but also on the geometry of the outcrop measured (e.g. hillslope concavity and aspect) and accuracy in following bedding features. Measurements from the same dataset and geologic unit can have completely different error structures depending on the shape of topography, presenting a challenge for error analysis. A statistical and data-visualization framework designed for planar orientation measurements will enable quantitative comparison between planar fits with completely different error structures. By increasing the robustness of orientation determination from heterogeneous data, such a framework extends the range of situations in which structural metrics can be reliably assessed from remote-sensing imagery, enabling statistically rigorous comparison of measurements with a wide variety of source data type, outcrop exposure and quality, and viewing geometry.

The methods developed in this study to improve the calculation and visualization of orientation errors were developed in conjunction with structural mapping of the layered sulfates at northeast Syrtis Major, Mars. These thick layered deposits occupy a critical stratigraphic interval, but their relatively poor exposure complicates orientation measurement. Additionally, because small changes in dip can imply completely different depositional processes, high-confidence angular measurements are crucial drivers of interpretation (**?**, submitted). Here, we detail the developed method. First, we describe a generalized approach to planar orientation errors for three-dimensional datasets [Section 4.2] and its implementation as a PCA-based statistical procedure for planar fitting [Section 4.3]. We test the method using terrestrial orientations recovered from satellite and UAV data [Section 4.4] and discuss potential alternative statistical parameterizations [Section 4.5]. Finally, we describe general geometric transformations for the error space of a plane [Section 4.A] and several open-source software packages supporting planar fitting and error visualization for orientation data.

4.2 Background: the structure of a remotely-sensed plane and its error space

A geologic surface is typically extracted from remote-sensing data by isolating representative points into a three-dimensional point dataset. A common procedure is the extraction of elevation for points along a bedding trace digitized from visible imagery and overlain on a gridded elevation model. Related procedures include the grouping of closely-spaced LIDAR points sampling the same surface (e.g. **?**) or direct elevation measurement along a feature trace by theodolite or differential GPS. Since remote-sensing datasets are typically defined in Cartesian spatial coordinates, all of these methods produce an array of three-dimensional points in

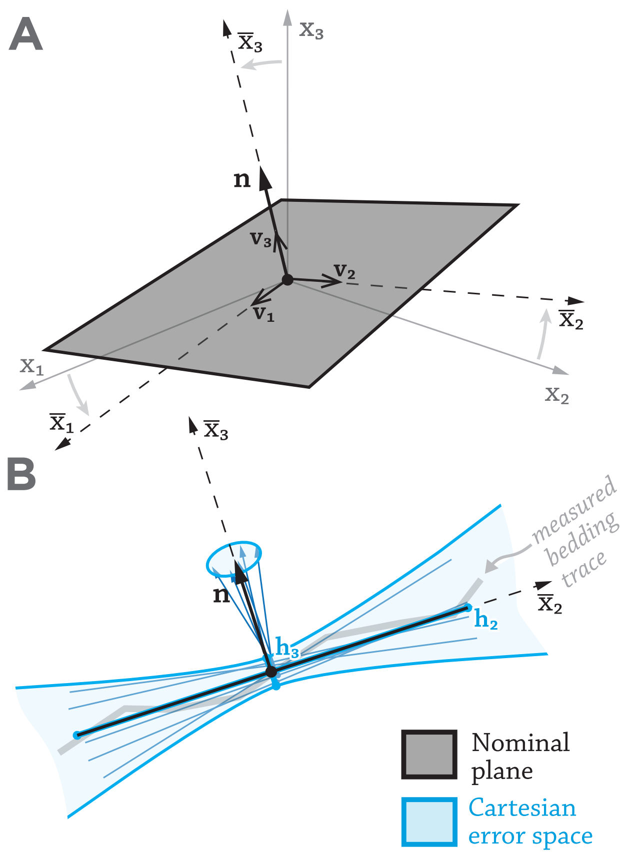

Figure 4.1: Schematic representation of the structure of a plane with errors and its relation to the global Cartesian coordinate system $\mathbf{x}$. **(a)** The plane and its associated normal vector $\mathbf{n}$. In unweighted PCA, $\mathbf{n}$ falls along the principal component axis $\overline{\mathbf{x}}_3$. The three unit vectors $\mathbf{v}_i$, oriented along $\overline{\mathbf{x}}_i$, form rows of the rotation matrix $\mathbf{V}$ that maps $\mathbf{x}$ to $\overline{\mathbf{x}}$. **(b)** A $\overline{\mathbf{x}}_2$-$\overline{\mathbf{x}}_3$ slice of the nominal plane and its normal vector, along with a bundle of planes with slightly different orientations and the encompassing hyperbolic error space (blue).

space that collectively represent a single feature.

Regression is the key method for extracting planar representations of geological surfaces from their spatial extent. The set of coordinates that represents a potential plane is converted to an orientation by finding the best-fitting plane through the dataset using minimization (e.g. PCA, OLS, and other regression frameworks) in Cartesian coordinate space (**??**). The idealized geologic surface that results from regression can be mathematically described as a plane, requiring three free parameters. Description of orientation alone requires only two free parameters, represented either as slopes in two directions or the orientation of a normal vector to the plane [Figure 4.1a].

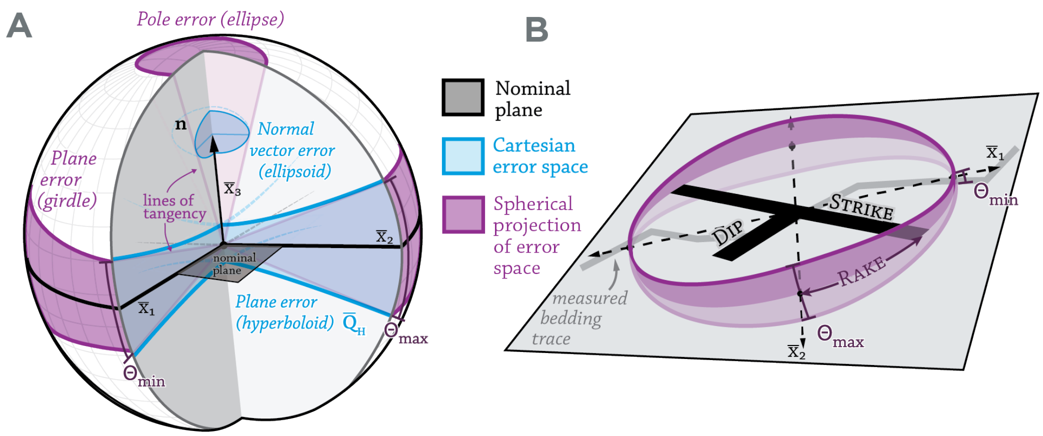

Figure 4.2: Schematic representation of the relationship between the nominal planar fit *(black)*, the hyperbolic error shell $\overline{\mathbf{Q}}_{\mathbf{H}}$ and inverse ellipsoid representing the normal vector endpoint *(blue)*, and the spherical error distribution formed by projecting the tangents to these error spaces onto the unit sphere *(purple)*. θ_{min} and θ_{max} define the scale of orientation errors along two axes within the plane, $\overline{\mathbf{x}}_1$ and $\overline{\mathbf{x}}_2$. **(a)** Projection of Cartesian error space to spherical coordinates, both as a planar girdle and pole error ellipse. **(b)** Orientation of the error space to the plane (defined by θ_{min} and θ_{max}) relative to the nominal plane, emphasizing the *rake* angle needed to report the directions of errors within the plane.

Regression of a best-fitting plane inherently involves uncertainty, which combines with irregularities in the input dataset to produce orientation errors. In Cartesian space terms, these errors can be represented as a hyperboloid of two sheets enclosing all possible planes in the dataset, varying around the nominal regression line, or alternatively as a set of normal vectors perpendicular to the plane. Assuming a fixed length, the error space for this normal vector forms an ellipsoid containing possible vector endpoints [Figure 4.1b].

In spherical coordinates, orientations are intuitively represented as a pair of angles (commonly, strike/dip, or dip/dip-direction). This two-angle representation supports visualization of orientation information on stereonets and related spherical plots. Previous studies of bedding orientation errors have parameterized orientation error in terms of strike and dip (**?**), and many workers have reported orientation errors in these terms (e.g. **??**). However, orientation errors are not necessarily aligned with the strike/dip parameters that describe the nominal plane, and errors expressed in terms of strike/dip rely implicitly on the small-angle assumption. Near-horizontal bedding (a common mode of stratigraphic exposure) has highly nonlinear angular dispersion in strike when approaching zero dip, with large covariances between the two.

Errors parameterized as pole error (angular error around the nominal orientation of a plane) yield error cones that are not subject to linearization error, however, the magnitudes of these pole errors must be defined with a statistical process. Directional statistical fitting mechanisms commonly used for geological orientations yield errors parameterized as pole error but operate entirely on data already expressed in angular terms (e.g. **?????**).

Regression errors defined in Cartesian space can be mapped to spherical coordinates using geometric projection. Hyperbolic and ellipsoidal error spaces to a planar fit in Cartesian coordinates can be projected on a unit sphere: hyperbolic errors to the plane map to a spherical girdle (a bundle of great circles), and normal vector errors project to an ellipse [Figure 4.2a]. The angular span of this spherical girdle or ellipse can be defined by θ_{max}, the maximum angular error to the plane, and θ_{min}, which is orthogonal to θ_{max} by definition (and spatial reasoning). θ_{max} need not be oriented along strike or along dip; instead, the orientation of θ_{max} with respect to the nominal plane is expressed using a *rake* angle between the strike of the plane and θ_{max} [Figure 4.2b]. This format generalizes pole error to allow the full expression of a Cartesian orientation error space in angular terms, with five free parameters. This error structure forms the foundation for this work.

4.3 Methods

4.3.1 PCA for planar fitting

Error treatment in OLS vs. PCA OLS regression is the most common technique for fitting orientations of lines and planes. However, many other regression techniques exist which chiefly differ in their mechanism for apportioning error along the coordinate axes of the fit. Many of these parameterizations can be used to define errors to a plane. In PCA, the focus of this study, errors are fitted orthogonal to the best-fitting plane.

OLS regression fundamentally tests the relationship of a dependent variable with a set of independent variables. All error is assumed to belong to the independent data, which in spatial data is usually assigned to the vertical plane. This

Table 4.1: Classification of dataset major axes

Scenario[a]	Hyperbolic axes[b]	Shape of variance ellipsoid	Notes
A	$h_1 \approx h_2 > h_3$	Prolate ellipsoid	Plane well-defined in two dimensions, with small error axis
B	$h_1 > h_2 > h_3$	Scalene ellipsoid	Quality of planar fit depends on axial dimensions and structure of dataset
C	$h_1 > h_2 \approx h_3$	Oblate ellipsoid	Defined along a line, but with no unique planar orientation
D	$h_1 \approx h_2 \approx h_3$	Spherical	Poorly constrained on all axes, no clear plane defined

[a] Scenario lettering corresponds to Figures 4.4, 4.5, and 4.6.
[b] $\mathbf{h} = \boldsymbol{\lambda}$ in **?**, and $\mathbf{h} = \boldsymbol{\lambda} + F\boldsymbol{\sigma}_{\boldsymbol{\lambda}}$ in this work (see Table 4.3 for notation definition).

property inhibits the fitting of steep slopes [Figure 4.3]. Geological planes are often expected to be steeply dipping, depending on their origin and geologic context, and the assumption that errors are chiefly vertical is not always reasonable.

Unlike OLS, PCA fits errors along all axes simultaneously, with no distinction between independent and dependent data. This is a significant advantage for fitting arbitrarily-oriented planes atop datasets with different error structures. For instance, errors for photogrammetric datasets are generally dependent on the viewing geometry of the image pair(s) used to assemble the 3D model; elevation models created from oblique UAV imagery of cliff faces e.g. 4.4.2 will have chiefly horizontal errors, and multi-view SfM datasets will have errors oriented along arbitrary, oblique view planes. This variability of error structure in a scene requires a flexible fitting mechanism that can incorporate off-vertical errors. Even elevations measured on a gridded dataset have several sources of non-vertical error: (1) error in the construction of the DEM (e.g. photogrammetric image-registration error), (2) resampling error (sub-post smoothing imparted by gridding) (3) sampling error (inexact digitization of measured features), and (4) downslope bias. Though often poorly quantified, these errors still influence the output of planar fitting. The PCA technique has been used for planar fitting in contexts ranging from paleomagnetism (**?**) to computer vision and depth-mapping, where orientation flexibility is required to map features such as vertical walls (**??**).

Much of the literature urges caution when applying PCA to estimate statistical confidence (e.g. **???**). PCA is not usually developed or motivated with a clear probabilistic framework (**?**), and is instead commonly used as a tool for dimensionality reduction, compressing the variation of a multidimensional dataset into a smaller set of explanatory variables. That process is difficult to statistically model, largely limiting PCA to algorithmic applications (e.g. image processing) and exploratory data analysis, except where explicit statistical rationale can be advanced for how many principal components to retain (**?**). For the fitting of spatial planes, both input and output data are tied to orthonormal spatial coordinates, and finding the best-fitting plane involves only rotation, not dimensionality reduction, allowing us to circumvent this source of uncertainty. Evaluating the orientation and scatter along the axes of the input data, rather than discarding some of them, is statistically straightforward [Section 4.3.3].

Orientation examples To exhibit the properties of the PCA algorithm applied to datasets of varying quality, we focus on four endmember type examples of digitized bedding traces [Figure 4.4] with a range of dataset structures corresponding to Table 4.1. These examples are digitized traces of sedimentary bedding measured within an area in NE Syrtis, Mars during the study described in **?**. Orientations were collected atop paired orthophotos and DEMs, which have different spatial resolutions and error structures due to to variable dust cover and stereo geometry. Additionally, these bedding traces cover a range of hillslope aspect and curvature, allowing them to query a wide range of potential error structures. We follow these bedding traces through transformation of their error space from Cartesian to spherical coordinates, and the numerical breakdown of their errors is summarized in Table 4.2.

4.3.2 The nominal plane in PCA

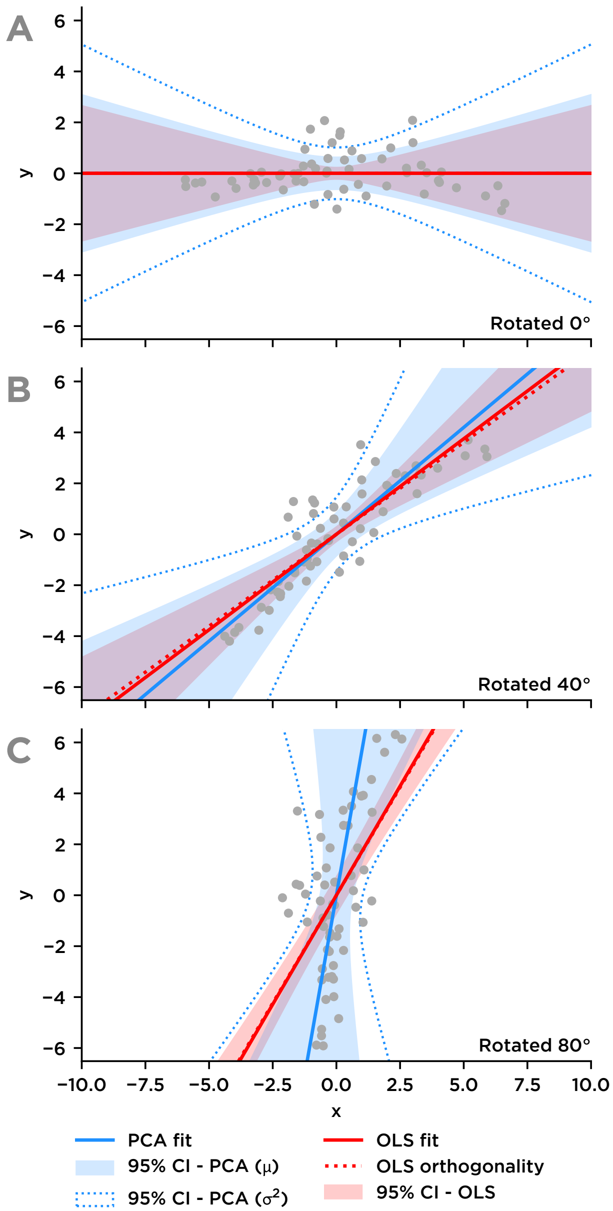

Figure 4.3: PCA and OLS regressions of a 2-dimensional, zero-centered point cloud rotated counterclockwise by **(a)** 0°, **(b)** 40°, and **(c)** 80°, emphasizing the nonlinear relationship between OLS and PCA regressions for differently-dipping planes with the same measurement scatter. Unweighted PCA retains the same error structure regardless of orientation, while the scale of OLS errors decrease as fitted orientations steepen. OLS is also structurally unwilling to fit near-vertical data. When it is not rigorously known that errors occur only in the vertical plane, PCA provides more potential to reconstruct orientation data.

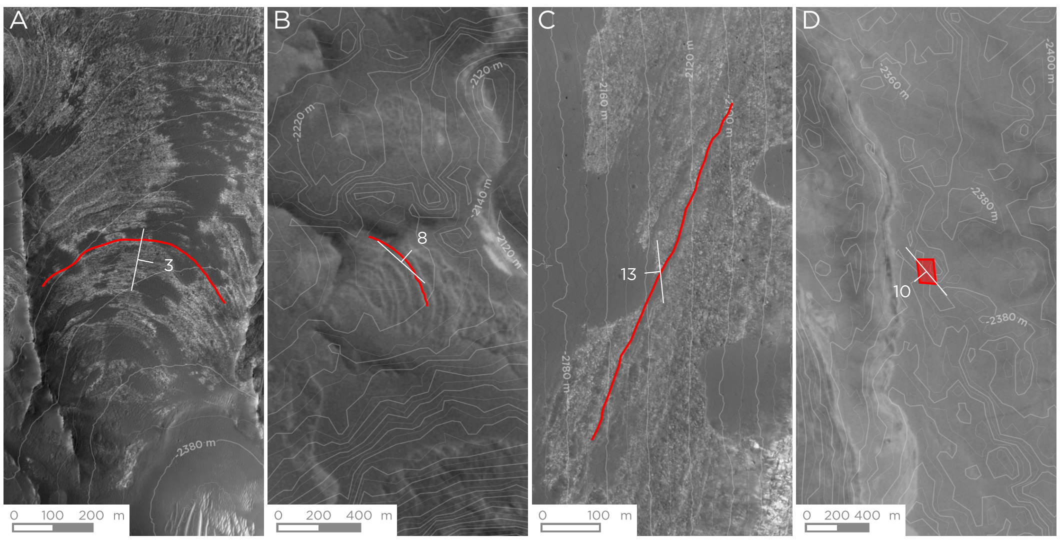

Figure 4.4: Context maps showing traced bedding planes (red) and nominal calculated bedding orientations for four orientation measurements in the NE Syrtis region of Mars. Imagery backdrop is HiRISE or CTX imagery, and 10 m contours derived from photogrammetry on the same dataset show the elevation data used to extract orientations. **(a)** a bedding exposure on a concave hillslope between two parallel raised ridges, atop a HiRISE image and elevation model. **(b)** A similar concave hillslope with slightly less 3D exposure, atop lower-resolution CTX data. **(c)** A linear bedding trace on a planar, west-facing hillslope. **(d)** A rectangular area of a dipping lava flow surface atop low-precision CTX topography.

Table 4.2: Data for orientation examples

n	L^1	R^2	Eigenvalues λ_1	λ_2	λ_3	Spherical summary (°) strike	dip	rake	θ_{min}	θ_{max}
Type examples [Table 4.1, Figures 4.5 and 4.6, ordered a-d]										
31	479	2.0	17228	422.9	0.82	311.7	7.6	81.5	0.59	3.88
546	584	1.1	21634	2079.3	0.11	11.3	3.5	172.7	0.15	0.48
593	615	2.4	31514	10.0	0.66	174.2	13.2	60.9	0.29	16.49
172	0	18.5	2163	948.1	73.74	139.6	10.1	119.2	13.17	19.92
Joint fitting of parallel planes [Figure 4.8]										
Well-constrained single-bed measurements										
476	507	0.7	16825	1437.8	0.09	9.3	3.5	9.9	0.15	0.51
546	584	1.1	21634	2079.3	0.11	11.3	3.5	172.7	0.15	0.48
Joint fit										
1217	–	1.3	6431	972.4	0.13	11.8	3.5	156.1	0.28	0.71
Components (ordered from north to south)										
315	332	0.5	8940	88.1	0.05	339.7	3.5	167.7	0.15	1.54
189	209	1.1	3544	14.1	0.09	38.3	6.7	112.5	0.34	5.43
367	389	0.9	12008	205.8	0.14	7.3	3.4	158.3	0.22	1.69
138	146	0.6	1746	5.7	0.06	358.1	6.1	70.7	0.43	7.69
208	217	0.3	3778	33.0	0.02	9.5	3.8	59.5	0.16	1.72

[1] L: length of bedding trace (m)
[2] R: maximum residual to plane (m)

Notation Matrices are uppercase and bold ($\mathbf{M}$), while vectors are lowercase and bold ($\mathbf{x}$). Vector components use upright characters (x_1) while scalar quantities are in script (n). The subscript i defines a range of indices over the dimensions of the coordinate basis $i = [1, 2, 3]$. Thus $\mathbf{x} = \mathrm{x}_i = [\mathrm{x}_1, \mathrm{x}_2, \mathrm{x}_3]$. When a vector component is given in subscript (e.g. σ_λ), its implicit i index is dropped. An index of all notation is contained in Table 4.3.

Finding principal components The original data matrix $\mathbf{D}$ is a $n \times 3$ matrix containing three-axis coordinates in a Cartesian coordinate system (commonly 3D geographical points in UTM or another local geodetic system). The centered data matrix $\mathbf{M}$ is centered

$$\mathbf{M} = \mathbf{D} - \boldsymbol{\mu}_\mathbf{D} \tag{4.1}$$

by subtraction of the mean along each axis.

PCA is formally described as an eigenvector decomposition of the sample covariance matrix $\mathbf{C}$, where

$$\mathbf{C} = \frac{1}{n-1}\mathbf{M}^\mathrm{T}\mathbf{M}, \tag{4.2}$$

the cross-product matrix of $\mathbf{M}$ scaled by the number of independent observations in the dataset. For our centered data, the decomposition is shown as

$$\mathbf{C} = \mathbf{V}\boldsymbol{\Lambda}\mathbf{V}^\mathrm{T} \tag{4.3}$$

where $\mathbf{V}$ is a rotation matrix composed of the eigenvectors and $\boldsymbol{\Lambda} = \boldsymbol{\lambda}\mathbf{I}$ is the diagonal matrix of eigenvalues of $\mathbf{C}$. These eigenvalues represent the variance of $\mathbf{M}$ along each eigenvector row of $\mathbf{V}$, denoted as $\mathbf{v}_i$.

Singular value decomposition, a more numerically stable technique to find the eigenvector decomposition of $\mathbf{C}$, is represented as

$$\mathbf{U}\,\mathbf{S}\,\mathbf{V}^\mathrm{T} = \mathbf{M}, \tag{4.4}$$

where $\mathbf{U}^\mathrm{T}\mathbf{U} = \mathbf{V}^\mathrm{T}\mathbf{V} = \mathbf{I}$ and $\mathbf{S}$ is a diagonal matrix of the singular values of the data matrix $\mathbf{M}$. The singular values are directly proportional to the eigenvalues of the data covariance matrix: $\boldsymbol{\Lambda} = \frac{1}{n-1}\mathbf{S}^2$. Expressed in scalar terms with $\mathbf{s} =$

Table 4.3: Summary of notation

Symbol	Meaning	
i	In subscript, represents component of 3D vector basis in 1-3	
n	Number of samples in data matrix	
$*$	In subscript, represents all n samples in data matrix.	
$\mathbf{x},\ \mathrm{x}_i$	Orthonormal basis vectors defining "world" coordinates	3×1
$\mathbf{D}$	Data matrix in "world" coordinates	$n \times 3$
$\boldsymbol{\mu}_{\mathbf{D}}$	Column-wise mean of data matrix	
Principal component analysis		
$\mathbf{M}$	Data matrix centered on all axes	$\mathbf{M} = \mathbf{D} - \mu_{\mathbf{D}}$
$\mathbf{C}$	Data covariance matrix for $\mathbf{M}$	$\mathbf{C}(n-1) = \mathbf{M}^{\mathrm{T}}\mathbf{M}$
$\boldsymbol{\lambda},\ \lambda_i$	Vector of eigenvalues of $\mathbf{M}$	
$\boldsymbol{\Lambda}$	Diagonal matrix of eigenvalues of $\mathbf{M}$	$\boldsymbol{\Lambda} = \mathbf{I}\,\boldsymbol{\lambda}$
$\mathbf{V}$	Rotation matrix of orthonormal eigenvectors	3×3
$\mathbf{v}_i$	Eigenvector rows making up $\mathbf{V}$	
$\mathbf{n}$	Normal vector to the best-fitting plane	$\mathbf{n} = \mathbf{v}_3$
$\overline{\mathbf{x}},\ \overline{\mathrm{x}}_i$	Orthonormal coordinate basis aligned with principal component axes $\mathbf{v}_i$	
$\overline{\mathbf{M}}$	Data matrix aligned with principal component axes	$\overline{\mathbf{M}} = \mathbf{M}\,\mathbf{V}^{\mathrm{T}}$
Singular value decomposition		
$\mathbf{U}$	Left singular vectors of $\mathbf{M}$	$n \times 3$
$\mathbf{S}$	Diagonal matrix of the singular values of $\mathbf{M}$	eigenvalues of $\mathbf{C}$
$\mathbf{s},\ \mathrm{s}_i$	Vector of singular values	$\mathbf{s} = \sqrt{\boldsymbol{\lambda}\,(n-1)}$
Statistical error analysis		
$\sigma_{\overline{\mathbf{M}}}$	Standard error of data matrix	$\sigma_{\overline{\mathbf{M}}} = \sqrt{\boldsymbol{\lambda}} = \frac{\mathbf{s}}{\sqrt{n-1}}$
$\sigma_{\boldsymbol{\lambda}}$	Standard error of the estimator	
d	Degrees of freedom of the estimator	$d = 2$ for angular error analysis
α	Confidence level for an error surface	$\alpha = 0.95$ is typical
$F_{\alpha,d,n-d}$	Fisher percent-point test statistic	
Construction of error surfaces		
$\mathbf{p}$	Parameters of the nominal plane in $\overline{\mathbf{x}}$	$\mathbf{p} = \boldsymbol{\lambda}$
$\mathbf{e}$	Errors to the nominal plane in $\overline{\mathbf{x}}$	$\mathbf{e} = F_{\alpha,d,n-d}\sigma_{\boldsymbol{\lambda}}$
$\mathbf{h}$	Semimajor axes of hyperbolic quadric defining an error surface	$\mathbf{h} = \mathbf{p} + \mathbf{e}$
$\mathbf{Q}$	5×5 matrix representation of a quadric surface	*as defined in text*
$\overline{\mathbf{Q}}_{\mathbf{H}}$	Tensor representation of a hyperbolic error quadric for semiaxes $\mathbf{h}$	
$\mathbf{T}$	An affine or projective transformation matrix	*as defined in text*
$\mathbf{C}$	4×4 matrix representation of conic section	*as defined in text*
Spherical errors		
γ	Angle in $[0, 2\pi]$ from $\overline{\mathrm{x}}_1$ within $\overline{\mathrm{x}}_{1,2}$ plane	
$\overline{\mathbf{x}}_\gamma$	2D coordinate basis orthogonal to nominal plane, defined by $\overline{\mathrm{x}}_\gamma, \overline{\mathrm{x}}_3$	
θ_γ	Angular error for an arbitrary direction within the plane	
$\theta_{\max},\ \theta_{\min}$	Maximum and minimum angular errors at $\gamma_{\min} = 0, \gamma_{\max} = \frac{\pi}{2}$	

trace $(\mathbf{S})$, this is equivalent to

$$\boldsymbol{\lambda} = \frac{\mathbf{s}^2}{n-1}. \tag{4.5}$$

Rotation into a principal-component aligned frame Geometrically, PCA corresponds to rotation of the dataset into a decorrelated reference frame. The rotation matrix $\mathbf{V}$ operates on the covariance matrix $\mathbf{C}$ to eliminate cross-correlations between components, defining a new coordinate basis aligned with the directions of maximum variability of the dataset. This rotated orthonormal coordinate basis, $\overline{\mathbf{x}}$, is aligned with the axes of $\mathbf{V}$ [Figure 4.1]. An arbitrary vector $\mathbf{a}$ in the global Cartesian plane can be rotated into this coordinate system using $\overline{\mathbf{a}} = \mathbf{a}\,\mathbf{V}^{\mathrm{T}}$.

Rotation of data into a principal-component aligned coordinate basis significantly eases error analysis and visualization of the structure of the dataset relative to its best-fitting plane. The "axis-aligned" projection of the input dataset $\overline{\mathbf{M}}$, defined as $\overline{\mathbf{M}} = \mathbf{M}\mathbf{V}^{\mathrm{T}}$, collapses the dataset onto its best-fitting plane. Inverting Equation 4.3, the sample covariance matrix $\mathbf{C}$ can be expressed in this coordinate system as

$$\overline{\mathbf{C}} = \boldsymbol{\Lambda} = \boldsymbol{\lambda}\mathbf{I} = \mathbf{V}^{\mathrm{T}}\mathbf{C}\mathbf{V}. \tag{4.6}$$

The rotated dataset $\overline{\mathbf{M}}$ varies independently along each axis of $\overline{\mathbf{x}}$, and the magnitude of the eigenvalues $\boldsymbol{\lambda}$ of the PCA fit is proportional to the scale of the dataset along each principal component axis. The eigenvalues are equivalent to the three-component vector variance of the decorrelated data along each axis of $\overline{\mathbf{x}}$:

$$\boldsymbol{\lambda} = \boldsymbol{\sigma}^2_{\overline{\mathbf{M}}}. \tag{4.7}$$

The axes $\overline{\mathbf{x}}_1$ and $\overline{\mathbf{x}}_2$ fall within the best-fitting plane through the dataset, and $\overline{\mathbf{x}}_3$ is along the normal to the plane. Scatter along this axis represents the error in the planar fit. Thus, the third column of the aligned data matrix, $\overline{\mathbf{M}}_{*,3}$, represents residuals from the nominal planar fit. Rotation of the dataset into $\overline{\mathbf{x}}$ provides a useful means to understand the distribution of residuals and potential nonrandom structure relative to the best-fitting plane. Plotting $\overline{\mathbf{M}}_{*,1}$ vs. $\overline{\mathbf{M}}_{*,2}$ yields a plan view of the dataset, and $\overline{\mathbf{M}}_{*,i}$ vs. $\overline{\mathbf{M}}_{*,3}$ for $i = 1, 2$ shows residuals [Figure 4.5].

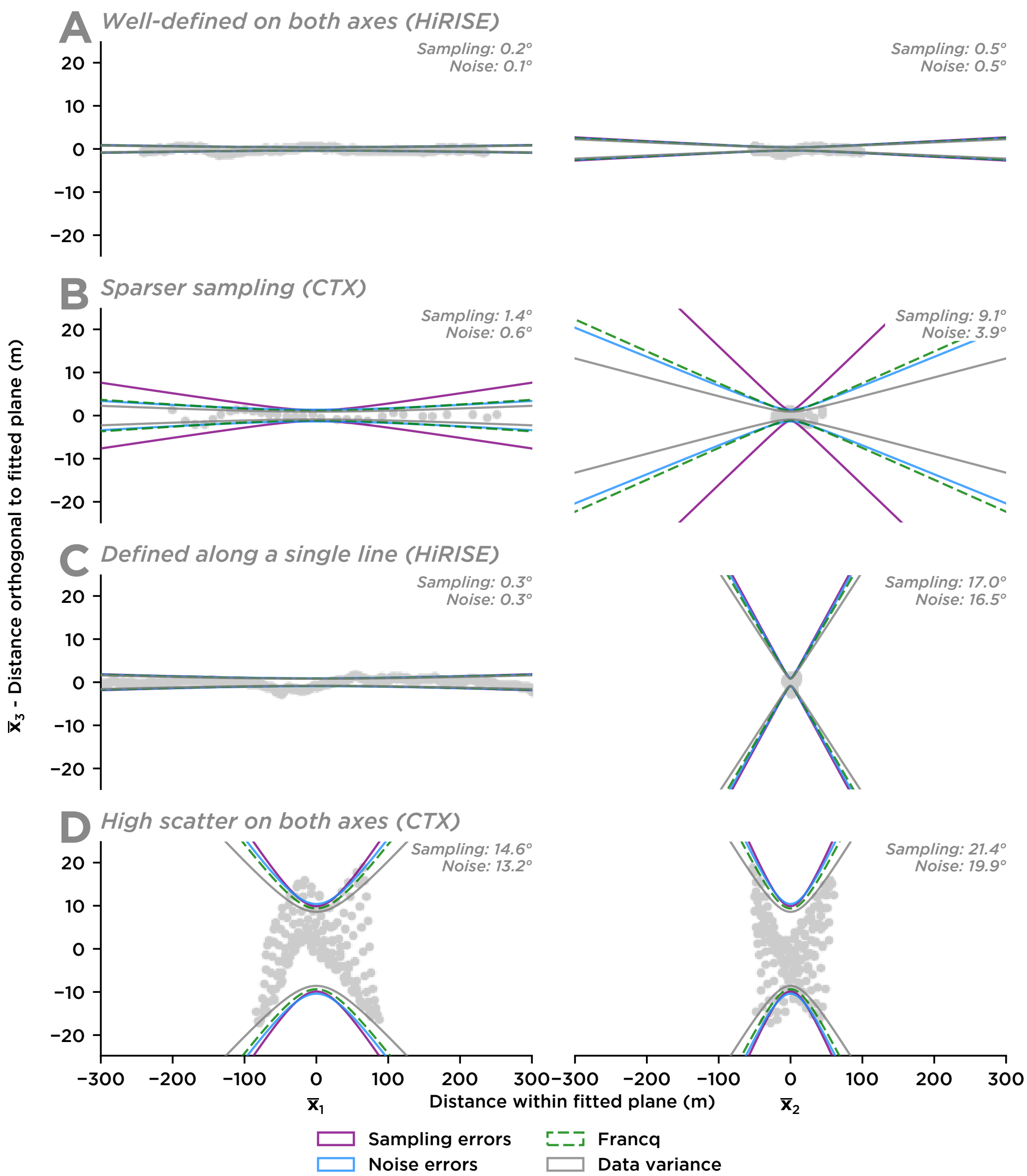

Figure 4.5: The Cartesian error space of fitted orientation measurements corresponding to example bedding traces [Figure 4.4]. Each plane is decomposed into two views aligned with $\overline{\mathbf{x}}$, with in-plane variation shown on the horizontal axis and out-of-plane variation on the vertical. The data making up the planar measurement is shown as grey points, and hyperbolic error bounds computed by several methods are overlain. Angular errors are not to scale. Each fitted plane has a distinct error structure depending on the characteristics of the input point cloud. **(a)** A well-fitted plane with low errors on all axes. **(b)** A slightly poorer fit with minimal definition along $\overline{\mathbf{x}}_2$. **(c)** A plane well-defined along $\overline{\mathbf{x}}_1$ but essentially undefined along $\overline{\mathbf{x}}_2$. **(d)** A fit poorly defined on both axes.

Strike and dip of the nominal plane The first and second eigenvector rows of $\mathbf{V}$ describe the planar fit in the absence of errors. The third eigenvector row of $\mathbf{V}$ is orthogonal to the plane; this normal vector $\mathbf{n} = \mathbf{v}_3$ can be used with the mean of the dataset $\boldsymbol{\mu}_\mathbf{D}$ (which the regression passes through by definition), to form an equation for the plane

$$\mathbf{n}\,\mathbf{X} + \mathbf{n} \cdot \boldsymbol{\mu}_\mathbf{D} = 0, \tag{4.8}$$

where $\mathbf{X}$ is a set of points within the plane. The nominal strike and dip in a geographic framework (*strike* defined relative to north) are calculated as follows:

$$(\textit{strike}, \textit{dip}) = \left(\tan^{-1}\frac{\mathrm{n}_1}{\mathrm{n}_2} - \frac{\pi}{2},\ \cos^{-1}\frac{\mathrm{n}_3}{\|\mathbf{n}\|}\right) \tag{4.9}$$

4.3.3 Confidence intervals for planar orientations

Errors to a planar measurements arise from statistical uncertainties on the parameters of a planar fit, and accurate modeling of errors requires the incorporation of a statistical distribution that is responsive to variation in input data quality. Given the formal relationship between PCA and OLS, we show that λ can be treated analogously to the OLS fit parameters $\hat{\beta}$ to define the error space to the plane, which can be represented as a hyperbolic error shell $\mathbf{h}$. Dataset orientation errors are scaled by the Fisher (F) statistical distribution to produce standardized orientation errors.

Eigenvectors as regression parameters The statistical basis for PCA regression errors can be developed from the widely-used OLS regression. The closed-form equation for OLS is given by

$$\hat{\beta}_{\mathrm{OLS}} = (\mathbf{X}^\mathrm{T}\mathbf{X})^{-1}\mathbf{X}^\mathrm{T}\mathbf{y} \tag{4.10}$$

where $\mathbf{X}$ is a matrix of explanatory variables (a $n \times 2$ matrix for 3D data), and $\mathbf{y}$ is a column vector of dependent variables. Errors to the regression coefficients $\hat{\beta}$ can be estimated using the variance of these parameters.

$$\operatorname{var}\left(\hat{\beta}_{\mathrm{OLS}}\right) = \sigma^2(\mathbf{X}^\mathrm{T}\mathbf{X})^{-1}, \tag{4.11}$$

where σ^2 is the mean squared error of the residuals to the fit.

Expressing the result of the PCA transformation in $\overline{\mathbf{x}}$ creates a degenerate case which is directly comparable to OLS and allows an equivalent construction of fit errors. Errors to PCA are by definition oriented along $\overline{\mathbf{x}}_3$, aligned with the vertical uniaxial errors assumed by OLS. In this framework, the regression parameters $\hat{\beta}$ can be recast as orthogonal slopes aligned with x_1 and x_2. The inputs to PCA can also be modified to conform to the notation used OLS: for a mean-centered point cloud, $\mathbf{M} = [\mathbf{X}\ \mathbf{y}]$, and the components of the fit can be represented as subspaces of the covariance matrix [Equation 4.2], where n is the number of data points:

$$\mathbf{C}(n-1) = \mathbf{M}^{\mathrm{T}}\mathbf{M} = \begin{bmatrix} \mathbf{X}^{\mathrm{T}}\mathbf{X} & \mathbf{X}^{\mathrm{T}}\mathbf{y} \\ \mathbf{y}^{\mathrm{T}}\mathbf{X} & \mathbf{y}^{\mathrm{T}}\mathbf{y} \end{bmatrix}_{3\times 3}. \tag{4.12}$$

In aligned coordinates, $\overline{\mathbf{M}}^{\mathrm{T}}\overline{\mathbf{M}} = \mathbf{\Lambda}(n-1)$; since $\mathbf{\Lambda}$ is a diagonal matrix, $\mathbf{X}^{\mathrm{T}}\mathbf{y}$ reduces to $[0,0]^{\mathrm{T}}$ because it is off the diagonal. In $\overline{\mathbf{x}}$ aligned with the PCA fit, the regression parameters $\hat{\beta}_{\text{PCA}} = [0,0]$ by definition. However, the variance of these parameters can illuminate the error structure to the planar fit. The variance of the regression parameters $\operatorname{var}\left(\hat{\beta}_{\text{PCA}}\right)$ can be modeled by substitution for $\mathbf{X}^{\mathrm{T}}\mathbf{X}$, yielding

$$\operatorname{var}\left(\hat{\beta}_{\text{PCA}}\right) = \sigma^2 \begin{bmatrix} \lambda_1(n-1) & 0 \\ 0 & \lambda_2(n-1) \end{bmatrix}^{-1}. \tag{4.13}$$

Substituting $\sigma^2 = \lambda_3$, this reduces to

$$\operatorname{var}\hat{\beta} = \begin{bmatrix} \frac{\lambda_3}{\lambda_1} & \frac{\lambda_3}{\lambda_2} \end{bmatrix}. \tag{4.14}$$

Even though "regression parameters" are a poor conceptual fit for PCA, regression errors are equivalent to a ratio of PCA eigenvalues.

This parallel can be extended to the statistical definition of errors. In OLS, $\operatorname{var}\hat{\beta}$ captures regression errors specific to the sample measured. This "sample parameter" is a maximum-likelihood estimator of the errors to the true population fit parameter, $\operatorname{var}\beta$, which can be parameterized as $\operatorname{var}\hat{\beta} + \operatorname{error}\left(\operatorname{var}\hat{\beta}\right)$ (**?**). This error adds a statistical distribution to abstract the sample size and degrees of freedom in the input dataset, creating errors that can be compared between measurements.

For PCA, the eigenvalues λ_i that represent the dataset are equivalent to the sample variance of the dataset along each major axis [Equation 4.7], and the population variance along each axis is equivalent to $\lambda_i + \text{error}\,(\operatorname{var}\lambda_i)$. Since PCA eigenvectors are orthogonal, their eigenvectors are statistically independent (**?**, p. 46) and can be straightforwardly ratioed. Extending Equation 4.14, statistical errors to the planar estimator can be expressed as a ratio of uncertain eigenvalues:

$$\operatorname{var}\beta_{\text{PCA}} = \begin{bmatrix} \frac{\lambda_3+\text{error}(\lambda_3)}{\lambda_1+\text{error}(\lambda_1)} & \frac{\lambda_3+\text{error}(\lambda_3)}{\lambda_2+\text{error}(\lambda_2)} \end{bmatrix}. \tag{4.15}$$

Although errors parameterized as slopes are directly comparable to OLS errors, the orthogonality of PCA allows the direct representation of regression error as a hyperbolic surface [Figure 4.2], which can be manipulated with vector and tensor algebra, increasing flexibility for data visualization [Section 4.3.4]. The two orthogonal slopes that make up $\operatorname{var}\beta_{\text{PCA}}$ are equivalent to tangents to an elliptic hyperboloid on two orthogonal axes aligned with the PCA fit. This error hyperboloid has semimajor axes defined by

$$\mathbf{h} = \boldsymbol{\lambda} + \text{error}\,(\boldsymbol{\lambda})\,. \tag{4.16}$$

This equation can also be parameterized as

$$\mathbf{h} = \mathbf{p} \pm \mathbf{e}, \tag{4.17}$$

with $\mathbf{p} = \boldsymbol{\lambda}$ representing the nominal plane parameters and $\mathbf{e} = \text{error}\,(\boldsymbol{\lambda})$ representing errors to each eigenvalue. $\mathbf{p}$, $\mathbf{e}$, and $\mathbf{h}$ are vectors with components along each axis in $\overline{\mathbf{x}}$. Below, we discuss formulations $\mathbf{p}$ and $\mathbf{e}$ used to construct the hyperbolic axes $\mathbf{h}$.

Regression error limited by data variance All regression fits must pass through the mean of the dataset, but the statistical definition of the central limit has important implications for the structure of planar orientation errors. The equivalence asserted between OLS variance and λ_3 [Equation 4.14] and carried through our

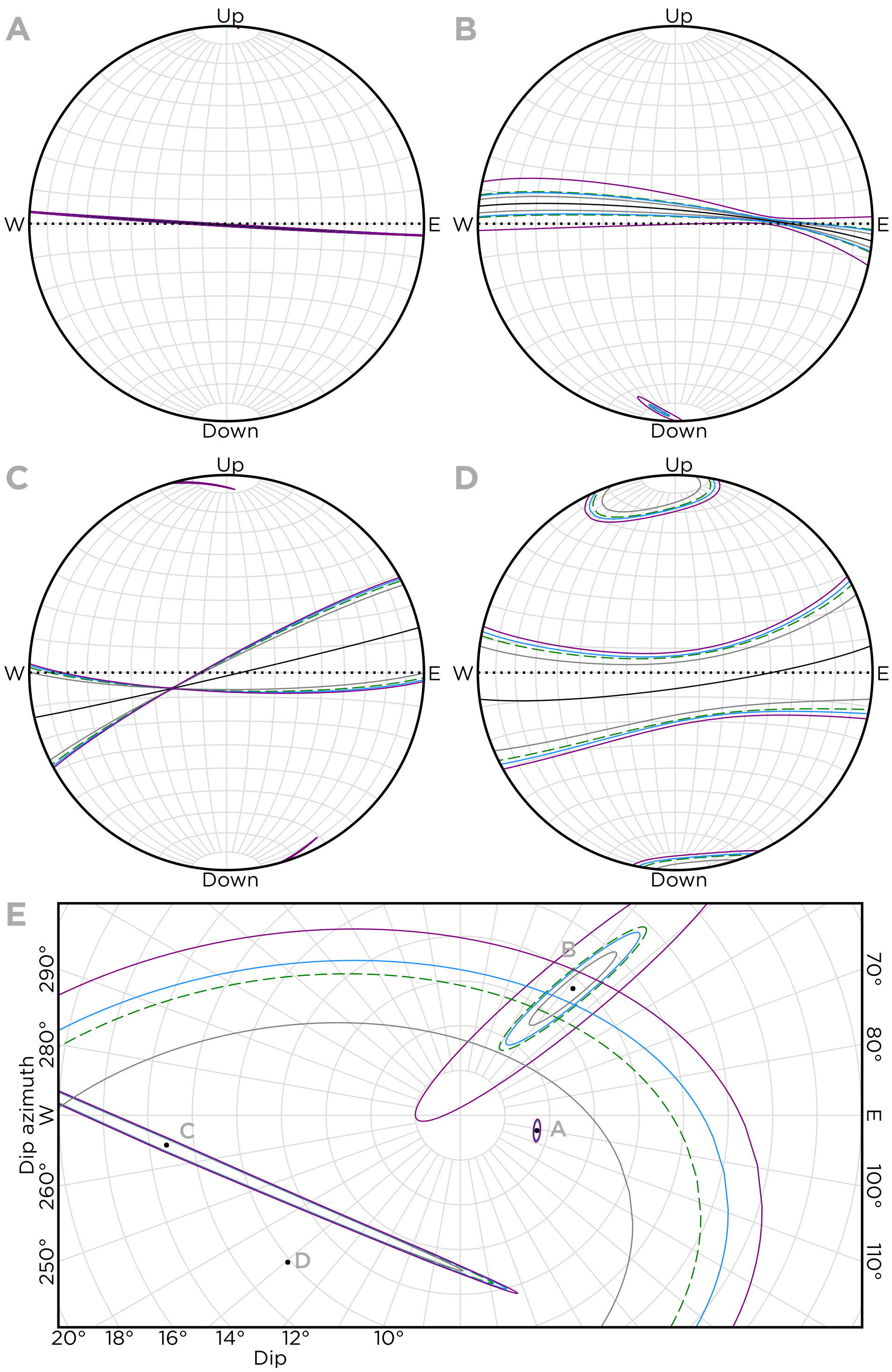

Figure 4.6: Projection of the hyperbolic errors to the plane into spherical coordinates to show angular errors. Estimates by different methods for computing **h** are colored as in Figure 4.5. **(a-d)** Spherical error space for each of the planes shown in Figure 4.5, projected onto oblique upper-hemisphere, equal area stereonets. **(e)** Error space to the bedding pole for each of the planes in panels *a-d*.

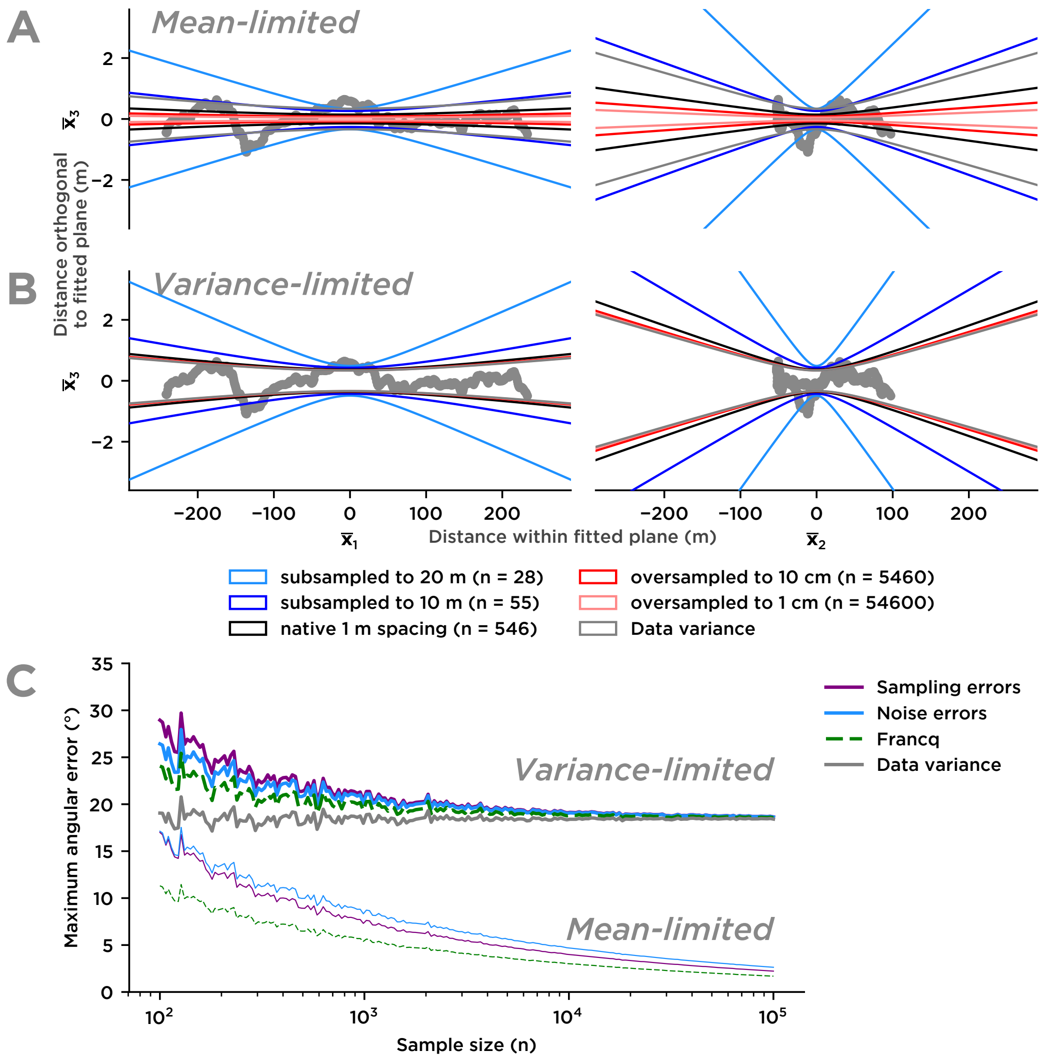

Figure 4.7: Exploration of centroid behavior with sample size. **(a)** Standard regression statistics applied to the "noise variance" method, with errors scaled to the quality of estimate of the mean. **(b)** Variance-limited regression modeling all points as estimates of a single true plane. This procedure is more resistant to dependence of error scaling on sample size. **(c)** Exploration of variance with sample size for a randomly generated plane with axial lengths $\mathbf{h} = [100, 10, 5]$, using several methods for variance estimation. All methods have errors that trend to 0 at large sample sizes when the dataset centroid is estimated by the mean.

definition of $\mathbf{p} = \boldsymbol{\lambda}$ [Equation 4.17] departs from standard regression statistics, with major effects on the modeled error structure of planes.

In standard regression statistics, the best-fitting plane is modeled as passing through the *mean* of the dataset, which is known with more precision as sample size increases. This "mean-limited" construction is tailored to modeling potential correlations between variables.

For fitting geological planes, all data points should be treated as estimates of the *true value* of a single plane. In this formulation of regression error, a high-quality fitted plane is defined by low variance, rather than well-known variance. This "variance-limited" framework explicitly models departures from a single plane, rather than the strength of correlations between scattered data.

The definition of the dataset centroid significantly alters the error structure on the out-of-plane axis $\overline{\mathbf{x}}_3$. For mean-limited scaling, λ_3 is not considered a regression error, and $\mathbf{p} = [\lambda_1,\ \lambda_2,\ 0]$. Since the standard error of the mean of a dataset is equivalent to the error of the variance, error (λ_3) represents the out-of-plane error and $\mathbf{e}$ is equivalent in both frameworks.

Mean-limited statistics significantly underestimate angular certainty in cases with large sample sizes [Figure 4.7a], complicating comparisons of measurements with different sampling characteristics. This is particularly relevant to fitting geologic planes, because spatial data from sensors can be at different spatial resolutions, or smoothed in a fashion that boosts sampling without changing the fundamental error structure.

In variance-limited statistics, data variance along $\overline{\mathbf{x}}_3$ sets a floor for errors to the plane. This parameterization of errors penalizes large departures from an idealized plane and preserves the basic structure of angular errors regardless of data density [Figure 4.7b]. This feature is crucial for comparing planes with different sampling characteristics. Most "off-the-shelf" packages for planar fitting use standard mean-centered statistics, suggesting that measurements made using these packages may be fundamentally biased by sample size effects.

Errors to eigenvectors To move from the decomposed variance of the dataset exposed by PCA to a statistically-based error distribution around a planar fit, we define $\mathbf{e}$ in terms of the certainty of the eigenvalues as such:

$$\mathbf{e} = \text{error}\,(\boldsymbol{\lambda}) = F_{\alpha,d,n-d}\,\sigma_{\boldsymbol{\lambda}}, \tag{4.18}$$

where F is the Fisher distribution statistic for $\alpha = 0.95$, $d = 2$, and the number of samples in the dataset (n). The statistical distribution incorporates the number of samples in the dataset (n) and the degrees of freedom of the statistical transformation (d). Several choices exist for the definition of $\sigma_{\boldsymbol{\lambda}}$, which we summarize below. Results for the four type cases are shown in Figure 4.5.

Data variance The most basic parametrization of orientation errors uses variance of the input dataset (i.e. eigenvalues) alone to represent the error space without $\sigma_{\boldsymbol{\lambda}}$, resulting simply in $\mathbf{h} = \mathbf{p} = \boldsymbol{\lambda}$. The data variance defines the basic structure of the plane, including its scaling based on out-of plane residuals [Section 4.3.3] and the directional dependence of fit quality. However, the lack of a statistical treatment of the accuracy of variance makes this method unresponsive to undersampling or differently-scaled datasets.

The data variance parameterization of orientation errors is developed in the paleomagnetism literature, where uncertain lines and planes model magnetometer response during laboratory measurements of rock remnant magnetism. These techniques treat the variance of the dataset (decomposed along its major axes by PCA) as a measure of fit quality for visualization and automated data-reduction pipelines (e.g. **?**). This literature describes the parameterization of the PCA fit as an ellipsoid (the "dual" quadric to the hyperbola enclosing the plane; see Appendix) with different potential shapes depending on dataset structure [Table 4.1, adapted from **?**].

Sampling variance The simplest method of statistically-based error scaling uses multivariate statistics based on sample size. In this framework, errors assume that the measured data is a random sampling of a population that conforms to a Gaussian distribution. The expression for variance of the eigenvectors for PCA,

$$\sigma_{\boldsymbol{\lambda}}^2 = \frac{2\boldsymbol{\lambda}^2}{n-1}, \tag{4.19}$$

arises directly from the estimation of population variance in sampling statistics (**?**, p. 48; **?**).

Noise variance The standard assumption of Gaussian population statistics, that the variance of the sample is primarily a function of its size, may be imperfect when applied to continuously sampled data. Datasets that include all of the available data over an interval (i.e. aren't random samples of a population) are implicitly highly correlated. In this situation, sample-size based statistics may be misleading. Interpolated elevation data can easily be smoothed and overfitted, increasing apparent statistical power with little to no improvement in the quality of the fit. Conversely, when the noise in the input dataset is low, even small samples can show significant results. The noise variance framework for PCA errors (**????**) is explicitly designed for use with continuously sampled data.

Instead of uniformly scaling errors along a given principal component axis $\overline{\mathbf{x}}_i$ with the singular values along that axis, noise covariance is based on the intuition that "measurement noise" defined along higher-dimensional axes provides a good estimate of the errors on all axes. In our case, scatter along $\overline{\mathbf{x}}_3$ is the "noise component" of the data, and may provide a better estimate of the scatter in $\overline{\mathbf{x}}_1$ and $\overline{\mathbf{x}}_2$ that the variance along these axes. Intuitively, the structure of the data cloud within the best-fitting plane is an artifact of digitization with no bearing on accuracy.

? shows that the variance of the PCA eigenvectors can be modeled as

$$\sigma^2_{\boldsymbol{\lambda}} = 4\,\boldsymbol{\lambda}\,\sigma^2_{\hat{\mathbf{M}}}, \tag{4.20}$$

where $\sigma^2_{\hat{\mathbf{M}}}$ is the "noise variance" of the data matrix. Methods to compute the noise variance $\sigma^2_{\hat{\mathbf{M}}}$ rely on the concept of "pseudorank", the rank of the aligned data matrix in the absence of noise. Detailed treatments of the noise variance framework (**??**) discuss adjustment of the pseudorank to incorporate nonlinear bias, but this is unnecessary for our low-dimensional case. For three-dimensional data aligned along a plane, errors will be entirely contained in scatter on $\overline{\mathbf{x}}_3$. A plane without noise will be contained in the $\overline{\mathbf{x}}_1$–$\overline{\mathbf{x}_2}$ plane, with a pseudorank of $K = 2$.

? describes the "real error" component

$$\sigma^2_{\hat{\mathbf{M}}} = \frac{\sum\limits_{p=K+1}^{c} \lambda_p}{r\,(c-K)} \tag{4.21}$$

where $r \times c$ is the dimensions of the data matrix $\mathbf{M}$. **?** slightly modifies this to

$$\sigma^2_{\hat{\mathbf{M}}} = \frac{\sum\limits_{p=K+1}^{c} \lambda_p}{(r-K)(c-K)} \tag{4.22}$$

based on experimental validation. For our purposes of planar fitting, $K = 2$, $r = n$, and $c = 3$, and these expressions collapse to $\sigma^2_{\hat{\mathbf{M}}} = \frac{\lambda_3}{n}$ (**?**) and $\sigma^2_{\hat{\mathbf{M}}} = \frac{\lambda_3}{n-2}$ (**?**). With sample sizes $n \gg K$, the difference between these estimators is negligible. Combining Equation 4.20 with Equation 4.22, we can express the noise variance of the dataset as

$$\sigma^2_{\boldsymbol{\lambda}} = \frac{4\,\boldsymbol{\lambda}\,\lambda_3}{n-2}. \tag{4.23}$$

Other statistical distributions Several other treatments of errors given in the literature provide direct alternatives for scaling $\mathbf{e}$ with different statistical assumptions. **?** provides a formulation of error bars for two-axis OLS, which can be generalized to the PCA framework, yielding error axes

$$\mathbf{e} = \boldsymbol{\lambda}\sqrt{\frac{2}{n-2}F_{\alpha,d,n-d}}. \tag{4.24}$$

This formulation provides slightly more constrained errors than both sampling and noise-based errors, due to the co-dependence of errors of variables defined in global Cartesian coordinates. **?** provides an implementation that closely tracks the "sampling variance" method with slightly different scaling for sample sizes. **?** describes a numerical method which applies OLS regression after PCA rotation, using the slope found by OLS in $\overline{\mathbf{x}}$ to estimate var β_{PCA}.

Choice of $\sigma_{\boldsymbol{\lambda}}$ or $\mathbf{e}$ The effect of using different test statistics is minimal for well-sampled data, and results asymptotically converge on the data variance at large sample sizes [Figure 4.5 and Figure 4.6]. The formulations tested show similar results, but the "noise error" is more resistant to changes in sample density [Figure 4.5c and d]. We use the noise error as the preferred scaling in software and graphical implementations of this method.

Statistical error scaling To create confidence intervals, we apply a Fisher $\left(F_{\alpha,d,n-d}\right)$ statistical distribution to $\sigma_{\boldsymbol{\lambda}}$ using Equation 4.18 with the $\sigma_{\boldsymbol{\lambda}}$ formulation in Equation 4.23. The eigenvalues of the dataset follow the $\chi^2_{\alpha,d}$ distribution. Since regression parameters are composed of ratios of eigenvalues [Equation 4.14], the appropriate test statistic for orientation data is the Fisher distribution, $F_{\alpha,d,n-d}$, which models ratios of χ^2-distributed parameters (**???**). At large sample sizes, $lim_{n\to\infty} F_{\alpha,d,n-d} = \frac{1}{d}\chi^2_{\alpha,d}$. For planar orientations, $d = 2$, since the orientation information contained in the three eigenvectors can be summarized as two ratios. The remaining parameter, α, is the confidence level at which the distribution should be queried. For typical analysis, $\alpha = 0.95$, corresponding to a 95% confidence interval, should suffice.

The resulting parameterization of the errors to the eigenvectors is summarized as

$$\mathbf{e}_{\boldsymbol{\lambda}} = F_{\alpha,d,n-d}\boldsymbol{\sigma}_{\boldsymbol{\lambda}}. \tag{4.25}$$

Thus, for noise errors,

$$\mathbf{e}_{\boldsymbol{\lambda}} = F_{\alpha,d,n-d}\sqrt{\frac{2\boldsymbol{\lambda}}{n-2}}\lambda_3. \tag{4.26}$$

Since the dataset variance itself is a source of error, $\mathbf{e} = \lambda_3 + \mathbf{e}_{\boldsymbol{\lambda}}$. To construct the hyperbolic error space of the plane, we recall that $\mathbf{h} = \mathbf{p} \pm \mathbf{e}$ [Equation 4.17]. At any level of error, the maximum bounding surface of $\mathbf{h}$ occurs when the length of in-plane axes of the hyperboloid are minimized and out-of-plane error is maximized. Thus, the maximum error shell used for visualization is

$$\mathbf{h}_* = [\lambda_1 - \mathrm{e}_1,\ \lambda_2 - \mathrm{e}_2,\ \lambda_1 + \mathrm{e}_3], \tag{4.27}$$

or alternatively

$$\mathbf{h} = \boldsymbol{\lambda} + \mathbf{a}F_{\alpha,d,n-d}\boldsymbol{\sigma}_{\boldsymbol{\lambda}}, \tag{4.28}$$

where $\mathbf{a} = [-1, -1, 1]$ denotes whether errors are subtracted or added along that axis to form the maximum error surface.

4.3.4 Displaying orientation error surfaces

Armed with a statistical framework for the errors to planar measurements, we turn to methods to display these errors graphically in Cartesian and spherical coordinates, represented schematically in Figure 4.2. Projections of error bounds as 2D hyperbolic slices and spherical ellipses and girdles provide useful visualizations of the error structure of the plane. These visualization techniques rely only on the statistically derived hyperboloid with semiaxes $\mathbf{h}$ which represents the uncertain plane, independent of the statistical assumptions used in its construction. In principle, the mechanisms for plotting error distributions apply equivalently to planes regressed using OLS, but the orthogonality of PCA errors to the regression line results in simpler linear algebra. Generalized equations for quadric surfaces that can be manipulated with transformation matrices and quaternion rotations are discussed in the Appendix; here we focus on common cases used to develop key visualizations of the error space.

Projection to hyperbolic errors Two-dimensional conic slices of the hyperbolic error space of the plane summarize dataset structure in PCA-aligned coordinates or projected into real space. Errors can assessed along any axis, but slices of the error hyperboloid aligned with the major axes of the planar fit are the most intuitive. These "axis-aligned" views of the dataset, with in-plane variation on the horizontal axis and out-of-plane variation on the vertical, are the ideal decomposition to assess the structure of a fitted dataset and verify the quality of the input data $\mathbf{D}$. Visual inspection of dataset quality in PCA-aligned coordinates [Figure 4.5] is an important quality check on measured orientations. The measurements shown in Figure 4.5b and d both show significant out-of-plane variation potentially related to both DEM errors and digitizing errors.

A hyperbola can by constructed for a two-dimensional slice of the error quadric, along a coordinate basis $\overline{\mathbf{x}}_\gamma = [\overline{\mathrm{x}}_\gamma, \overline{\mathrm{x}}_3]$ with axis $\overline{\mathrm{x}}_\gamma$ within the plane defined as a linear combination of $\overline{\mathrm{x}}_1$ and $\overline{\mathrm{x}}_2$ as

$$\overline{\mathrm{x}}_\gamma = \sqrt{\overline{\mathrm{x}}_1 \cos^2\gamma + \overline{\mathrm{x}}_2 \sin^2\gamma}, \tag{4.29}$$

where $\gamma = [0, 2\pi]$ is the angle from $\overline{\mathrm{x}}_1$ within the plane. In this set of coordinates, h_γ can be defined a major axis to the 2D conic,

$$\mathrm{h}_\gamma = \sqrt{\mathrm{h}_1 \cos^2\gamma + \mathrm{h}_2 \sin^2\gamma}, \tag{4.30}$$

the radius of an ellipse defined by major axes h_1 and h_2 within the best-fitting plane. The axis-aligned hyperbolic slice of the hyperbolic error quadric can be represented as

$$\mathbf{C} = \mathrm{diag}\left(\frac{1}{\mathrm{h}_\gamma^2}, -\frac{1}{\mathrm{h}_3^2}, 1\right). \tag{4.31}$$

For a slice of the plane oriented along $\frac{1}{\mathrm{h}_1^2}$, $\gamma = 0$ and $\mathbf{h}_\gamma = [\mathrm{h}_1, \mathrm{h}_3]$. For an axis-aligned and mean-centered conic, the hyperbolic error bounds in are given by the equivalent representations

$$\overline{\mathrm{x}}_3 = \pm\mathrm{h}_3 \cosh\left(\sinh^{-1}\left(\frac{\overline{\mathrm{x}}_\gamma}{\mathrm{h}_\gamma}\right)\right) = \pm\mathrm{h}_3 \sqrt{\left(\frac{\overline{\mathrm{x}}_\gamma}{\mathrm{h}_\gamma}\right)^2 + 1}. \tag{4.32}$$

These error bars can be plotted as-is (e.g. Figure 4.5) or shifted from $\overline{\mathbf{x}}_\gamma$ to $\mathbf{x}$ using scaling and rotation as necessary. We discuss this more general transformation in the Appendix.

Spherical representation of errors The discussion and display of orientation errors has thus far been carried out in a Cartesian reference frame, but it is useful to represent uncertain planar fits in an angular framework. This allows plotting on stereonets and direct comparison to other orientation data.

For our rotational construction, given any in-plane axis h_γ, the angular errors from the nominal plane are defined by tangents to the hyperbolic error sheets,

$$\theta_\gamma = 2\tan^{-1}\left(\mathrm{h}_3/\mathrm{h}_\gamma\right), \tag{4.33}$$

the factor of 2 arising from combining errors for both the upper and lower sheets of the hyperboloid. Solving this for $\gamma = [0, 2\pi]$ yields a girdle of angular error magnitudes relative to the great circle defining the nominal plane. The resulting distribution is a graphical representation of angular errors for all directions of the planar fit [Figure 4.6].

The angular error surfaces for the normal vector fall 90° from those representing the plane, forming an elliptical error space encompassing poles to the plane. Normal vector errors can be can be computed by a similar process to that used to generate a hyperbolic girdle around the plane, using the inverse of the tangents.

$$\mathrm{a}_\gamma = \tan^{-1}\left(\mathrm{h}_\gamma/\mathrm{h}_3\right) \tag{4.34}$$

evaluated over $\gamma = [0, 2\pi]$ defines the angular dimension of an error ellipse in spherical coordinates, defined relative to $\overline{\mathbf{x}}_3$. This ellipse can be rotated into global coordinates using the rotation matrix $\mathbf{V}$. A more general solution is discussed in Section 4.A.2.

Maximum and minimum angular errors The best numerical summary of errors to an orientation measurement are the maximum and minimum angular errors, which are defined orthogonal to the plane and aligned with the major axes of the best-fitting plane. This concept can be applied to statistically derived error surfaces as well, given a set of axial lengths calculated by one of the methods above. For the semiaxes $\mathbf{h}$ corresponding to errors at a particular level,

$$(\theta_{\mathrm{max}},\, \theta_{\mathrm{min}}) = \left(2\tan^{-1}(\mathrm{h}_3/\mathrm{h}_2)\,,\; 2\tan^{-1}(\mathrm{h}_3/\mathrm{h}_1)\right) \tag{4.35}$$

provides the angular width of the error distribution aligned with the major axes of the dataset. This allows errors to be reported in angular space, though their statistical development is undertaken entirely in Cartesian space. Because of the nonlinearity associated with angular transformations, there is no natural correspondence between the dip direction of a best-fitting plane and the direction of θ_{max}. To form a full representation of the errors, we must also report the azimuth of the error axis within the plane. This *rake* angle [Table 4.2] is defined as the angle between the strike and θ_{max} (which is oriented along $\overline{\mathbf{x}}_2$) , calculated as

$$\mathit{rake} = \cos\left((\mathbf{v}_3 \times \mathbf{z}) \cdot \mathbf{v}_2\right), \tag{4.36}$$

where $\mathbf{z} = [0, 0, 1]$ is a vertical vector.

4.3.5 Joint fitting of parallel bedding planes

A common problem for remote sensing of geologically relevant areas is lack of continuous exposure, and planes that are unconstrained in one dimension are common [Figure 4.4]. However, exposures of bedding in close spatial association often capture slightly different cuts of topography with different orientation error structures. This is statistically useful: under the assumption of parallel bedding, multiple bedding traces can be jointly fitted to increase the three-dimensional definition of a planar dataset. Error metrics computed after fitting can be used to test the validity of this assumption.

In Figure 4.8, several bedding traces digitized on opposing hillslopes in the same cuesta show different error structures. Bedding traces that could be followed around the entire range of hillslope aspect have much more restricted error spaces. Grouping of the low-quality planar fits creates a much higher-precision joint measurement at the intersection of the error spaces of individual beds, showing nearly the same orientation as high-precision single-bed measurements.

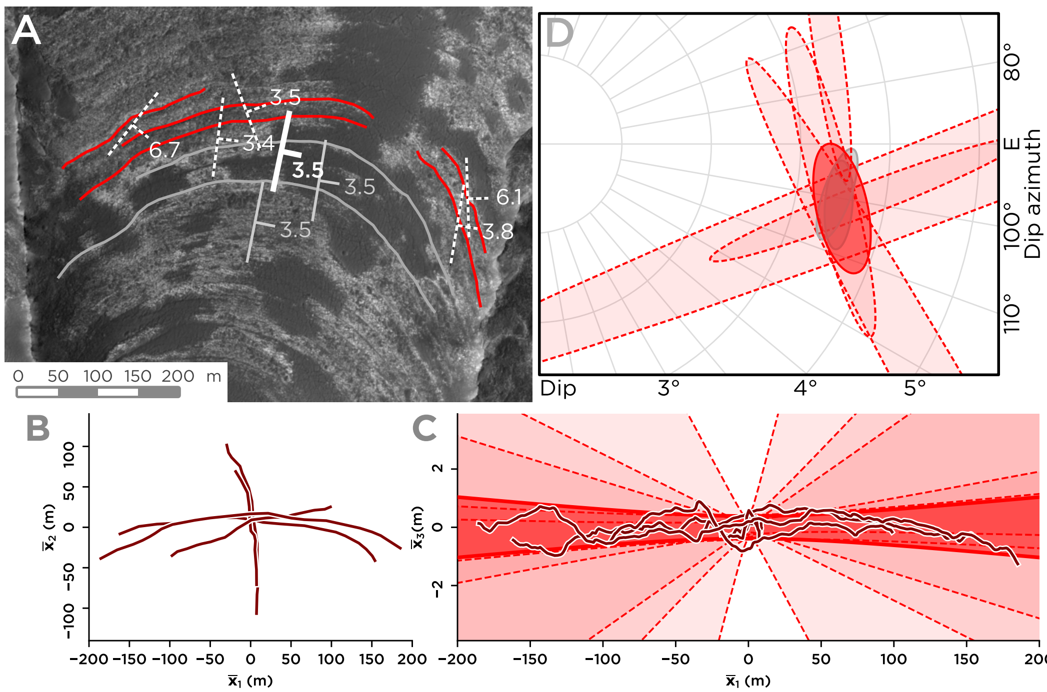

Figure 4.8: Joint fitting of bedding traces within a single stratigraphy to minimize errors for parallel planes. **(a)** Map view of bedding traces showing scattered nominal dips for bedding traces on opposing hillslopes (dashed), along with better-constrained orientations digitized around the entire range of hillslope aspect (solid bold). **(b)** Plan view of bedding traces centered and stacked atop each other for joint fitting, showing definition of a plane in two dimensions. **(c)** Side view of the plane showing residuals within the digitized dataset. Jagged lines are due to digitization errors. **(d)** Projection of errors to bedding poles on an upper-hemisphere stereonet, showing the grouped error range (red filled) at the intersection of the individual error spaces (dashed), and overlapping the error spaces of well-digitized single planes.

The process of joint fitting is nearly the same as the single-plane fitting procedure outlined in Section 4.3.2 and Section 4.3.3. The only difference is in processing of the input data: prior to PCA regression, the data matrix $\mathbf{D}$ corresponding to each input point cloud is independently centered on its mean using Equation 4.1. The resulting matrices are stacked to form a single centered data matrix $\mathbf{M}$. This combined representation contains orientation info for each bedding traces, but discards information on the relative locations of the planes. The orientation of the combined data matrix is regressed using PCA and error is modeled using standard techniques. If the assumption of a shared bedding orientation is valid, this can vastly increase statistical power.

This technique removes the need for certainty in the bed-to-bed correspondence of adjacent but discontinuous stratigraphic exposures, which is often difficult to determine. However, the method must be applied with care: it is only valid where the assumption of parallel bedding holds. For this reason, the combination of this method with views of decomposed variance and statistical error bounds is particularly powerful. Evaluation of misfits from the joint plane can illuminate whether the assumption of shared stratigraphy is valid. If a grouping cannot be adequately modeled as a parallel stratigraphy, this will be clear from the input data. Joint fitting of planes can be valuable both for precise statistical modeling of parallel-bedded stratigraphies and as an exploratory tool to evaluate whether stratigraphies conform to a parallel-bedding assumption.

4.4 Method demonstration and performance

4.4.1 Orbital imagery of the San Rafael Swell, Utah

The San Rafael Swell in eastern Utah, USA, is a ~20×40 km Paleocene Laramide anticline formed above a west-dipping thrust fault in the subsurface that tilted the strata to nearly vertical, creating the imposing San Rafael "Reef" [Figure 4.9a]. This structure is cored by a Jurassic stratigraphy including the distinctive, thick aeolian Navajo sandstone (**?**). In the middle of the swell, these strata are eroded away. The dramatic transect of Interstate 70 across the center of the structure makes the San Rafael Swell a world-famous structural locale. At the eastern edge of the swell, east dips steepen from near-flat to a maximum of ~60° before shallowing outside of the reef [Figure 4.9b]. The simple fold pattern and well-exposed stratigraphic layering provide an ideal setting to test the recovery of orientation errors from orbital or airborne data, allowing orientation recovery to be tested at a wide range of dips against data collected *in-situ*.

Datasets The map database accompanying the recently published geologic map of the San Rafael Desert (**?**) provides bedding orientations from the structural map, which were measured in the field at outcrop scale using a compass clinometer. At regional scale, they outline the convex structure and N-S axis of the swell [Figure 4.9c]

A 5 m ground-sample distance DEM from the Utah Automated Geographic Reference Center was used as the elevation layer for digitized bedding traces. This DEM was created from autocorrelated 1-meter resolution stereo aerial imagery,

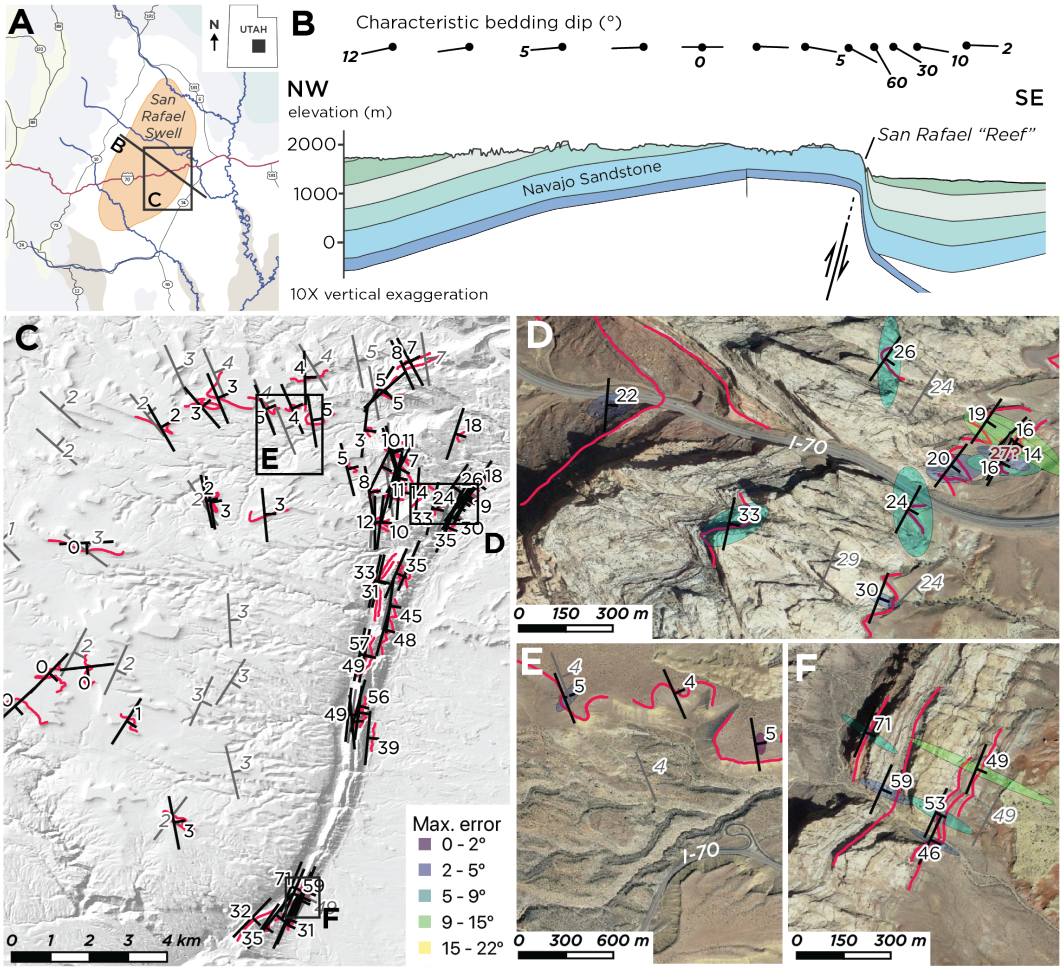

Figure 4.9: **(a)** Physiographic context of the San Rafael Swell in southeast Utah, USA. **(b)** Cross-section of the San Rafael Swell anticline (after **?**) showing the asymmetric dips of strata across the structure. **(c)** Field-measured bedding orientations (grey numbered symbols) from the San Rafael Desert geologic map (**?**), nominal remotely-sensed bedding orientations (black numbered symbols), and corresponding digitized bedding traces (red lines) atop a hillshade of the of the 5m aerial photogrammetric DEM used as input data for orientation reconstruction. Field-measured and remotely-sensed bedding orientations follow the same structural pattern. **(d-f)** Digitized bedding traces, remotely-measured orientations and field orientations atop orthorectified, coregistered *Google Maps* satellite data (accessed Feb. 2018) for key areas. Remotely-sensed orientations are underlain by an error-ellipse with axial lengths corresponding to θ_{max} and θ_{min}, oriented along the maximum direction of error.

using the SOCET Set software package. Elevation contours and a shaded-relief map were generated from the DEM to inspect alignment and data fidelity. In general, the DEM is of high quality, with a few artifacts in high-slope regions on the eastern side of steep hillsides where shadows lead to poor correlations. Locally, the data is significantly higher fidelity than the 10-meter resolution National Elevation Dataset (**?**)

Orthorectified, mosaicked ~25 cm/px satellite imagery from Google Maps was used to digitize bedding traces atop the DEM. The satellite imagery had been warped over a somewhat lower-resolution DEM than used here, leading to registration errors of up to 5 meters between the DEM and imagery datasets. Areas with obvious mismatch were avoided for digitization of features.

Bedding traces were digitized atop the satellite imagery using QGIS. Outcrops were chosen to maximize the 3D structure of captured planes, and areas near field-measured observations were targeted for direct comparison. Lengths of bedding traces range from 100 to 2500 m (median length 415 m). The longest traces are in low-dipping strata in the western portion of the study area. Digitized bedding traces are shown in Figure 4.9c.

The `orienteer` software package (see Appendix) was used to conduct planar fitting and evaluate the resulting planes for quality. During elevation extraction, lines were subset at 5 meter intervals to fully query the DEM. Planes were examined visually and quantitatively after PCA fits as described above. Those with large residuals (typically > 10 m out-of-plane) were re-measured if the blunder was due to an obvious mis-digitization, or discarded [Figure 4.10]. Sixty-eight planes were retained. Since only planes with favorable exposure were measured, no data grouping of beds was required to increase statistical power.

Orbital and field data comparison Overall, the map pattern of remotely-measured orientations mimics the large-scale structural trend of steepening dips towards the eastern monocline of the swell [Figure 4.9c]. Dip magnitudes are very close to those measured in the field. The direction and magnitude of errors are summarized as ellipses on the dip symbols. For the shallowest bedding, errors are extremely low [Figure 4.9d], while for the steepest measurements, errors are almost entirely in the dip direction [Figure 4.9e]. Error magnitudes are small for low-dipping strata and increase substantially with steeper dips. This is intuitive as the effects of DEM errors, poor registration of imagery, and digitizing errors will increase in rugged topography.

Selected closely spaced in-situ and remotely sensed orientation measurements paired for direct comparison [Figure 4.11] show that remotely-sensed orientations typically closely match the in-situ measurements, typically within error. Mismatch of a few degrees, especially in strike, can be explained by actual localized variation in bed orientation or slight measurement errors either in remote or in-situ gathered data. One measurement pair, highlighted in red on Figure 4.11, has an unusually large dip error. This in-situ measurement, at the eastern margin of the swell immediately north of the I-70 freeway, has a reported dip of 27°. We instead measure a dip, with error, of 10-20°. We replicate this result with additional

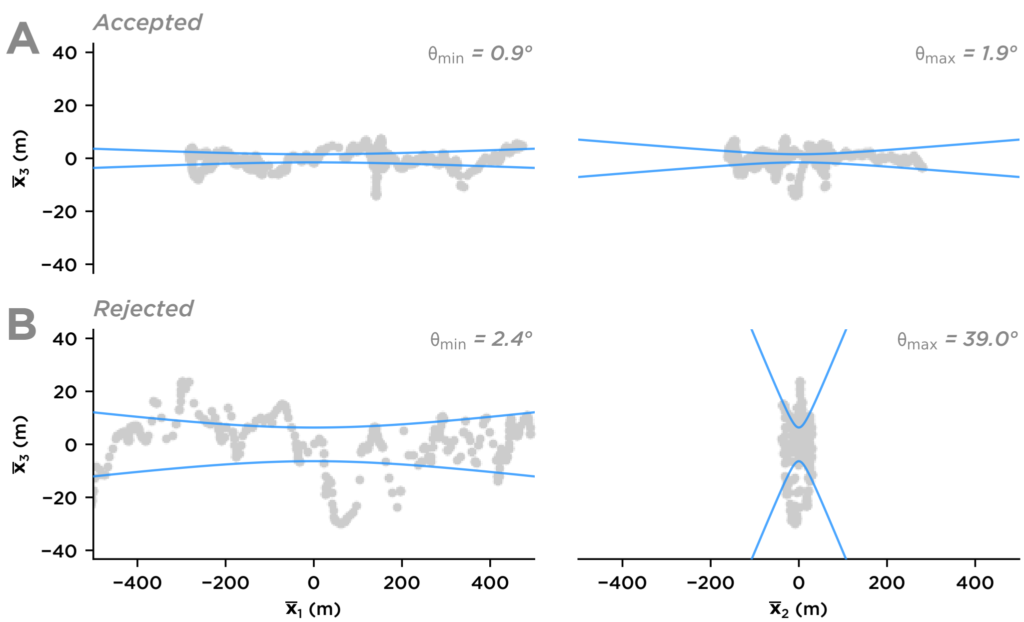

Figure 4.10: Axis-aligned visualization of fit errors to illustrate filtering criteria for poor bedding traces during creation of the San Rafael Swell dataset. **(a)** An accepted fit with relatively low out-of-plane scatter, defined over a significant length along both $\overline{x}_1$ and $\overline{x}_2$. **(b)** A poor fit, with higher out-of-plane scatter and no definition along $\overline{x}_2$. This bedding trace was discarded from the dataset.

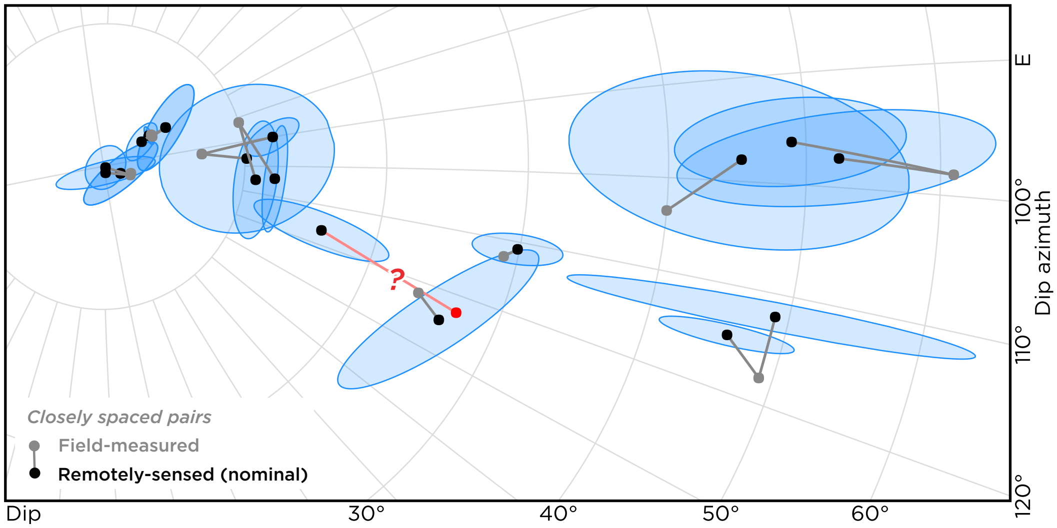

Figure 4.11: Upper-hemisphere stereonet showing poles to bedding for pairs of closely spaced field- and remotely-measured bedding orientations in the San Rafael Swell [Figure 4.9]. Errors generally increase at steeper dips (towards the right). One literature measurement (highlighted with a red ? and corresponding to the same symbol in Figure 4.9d) is steeper than all nearby remotely-sensed dips and does not conform to the regional structural pattern, suggesting that it may be an error in the preparation of the geologic map.

measurements of several closely spaced beds. The 27° dip is steeper than those immediately westward, putting it at odds with the localized structural pattern of shallowing dips at the eastern edge of the swell. This suggests that the published dip measurement on this outcrop may be in error.

Although basic correspondence between the DEM and imagery was manually checked, no processing or alignment was applied to the input data. A higher level of processing might increase the fidelity of the digital surface model, but this example demonstrates that reasonable planar orientations can be extracted from minimally-processed, publicly available imagery datasets, especially when good exposure is available. The addition of error and its visualization to the analytical product enables much more flexibility in input data quality, as errors arising from poorly registered data or sloppy digitizing will be penalized by poor confidence metrics and readily recognized [e.g. Figure 4.10].

4.4.2 UAV photogrammetry in the Naukluft Mountains, Namibia

The eastern face of the Naukluft mountains adjacent to Onis Farm (24.32° S, 16.23° E) contains mixed siliciclastic and carbonate strata above a regionally significant thrust fault (**?**). Recent mapping and stratigraphic studies in the area identified a minimally deformed stratigraphic section of the Zebra Nappe above this basal thrust fault (**?**). Using UAV imagery gathered during this field study [Figure 4.12a], we construct a coarse-resolution digital outcrop model of this area [Figure 4.12a]; this dataset is used to test the recovery of bedding orientations by the techniques

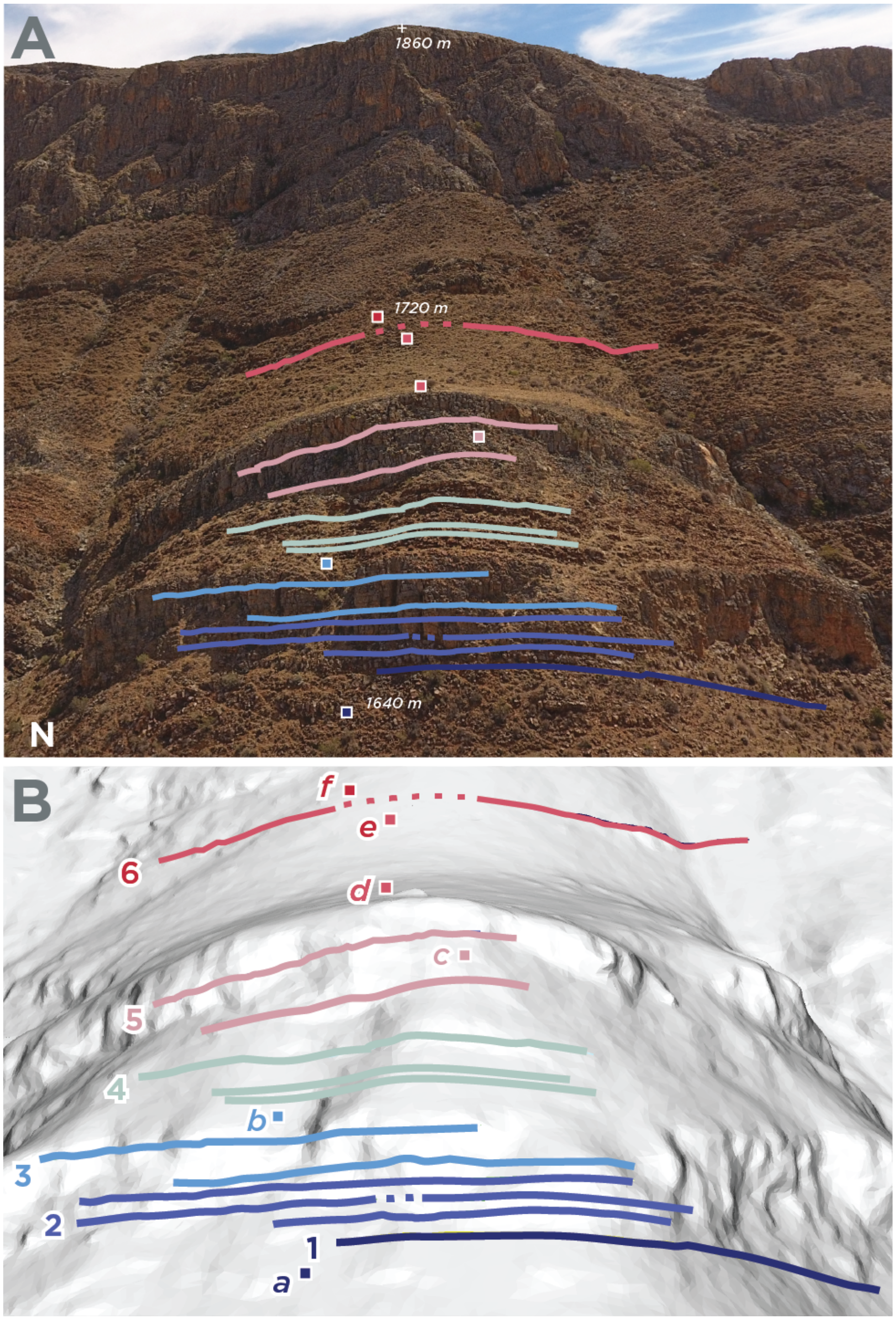

Figure 4.12: (a) UAV photograph (~500 m standoff) looking NW towards the cliffs at Onis Farm, Naukluft Mountains, Namibia. Digitized bedding traces (colored lines) and the locations of field-measured orientations (colored squares) are superposed. Beds dip ~30-45° degrees into the hillslope (away from viewer). 230 m of topographic relief is shown in the photo. **(b)** Digital surface model from UAV photogrammetry, viewed from slightly below the viewpoint of panel *a*, with digitized bedding traces superposed. Bedding traces grouped for analysis are connected by dashed lines. Groups of bedding traces with similar properties are numbered 1-6; field-measured orientations are lettered *a-f*.

described in this paper. Assessing the quality of measurements by UAVs is of significant interest for terrestrial field geological studies (e.g. **?**), and multi-view aerial data tests the functionality of the method with off-vertical errors and ad-hoc photogrammetry that characterize UAV-based surface model creation.

Datasets An 80-meter elevation range within the ~300 m cliff face at Onis Farm was chosen for this comparison, comprising the upper Ubisis Formation, the Tsams Formation, and the lower Lemoenputs Formation of the Zebra Nappe; field structural data was subset from a stratigraphic dataset assembled for the entire cliff (**?**). Within the target elevation range, bedding orientation measurements were collected at six locations with a Brunton compass clinometer, and the GPS position and description of the measured bed were logged [Figure 4.12]. The elevation of each measurement was determined after measurement by draping the georeferenced data atop an Advanced Land Observing Satellite (ALOS) global 15-m resolution photogrammetric DEM, which was used as a regional topographic basemap.

Outcrop images were acquired for processing into a 3D model using a remotely piloted DJI Phantom 4 quadcopter UAV, from an altitude of ~200 m above ground and ~500-800 m lateral standoff southeast of the target cliff. The aircraft was approximately level with the target stratigraphic interval [Figure 4.12a]. UAV images were combined into a photogrammetric 3D model using the Agisoft Photoscan Professional v1.2 structure-from-motion software package [Figure 4.12b]. The 3D model was assembled with the "very high" quality setting and has ~4 million constituent points and a horizontal resolution of ~15 cm per pixel. The model extends ~1.5 km laterally along the cliff face and captures ~400 m of relief on the east-facing cliff. The model has an approximate horizontal resolution of 15 cm per pixel, though precision on all axes varies within the scene depending on the stereo convergence geometry of individual image pairs.

The stratigraphic interval studied contains two cliff faces with intervening float-covered slopes; beds traceable in UAV imagery primarily occur on the cliffs. The traces of 14 bedding surfaces were digitized manually in Agisoft Photoscan atop oblique images registered to the 3D model [Figure 4.12]. Agisoft Photoscan automatically drapes digitized bedding traces onto the surface model, creating a 3D point dataset without an additional software package or conversion to a gridded DEM. Digitized bedding traces were exported as a `dxf`-format file using the UTM Zone 33S coordinate system. The `fiona` Python module was used to read this data, and the `attitude` software package was used for planar fitting. Four bedding traces were grouped with other traces at similar stratigraphic levels to increase statistical power, yielding a final set of 12 distinct orientation measurements. An `iPython` notebook containing the analytical pipeline for this example is available as supplementary material to this publication.

UAV and field data comparison Field-measured bedding orientations for the target stratigraphic interval range in strike from 225-245°, corresponding to dip azimuths of 315-335°. Dips range from 30 to 45° to the northwest (into the hillslope). Field-measured orientations are lettered *a-f*, and sets of remotely-sensed measurements are numbered 1-6 [Figure 4.12b and Figure 4.13].

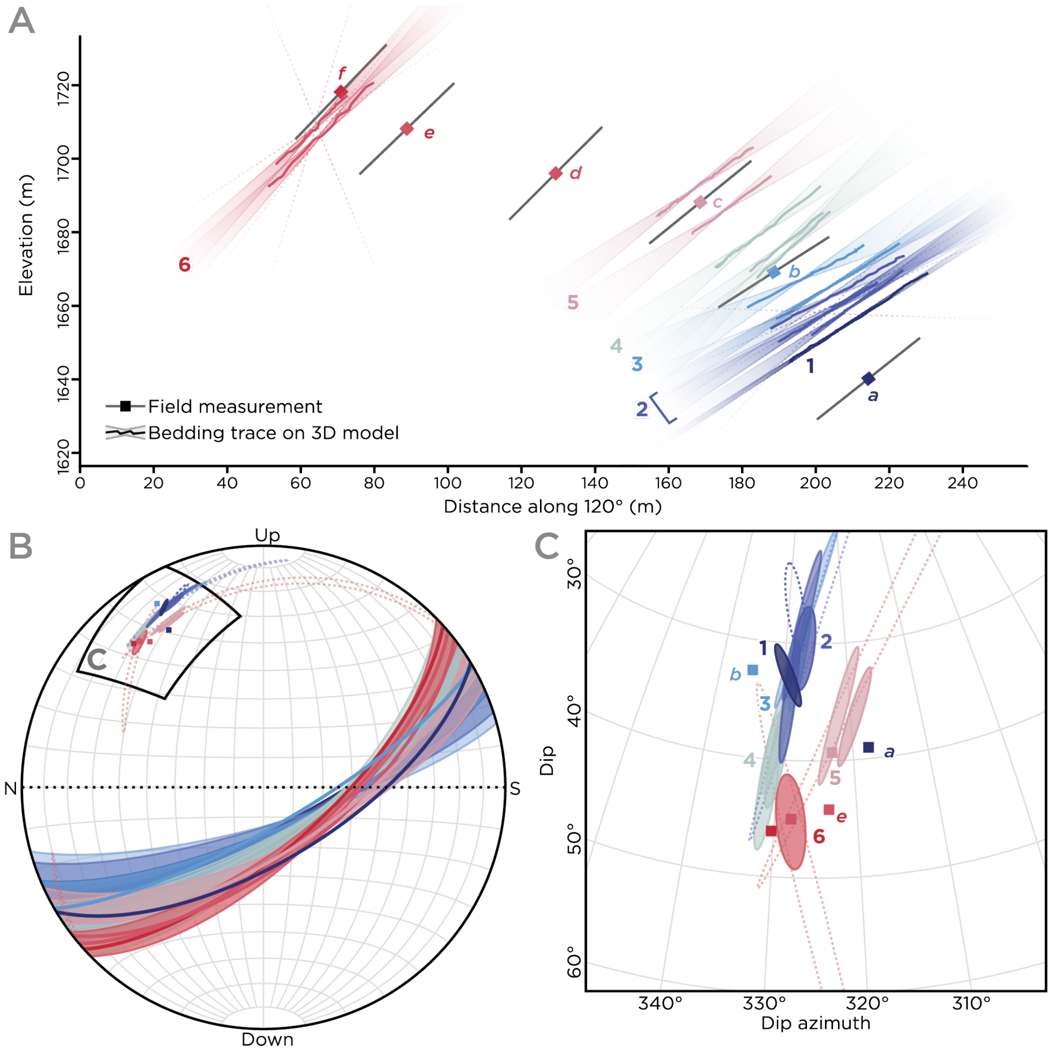

Figure 4.13: Comparison of field-measured and UAV photogrammetric bedding orientations for the Onis cliffs. Remotely-sensed and field-measured bedding orientations are colorized by height. In each panel, error spaces for individual remotely-sensed measurements are shown as colored fields. Dotted lines show the error bounds of measurements prior to grouping. **(a)** Orthographic projection of bedding orientations, with the horizontal axis showing distance to the southeast, approximately along the dip direction measured beds Remotely-measured beds are shown as residuals to their best-fitting plane and overlain by hyperbolic error bounds. The recovery of dips into the hillslope by remotely-sensed orientations is apparent. **(b)** Upper-hemisphere oblique equal-area stereonet showing NW-dipping bedding girdles for remotely-sensed and field measurements. Dotted lines represent the edges of error ellipses for components of grouped measurements. **(c)** Errors to poles of bedding, showing close correspondence with field measurements (squares) and the orientation of maximum errors in dip.

The lowest-elevation extracted bedding trace (1) follows a coarse sandstone bed across the nose of the hillslope. Its orientation is well-constrained, with a maximum angular error of ~5°, but significantly different from the field-measured orientation of a siltstone bed ~10 m stratigraphically below (*a*). This mismatch may result from an actual dip change due to slight folding across the lithologic boundary at the base of the cliff.

The next intervals (2 and 3) contain five beds within a dolomite cliff; two of these measurements were grouped. The beds in 2 and 3 have error ellipses elongated in the dip direction, representing measurements well-constrained on a single axis (roughly, their apparent dip in standoff imagery); their error spaces overlap that of (1), suggesting consistent bedding orientations for the entire lower cliff.

Beds marked as 4 occur in a fine–medium sandstone interval where stairstep beds are easily traced; these beds are individually well-resolved and generally steeper than the beds of 2 and 3. These measurements closely correspond to field measurement *b* in dip but suggest a strike ~5° to the west. Since several remotely-sensed beds agree closely, this rotation may be caused by a slight error in field measurement.

Beds in 5 were measured in a dolomite cliff, and the extracted error distributions overlap the field measurement *c* within the same interval, suggesting orientation reconstruction to within a few degrees. Field measurements *d*, *e*, and *f* were measured on a float-covered slope of the Lemoenputs Formation with few traceable bedding planes. One somewhat resistant dolomite bed (6) can be traced on both sides of the hillslope but not over its nose. When grouped, these measurements outline a single plane dipping at ~45° that corresponds closely in orientation to *d*, *e*, and *f*.

Bedding orientations extracted from the UAV dataset correspond closely to field-measured orientations, recording bedding dips 30-50° northwest (into the hillslope) and steepening with elevation. In general, strike is constrained to within a few degrees, while dips are constrained to within ~5-15°. This error structure is consistent with the relatively stronger constraints on apparent dips along the cliff face than dips in and out of the cliff. Flights only on a single side of a relatively planar outcrop entail little 3D structure with which to derive well-constrained orientations. However, even with a relatively low-resolution (15 cm/pixel) SfM photogrammetric elevation model, the crucial observation of beds steeply dipping into the outcrop is easily captured.

4.5 Potential future improvements to the statistical framework

4.5.1 Modeling data with different error structures

The statistical error bounds developed for unweighted PCA regression in Section 4.3.3 are general and adaptable to a wide variety of data types. Different statistical frameworks can be substituted, and supplements to this statistical framework can be used to model errors for uncertain orientations using situation-specific information as described below.

Adding a noise floor PCA-based regression is responsive to the scale of errors, but known errors in the input data are not automatically accounted for in the fitting process. If there exists a measure of data input error, a "noise floor" can be imposed that defines a minimum amount of noise expected for the input dataset. This can be accomplished by conditionally replacing λ_3 in Equation 4.23 with a standard value for the minimum noise variance, to ensure that $\lambda_3 \geq \min \sigma^2_{\hat{\mathbf{M}}}$.

For instance, if the accuracy of a point cloud is 1 m, as computed based on external criteria (e.g. the input stereo geometry of a gridded elevation model or measurement error for LIDAR or radar ranging), introducing a noise floor of $\min \sigma^2_{\hat{\mathbf{M}}} = 1$ into calculations of the noise covariance could correct for false certainty arising from possible local smoothing of data.

Rescaling error sensitivity An advantage of the isotropic error framework of PCA is its flexibility: because coordinates are not fixed, the input dataset can be rescaled along any axis. Different axial weightings can be a useful way to incorporate known errors on single-axis parameters of the input data (e.g. photogrammetric image-registration errors).

This property can be used to control the relative sensitivity of the fit to errors along each axis of the input data. It is often desirable to set error sensitivities separately based on informed criteria around dataset-specific error sources (**?**). For instance, orbital photogrammetric DEMs might be tuned for chiefly vertical errors, while oblique SfM photogrammetry would be given higher sensitivity in the oblique view direction. While our current statistical framework treats errors along all axes equally, the software can be modified to fit different errors along each axis. The PCA framework can be limited to only vertical errors, mimicking OLS, or utilized in a variety of other weighted schemes (e.g. **??**).

Applying other statistical models In addition to the asymptotic Gaussian and noise-based statistical models described in this paper [Section 4.3.3], numerical methods such as bootstrap resampling and Monte Carlo sensitivity analysis can also be used to generate high-quality errors in the fit parameters of the plane. These methods are numerically intensive and difficult to generalize, but allow the incorporation of detailed assumptions about dataset errors. Additionally, a variety of situation-specific statistical techniques can be substituted for PCA, such as OLS and weighted schemes described above. No matter which statistical framework is used, the fitting and data-visualization methods described outlined in this paper can be used to represent uncertain planes.

4.5.2 The link with Bingham statistics

The Bingham statistical distribution is a generalized statistical distribution of undirected orientations (**?**). The core assumption of the Bingham framework is that for the axes of a distribution $\mathbf{a}$, $\mathrm{trace}(\mathbf{a}^2) = 1$. Applying the Bingham transformation to a Cartesian set of error axes is functionally equivalent to finding the tangents to a hyperbolic error range. As such, our hyperbolic axes $\mathbf{h}$ can be transformed into the Bingham structural parameters κ_1 and κ_2 (**??**).

When fully explored, the formal link between PCA regression and Bingham statistics will allow uncertain orientation measurements to be treated as probability density functions in spherical space. This will allow higher-level statistical transforms to be applied to measurements, including combination using error-propagation techniques, and the application of statistical significance tests. Formalizing the conceptual link between Cartesian and Bingham statistics may unlock new potential applications for this error-analysis framework.

4.6 Conclusion and recommendations

We have described a complete error-analysis workflow for the orientation of geological planes, especially stratigraphic bedding, that improves on typical regression statistics for the assessment of geological planes. Our PCA-based analysis includes a regression method, a framework for statistically-based errors, mathematical approaches for the 2D visualization and reporting of structural data with errors, and software to handle calculations and data management.

As shown by the two terrestrial examples, these analytical procedures are generalized and flexible. They can be used to model the orientation of planes on map-projected satellite and aerial imagery, as well as digital surface models built with LIDAR, UAV photogrammetry, and radar techniques. Application of the error analysis method in the San Rafael Swell successfully captures the structural pattern of this geological area. The relatively good conformance with in-situ measurements was gained despite the use of off-the-shelf data products, reflecting the flexibility and wide applicability of this method to readily available nadir-looking imagery and elevation datasets. Application of the method to oblique-looking UAV data on the Naukluft plateau demonstrated the viability of PCA-based orientation calculation in a reconnaissance study using high-obliquity aerial imagery with relatively inexpensive equipment and SfM photogrammetry software.

The coupling of a robust error-analysis framework with techniques to visualize the error space allows simple and transparent analytical workflows. Error-minimizing data collection strategies can be easily compared, and heterogeneous data can be used with full knowledge of the errors involved. We propose a standardized method for numerical reporting of uncertain planar orientations, combining the basic strike/dip representation with terms for angular errors on two axes, and the rake of these error axes within the best-fitting plane [Section 4.2], and yielding [*strike, dip, rake, min. angular error, max. angular error*] for each measurement. Additionally, we create intuitive stereonet display methods that provide a natural means to visualize uncertain planar orientations alongside traditional structural data.

Overall, the results of this study suggest that errors arising from outcrop geometry are at least as important as precision of the input remote-sensing dataset in defining the error space of a fitted plane. Traces of geologic features can only be modeled as unique planes when they query a three-dimensional point dataset, and error structures for different outcrops can be completely different within the same dataset. For characterization of orientations in an outcrop, we recommend that care be taken to find beds that sample a wide range of hillslope aspect or depth within an obliquely-measured scene (or groups of closely-spaced beds that collectively sample such a range). Furthermore, we suggest that digitizing precision is of subsidiary importance to collecting such a varied sample set: small errors in describing a fitted plane are will not significantly diminish the quality of the fit relative to poor sampling of three-dimensional outcrop variability. Thus, measuring a large quantity of adjacent bed surfaces provides the best opportunity to remove poor measurements and group incomplete ones.

We expect the methods described here will push the scale of geologic inference towards the resolution limit of 3D surface models, broadening the range of structural interpretations that can be made from remotely sensed imagery. This will increase the fidelity of structural measurements supported by UAVs and LIDAR scanners in terrestrial research, rover-based cameras for *in-situ* planetary exploration, and satellite data for regional planetary mapping. To that end, we release the software we developed to implement these methods and visualize strike and dip in the Appendix.

4.7 Acknowledgements

We would like to thank NASA for the NASA Earth and Space Science Fellowship to D.P. Quinn that funded this work. Our software tools are archived with Caltech-DATA (*DOI not yet created*) in conjunction with this work. Data for the examples shown in the paper is part of the testing suite for the `attitude` software package.

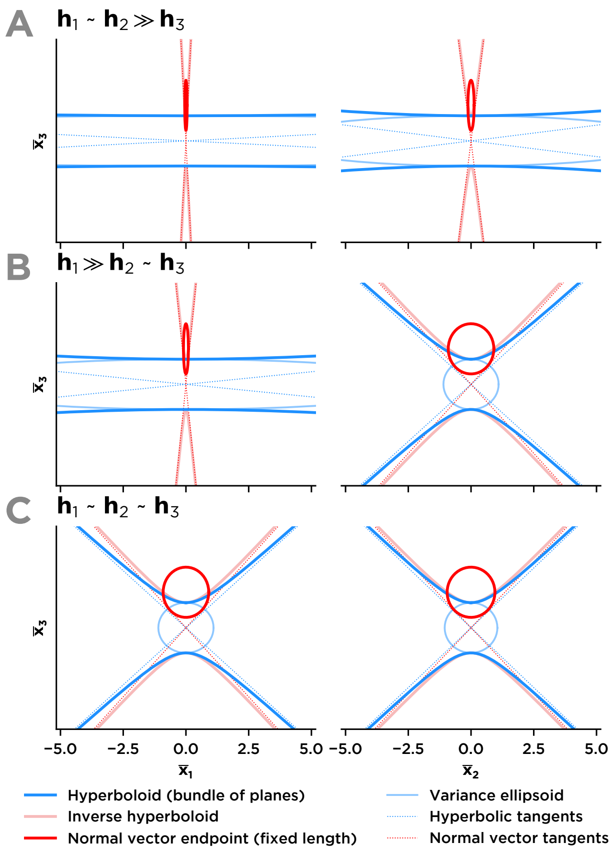

Figure 4.14: Several mathematically related constructions of the error space of a uncertain plane as hyperbolic quadrics and ellipsoids. Correspondence of the error space of a plane defined by semiaxes $\mathbf{h}$ with hyperbolic and ellipsoidal representations of the error space of the normal vector to the plane, showing angular scaling of the subtended area of these constructions depending on the ratio of the semiaxes.

4.A Quadric representation of the orientation error space

We represent error surfaces for planar orientation measurements as 3D generalized conic sections, or quadric surfaces [Figure 4.2]. Planar fit errors can represented as matrices, plotted as quadrics, and translated between representations of the error space as hyperboloids, ellipsoids, and cones of tangency by linear algebraic methods, such as the geometric (e.g. affine and projective) transformations described below.

In three-dimensional space, an uncertain planar measurement is structured as a hyperboloid of two sheets (an elliptic hyperboloid), opening along the error axis (λ_3). Conceptually, this hyperboloid represents the minimal enclosing surface of a bundle of all possible planes corresponding to the regression (**?**). Another possible representation is as a bundle of possible normal vectors to the plane, which can be defined by a hyperboloid encompassing all vectors or an ellipsoid containing the endpoints of equal-length vectors [Figure 4.1]. Representation of errors in a normal-vector framework is less inherently meaningful than the hyperbolic construction, since normal vectors do not “contain” the modeled plane. However, the manipulation of uncertain vectors is simpler than uncertain planar bundles, and the vector representation of orientation errors eases comparison and transformation [Figure 4.14].

4.A.1 A hyperboloid enclosing the plane

The axes h define a hyperboloid representing the errors to the planar fit, conforming to the general equation for an origin-centered hyperbola opening along $\overline{\mathrm{x}}_3$ of

$$\frac{\overline{\mathrm{x}}_1^2}{\mathrm{h}_1^2} + \frac{\overline{\mathrm{x}}_2^2}{\mathrm{h}_2^2} - \frac{\overline{\mathrm{x}}_3^2}{\mathrm{h}_3^2} = -1. \tag{4.37}$$

When incorporated into a 4×4 matrix representation of the PCA-aligned error quadric,

$$\overline{\mathbf{Q}}_{\mathbf{H}} = \mathrm{diag}([\tfrac{1}{\mathrm{h}_1^2}, \tfrac{1}{\mathrm{h}_2^2}, -\tfrac{1}{\mathrm{h}_3^2}, -1]), \tag{4.38}$$

forms part of a general equation for a quadric surface

$$\overline{\mathbf{x}}^{\mathrm{T}} \overline{\mathbf{Q}}_{\mathbf{H}} \overline{\mathbf{x}} = 0 \tag{4.39}$$

(e.g. **?**).

This matrix representation allows manipulation of the error distribution in three dimensions. For example, the PCA-aligned error hyperboloid can be transformed into real space by sequentially applying two affine transformations to $\overline{\mathbf{Q}}_{\mathbf{H}}$: first a rotation into the real coordinate vectors with the augmented rotation matrix $\mathbf{V}_{\mathrm{A}}$ ($\mathbf{V}$ augmented with the 4×4 identity matrix) and translation defined by $\mathbf{T}_{\boldsymbol{\mu}}$, an identity matrix with a last column $[-\boldsymbol{\mu}_{\mathbf{D}}, 1]$, to shift the center of the coordinate system to the origin from the mean of the measured plane. Thus,

$$\mathbf{Q}_{\mathbf{H}} = (\mathbf{V}_{\mathrm{A}} \mathbf{T})^{\mathrm{T}} \overline{\mathbf{Q}}_{\mathbf{H}} \mathbf{V}_{\mathrm{A}} \mathbf{T}, \tag{4.40}$$

and the quadric representing the uncertain plane becomes

$$\mathbf{x}^{\mathrm{T}} \mathbf{Q}_{\mathbf{H}} \mathbf{x} = 0. \tag{4.41}$$

4.A.2 Errors to normal vectors

Errors to normal vectors can be defined as both a hyperboloid containing all possible normal vectors passing through the center of the plane, and an offset ellipsoid representing errors to a normal vector with fixed length. Projected from the origin, all error spaces for the normal vector subtend the same angle, equivalent but orthogonal to that subtended by $\overline{\mathbf{Q}}_{\mathbf{H}}$ [Figure 4.14].

The hyperbolic formulation of normal-vector errors is the "dual" quadric surface to $\overline{\mathbf{Q}}_{\mathbf{H}}$, related by inversion:

$$\overline{\mathbf{Q}}_{\mathbf{H}}' = \overline{\mathbf{Q}}_{\mathbf{H}}^{-1} = \mathrm{diag}([\mathrm{h}_1^2, \mathrm{h}_2^2, -\mathrm{h}_3^2, -1]). \tag{4.42}$$

This defines a hyperboloid of two sheets with a cone of tangency spanning the same angular distance as $\overline{\mathbf{Q}}_{\mathbf{H}}$, but normal to it. The hyperboloid defining normal vector error is a *point quadric*, dual tothe hyperbolic *plane quadric* surrounding the nominal value of the plane. Duality is a generalization of the concept of "inversion poles", which shows that for a given conic section, any interior point (a "pole") can be related to a unique reciprocal line outside the conic (a "polar") (**?**).

A more intuitive ellipsoidal representation of the normal vector error space is arrived at when a fixed-length normal vector is assumed. Normal vector errors can be defined as an ellipsoid with semiaxes proportional to $\frac{1}{\mathrm{h}_i^2}$ and an arbitrary scale. For a normal vector of length $\sqrt{2}\mathrm{h}_3$, the ellipsoid semiaxes are scaled by a factor of h_3^2, resulting in an ellipsoid with major axes $[\frac{\mathrm{h}_3^2}{\mathrm{h}_1}, \frac{\mathrm{h}_3^2}{\mathrm{h}_2}, \mathrm{h}_3]$ with a center offset $\sqrt{2}\mathrm{h}_3$ from the origin along the 3 axis. This construction of the normal vector errors keeps the same relationship with the angular tangents to the normal vectors [Figure 4.14].

4.A.3 General method to map a quadric to a conic

Quadric surfaces can be sliced in any plane to form a 2D conic section. The ability to transform and slice the matrix representation of the error space along arbitrary axes allows the plotting of planar errors to single or multiple planes into common Cartesian coordinates for projection along arbitrary view axes [Figure 4.13].

Using a plane defined by two perpendicular vectors $\mathbf{v}_1$ and $\mathbf{v}_2$, and a point $\mathbf{a}$ within the plane, we can define a 4×3 transformation matrix to map the quadric down to a 2D conic section, stacking these vectors as columns, augmented with a final row $k = [0, 0, 1]$:

$$\mathbf{T} = \begin{bmatrix} \mathbf{v}_1 & \mathbf{v}_2 & \mathbf{a} \\ 0 & 0 & 1 \end{bmatrix}. \tag{4.43}$$

The conic section

$$\mathbf{C_H} = \mathbf{T}^{\mathrm{T}}\mathbf{Q_H}\mathbf{T} \tag{4.44}$$

defines the slice of the error space along that plane. The mapping to a hyperbolic slice of the error hyperboloid at any angle γ within the fitted plane can be found using the transformation matrix for axes $\overline{\mathrm{x}}_\gamma = [\cos\gamma, \sin\gamma, 0]$ and $\overline{\mathrm{x}}_3 = [0, 0, 1]$:

$$\mathbf{T} = \begin{bmatrix} \cos\gamma & 0 & 0 \\ \sin\gamma & 0 & 0 \\ 0 & 1 & 0 \\ 0 & 0 & 1 \end{bmatrix}. \tag{4.45}$$

For the simple case of the slice of the error space aligned with $\overline{\mathbf{x}}_1 = [1, 0, 0]$ and $\overline{\mathbf{x}}_3 = [0, 0, 1]$ and centered at the origin, a transformation matrix

$$\mathbf{T} = \begin{bmatrix} 1 & 0 & 0 \\ 0 & 0 & 0 \\ 0 & 1 & 0 \\ 0 & 0 & 1 \end{bmatrix} \tag{4.46}$$

resolves

$$\mathbf{C_H} = \mathbf{T}^{\mathrm{T}}\overline{\mathbf{Q}}_{\mathbf{H}}\mathbf{T} = \mathrm{diag}([\tfrac{1}{\mathrm{h}_1^2},\ -\tfrac{1}{\mathrm{h}_3^2},\ 1]), \tag{4.47}$$

a hyperbola of two sheets, opening along h_3.

4.A.4 General method to move to spherical coordinates

A general representation for the tangents to the hyperbolic error spaces discussed above can be constructed as a cone of tangency, which can be easily transformed into spherical coordinates. This elliptic cone has the same semiaxes as the elliptic hyperboloid $\mathbf{Q_H}$ and can be represented as

$$\overline{\mathbf{Q}}_{\mathbf{T}} = \mathrm{diag}([\tfrac{1}{\mathrm{h}_1^2},\ \tfrac{1}{\mathrm{h}_2^2},\ -\tfrac{1}{\mathrm{h}_3^2}, 0]) \tag{4.48}$$

(with the last -1 in $\overline{\mathbf{Q}}_{\mathbf{H}}$ replaced with a 0). The orthogonal angular cone defining the normal vector can be found in general by inverting the cone of tangents $\overline{\mathbf{Q}}_{\mathbf{T}}$ to form

$$\overline{\mathbf{Q}}_{\mathbf{N}} = \mathrm{diag}([\mathrm{h}_1^2,\ \mathrm{h}_2^2,\ -\mathrm{h}_3^2,\ 0]). \tag{4.49}$$

4.B Software tools

We provide a software implementation that supports the orientation-analysis statistics and visualizations described here. The core software is the `attitude` Python module, which contains regression code and functions for importing point-based bedding traces from GIS data and other formats. This package also contains methods for plotting uncertain orientations in spherical coordinates using the Python libraries `matplotlib` and `cartopy`. The `attitude` module also includes a Javascript component implementing tools based on the d3 visualization library for interactive stereonets and plots of decomposed axial variance. The Python and Javascript components can be used together in the **iPython Notebook** analytical environment, allowing interactive data inspection and exploratory grouping of jointly fitted planes, with minimal setup [Figure 4.15a]. The `attitude` module is open-source and available on GitHub (https://github.com/davenquinn/Attitude). Documentation and example notebooks are available at https://github.io/davenquinn/Attitude. Version 1.0 of the software and documentation has been archived with CaltechDATA in conjunction with this publication.

The `Orienteer` software application [Figure 4.15b] was created to ease the management of orientation data over a large mapping project. This cross-platform desktop application interfaces with the `attitude` module and supports the management of orientation measurements and their underlying raster elevation models in a `PostGIS` spatial database. This application eases the filtering of planes by quality and grouping and splitting to assess the viability of joint fitting for data reduction, and serves as a companion to GIS software [Figure 4.16]. Although `Orienteer` adds powerful data management capabilities to the `attitude` software, it is more difficult to set up, requiring a `PostgreSQL` server, and is somewhat unstable due to its relative complexity. This application is also open-source and is available on GitHub (https://github.com/davenquinn/Orienteer) as well as archived with CaltechDATA in conjunction with publication.

The statistical method developed here can be expressed with basic linear algebra and should be straightforward to implement in programming environments such as MATLAB or R. Test cases are provided with the `attitude` module that can be used to verify accuracy. Additionally, since both QGIS and ArcGIS expose

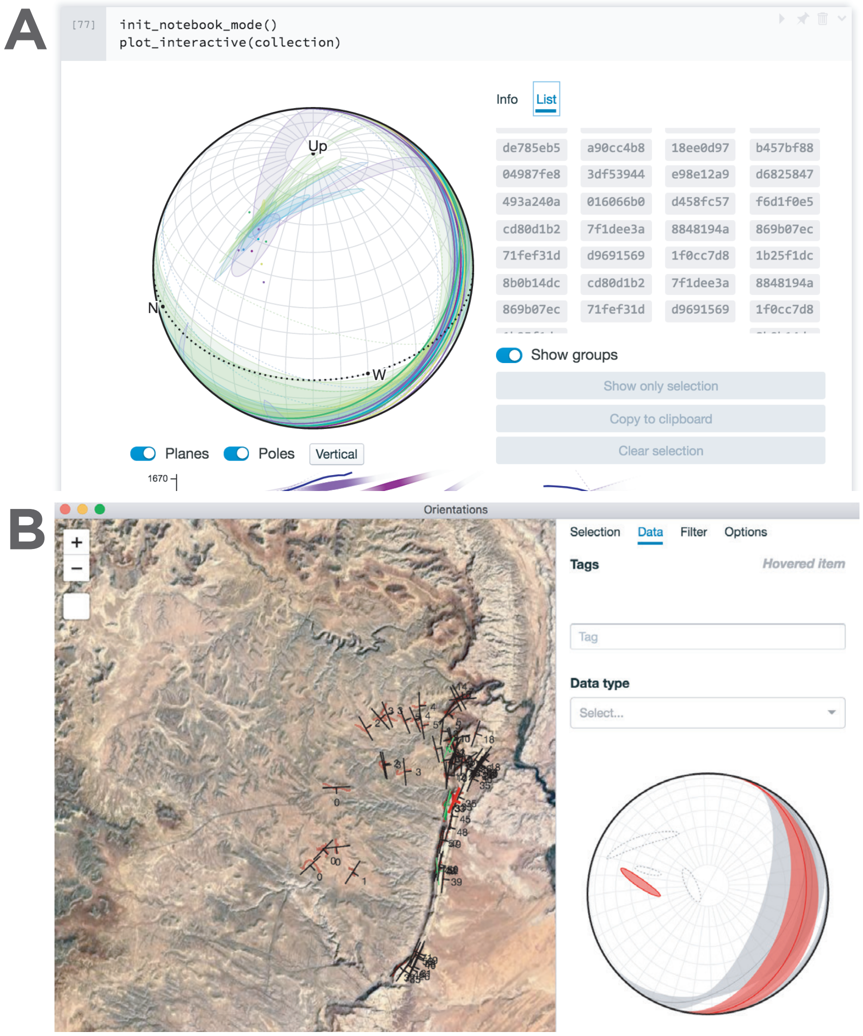

Figure 4.15: Screenshots of software developed in this study. **(a)** The `attitude` Python module running in an *iPython* notebook. **(b)** The *Orienteer* application in use for filtering a database of orientations atop Google Maps data for the San Rafael Swell, Utah.

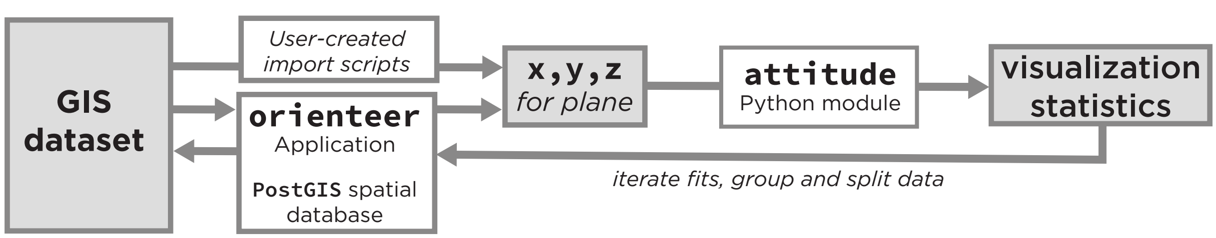

Figure 4.16: Workflow diagram showing the roles of the `attitude` Python module and `Orienteer` data-management application in an orientation-measurement software project. The `attitude` module supports a linear process flow, while the `Orienteer` application enables the management of orientation data across a large mapping project.

Python bindings, it is possible to use the `attitude` module directly within standard GIS software.

5 The deposition and alteration history of the northeast Syrtis Major layered sulfates

Daven P. Quinn[1] B.L. Ehlmann[1,2]

1 Division of Geological and Planetary Sciences, California Institute of Technology, Pasadena, California, USA

2 Jet Propulsion Laboratory, California Institute of Technology, Pasadena, California, USA

Abstract

The ancient stratigraphy exposed on the western rim of the Isidis basin records the history of water on early Mars. Noachian units are overlain by layered sulfates and capped by Early Hesperian Syrtis Major lavas. The layered sulfates – uniquely exposed at northeast Syrtis Major – comprise a sedimentary sequence up to 600-m thick that has undergone a multi-stage history of deposition, alteration, and erosion. Polyhydrated sulfates are bedded at m-scale and were deposited on slopes up to 10°, embaying and thinning against pre-existing Noachian highlands around the Isidis basin rim. The sulfates were then modified by volume-loss fracturing during diagenesis, and the fractures hosted channelized flow and jarosite mineral precipitation to form resistant ridges upon erosion. The depositional form and diagenetic volume-loss recorded by the layered sulfates suggest deposition in a deep aqueous basin. After their formation, the layered sulfates were first capped by a "smooth capping unit" and then eroded to form paleovalleys. The Syrtis Major lavas were channelized by this paleotopography, capping it in some places and filling it in others. Later fluvial features and lacustrine deposits, which share a consistent regional base level (~-2300 m), were superimposed on the sulfate-lava stratigraphy. The progressive evolution of the layered sulfate stratigraphy demonstrates a long and varied interaction with water over early Mars history. The layered sulfates imply surface bodies of water at northeast Syrtis Major, deep basin lakes/seas, and river systems, with activity spanning from Noachian to early Amazonian time.

A major focus of Mars science is deciphering the nature and drivers of changing environmental conditions during the planet's early history. Orbital observations of late-Noachian fluvial and alluvial systems (e.g. *Howard et al.*, 2005; *Irwin et al.*, 2005; *Fassett and Head*, 2005; *Andrews-Hanna and Lewis*, 2011; *Schon et al.*, 2012) and phyllosilicate and carbonate alteration of igneous bedrock by surface and subsurface waters (e.g. *Bibring et al.*, 2006; *Ehlmann et al.*, 2008a, 2011; *Mustard et al.*, 2009; *Murchie et al.*, 2009), as well as *in-situ* examination of lacustrine deposits and groundwater diagenesis by the *Opportunity* and *Curiosity* rovers (*Squyres et al.*, 2004; *Grotzinger et al.*, 2013), present powerful evidence of the active role of liquid water on early Mars. From this initial active hydrosphere, the Martian climate underwent a secular drying through the Hesperian period to arrive at the cold, arid environment that prevailed through most of the Amazonian period. However, the timing and character of this global shift is unclear.

The character of environmental change during the Noachian and Hesperian is best constrained by analyses of stratigraphic sections that span portions of this time interval. Stratified sedimentary deposits with hydrated minerals stand out as key environmental records (*Gendrin et al.*, 2005; *Niles and Michalski*, 2009; *Milliken et al.*, 2010; *Ehlmann and Mustard*, 2012; *Grotzinger et al.*, 2012). The stratigraphy exposed at the northeast margin of the Syrtis Major lavas [Figure 5.1, NE Syrtis] presents an opportunity to examine environmental change from approximately the early Noachian to the Hesperian, and possibly Amazonian, in a sequence of geologic units whose timing is well-constrained. The lower units were emplaced after the Isidis Basin-forming impact (*Mangold et al.*, 2007; *Mustard et al.*, 2007, 2009) and are capped by Hesperian Syrtis Major lavas (*Hiesinger and Head*, 2004). The units record a characteristic change in Martian igneous materials, including the a transition from low-Ca pyroxene bearing units to high-Ca pyroxene bearing units as well as a high Fo#, olivine-enriched deposit whose formation is related to the Isidis impact (*Mustard et al.*, 2005, 2007, 2009; *Koeppen and Hamilton*, 2008; *Baratoux et al.*, 2013). Importantly, the NE Syrtis stratigraphy contains most of the hydrated mineral diversity recognized on Mars in an organized stratigraphic sequence. Layered sulfates with jarosite ridges are superposed over carbonate-bearing units, which are superposed over clay-bearing units (*Ehlmann and Mustard*, 2012). This straigraphic sequence records a transition from neutral-alkaline (clay- and carbonate-forming) to acidic (iron sulfate-forming) aqueous environments that corresponds to a global pattern indicating increasing aridity (*Bibring et al.*, 2006). Thus, the mesas of NE Syrtis stratigraphy represent a rare temporally-constrained and in-place record of changing hydrological conditions during the Noachian–Hesperian transition.

The thick layered sedimentary sulfates represent a major change in formation style from the impact- and volcanically emplaced units dominating the rest of the stratigraphy (*Ehlmann and Mustard*, 2012; *Bramble et al.*, 2017). The lower Noachian clay and carbonate units have been well-studied by prior workers because they are exposed regionally to the north over an area spanning hundreds of thousands of square kilometers (e.g. *Mangold et al.*, 2007; *Ehlmann et al.*, 2009; *Mustard et al.*, 2009; *Michalski et al.*, 2010; *Viviano-Beck et al.*, 2014; *Ehlmann and Edwards*, 2014).

However, only the basics of sulfate mineralogy (polyhydrated sulfates, jarosite), texture (ridged, layered), and stratigraphic position have been previously reported (*Ehlmann and Mustard*, 2012). What is the extent of this sulfate unit? How did it form? What controls the layering, ridges, and specific sulfate mineralogy? These questions hold particular significance because at the time of this writing, the NE Syrtis landing site is under consideration by the Mars-2020 rover mission and the sulfates and Syrtis Major lavas are the key extended mission target.

In this paper, we examine the structural geology of the layered sulfates at NE Syrtis to determine their emplacement mechanism. We comprehensively map the sulfate unit's extent, thickness, bedding characteristics, ridge characteristics, and mineralogy. We further examine the contact relationships with units above and below, evaluate the capping materials, and determine the temporal relationship with regional fluvial features. We then evaluate these observations of the NE Syrtis Major layered sulfates critically against the range of possible formation mechanisms and propose a multistage formation and modification history that implies a significant role for water on the surface of Mars over a long period of time.

5.2 Geologic context

5.2.1 Physiography

The study area is situated on the western rim of Isidis Basin, about 40 km southwest of Jezero crater and along the northeastern margin of the Syrtis Major volcanic province [Figure 5.1 and Figure 5.2]. The layered sulfates are exposed just inside the sharp topographic inflection that marks the 1100-km diameter inner ring of Isidis Basin, as defined by *Mustard et al.* (2007), based on the concentric tectonic expressions of post-Isidis faulting that comprise the Nili Fossae (*Wichman and Schultz*, 1989; *Ritzer and Hauck*, 2009).

Broadly, both the Syrtis Major lavas south of the study area and the bedrock peneplain of Noachian units extending north of the study area gently slope into Isidis basin. East of the study area, elevations decline into the knobby plains of Isidis basin and the Vastitas Borealis formation (*Ivanov and Head*, 2003; *Ivanov et al.*, 2012).

In contrast, the study area itself contains a relatively abrupt topographic step from highland units at -0.5 to 0 km, which define the inner ring of Isidis basin, to flat-bottomed valleys with floors at less than −2.5 km on the Mars Orbiter Laser Altimeter (MOLA) datum (*North Basin* and *Deep Basin* on Figure 5.2). The valleys are bounded by exposures of highland crust that form mountains up to 1.5 km higher than the surrounding terrain. The degree of east-west topographic variation within the study area contrasts with smooth east-west slopes into Isidis basin to the north and south. The steep basin rim in our study area could be inherited from basin formation or modified by valley erosion. A major valley cutting across the innermost Nili Fossae graben [Figure 5.2, "I-80" from *Harvey and Griswold* (2010)] cuts the Isidis crater rim and channelized distal Syrtis Major lavas into the northwest portion of the study area. Southeast of the study area, a topographic scarp at ~-3.5 km is cut into the outer edge of the Syrtis Major lavas. This scarp contin-

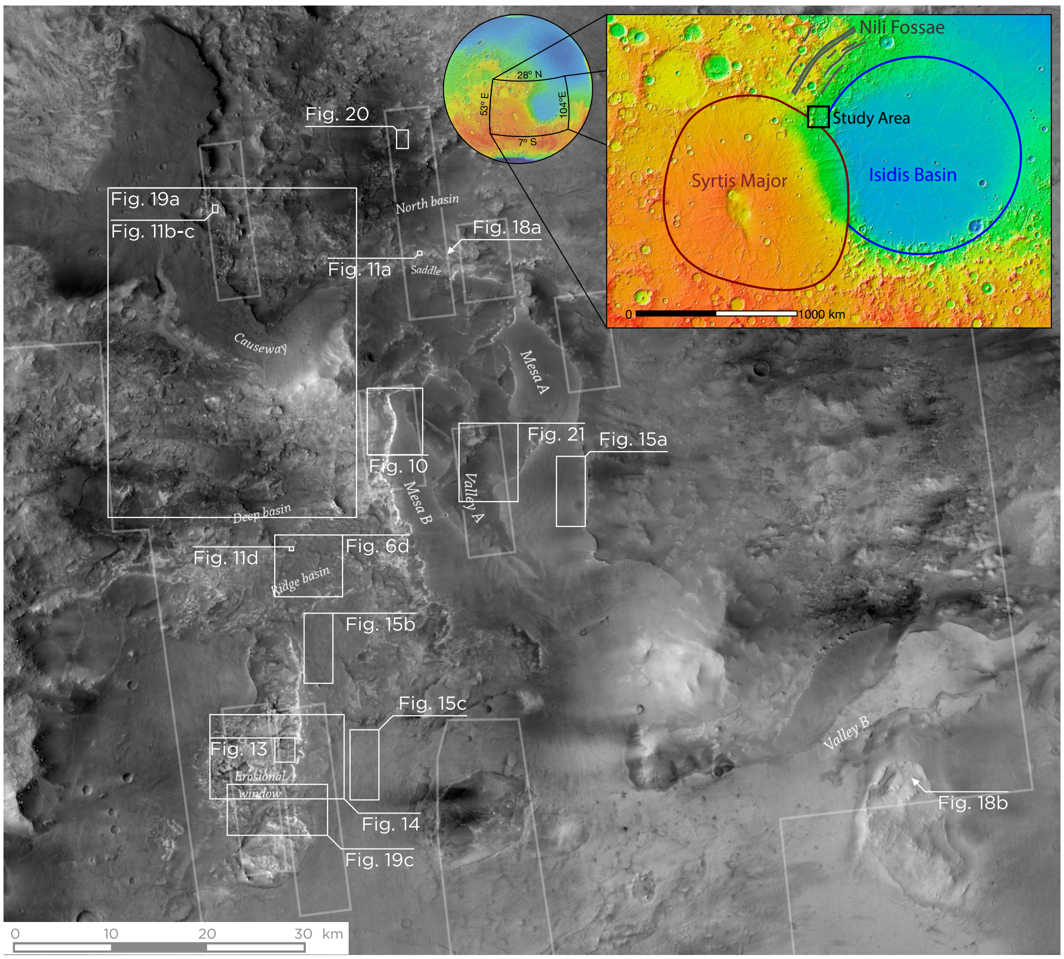

Figure 5.1: CTX mosaic of the study area showing the location of elevation models and figures referred to in text. The unofficial names used to refer to physiographic features in this study are shown.

ues southward and represents erosional modification of the basinward edge of the Syrtis Major volcanic province (*Ivanov and Head*, 2003).

5.2.2 The Northeast Syrtis plains

We will refer to the bedrock peneplain of Noachian units as the NE Syrtis plains. The NE Syrtis plains are the lowest exposed stratigraphic units and consist of two lithologic units. A low-calcium pyroxene- and Fe/Mg phyllosilicate-enriched bedrock (the 'basement') comprises the lowermost unit. The phyllosilicate-bearing hydrated basement contains exposures of megabreccia related to the Isidis-Basin-forming impact (*Mustard et al.*, 2009). It was formed and/or modified by the Isidis Basin impact, which was in the Early to Middle Noachian (*Werner*, 2008; *Frey*, 2008). The basement is unconformably overlain by a later-emplaced, olivine-enriched unit partially altered to carbonate (*Hoefen et al.*, 2003; *Hamilton and Christensen*, 2005; *Mangold et al.*, 2007; *Koeppen and Hamilton*, 2008; *Mustard et al.*, 2007, 2009; *Ehlmann et al.*, 2008a, 2009). Both of these units are determined to be Noachian in age because they are disrupted by tectonics associated with the opening of the Nili Fossae graben (shortly after Isidis; *Wichman and Schultz* (1989)) and are dissected by Noachian-aged valley networks, including the Jezero valley system (*Fassett and Head*, 2005, 2008; *Mangold et al.*, 2007; *Ehlmann et al.*, 2008b; *Schon et al.*, 2012; *Goudge et al.*, 2015).

Bramble et al. (2017) completed a geomorphic mapping study of the beveled NE Syrtis plains directly to the north of the study area (in the area of interest for the candidate Mars 2020 landing site), focusing on relationships between the Nili Fossae basement, olivine-carbonate unit, and overlying capping mesas. Though these two units in the NE Syrtis plains are clearly distinct and well-resolved from orbital mapping, this study treats them collectively as "Noachian highlands" units stratigraphically below the sulfates.

5.2.3 Layered sulfates

The layered sulfates are layered basaltic-composition materials enriched in polyhydrated sulfates relative to other materials. While the Noachian plains are found over a >100 000 km^2 area, layered sulfates are uniquely preserved and exposed at the northeastern margin of the Syrtis Major lava flows (*Ehlmann and Mustard*, 2012). The layered sulfates unconformably overlie the Noachian plains. They are layered at meters-scale, thick (>300 m in several places), and exposed recessively beneath a cliff-forming capping unit(s), previously interpreted to be the Syrtis Major lavas. These layered domains have mineral signatures of polyhydrated sulfates. In parts of the region, the sulfates are cut by a boxwork of polygonal raised ridges, which show near-infrared spectral signatures of jarosite, signifying acidic (pH < 4) aqueous conditions and a distinctive change relative to the clay and carbonate minerals formed earlier in the NE Syrtis plains (*Ehlmann and Mustard*, 2012). The sulfates are exposed at the southeast margin of the area mapped by *Bramble et al.* (2017) (their *feature-bearing slope* and *raised boxwork ridges*). The formation of these layered sulfates and their modification by subsequent events are the focus of this work.

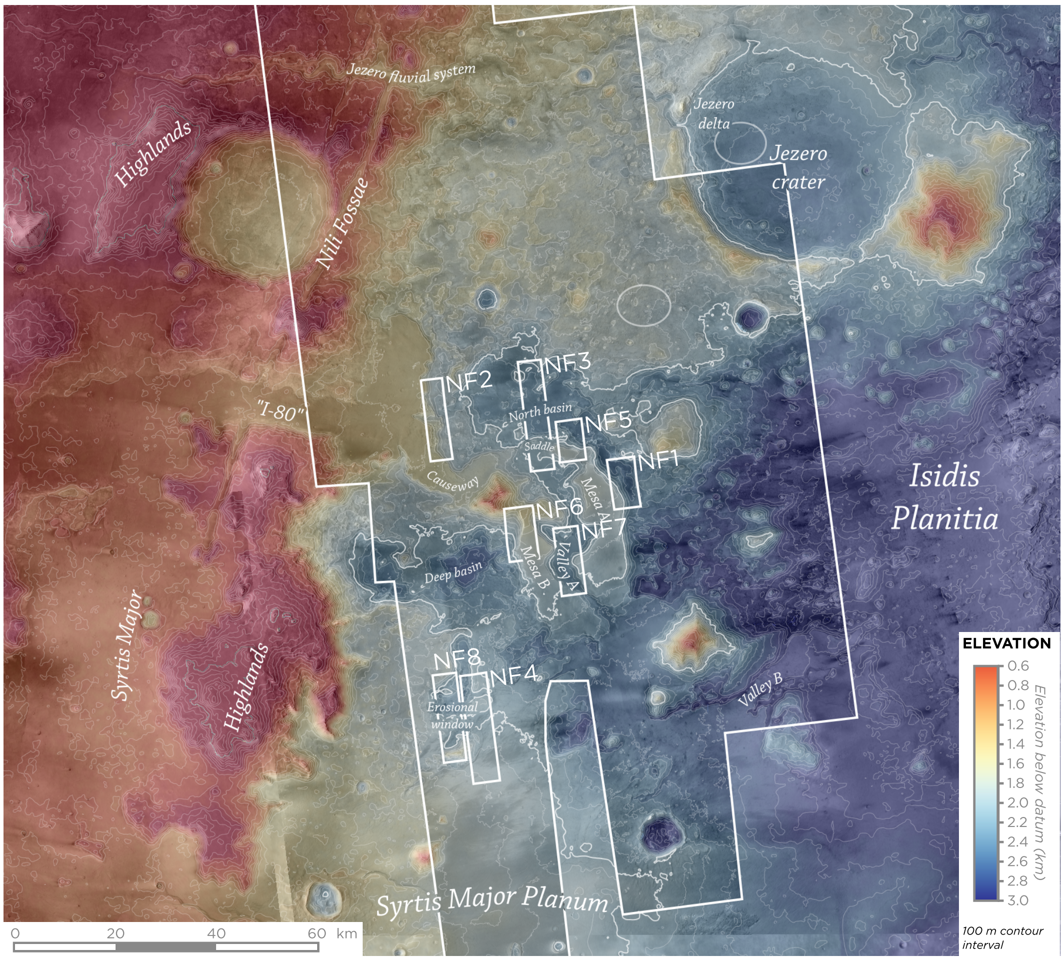

Figure 5.2: Context map of the NE Syrtis region. The white outlines `nf1`-`nf8` and the larger regional outline show the nine elevation datasets prepared for the study using HiRISE and CTX stereo images, respectively [Table 5.1]. A CTX mosaic basemap is color shaded by elevation to show the broad topographic context of NE Syrtis. For elevation shading, our study-created elevation models are supplemented by HRSC elevation models outside the study area. The names of major physiographic features, including unofficial names assigned in this study, are shown. The working landing ellipses for the Jezero and NE Syrtis landing sites (as of late 2017) are also shown.

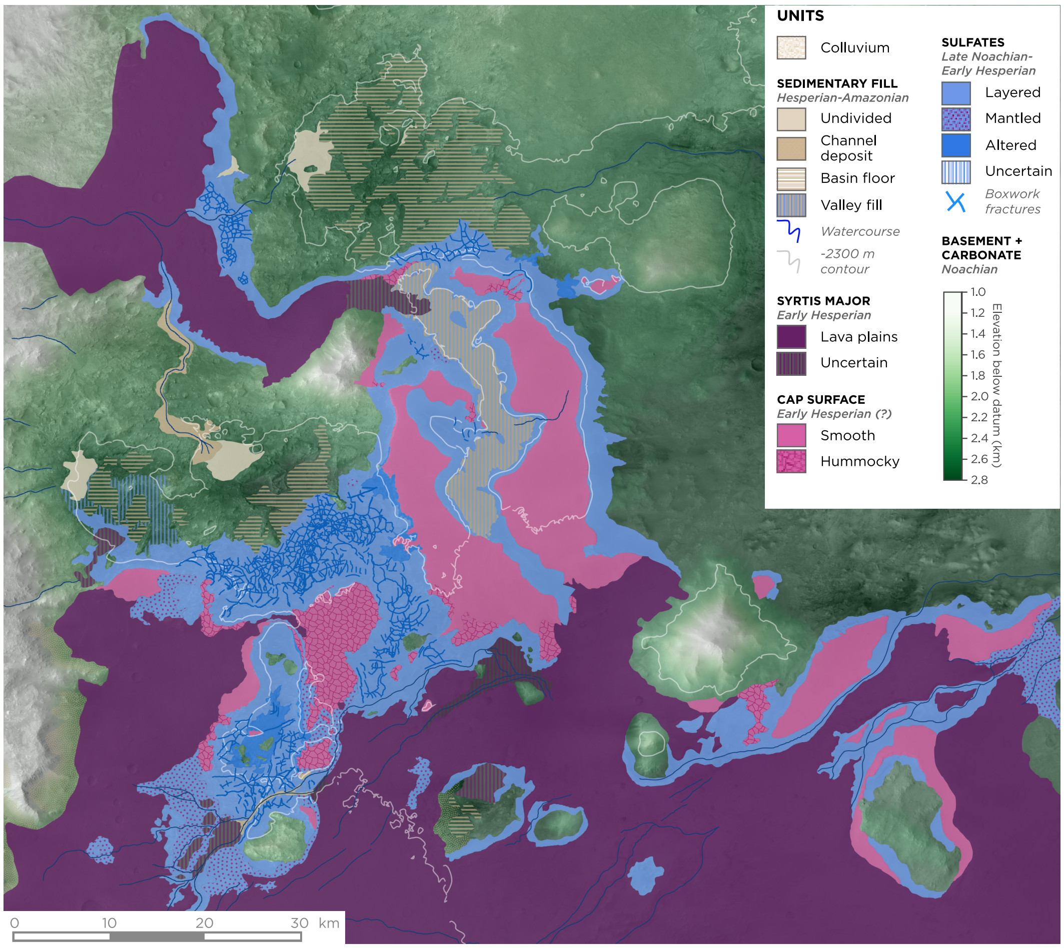

Figure 5.3: Geologic map of the layered sulfates, Syrtis Major lavas, and capping and sedimentary units discussed in this study. This map compliments that of *Bramble et al.* (2017), which focuses on basement morphologic units in the Northeast Syrtis plains, just to the north of this map area. Here, the basement and olivine-carbonate unit of the northeast Syrtis regional stratigraphy are undivided, while sulfates, capping materials, and Hesperian/Amazonian sedimentary deposits are detailed.

5.2.4 The Syrtis Major lavas

To the south, the Isidis rim is covered by the Syrtis Major volcanic province, a ~1100 km (E-W) region of effusive lava flows averaging ~500 m thick (*Hiesinger and Head*, 2004) which extends eastward into Isidis basin. Syrtis Major lava flows are sourced in the vicinity of Nili Patera and Meroe Patera near 8°N, 67°E (*Fawdon et al.*, 2015) and descend westward into Isidis Basin, extensively blanketing its rim to the south of the study area (*Ivanov et al.*, 2012). The Syrtis Major edifice has been dated to the early Hesperian by crater counting, with model ages ranging from 3.4 Ga (*Skok et al.*, 2010) to 3.6 Ga (*Hiesinger and Head*, 2004). The Syrtis Major lava flows are enriched in high-Ca pyroxene and distinct from the low-Ca pyroxene basement alteration (*Baratoux et al.*, 2007; *Skok et al.*, 2010; *Clenet et al.*, 2013), but in contrast to the Noachian plains to the north, no crystalline hydrous minerals are seen in orbital infrared remote sensing data.

The Syrtis Major lavas are the stratigraphically highest unit in portions of our study area, and their relatively unaltered character suggests that they postdate pervasive aqueous alteration in the region. Nevertheless, the margin is eroded by numerous fluvial channels and valleys that point to Hesperian and/or Amazonian surface waters, at least episodically after lava emplacement. *Mangold et al.* (2008) identified outflow channels inscribed on the surface of the Syrtis Major lava flows near the southern margin of the study area, where canyons and channels are cut into the edge of the Syrtis Major lava plains. These form an outflow system originating west of the study area and flowing south and east towards Isidis basin, demonstrating hydrologic systems postdating the emplacement of the Syrtis Major sequence.

5.3 Methods

5.3.1 Conceptual Approach: Formation mechanisms for the layered sulfates

The polyhydrated sulfates within the layered sulfate unit are not indicative of specific aqueous geochemical conditions (*Ehlmann and Mustard*, 2012), and jarosite within the ridges indicates only precipitation from acidic waters (*Papike et al.*, 2006; *Ehlmann and Mustard*, 2012). Precipitation of sulfate minerals can occur both subaerially during evaporitic deposition (e.g. *Hurowitz et al.*, 2010) and due to pore-occluding cementation by groundwater circulation (e.g. *Siebach and Grotzinger*, 2014). Consequently, both polyhydrated sulfates and jarosite-bearing ridges may record an alteration signature do not uniquely distinguish the original depositional environment for the sulfate-bearing sediments.

Examination of physical characteristics of the layered sulfates provides a separate set of metrics for use to understand the formation and evolution of the unit. A wide range of potential mechanisms has been invoked for the deposition of layered rocks on Mars (*Grotzinger and Milliken*, 2012), each of which possesses distinctive structural characteristics that are potentially observable at orbital scale [Figure 5.4].

Volcanic origin scenarios such as lava flows, ash flows, and ash falls have been

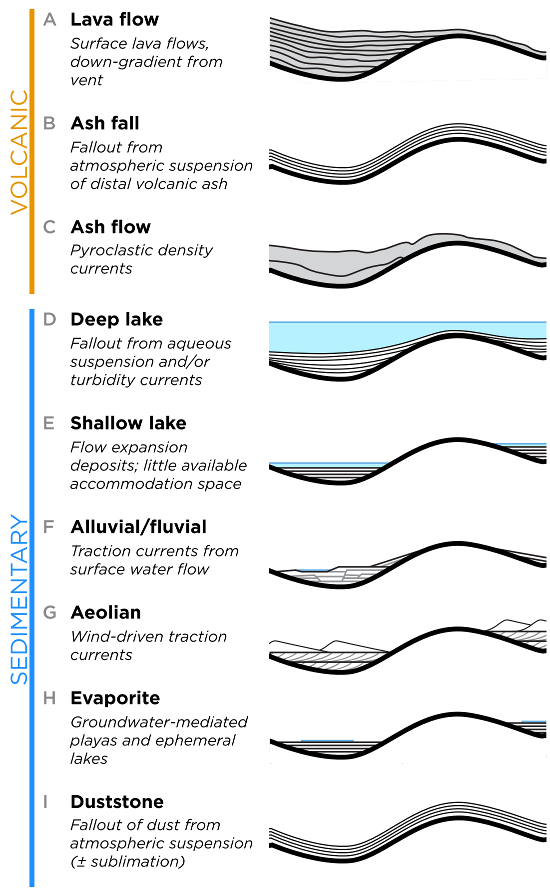

Figure 5.4: A graphical summary of depositional settings proposed for layered deposits on Mars, with applicability to the layered sulfates. Each potential mechanism varies in the structure and style of bedding predicted, which can be diagnostic of the unit's original form.

proposed for layered deposits elsewhere on Mars (e.g. *Kerber et al.*, 2012; *McCollom et al.*, 2013). These emplacement mechanisms do not require abundant surface water; their potential alteration to sulfates could be enhanced by the circulation of volcanic hydrothermal fluids (e.g. *Kaasalainen and Stefánsson*, 2011). Lava and ash deposits are typically thick and internally jointed (*Bondre et al.*, 2004), and lavas are usually erosionally resistant.

Layered sedimentary sulfate deposits can form by the primary precipitation of evaporite sediments or by sulfate cementation of detrital sediments. Layered sediments can arise from different physical processes, implying a range of fluvial-lacustrine, aeolian, and dust-dominated depositional settings. Rover (*McLennan et al.*, 2005; *Grotzinger et al.*, 2005) and orbital (*Milliken et al.*, 2014) studies indicate the presence of sulfates in layered deposits in lacustrine, evaporite playa, and reworked eolian settings. In these environments, sediment transport is dominated by traction currents (along with sulfate precipitation in the playa case). In deep lacustrine settings, transport is dominated by sediment density currents and fallout from aqueous suspension. "Duststone" models of sedimentation (*Lewis et al.*, 2008; *Bridges and Muhs*, 2012) imply the fallout of particles from aerial suspension. A related model also incorporates icy aerosols that sublimate after settling (*Michalski and Niles*, 2012). The different potential origins for the layered deposits have radically different implications for geological processes and the surface water budget at the time of emplacement.

Contact relationships and bedding orientations are key measures of the internal geometry of sedimentary sequences that distinguish depositional processes and their timing. Certain types of sedimentary sequences have characteristic limitations on the distribution of bedding orientations (i.e., strike and dip) imposed by their depositional process. Other important criteria include the assessment of sedimentary onlap and downlap onto pre-existing surfaces, versus bedding entirely concordant or draping topographic highs. For example, traction-current sediments (e.g. shallow lacustrine deposits) typically onlap pre-existing topography as they aggrade, while fallout of suspended sediment (e.g. ash falls, duststones, and deep lacustrine sediments) form draping, concordant layers. Subaqueous basin-margin sedimentation occupies an intermediate case, where dipping sediments are emplaced by both density currents and fallout from suspension; these sediments are sometimes base-concordant but often thin over, onlap, and in some cases embay basement highs (*Mitchum et al.*, 1977).

The origin of the layered sulfate unit and its relationship to the overlying Syrtis Major lavas remains enigmatic. In this work, we attempt to determine the formation mechanism and post-depositional history of the layered sulfate unit primarily from its structural characteristics.

5.3.2 Digital elevation models and dataset registration

Images from the HiRISE instrument on the Mars Reconnaissance Orbiter (*McEwen et al.*, 2007) were acquired covering key parts of the study area. Overlapping pairs of images were acquired with one near-nadir and one oblique image for stereo convergence angles of 15°-30° [Table 5.1]. These stereo pairs were processed us-

Table 5.1: HiRISE and CTX scenes used in elevation models

ID	Nadir	Oblique	CA[a] (°)	EP[b] (m)
HiRISE				
NF1	PSP_009217_1975	ESP_027625_1975	18.4	0.15
NF2	ESP_018065_1975	ESP_019133_1975	22.5	0.12
NF3	ESP_026280_1975	ESP_027902_1975	13.0	0.21
NF4	PSP_002809_1965	PSP_006000_1965	24.9	0.11
NF5	ESP_013041_1975	ESP_030025_1975	17.3	0.16
NF6	ESP_021612_1975	ESP_021757_1975	11.8	0.24
NF7	ESP_027269_1970	ESP_042671_1970	21.3	0.13
NF8	ESP_047194_1965	ESP_046983_1965	12.9	0.22
CTX (single multistrip elevation model)				
	G21_026280_1976	D02_027902_1975	13.2	5.1
	B01_010206_1975	B03_010628_1974	15.7	4.3
—	*same as above*	G02_019133_1977	13.5	5.0
	G09_021612_1972	G09_021757_1972	11.9	5.7
	B18_016720_1978	B18_016786_1978	22.0	3.0
	B19_016931_1975	B19_017076_1975	14.0	4.8
	D14_032504_1996	D14_032649_1996	14.8	4.5
	P15_006778_2002	D17_033849_2002	22.9	2.8
	D14_032715_1995	D15_033137_1996	20.2	3.3
	G11_022680_1976	G12_022746_1976	23.2	2.8
—	P05_002809_1975	P13_006000_1974	24.8	2.6

[a] Convergence angle
[b] Expected vertical precision (assuming resolution of 0.25 m/px for HiRISE and 6 m/px for CTX)
— Not acquired as a stereo pair

ing standard pipelines, and digital elevation models (DEMs) were created in the SOCET SET software using the techniques described in *Kirk et al.* (2008). In this pipeline, the stereo images are individually photometrically corrected and horizontally and vertically controlled to the Mars Orbiter Laser Altimeter (MOLA) datum. MOLA shot data are used to correct the elevation of ground control points, and the gridded MOLA DEM is used to anchor the DEM solution. In total, eight HiRISE stereo models were constructed, typically covering 5 ×10-20 km areas of the surface in overlapping HiRISE scenes at a ground sample spacing of 1 m/px. Relative vertical accuracy is ~0.25 m in textured areas of the scenes (based on the *expected precision* metric of *Kirk et al.* (2003) and their estimate of 0.2 px typical image-registration accuracy within SOCET Set). The resulting elevation models were used to create 0.25 m/px orthorectified images aligned exactly to the DEM.

In addition to the HiRISE DEMs, a single CTX DEM covering the entire study area was constructed using 21 images from 11 overlapping stereo pairs. The dataset was prepared in SOCET SET using methods that closely followed the procedures used for HiRISE, and resulted in a DEM with 10 m/px horizontal scale and ~5-20 m vertical fidelity, varying based on the specific stereo pair.

The scale gap between HiRISE and MOLA can produce systematic bias when MOLA data is sparsely sampled, especially in the presence of N-S (along-track) sloping topography. Our CTX DEM is not susceptible to such bias due to its much larger coverage area, allowing its use as an external check on the whole-image tilt of the HiRISE DEMs. Elevation models `nf1`, `nf2`, and `nf4` had negligible slope, but `nf3` and `nf5` at the northern margin of the study area had artificial southward slopes of ~0.25 and 0.38°, respectively, corresponding to elevation differences of 30-100 m within *North Basin* relative to CTX. HiRISE elevation models `nf6`-`nf8` were explicitly controlled to the CTX DEM during creation, removing this source of error. These tilts are much smaller than dip magnitudes measured in this study, but do limit the precision with which true horizontality can be recovered.

The internal quality of stereo DEMs varies based on the stereo convergence angle between scenes. Also, image-matching algorithms perform better on areas with fine-scale surface features. In general, DEM quality is much higher in areas with significant slopes and high local contrast. DEM errors are summarized by the "Figure of Merit" dataset produced by SOCET SET. Errors can additionally be visually inspected using contour lines (following procedures described by *Kirk et al.* (2003)). Areas with errors were avoided for our quantitative analyses, but all areas have sufficient data quality for 3D visualization. The CTX DEM suffers from noise for images with low-contrast or poor stereo separation. This manifests as noisy, discontinuous contours and uneven topography in 3D model views. The poorer results of this registration are propagated through our elevation models and are responsible for larger error ellipses on some bedding poles for CTX images e.g. 5.3.4.

Each topographic dataset (consisting of a DEM, quality metrics, and aligned orthoimages) is warped to a transverse mercator projection centered on 76.5° to retain angular conformality and approximate true scale over the study area. The datasets were coregistered using significant shared landmarks to build a unified geodetic framework tied to regional CTX imagery. The result is a network of aligned images forming a regionally consistent basemap of the study areas. Other imagery datasets, such as thermal inertia, imaging-spectrometer, and non-stereo HiRISE images, were aligned to this framework.

The DEM and imagery basemap was integrated into a 3D computer vision system with a NVIDIA 3D Vision system used for stereo display. HiRISE and CTX stereo pairs were examined in their original viewing geometry using SOCET Set photogrammetry software, and synthetic stereo reconstructions [e.g. Figure 5.6a] were created using the OSGEarth 3D toolkit to examine the region from arbitrary oblique viewpoints.

5.3.3 Regional mapping

The morphological character of the layered sulfates and surrounding units was evaluated in detail within the 8 HiRISE stereo pairs used in the project, and their local character is correlated to larger-scale features visible in CTX orthoimages. Regional mapping across all images focused primarily on the internal character of the layered sulfates and on the nature of capping units. Map units were identified based on their morphological characteristics, and small-scale features from HiRISE scenes were extrapolated into CTX data. Morphological identification of map units is augmented by Compact Reconnaissance Imaging Spectrometer for Mars (CRISM) hyperspectral data (*Murchie et al.*, 2007). In areas with available CRISM coverage, morphological mapping was cross-correlated with spectral data for verification. Spectra were ratioed to relatively featureless terrains to accentuate the compositional differences in the area of interest. These ratioed spectra were classified broadly into spectral types. The sulfate units have characteristic absorbtions for jarosite and polyhydrated sulfates [Figure 5.5].

Contacts between map units, morphological features indicative of channels, and over 850 km of boxwork fractures were mapped. Within the layered sulfates, surface traces of bedding were captured for the structural interpretation of the layered sulfates. Polygonal swatches of surficial units are captured to estimate the orientation of unit surfaces. Mapped contacts are correlated with the topographic dataset to create elevation constraints on the top and bottom of the layered sulfates, which can be interpolated throughout the study area to form a 3D structural model of the layered sulfates before large-scale erosion of the unit.

5.3.4 Orientation measurements

To understand stratal relationships, bedding orientations are typically evaluated alongside outcrop-scale observations of angular relationships along a contact. However, where the contact is obscured (as is often the case in remote sensing), the local nature of the contact between sedimentary packages must be assessed using bedding orientation differences observed in portions of units in isolation. This approach has been employed since the advent of seismic stratigraphy (*Mitchum et al.*, 1977), including on Mars. For instance, angular relationships and approximate unit bounding surfaces have led to the identification of downlap surfaces associated with prograding sedimentation in the nearby Jezero Crater deltaic system (*Schon et al.*, 2012; *Goudge et al.*, 2017) and other deltas on Mars (*Lewis and Aharonson*, 2006; *DiBiase et al.*, 2013).

In order to compare structural data collected from differently oriented hillslopes and DEMs with different levels of inherent accuracy in the NE Syrtis sulfates and capping units, we have developed a new statistical approach and software pipeline for making orientation measurements in the presence of errors. This technique is described in detail in [*Quinn and Ehlmann* (2017); *Quinn and Ehlmann* (2018); submitted]. In brief, we use principal-components regression to fit planes to DEM data points, form error distributions for planar estimates, and convert these errors to major- and minor-axis error bounds in spherical coordinates. These errors are hyperbolic error bounds on a nominal plane, or ellipsoidal error bounds around the normal vector to the plane. This new technique allows us to build a regional database of comparable bedding orientation measurements of geologic units with statistically rigorous error bars to assess the quality of calculated strikes

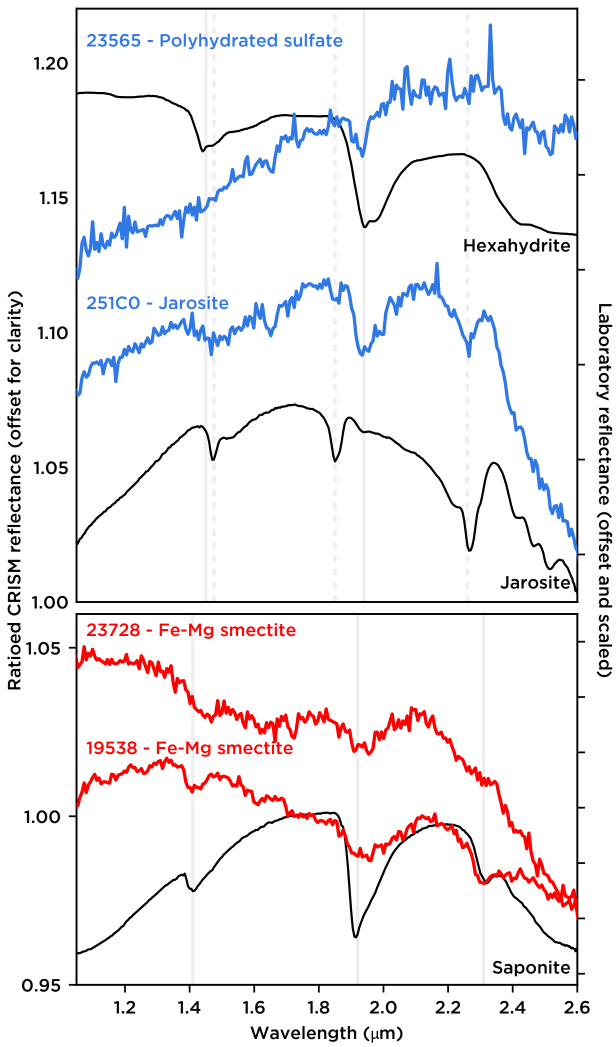

Figure 5.5: Examples of CRISM spectra used to verify new mapping of the layered sulfates and surrounding units at several locations within the study area. CRISM scenes are identified by 5-digit ID, and mineral identification is shown. Laboratory reflectance spectra shown for comparison are from Brown RELAB, available at `http://psf.uwinnipeg.ca/Sample_Database/`). The top panel shows sulfate identifications, and characteristic absorbtions for polyhydrated sulfates (solid) and jarosite (dotted) are shown as vertical lines. The lower panel shows smectite clay identifications in late sedimentary deposits [Section 5.4.5], with characteristic absorbtions for smectite clay shown as vertical lines.

and dips.

Uncertainties are higher for CTX than HiRISE, reflecting high levels of noise in low-relief areas and between poorly-registered image pairs in the CTX DEM. Within individual images, several techniques were used to find the local orientations of geologic units at high resolution. In several cases, beds could be traced and evaluated individually. In other cases, individual bedding traces do not form a 3D exposure adequate to capture a unique bedding orientation. To mitigate this, closely-spaced individual measurements were grouped under the assumption of parallel bedding within the same stratigraphy. The resulting jointly fitted orientation was tested against the residuals of each measured plane. Groupings with low out-of-plane variation are accepted as likely representative of the true dips of a consistent package of beds. An additional method used for several resistant units primarily exposed at the surface is the measurement of slopes of the current topographic surface. Absent differential erosion, which would impart tilt, surface orientations can be examined alongside outcrop-traced bedding measurements.

5.4 Results

5.4.1 The layered sulfates

Basic morphological and mineralogical characteristics The general character of the layered sulfates has been reported in previous investigations (*Ehlmann and Mustard*, 2012) and was used along with CRISM to map their full extent in the CTX and HiRISE basemaps. The sulfates are light-toned where exposed, exhibiting a polyhydrated sulfate mineral signature and continuous bedding with meter-scale thicknesses. Layers can be followed for several kilometers in a few cases [Figure 5.6a], but are often obscured by dark debris. The layered sulfates have been eroded to their present form by fluvial activity [Section 5.4.5].

Capping units and post-deposition alteration appear essential for the sulfates' preservation. The layered sulfates are recessive in general, and are only preserved where beneath more resistant caprock or buttressed by polygonal ridges, forming slopes otherwise. Locally, ridged [Figure 5.6c] regions of the layered sulfates show strong signatures of jarosite mineralogy (as previously reported for select locations in *Ehlmann and Mustard* (2012)) and are more resistant to erosion. We have also found jarosite in a horizon with localized pervasively altered sulfate that appears texturally distinct [Section 5.4.3]. Craters are not generally preserved in the sulfate unit, potentially due to continuous refreshing of the surface of the unit by scarp retreat.

Extent The layered sulfates are exposed over ~100 km east-west along the transition zone between the Syrtis Major lava flows and the Noachian Plains. They extend from ~74-76°E and ~14-16°N. Their northern boundary can be mapped but the southern boundary is not fully characterized, as it lies beneath the Syrtis Major lava flows. The southernmost well-characterized exposure is within an erosional window at 74°E, 14°N. The layered sulfates range in elevation from −1600 m to −2800 m at their southeastern eroded margin. The highest exposures of the layered sulfates broadly coincide with the elevation of the regional topographic step

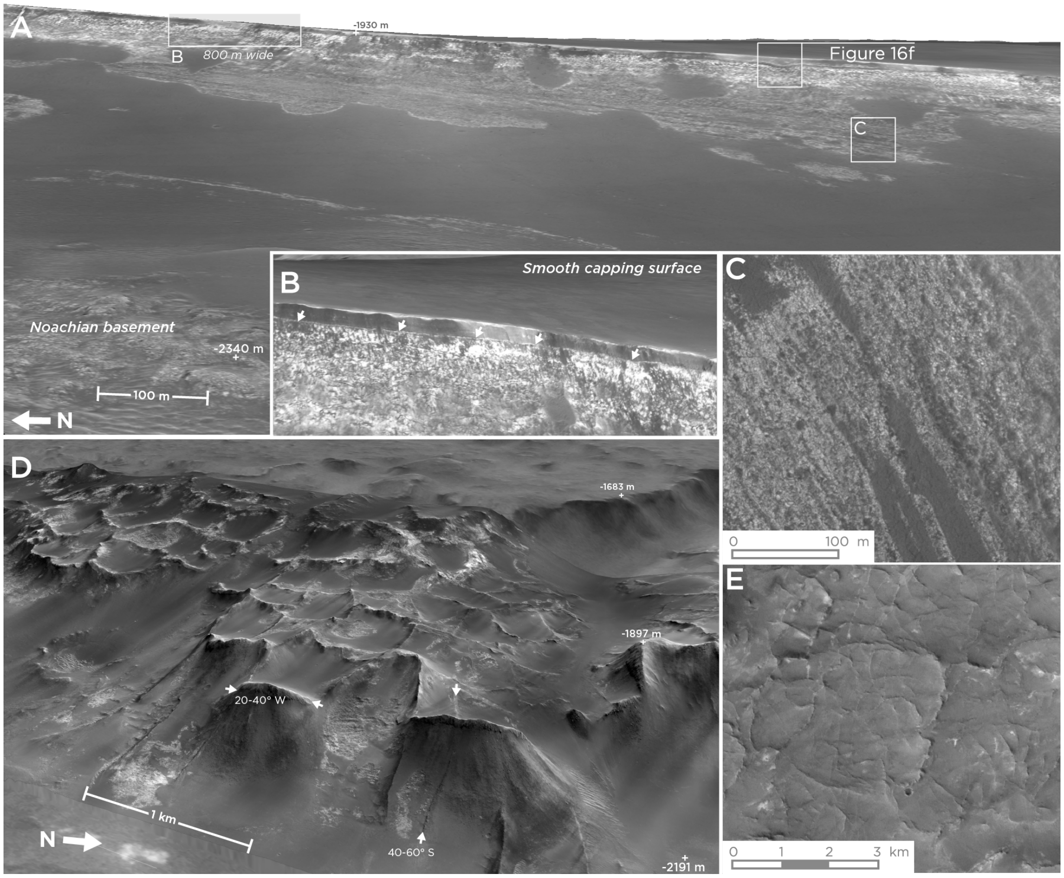

Figure 5.6: Examples of key morphologies of the layered sulfates. **(a)** HiRISE stereo (`nf6`) perspective image of a 2.7 km segment of the west face of Mesa B (no vertical exaggeration), showing a 400 m thick stratigraphy of layered sulfates beneath the "smooth capping surface." The beds in this stratigraphy dip consistently at ~7° to the southwest [Figure 5.10]. **(b)** Oblique view (2× vertical exaggeration) of an 800-meter segment of the bright top contact of the layered sulfates beneath the darker "smooth capping surface." Arrows show truncations of bedding by the contact. **(c)** Plan-view image of typical bedding features in the layered sulfates. **(d)** HiRISE stereo (`nf2`) perspective image of boxwork polygons, which cover large parts of the study area and have a characteristic scale of ~500 m on a side. The approximate dips (within error) of several relatively planar boxwork fracture segments are shown. **(e)** CTX map view of boxwork ridge network in the *Ridge Basin* area of the unit.

that defines the inner ring of Isidis basin.

We construct a 3D model of the layered sulfates using simple structural rules constrained by mapping data. First, contacts between the layered sulfates and other map units provide direct elevation constraints on the top and bottom boundaries of the layered sulfates [Figure 5.7a]. Contacts with the Syrtis Major lavas and other capping units represent the top surface of the sulfates, and contacts with the NE Syrtis plains units form its base. In select locations, both contacts are exposed in close proximity, allowing a direct measurement of thickness. Unconformities where a capping surface instead directly meets the basement constrain both the top and bottom surfaces of the sulfates, i.e., indicating places where they are absent. Additional constraints on the bottom surface of the sulfates are imposed in some covered areas to improve the smoothness of the overall result and mitigate the shallowing bias on the sulfates imparted by contacts on localized Noachian basement highs.

Second, the interpolated surfaces are constructed using kriging, a statistical procedure commonly used for interpolating geological surfaces (e.g. *Oliver and Webster*, 1990; *Caumon et al.*, 2009). The kriging model is implemented on a 200 m grid using the Python program `PyKrige`. Separate kriged surfaces for the top and bottom of the layered sulfate are interpolated beneath present topography and projected into space to model the extent of the layered sulfates in areas they likely occupied in the past but were since eroded. The uncertainty of each surface is calculated based on the RMS distance to the nearest control point.

The interpolated structural surfaces provide key limits on the regional form and thickness of the layered sulfates. The sulfates form a thick regional package that has been partially eroded in some areas. Cross-sections extracted along arbitrary axes through the structural model provide a means to assess the performance of the modeling approach and evaluate the deposit-scale character of the layered sulfates [Figure 5.8]. The layered sulfates have a variable thickness throughout the study area and embay and thin to zero against inherited highs of Noachian highlands topography. The sulfates have a mean thickness of 197 m, varying from 0 to a maximum of over 600 m over the topographic depression we term Deep Basin [Figure 5.7b]. Our structural model suggests a prior total volume of layered sulfates of 1245 km^3 within the ~5800 km^2 polygonal area with high-quality mapping constraints, with a volume of 460 km^3 (37%) still buried. These volume estimates constitute a minimum constraint on the original volume of the layered sulfates.

Bedding orientations Resolvable bedding traces in the layered sulfates were challenging to assess as they are only exposed in some areas, where broad hillslopes or the interiors of boxwork domains are stripped of debris cover. In many cases, instead of surface-exposed bedding planes that are ideal for measurement, the strikes and dips of sulfates were constructed from the trace of linear features on hillslopes. The quality of local bedding exposures provides varying levels of confidence in bedding between areas [Section 5.3.4]. A regional set of representative bedding orientation for sulfates and surface orientations for capping units was determined using measurements along outcrops that had low errors and agreed with

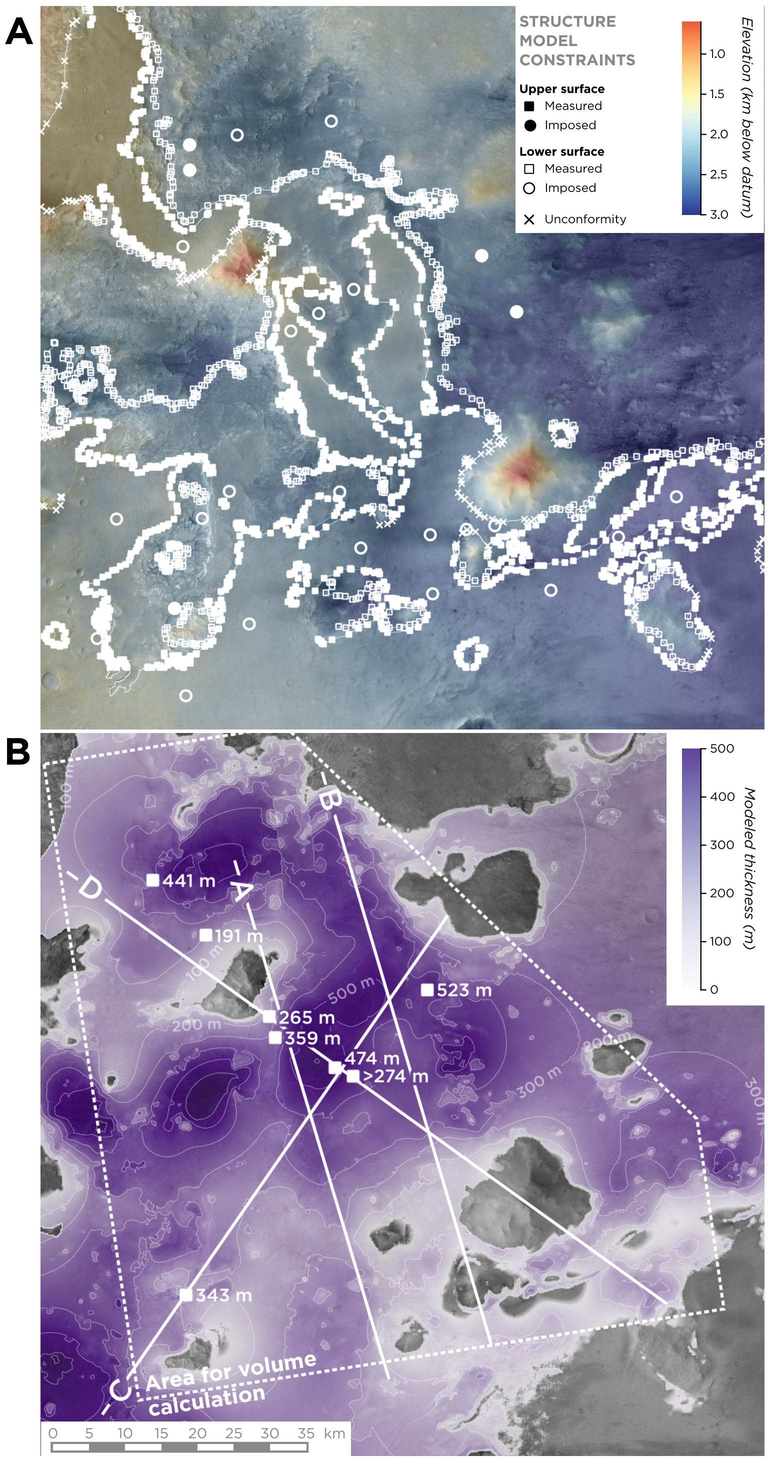

Figure 5.7: Maps of parameters derived from structural modeling of the top and bottom surfaces of the layered sulfate. **(a)** Point constraints used for the kriging model underlying the structural model (filled symbols also shown in Figure 5.8). These points are at the edges of the surface exposure of the layered sulfate and constrain the 3D volume of the unit relative to present topography. Additional constraints (open symbols) are imposed on the top and bottom surface of the layered sulfates to maintain consistent thickness in areas without exposures. **(b)** Modeled thickness of the layered sulfate prior to erosion of NE Syrtis mesas, showing the tapering of the deposit away from the center of the study area. Locations with known thicknesses (measured from the top to bottom of sulfate exposures) are shown numerically atop the kriged surface. Section lines for Figure 5.8 are shown.

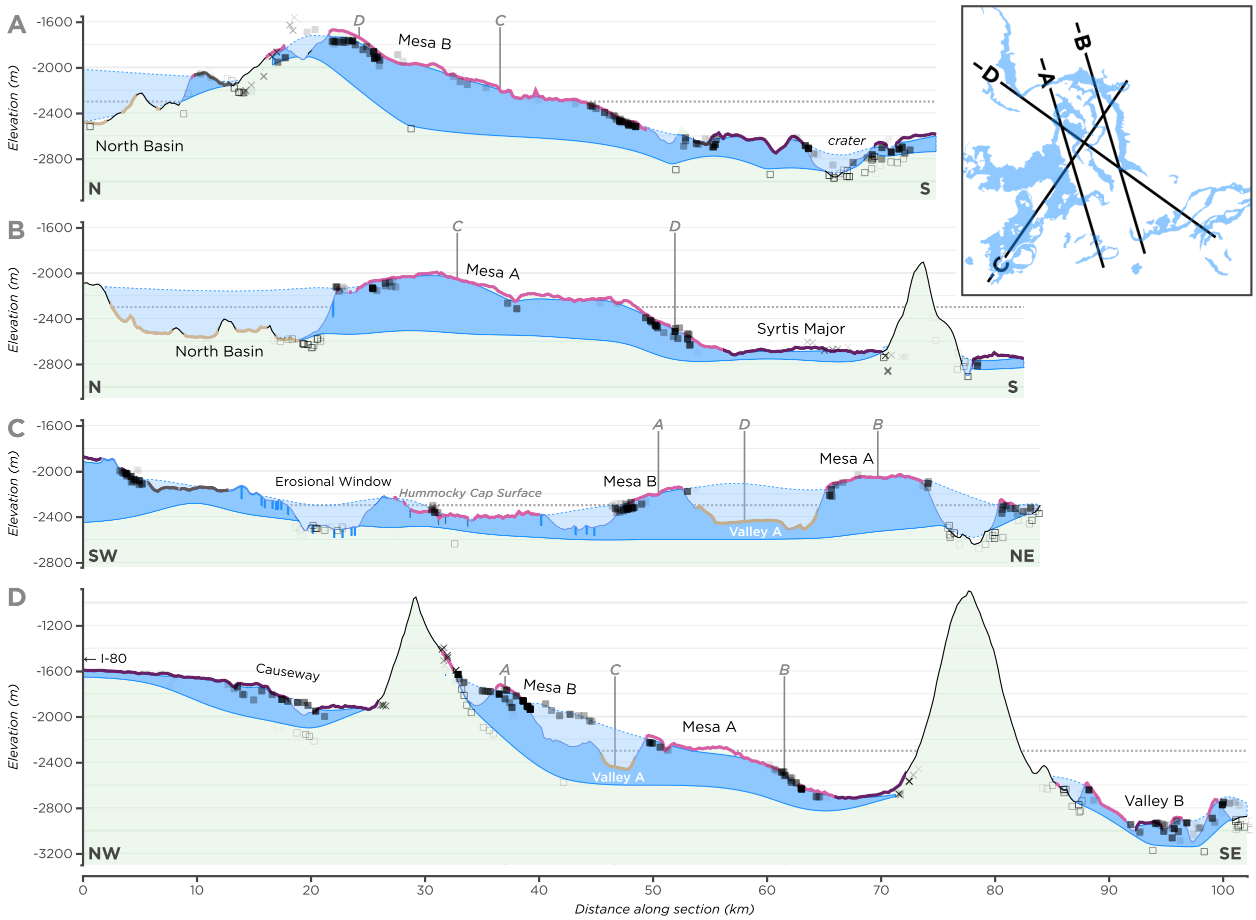

Figure 5.8: Cross-sections of the study area showing profiles through the layered sulfates created using the structural model [Figure 5.7]. Model constraints are shown on the section using the symbology of Figure 5.7, faded with distance from the section line, with constraints up to 2km away shown. All sections are at the same scale, with 10× vertical exaggeration. **(a)** A north–south transect through *Mesa B* showing the draping of the sulfates atop basement topography. **(b)** A north-south transect across Mesa A and the adjacent low-elevation *North Basin* and Syrtis Major lava flow surface. **(c)** A southwest–northeast transect showing the erosional window at the southwest of the study area, and Mesas A and B. **(d)** A northwest–southeast transect including both of the basement buttes and paleovalley relationships shown in Figure 5.18.

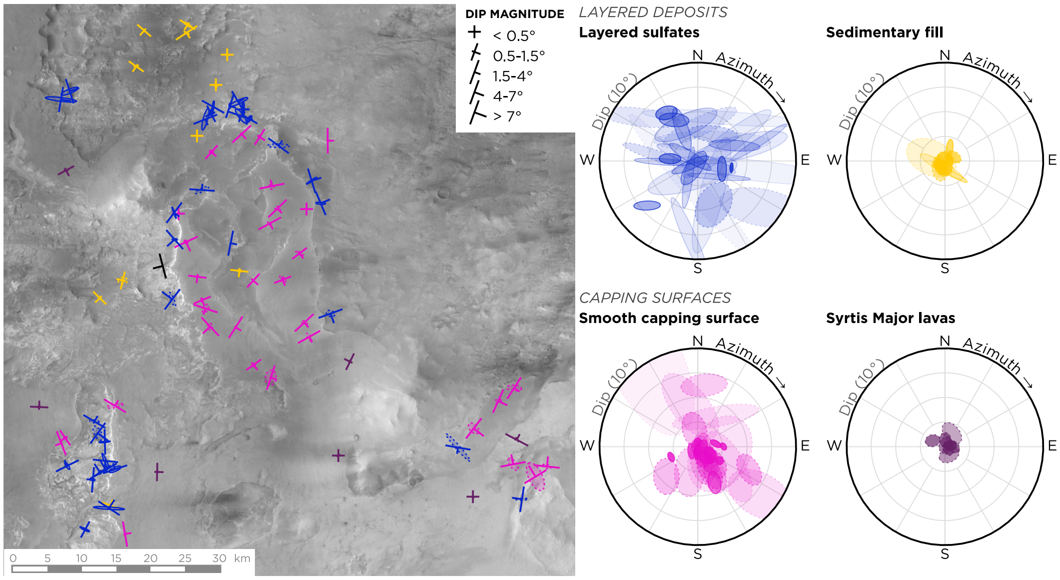

Figure 5.9: Representative bedding orientations for the study area showing the variation of dips within each class of units. On the map (left panel), nominal bedding orientations are underlain by error ellipses showing the direction of errors. Measurements derived from lower-resolution CTX data have a dotted error ellipse. These ellipses correspond to the data plotted to the right as poles to bedding on upper-hemisphere stereonets. Measured bedding orientations for sulfates and later layered deposits (e.g. late fluvial features) are shown along with surface orientations of the Syrtis Major lava flows and the smooth capping surface.

surrounding measurements [Figure 5.9].

Bedding within the layered sulfates always dips at low angles (<10° and usually <7°) in a variety of directions. There is no systematic trend in dips that might suggest that the orientation of the sulfate unit was modified by large-scale tilting or regional folding. Instead, the relatively wide range of dips measured within the layered sulfates suggests that the unit was not deposited as an originally flat surface. Some areas of the layered sulfates are nearly flat, such as near the northern boundary of the unit in `nf3` and `nf5`. Despite this, truly flat deposition is well outside of the confidence bounds for many individual measurements. Both CTX and HiRISE produce orientations with low-angle nonzero dips with a magnitude greater than measurement errors.

The layered sulfates onlap basement topography at both deposit- and bed-scale. The unit thins over and embays basement highs [Figure 5.8], and bedding often dips away from high topography as well. Bed-scale contact relationships are not directly resolvable from remote sensing but can be inferred from dip relationships: while individual beds may thin somewhat over localized highs, bedding dips shallower than and projecting into adjacent basement topography imply an onlapping relationship.

Relatively steep dips of 5-10° are persistent over large areas of the layered sulfates. For example, the ~7 km west-facing hillslope in `nf6` exposes a stratigraphy dipping 5-7° to the southwest [Figure 5.10]. Grouping bedding traces across the entire hillslope yields a maximum orientation error of <1°, consistent with a planar, dipping stratigraphy. Dips slightly steeper than the underlying basement surface suggest that the sulfate package may downlap at its base. The shallower slope of the capping surface above the sulfates [Section 5.4.4], which dips to the south instead of southwest, imply a low-angle unconformity between the two. Bedding truncations at the base of the cap are visible in draped HiRISE imagery [Figure 5.6b].

Although layers within ~5 km packages are often consistently oriented, these exposures differ substantially in orientation across the study area. In `nf7`, 5 km to the west of `nf6`, dips are consistently ~2-3° to the east. In `nf1`, still further west, layers dip ~5° northeast. Orientations may change gradually within a single stratigraphic package or at unconformities between relatively planar packages but this cannot be further addressed with current data.

Some exposures of the layered sulfates are less internally consistent, with variable bedding orientations at sub-kilometer lateral scale. In the northern part of `nf6`, dips shallow from ~7° (southwest-directed) to ~4° (south-directed) [Figure 5.10]. In the northern part of the *Erosional Window* (covered only by CTX topography), east-dipping exposures contain bedding traces that are kinked relative to their best-fitting plane, signifying localized variation. Discordant layer orientations at hundred-meter to 1-km scale are particularly evident in areas with abundant boxwork polygonal fractures, which we discuss further in Section 5.4.2.

5.4.2 Boxwork polygons

Boxwork polygonal ridges are a striking feature of parts of the layered sulfates. They occur in many areas including the central *Ridge Basin*, along the northern erosional margin of the unit, and in the southern *Erosional Window*. While geographically widespread in occurrence, they are found only patchily throughout the unit. For simplicity, we will discuss these ridge-forming features as fractures while we discuss the data supporting this classification.

Fracture morphology The boxwork polygons have a characteristic length scale of ~500 m and have strong positive relief with exposures defining ridges standing as much as 30 m above polygon interiors. The features have a significant vertical dimension within the layered sulfates: some single ridges continue through an elevation range of greater than 200 m [Figure 5.13]. In `nf2` and `nf5`, the boxwork features penetrate the entire ~400 m thickness of the unit [Figure 5.6d]. The thickness of the linear feature varies markedly between different examples of polygonal fractures. Some ridges are thin and have little topographic expression, while others are thick, prominent, and shed boulders [Figure 5.11].

Morphological features of the polygonal ridges suggest that they may be filled fractures instead of single-origin injective features. Many boxwork ridges show light-toned bands parallel to and on either side of the fracture centerline [Figure 5.11b-d]. This parallel-sided geometry varies from ~5 m [Figure 5.11b and c] to up to 20 m in width [Figure 5.11d]. Several examples show additional features such as a light-toned central zone ranging from ~1 to ~30 m across [Figure 5.11d] or a

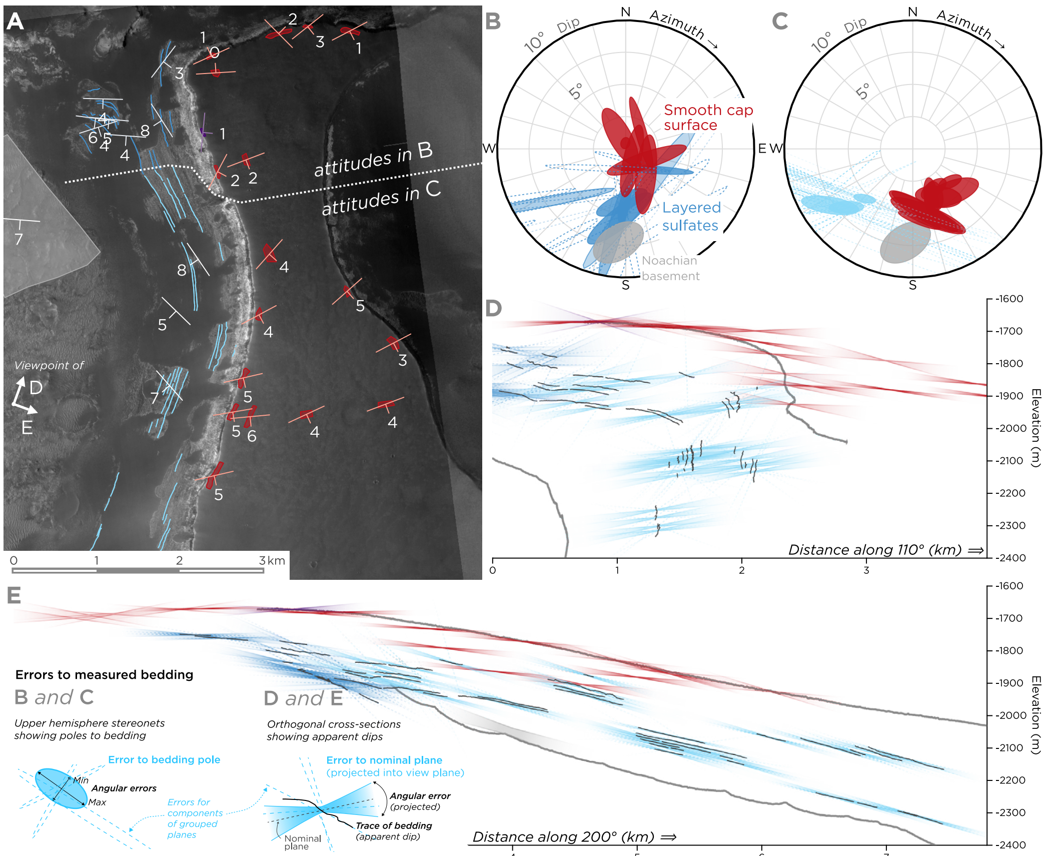

Figure 5.10: Bedding orientations collected for the top and west face of *Mesa B* in HiRISE orthomosaic `nf6`, showing the surface slope of the smooth capping surface in red and the layered sulfates in blue. **(a)** Map view of bedding orientations. **(b** and **c)** upper-hemisphere stereonets showing poles to bedding with error ellipses for the north and south parts of *(a)*, respectively. Dotted, unfilled ellipses represent components of grouped measurements. **(d** and **e)** Projections of the entire stratigraphy along orthogonal axes as shown in *(a)*, with apparent dips of bedding traces and hyperbolic error bounds to planar fits. The difference in orientation of the capping surface and layered sulfates suggests a low-angle unconformity at the top of the layered sulfates. The difference in dips between the northern and southern section corresponds to a "kink" in projected bedding traces in **d**.

diffuse bright-toned halo ~2-20 m on each side of the fracture itself [Figure 5.11c and d]. No cross-cutting relationships are observed at fracture intersections, suggesting that the fractures were filled separately from their propagation.

Parallel-sided fills are indicative of channelization of fluid along pre-existing fractures. Relatively narrow, zoned fractures surrounded by wide zones of light-toned material texturally continuous with the groundmass of the unit [e.g. Figure 5.11d] suggest the formation of a zone of alteration around a relatively narrow original fracture. The considerable width range of altered zones along fractures suggests that the intensity of fluid channelization along boxwork fractures varied significantly within the sulfate unit.

Fracture orientations Over 850 km of boxwork ridges exposed within the layered sulfates were digitized as lines atop regional CTX imagery [Figure 5.3]. Ridge orientations were measured across the dataset, and intersection angles were calculated for any point where three or more digitized fracture segments met. Angles were calculated at 10 m–radius buffers around each intersection, which corrects for digitization noise and changes in orientation within this radius.

Boxwork ridges commonly intersect at right angles, both crossing and forming "T-junctions" [Figure 5.12]. They do not have 120° orientations characteristic of progressively annealed drying polygons and permafrost patterned ground (*El-Maarry et al.*, 2010) or cooling polygons where rock tensile strength exceeds fracture propagation stresses (*Shorlin et al.*, 2000). Individual ridges can run for several km, over which they range from relatively straight to curvilinear. In some areas (particularly the *Ridge Basin*) ridges follow gentle arcs with radii of ~8-10 km. However, these circular trends are commonly disrupted by cross-cutting fractures. The dominant map pattern of the boxwork ridges is of a coarsely gridlike, sometimes weakly concentric, network.

The summary of fracture orientations suggests a complete lack of preferred orientation for the fractures [Figure 5.12b]. This suggests that the features were not formed by injection or in a regionally consistent stress field. The curvilinear nature of individual fractures makes it difficult to assess their dip in many cases, and most appear to be near vertical. However, some apparently planar fractures have steep (40-60°) non-vertical dips [Figure 5.6d].

Dip changes at small spatial scale Changes in local bedding orientations of 2-3° are resolvable in many areas of the layered sulfates with boxwork fractures. `nf3` and `nf5` contain a 200 m thick exposure of sulfates cut by boxwork fractures which range from near-flat to ~2° south- or northeast-dipping. `nf7` contains planar dipping boxwork domains, with southeast dips steepening from ~1° to 3° over a few hundred meters in successive fracture polygons. The best-exposed example of localized bedding variation associated with boxwork contains more dramatic changes of bedding orientation (up to 10° over a kilometer) on a west-facing slope in `nf4`, within the southern part of the *Erosional Window* [Figure 5.13]. The slope contains sulfate material layered at meter-scale and buttressed by resistant polygonal ridges. In the northern part of this exposure, dips are variable but generally southward. Scatter to the northwest represents high uncertainties aligned with

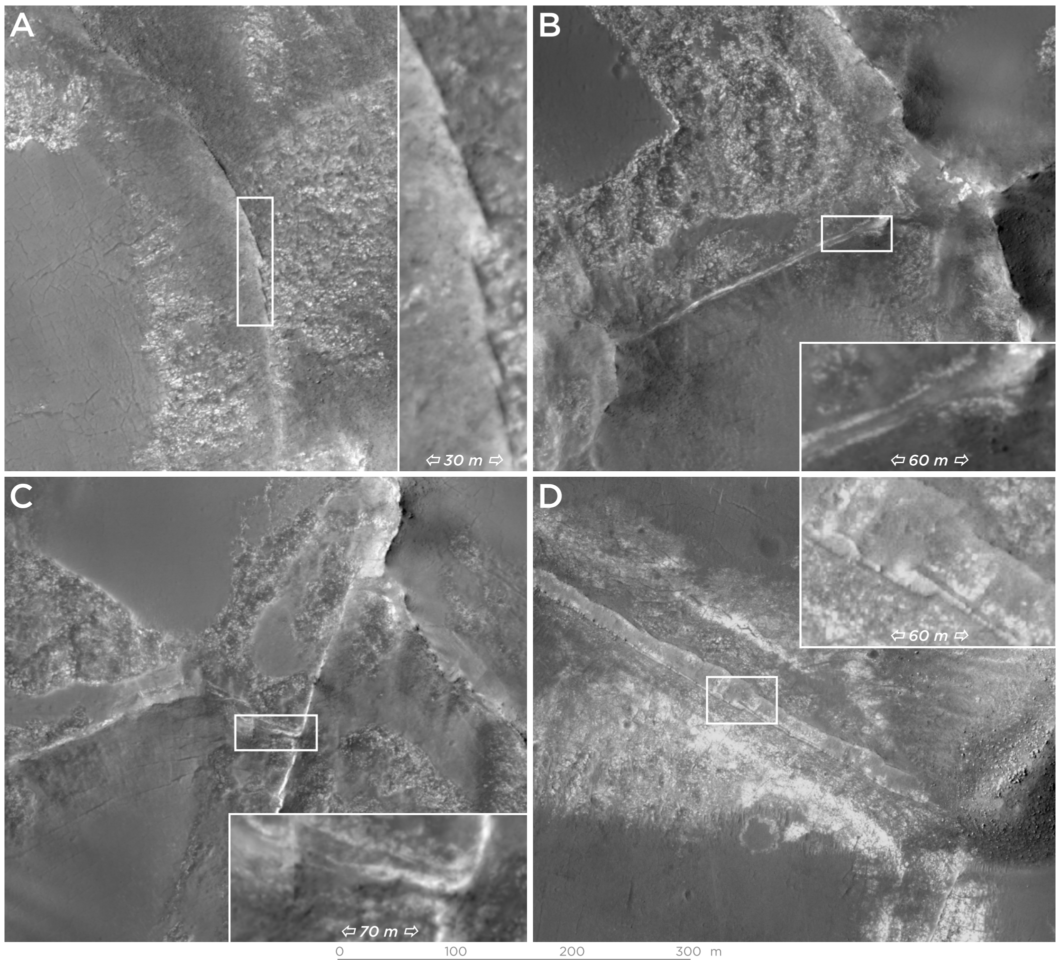

Figure 5.11: Examples of boxwork fractures from HiRISE images within the study area. **(a)** A minimally altered fracture <1 m thick (nf3). **(b)** A slightly thicker fracture showing a characteristic double-walled morphology of channelized fluid along the fracture (nf2). **(c)** A fracture junction showing a dark-toned halo around the fracture (nf2). **(d)** A wide fracture zone showing a light-toned fracture surrounded by a halo, with the entire alteration zone > 100 m wide (HiRISE ESP_026069_1970).

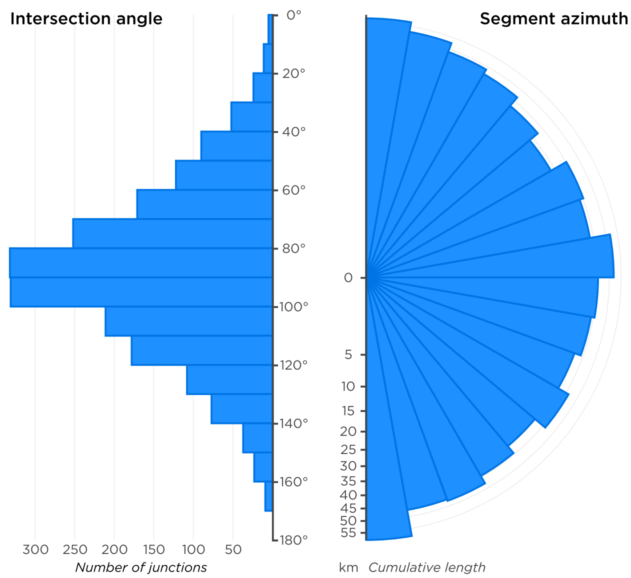

Figure 5.12: Summary parameters for boxwork fractures measured across the study area [Figure 5.3]. **(a)** Frequency distribution of boxwork fracture intersection angles. The largest angle is redundant and is excluded (all angles must sum to 360°). Thus, "T-junctions" between fractures are plotted as two ~90° angles with an implicit 180° angle between parallel segments. **(b)** Frequency diagram of boxwork fracture azimuth, demonstrating a lack of preferred orientation for the fractures.

the local hillslope. The southern part of this exposure contains dips that are generally northwestward. The opposing dips occur within a 2-km section over several boxwork domains. A projected cross-section [Figure 5.13d] shows dip changes both gradually within boxwork domains and abruptly between them. Many of the individual measured bedding traces are curved relative to their best-fitting plane, suggesting that individual layers are not planar and leading to large error magnitudes for orientation data.

The association of bedding-orientation changes at small spatial scale with the boxwork ridges suggests that the formation of the ridges may have modified dips of the nearby beds. The proposed mechanism for creating these boxwork fractures can lead to localized bed orientation changes at sub-kilometer scale [Section 5.5.2].

Fracture mineralogy Some of the boxwork polygons, particularly in `nf2`, are within a CRISM scene and wide enough to be covered by a single pixel. *Ehlmann and Mustard* (2012) presented measurements showing spectral signatures of jarosite-family minerals ($(K, Na, H_3O)\, Fe_3^{3+}\, (OH)_6\, (SO_4)_2$) in the boxwork polygonal ridges. Applying the same methods to other ridged areas within the layered sulfates, we have found several other examples of polygonal ridges enriched in jarosite [Figure 5.5]. Given the similar morphology and erosional resistance of ridges across the study area, jarosite is likely a key feature of the boxwork fractures across the entire study area.

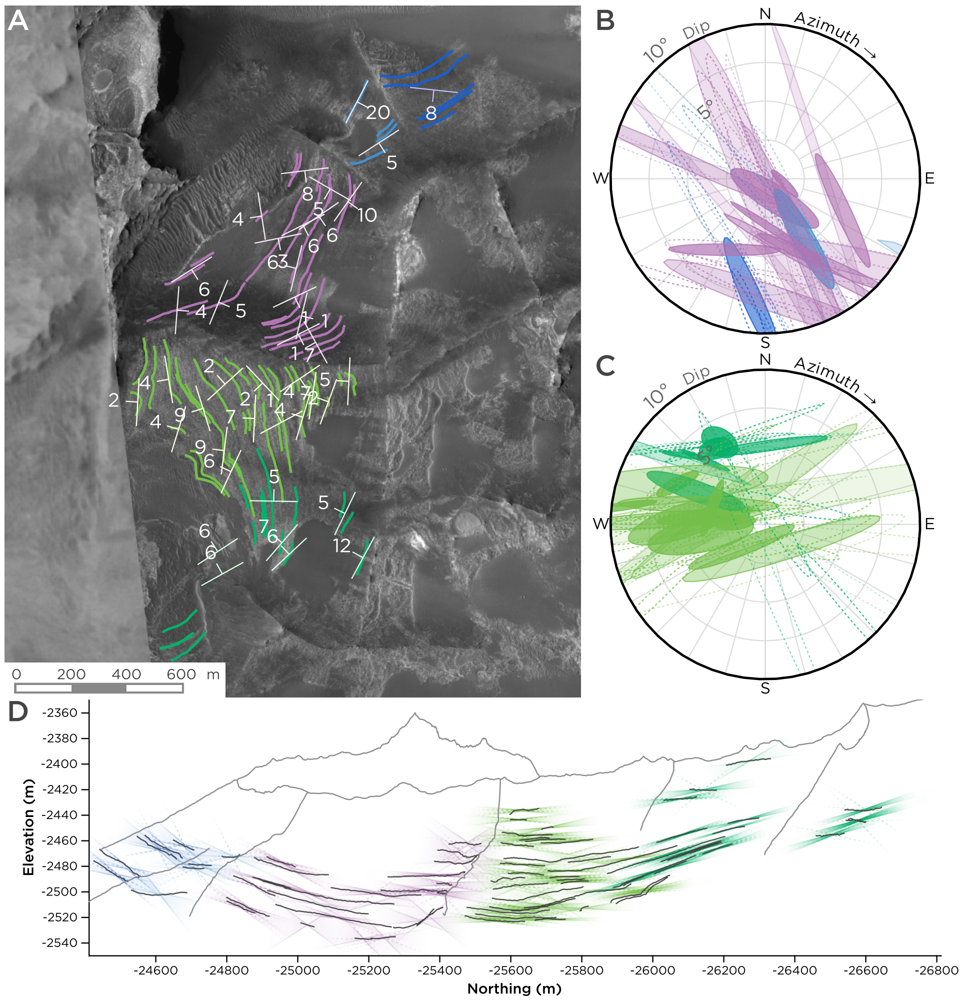

Figure 5.13: Attitude measurements of layered sulfates in boxwork fracture domains within HiRISE scene `nf4` in the southern *erosional window*. The measurements show a change in bedding dips from dominantly south to north-dipping over ~2 km north to south. **(a)** Map view of bedding orientation measurements. **(b** and **c)** Upper-hemisphere stereonets showing poles to bedding for the north and south parts of **a**. Measurements are color-coded by boxwork domain and shaded by confidence. Dotted, unfilled ellipses represent components of grouped measurements. **(d)** a N–S cross section within the measurement domain, showing the apparent dip of bedding traces and hyperbolic error bounds to planar fits. The poles to bedding and projected cross-section show a change in apparent dip from north to south along the cross section, and sudden small-scale dip changes across boxwork fractures.

5.4.3 Penetrative alteration

Some areas of the layered sulfates are characterized by pervasive mineralization not channelized along boxwork fractures. In all cases with CRISM coverage, the "altered sulfate" shows spectral signatures of jarosite. This light-toned, erosionally resistant "altered sulfate" is notably present in the north part of `nf1`, the *Erosional Window* (`nf4` and `nf8`), and the central part of `nf6` [Figure 5.3]. In the *Erosional Window*, several sub-kilometer scale flat-topped outcrops of the olivine-carbonate unit (*Ehlmann and Mustard*, 2012) are are surrounded by erosionally resistant, massive, and light-toned altered sulfates [Figure 5.14]. The valley containing these materials is ringed by eroded layered sulfates with raised boxwork ridges. The margins of the altered sulfates show finely patterned fractures at the boundary and wider, linear fractures extending ~200 m into the sulfates [Figure 5.14b]. This pattern of fracturing is much denser than the boxwork domains, suggesting a localized and intense fluid interaction at the basal contact of the sulfates in this location.

Light-toned, mineralized zones are also associated with the upper surface of layered sulfates, just below the smooth capping surface [e.g. Figure 5.6c]. Unlike the more intense fluid alteration overprint described above, these zones show no contrast in erosional resistance relative to the groundmass of the sulfates. However, they do have jarosite spectral signatures [251C0 – Jarosite in Figure 5.5]. In the *Erosional Window*, this light-toned material includes a collection of coarsely patterned, rounded alteration domains, with a ~10 m characteristic scale [Figure 5.14c]. The patterned material grades laterally eastward into boxwork ridges which cut visibly layered material, and the light-toned material in these domains appears to be channelized along boxwork ridges. The mineralogical parallels between massive, altered domains and the boxwork ridges suggests that these features were formed in the same or a similar episode of fluid interaction.

5.4.4 Capping units

The layered sulfates are exposed at the boundary of the Syrtis Major volcanic province, and studies of the unit to date have it have identified its capping surface as the Syrtis Major lava throughout the region (*Ehlmann and Mustard*, 2012; *Bramble et al.*, 2017). We find that a smooth capping surface in the central part of the study area is distinct from the Syrtis Major lavas, which we interpret to have formed by a fundamentally different process.

Morphology Two distinct types of unit locally overlie the layered sulfates within the study area [Figure 5.15]. The "smooth capping surface" is uniformly dark and relatively featureless. It preserves a few small, fresh craters, but there is a relative lack of intermediate-sized preserved craters and craters that are preserved show a "ghost" or subdued morphology. Larger craters appear as poorly defined "ghost" features [Figure 5.15a].

The "hummocky capping surface" is broadly similar in appearance to the smooth capping surface, with increased visual complexity at 100-m lateral scale [Figure 5.15b]. This visual complexity is associated with small-scale topographic variations (on the

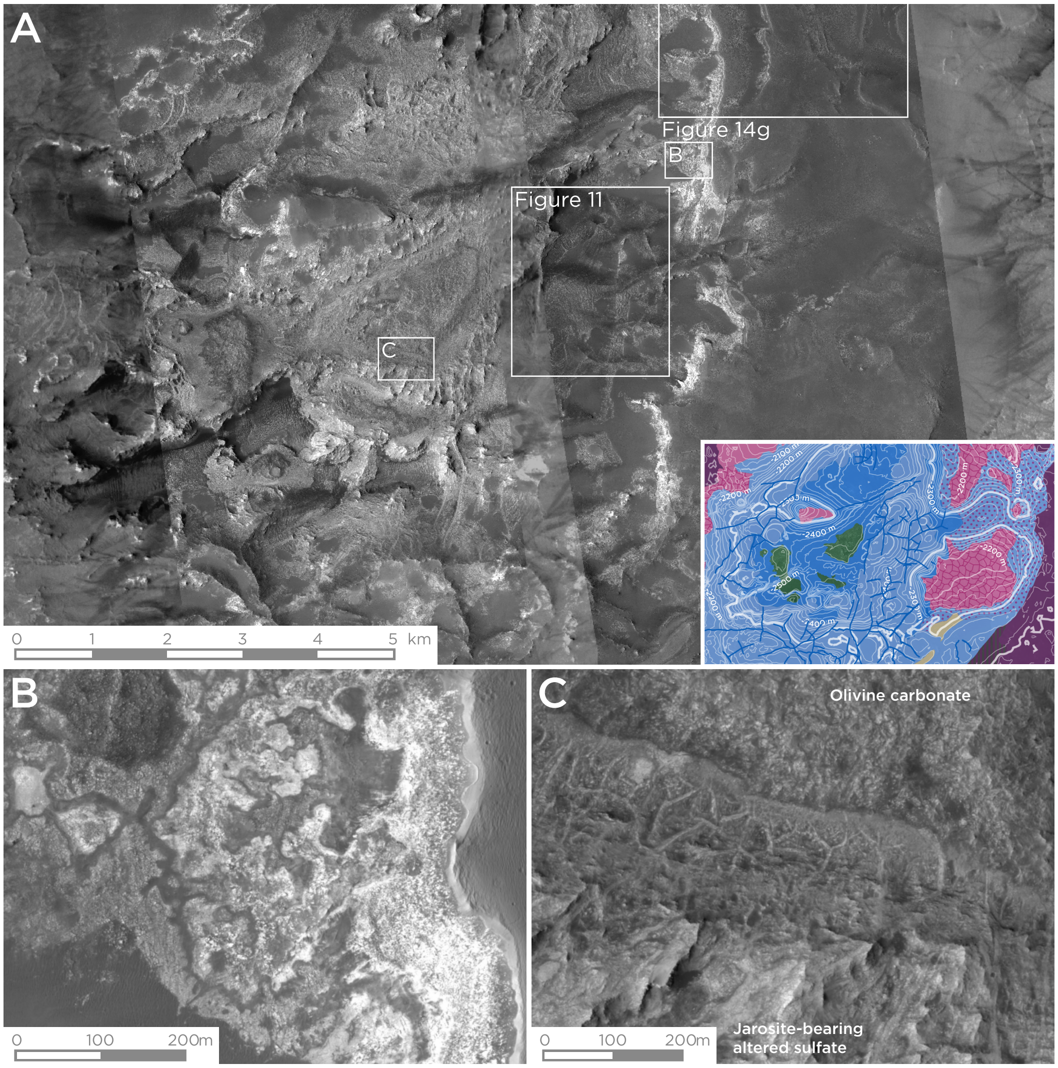

Figure 5.14: (a) The *Erosional Window* at the southwest margin of the study area, showing parts of HiRISE scenes `nf4` and `nf8`, where the layered sulfates are erosionally resistant and carry strong jarosite signatures. The inset geologic map (from Figure 5.3) covers the same area. **(b)** Mottled light-toned altered domains associated with the contact between the "hummocky capping surface" and unaltered exposures of layered sulfate. Light-toned material is partially channelized along boxwork fractures, suggesting that the two features are linked. **(c)** Jarosite-bearing, erosionally resistant altered sulfates adjacent to and stratigraphically above an exposure of olivine-carbonate, with dense fractures indicative of fluid flux at the interface.

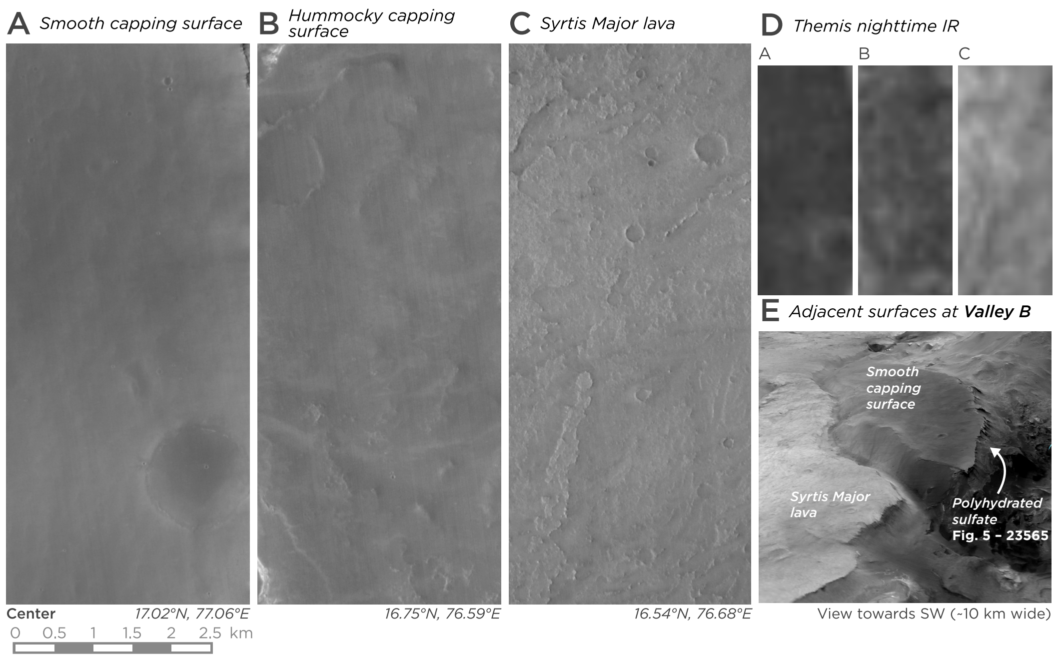

Figure 5.15: Same-scale views atop a CTX orthomosaic of morphological characteristics of **(a)** the smooth capping surface, **(b)** the hummocky capping surface, and **(c)** the Syrtis Major lavas. **(d)** THEMIS nighttime temperature corresponding to panels *(a-c)*. **(e)** an example of the smooth capping surface and the Syrtis Major lavas in contact.

order of 10-50 m) as shown in the western part of Figure 5.16g. The smooth and hummocky capping surfaces are predominantly found in the central and southeast parts of the study area.

The Syrtis Major lavas mapped within the study area are continuous with a regionally eastward-sloping surface of the Syrtis Major volcanic province (*Hiesinger and Head*, 2004; *Ivanov and Head*, 2003). This surface has a notably different character than the other capping units, preserving small-scale features (e.g. low-relief benches and scarps), retaining craters well [Figure 5.15c], and preserving evidence of fluvial incision on its surface and edges [Figure 5.18b; see also Section 5.4.5]

Structural characteristics The range of surface orientations of the capping surface is more restricted than the range of bedding dips within the layered sulfates [Figure 5.9]. The capping surface dominantly slopes southeast, with surface slopes of up to 5°. The difference in orientation distributions of the smooth cap and the underlying layered sulfates suggests a low-angle unconformity, with the smooth capping surface emplaced atop the layered sulfates after a period of erosion.

The relatively high-angle surfaces of the smooth capping surface are likely to have formed in-situ atop dipping exposures of the layered sulfates. In contrast, the Syrtis Major lavas are low-dipping and generally sloped to the east with dips of less than 2° [Figure 5.9]. Broadly, the lavas form surfaces with regionally consistent dips at 10-20 km scale, oriented with the topographic gradient into Isidis Basin.

Spectral and thermophysical characteristics The Syrtis Major lavas and smooth capping surface have an indistinctly mafic mineralogy with olivine and pyroxene absorptions in CRISM data. The smooth capping unit has generally lower nighttime infrared emissions (a proxy for thermal inertia) than the Syrtis Major lava flow [Figure 5.17]. Low thermal inertia is typically the result of lesser induration, higher porosity, or mantling fine-grained debris. Since the smooth capping unit is relatively erosionally resistant and not penetrated by light-toned alteration in the underlying layered sulfates (suggesting a lower porosity) [Figure 5.6a and b], the low thermal inertia of the smooth cap most straightforwardly suggests fine-grained constituent material.

Thickness of the smooth capping surface The low thermal-inertia character of the smooth capping surface is coupled with a resistant erosional style. The measured thicknesses of the cap unit [Figure 5.16b] are largely between 10 and 20 m with several outliers in `nf3` and `nf4`. Close-up views of the internal structure of this interval show coarse internal layering and boulder-shedding scarps [Figure 5.16c-f]. Figure 5.16f shows warping of the lower contact by an impact and continuous dark bands within the light-toned material at the base of the cap surface.

The "hummocky cap surface" subtype of the smooth capping surface is topographically rough and may be affected by dislocations in the underlying layered sulfates. Figure 5.16g shows 10-20 m elevation steps separating differently-dipping "plates" of capping material at sub-kilometer scale. In the center, the capping surface is resolved into two distinct surfaces, the lower of which is thinner (~5 m) and slopes eastward and slightly away from the scarp defining the edge of the window.

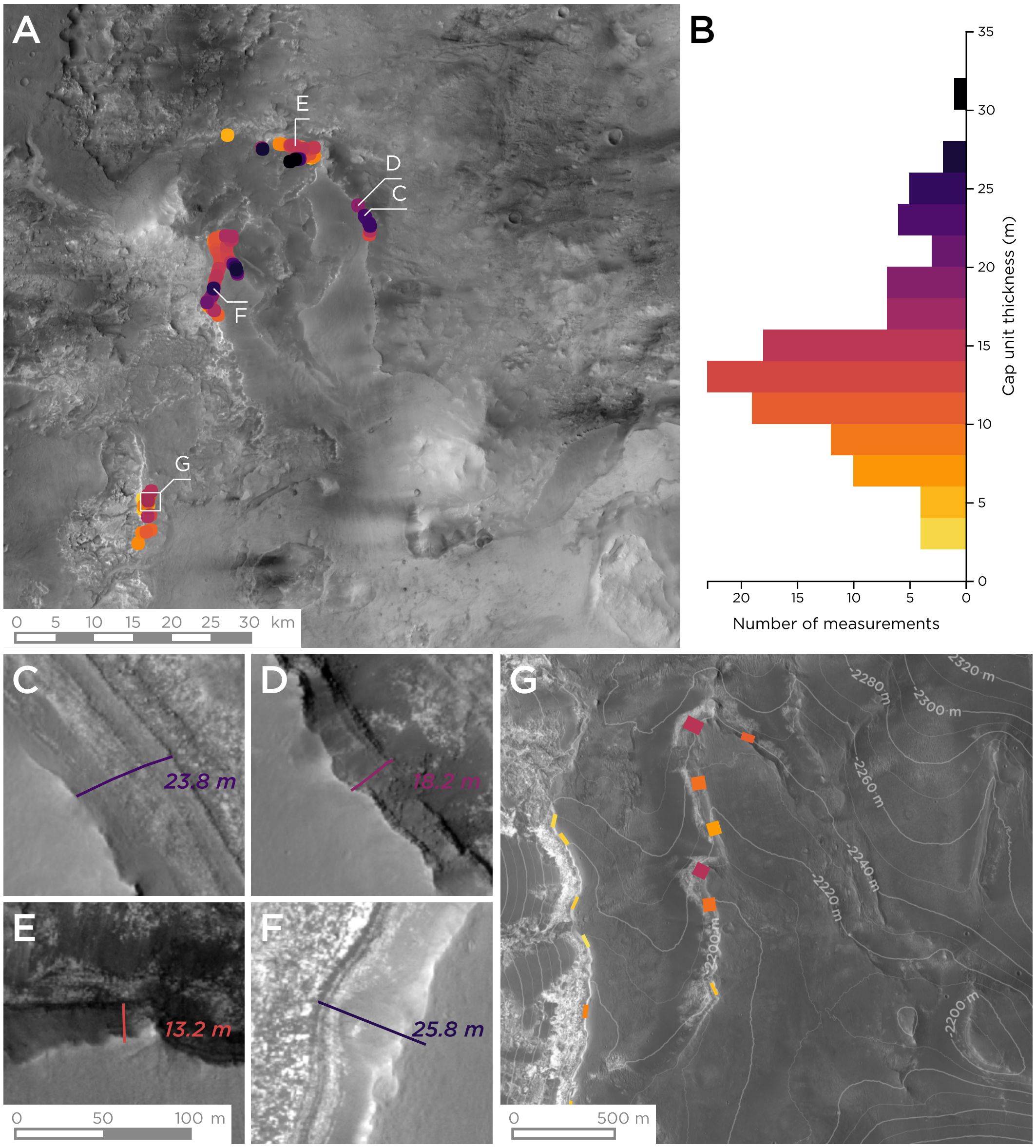

Figure 5.16: Thickness and morphology of the smooth capping surface in HiRISE scenes within the study area. **(a)** A summary of sampling, with measured locations color-coded by thickness. **(b)** Histogram of thicknesses sampled throughout the study area. The coloration of histogram bands corresponds to the points on **a**. Thickness ranges from 5 to 25 m across the sampled HiRISE scenes. **(c-f)** Close-ups of capping unit margin showing thickness and morphology at a single location: **(c)** coarse internal layers within the capping surface; **(d)** poorly resolved layers and shedding of boulders downslope; **(e)** poorly resolved internal structure; **(f)** downwarping of the basal contact by cratering. **(g)** The "hummocky cap surface" at the eastern edge of the *Erosional Window*. This area hosts the thinnest recorded examples of the capping unit and two parallel curved scarps (left side of image) doubling the edge of the capping surface.

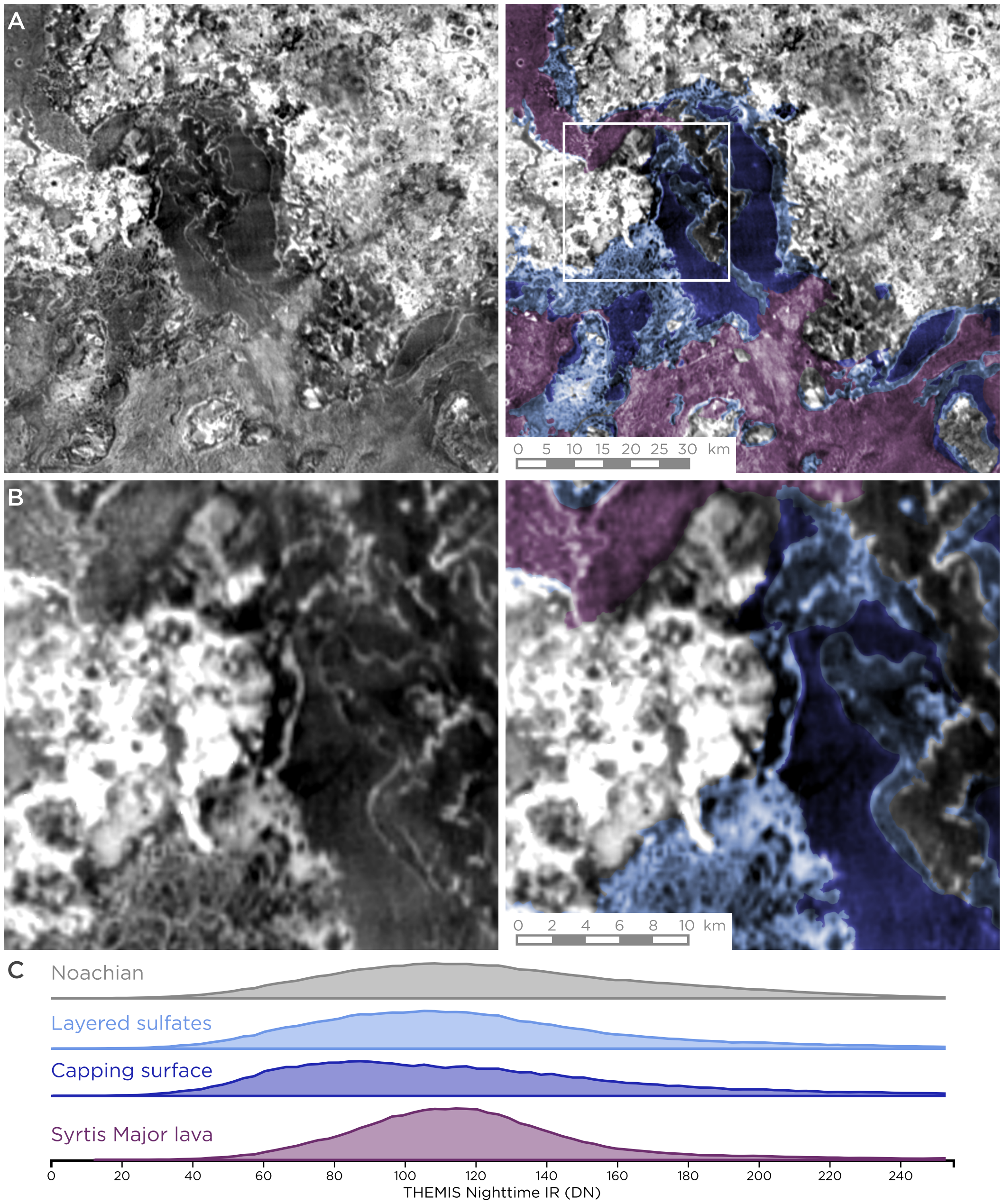

Figure 5.17: **(a)** THEMIS nighttime infrared mosaic with boundaries of the sulfate unit overlaid (right panel). This dataset can be used as a proxy for thermal inertia, and shows the low thermal retentivity of the smooth capping surface. **(b)** Zoom showing the distinct character of the capping surface in the central part of the study area. **(c)** A histogram of nighttime infrared emission over the study area, showing that the capping surface has substantially lower infrared emission than the rest of the units in the study area.

The two scarps are at nearly the same elevation, and may be the result of small-offset (~10 m) normal faulting within the underlying layered sulfates, propagated upwards to cause dislocations in the hummocky capping surface.

Relationship with the Syrtis Major lavas A key set of observations separating the smooth capping surface from the Syrtis Major lavas is the local relationships between the two units. In the central portion of the study area, the distal Syrtis Major lavas flow eastwards from the outlet of the *I-80* valley, capping a mesa of the layered sulfates (the *Causeway*) and embaying a major basement peak [Figure 5.18a]. The lava flow terminates at an indistinct point in the upper part of *Valley A*, with morphologically similar surfaces forming "steps" at progressively lower elevation. Below this transition zone, *Valley A* is mantled by the "draping valley fill" [Section 5.4.5] in its lower reaches. On the valley's southwest flank, the layered sulfates form the bulk of *Mesa B*, which is capped by the smooth capping surface at ~-1600 m. The smooth capping unit is ~200 m higher than adjacent Syrtis Major flows. This elevation relationship suggests that the smooth capping surface was formed atop the sulfates prior to and at significantly higher elevations than the Syrtis Major lavas. The Syrtis Major lavas appear to have flowed down a valley taht was eroded through the layered sulfates and cap and into the upper reaches of *Valley A*. The topography is now inverted to form the *Causeway*, capped by lavas. The presence of an unconformity below the smooth capping surface, along with its erosion to form the mesas flanking *Valley A*, imply significant erosion both before and after the formation of the smooth capping surface.

A similar relationship exists in *Valley B* at the southeastern margin of the study area [Figure 5.18b]. The northwest flank of the valley slopes inward at ~5°, and is composed of CRISM-verified layered sulfates capped by the smooth capping surface; the southwest side does not have CRISM coverage but is morphologically similar. The floor of the valley contains a lobe of Syrtis Major lava, which has a rougher surface with an indurated, crater-retentive character. On both sides of the valley, the contact between the lavas and smooth capping surface is erosionally modified, with channels cut into the boundary (discussed in Section 5.4.5). This relationship demonstrates that the Syrtis Major lavas flowed through significant pre-existing relief, with paleovalleys formed in capped layered sulfates.

5.4.5 Late fluvial history

Channels atop the lava flows Fluvial activity continued after sulfate and smooth cap unit erosion and Syrtis Major lava emplacement, substantially reworking parts of the Syrtis Major lava flows. The Syrtis Major lavas are modified by inscribed channels across the surface and at the edges of the lava throughout the study area, in agreement with the outflow channels reported to the south of the study area by *Mangold et al.* (2008). The down gradient and incised nature of the inscribed channels distinguishes them from lava channel features.

The inscribed fluvial features are paired with deeper (~100 m) canyons cut into the surface of the lava flow. In Figure 5.8b, these features separate parts of the lava flow at discrete elevation steps, suggesting that different flow bodies formed at different times, during progressive erosion of the layered sulfates.

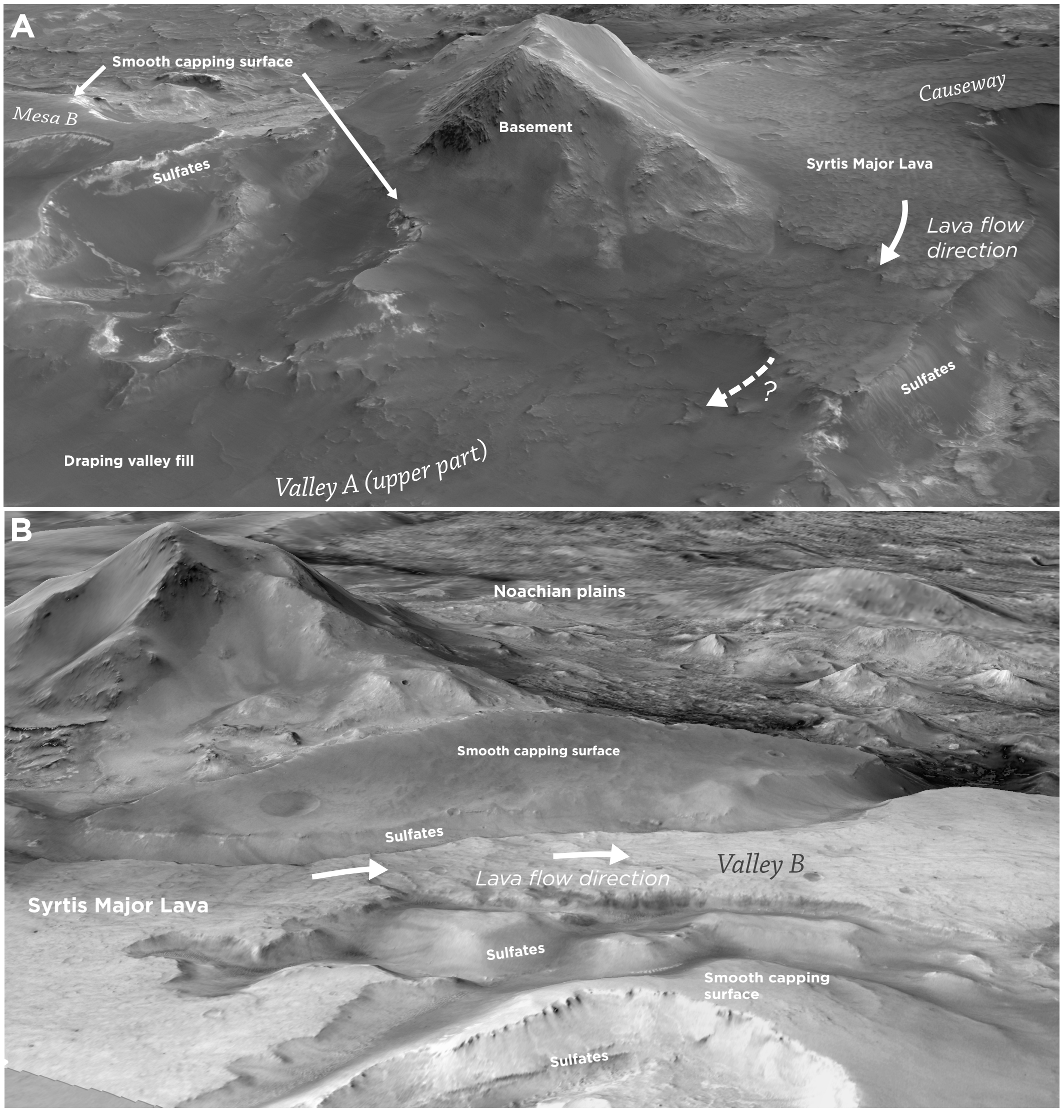

Figure 5.18: Key examples of the relationship between the smooth capping surface and the Syrtis Major Lavas, with orthoimagery atop CTX and HiRISE elevation models. **(a)** view southwestward towards *Mesa B*. The Syrtis Major lava flow lobe of the *Causeway* ends in the foreground, embaying the basement exposures and flowing down a gradient towards *Valley A*. The smooth capping surface crops out ~200 m higher on the south flank of this basement exposure. **(b)** View of *Valley B* with the smooth capping surface mantling layered sulfates on the flanks of the valley. The Syrtis Major lavas flows are channelized between these elevated exposures, and secondary channels have eroded the edge of the lava flow.

These channels and canyons cut into the lava flow surface postdate the sulfate-hosted paleovalleys described in Section 5.4.4. After *Valley B* in the southern part of the study area was filled with a lobe of the Syrtis Major lava flows, smaller canyons were inscribed at the contact between the lavas and the capping surface forming the slopes of the valley [Figure 5.8a and Figure 5.18b]. *Valley A* did not experience similar reoccupation, which we discuss in Section 5.4.5.

Fluvial and lacustrine deposits The north margin of *Deep Basin* contains an integrated fluvial system, with an ampitheatre-shaped canyon incised into the edge of the Syrtis Major lavas connected by a preserved channel to a small delta (elevation −2320 m) [Figure 5.19a and b]. This channel formed atop Noachian basement, layered sulfates, and the Syrtis Major lavas and clearly postdates all geologic units in the area. Distal to this delta, a flat-lying surface of presumably lacustrine origin is preserved at −2340 m. These features are perched ~500 m above the floor of *Deep Basin*, which has its deepest point at −2800 m only 3.5 km to the southwest. The canyon cut into the Syrtis Major lavas is tied to lightly incised channels on the flow surface, and to the similar canyon at the flow scarp in `nf4` [Figure 5.6c], which feeds into *North Basin*.

An inverted channel cuts fractured exposures of the layered sulfates within the *Erosional Window* at the southern part of the study area [Figure 5.19c]. Layers within this channel body are nearly flat, dipping at most 1° to the east. The channel flows north of a Noachian basement peak, overtops and cuts boxwork ridges with in the layered sulfates, and is confined to a narrow belt roughly 300 m wide. The channel deposit aligns with valleys cut into the edge of the Syrtis Major lavas to the west [Figure 5.3], and a valley at the northern edge of the Syrtis Major lavas that results from focused erosion of the layered sulfates along this boundary.

Basin-floor deposits Parts of *North Basin* and *Deep Basin* are floored with flat, smooth surfaces that suggest fluvial or lacustrine deposition. These low-elevation exposures form nearly flat surfaces (<1° east dips) within an interconnected network of basins; dipping sediments suggestive of alluvial fans are sometimes found at the margin of these surfaces [Figure 5.20]. In *North Basin*, the fluvial system discussed above feeds into these basins, and an outlet channel is preserved to the east [Figure 5.3]. The sourcing of associated channels atop the Syrtis Major lavas suggests Hesperian or later deposition, and crater-counting of *North Basin* surfaces (*Skok and Mustard*, 2014) yields an Amazonian age of 1.29 Ga. These surfaces were mapped as "Capping unit" by *Bramble et al.* (2017) but appear to be fundamentally different than the exposures of the same morphological unit at higher elevations atop the *NE Syrtis Plains*. *Bramble et al.* (2017) grouped these units based primarily on their crater-retentive character, but they are likely much younger than these cratered plains. We reinterpret these surfaces as fluvial/lacustrine sediment sheets, and suggest that they are late deposits, based on their association with clearly post-sulfate fluvial systems. We map these deposits as "Basin Floor" on Figure 5.3.

Low-relief layered scarps in HiRISE scenes `nf1`, `nf3`, and `nf5` in *North Basin* are mapped as undifferentiated sedimentary fill, closely associated with the Basin

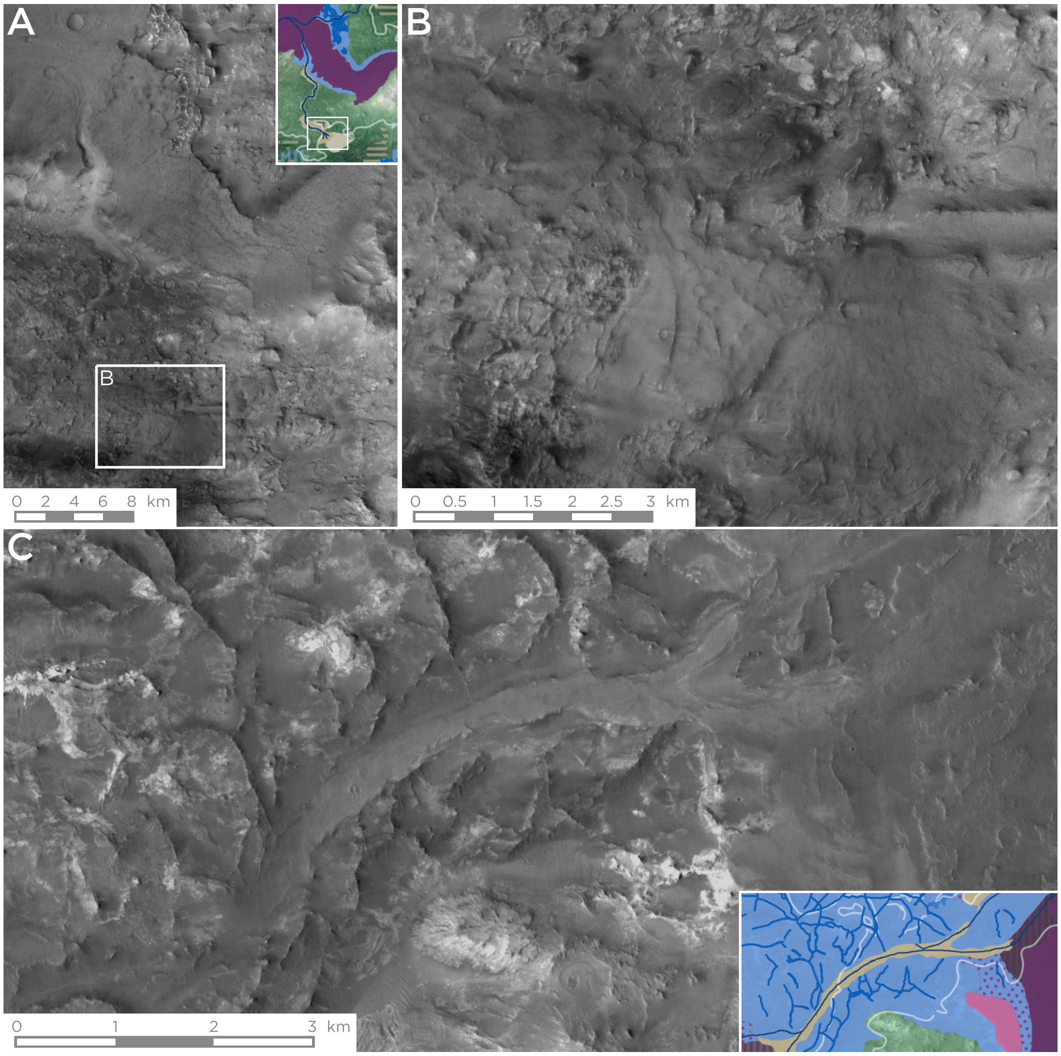

Figure 5.19: **(a)** Canyons cut into the edge of the Syrtis Major lava flows in the northwest of the study area, with a preserved downstream channel system and a 1.5 km–wide delta deposit at roughly -2300m elevation at its terminus. Inset geologic map covers the same area. **(b)** Close-up of the delta deposit, with basement megabreccia in the upper right. **(c)** An inverted fluvial deposit ~10-20 m thick in the *Erosional Window* in the southwestern part of the study area. The fluvial deposit is sourced from atop the Syrtis Major lavas. Inset geologic map is of the same area.

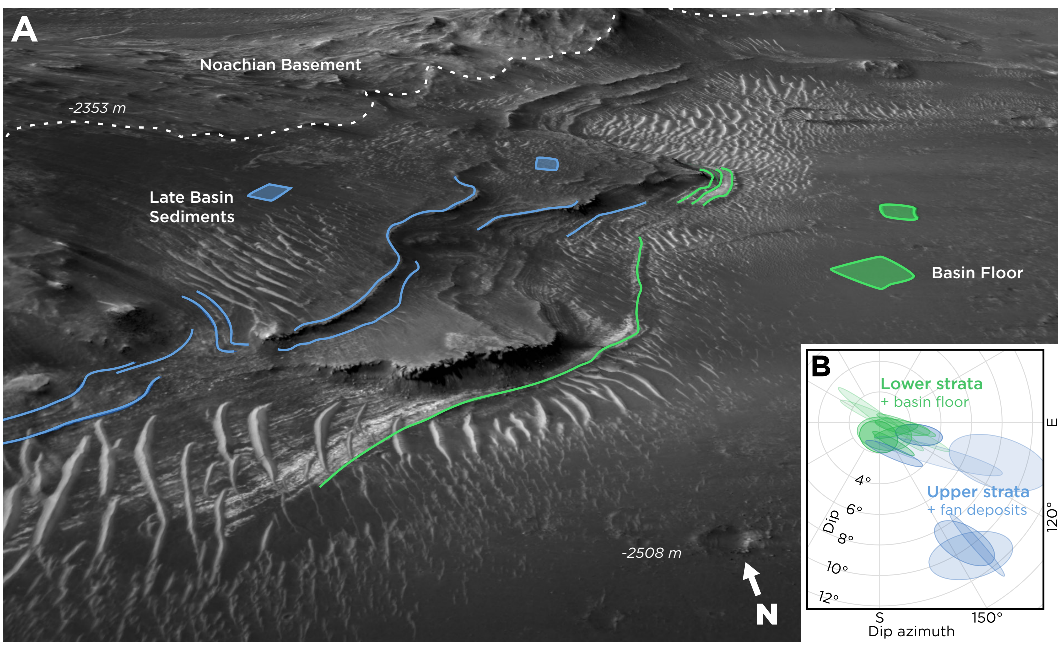

Figure 5.20: N-looking oblique view in `nf3` (no vertical exaggeration) showing the Basin Floor units and layered scarps and fans of the Sedimentary Fill deposits. Measured bedding traces (green for the lower scarp and basin floor, blue for the upper fan) are shown. Calculated orientations for these traces (bottom right) show upper fan deposits dipping up to 10° into the basin. Approximate locations for CRISM spectra [Figure 5.5] showing smectite clay signatures within the basement and detrital sediment are shown. View is ~1 km wide.

Floor deposits. These features are associated with topographic scarps ~10 to 20 m high and are flat-lying to ~2° east-dipping, similar to the adjacent Basin Floor surfaces. In `nf3`, they increase in dip to ~10° over ~100 m of elevation, grading into thin fan deposits mantling the Noachian basement [Figure 5.20]. In `nf2` and `nf4`, similar layered scarps at somewhat higher elevation are associated with the "Channel Fill" deposits discussed above.

In `nf2` and `nf3`, these scarps contain planar, bright-toned layers with CRISM signatures indicative of phyllosilicates. In *Bramble et al.* (2017), these exposures are mapped as "Undifferentiated" and are typically adjacent and slightly above exposures of the "Capping Unit". The thin packaging of beds, confinement to deep basins in modern topographic lows, and formation of crater-retaining flat floors contrast with the thickly packaged layered sulfates. We interpret these features as representing late fluvial and lacustrine deposits, and map them as "Late basin sediments" [Figure 5.3].

Draping valley fill Despite the significant erosion of *Mesas A* and *B* on its flanks and its overall southward slope, *Valley A* does not contain a clear channel system. It is instead floored by the "Draping Valley Fill", a unit unique to the interior of *Valley A* [Figure 5.21]. Within the footprint of `nf7`, this unit is characterised by a flat surface with <2° slopes to the southeast (truncated at a 40 m layered scarp in the foreground of Figure 5.21a). Continuous with the surface capping the valley floor, resistant thin surfaces dip steeply (15-20°) into the valley, mantling the layered sulfates below and forming distinctive, sinuous hogback ridges up to 40 m high at its erosional boundary [Figure 5.21b]. Fine cracks near the break in slope in this continuous surface [Figure 5.21c], just inside of the eastern slope of the valley, are interpreted as tension cracks caused by differential deflation of the unit after emplacement. The draping valley fill has low thermal inertia and shows indistinct mafic infrared signatures similar to the basin-fill deposits in the region. These characteristics are similar to the "Basin Fill" deposits discussed above. The restricted elevation range and draping sedimentary style suggests that this unit was formed during partial inundation of a previously-existing valley.

The draping valley fill mantles the entire bottom of *Valley A*, and extends north to an uncertain boundary with the Syrtis Major lava flow lobe that flows south towards the upstream entry to this valley. This zone (the foreground of Figure 5.18a) suggests termination of the lava flow at the northernmost margin of the draping valley fill. It is also possible that the lava flow continues down-gradient into *Valley A* beneath a thin veneer of draping valley fill, but lavas are not exposed at the surface anywhere further down the valley.

Elevation alignment of fluvial features With the exception of the inscribed channels, the late fluvial-lacustrine features discussed above occur at or below −2300 m across the entire study area. This elevation (highlighted on Figure 5.2, Figure 5.3, and Figure 5.8) is an open contour connecting all the major valleys in the study area, including the closed *Deep Basin* and *Erosional Window*. The delta shown in Figure 5.19 has topsets just below an elevation of −2300 m, and the "basin floor" surfaces and associated draping sedimentary deposits within *North Basin* and *Deep*

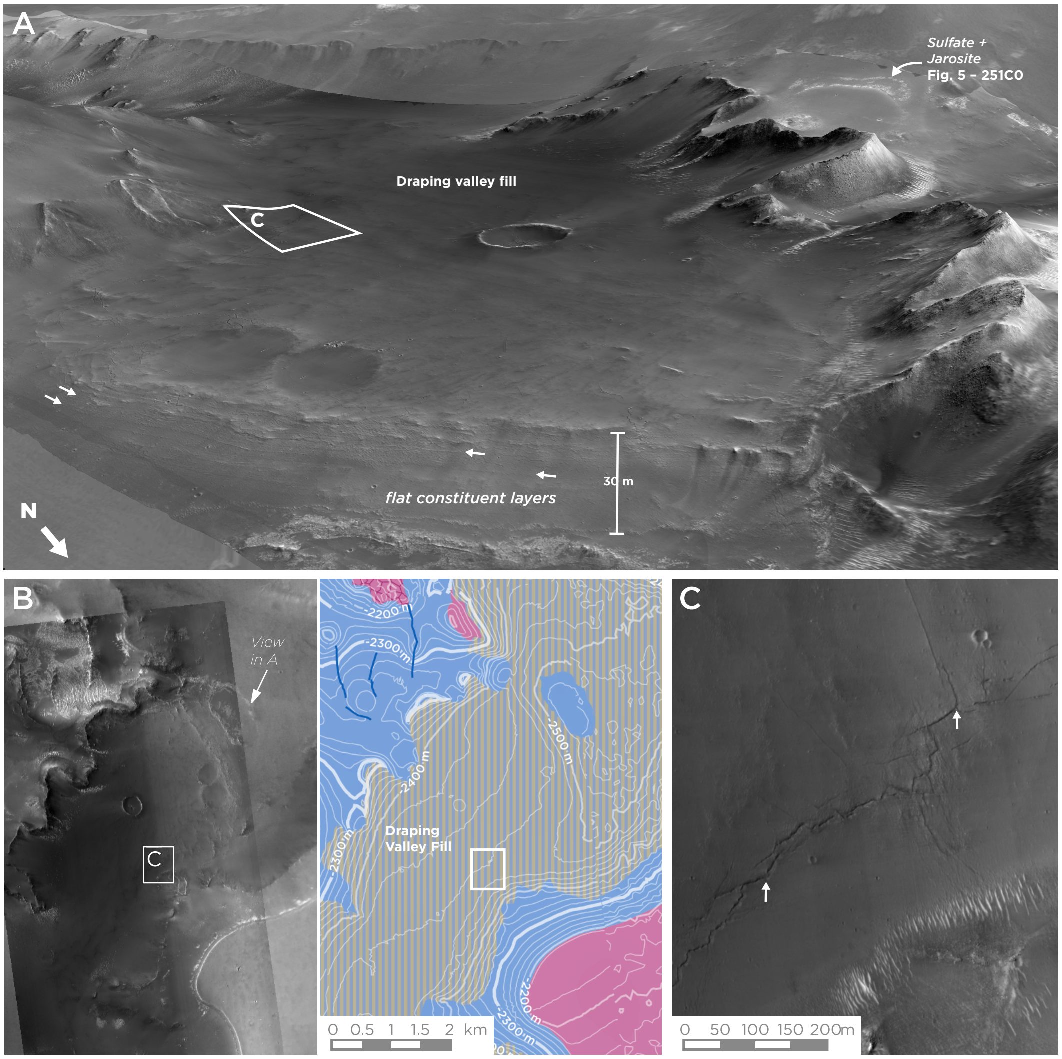

Figure 5.21: The draping valley fill in *Valley A*. **(a)** Southwest-looking HiRISE (`nf7`) oblique view of the unit, showing its nearly-flat base and a rim that extends up the side of the valley to roughly the −2300 m contour. The raised edges of the unit appear thin and buttress the material beneath them, and the inconsistent erosion creates a sinuous map pattern on the edge. **(b)** Paired map views of corresponding to **a**, showing imagery datasets and elevation overlaid on geology. **(c)** Cracks in the unit located just inside the slope break at the edge of the valley floor.

Basin [Figure 5.20] are at or below this level (as low as −2800 m in *Deep Basin*). In *North Basin*, flat basin-floor surfaces cover most of the area within this contour. The Draping Valley Fill is also consistently associated with this contour, draping the interior of *Valley A* to an elevation of −2300 m over the entire length of the valley; −2300 m is also the transition elevation between the Syrtis Major lavas and the draping valley fill [Figure 5.18a]; this transition zone at the upstream end of *Valley A* is separated from *North Basin* by the narrow *Saddle Ridge*, which has elevations just over −2300 m. The alignment of post-sulfate fluvial and lacustrine deposits at a single elevation suggests that this stage of deposition involved inundation of the entire study area to a single base level.

5.5 Discussion

5.5.1 Deposition of the layered sulfates

There are five key characteristics of the sulfates: (1) their parallel, closely-spaced bedding, which indicates sedimentary accumulation; (2) their poor induration and susceptibility to erosion; (3) dips always <10° and mostly <7° with regionally variable orientations; (4) variable thickness, ranging up to 600 m; (5) unconformable emplacement on and thinning up to basin highs. We reject the possibility of flexure of layers at km scale to form the observed orientation distribution of the layered sulfates because of the inability of dewatering to explain consistent dip changes at multi-kilometer scale, the lack of tectonic stresses during diagenetic fracturing [Section 5.4.2], and the lack of a compelling mechanism to generate coherent, kilometer-scale, low-angle tectonic folds. Thus, potential types of sedimentation are those that can explain strata with shallow but non-zero depositional dips.

Of all possible depositional mechanisms [Figure 5.4], some can be rejected. The layered sulfate deposits are marked by laterally continuous, meter-scale layering, and show no structures associated with chaotic pyroclastic emplacement or devolatilization that would be expected for large-volume ash flow deposits (e.g. *Ghent et al.*, 2012). In general, environments dominated by sediment traction are excluded: Traction currents such as shallow lake or evaporite playa deposits could have meter-scale layering but typically onlap pre-existing topography and fill localized, low-lying basins, with near-zero depositional dips (the "Basin Floor" unit is interpreted to represent this type of environment). Deposits formed by fluvial networks would additionally be limited in extent and associated with clear erosive and constructional features such as valley networks and inverted channel casts (*Fassett and Head*, 2008; *DiBiase et al.*, 2013). The sulfates extend at least 50 km east of the Isidis inner rim, too far to have been formed from proximal alluvial sediments shed from local topographic highs, as has been proposed for some layered deposits in Valles Marineris (*Fueten et al.*, 2011). Thick eolian sedimentary deposits often have cross-bedding, which is observable at orbital HiRISE scale in Gale Crater (*Milliken et al.*, 2014) but not at Meridiani Planum (e.g. *Grotzinger et al.*, 2005; *Hayes et al.*, 2011). Three sedimentation mechanisms remain viable, all of which are based around sediment fallout from suspension: distal ash fall, duststone deposition, and deposition in a deep lake (or lakes).

There is significant global evidence of explosive volcanism on Mars (e.g. *Brož and Hauber*, 2012), and ash falls have been suggested as a likely depositional mechanism for other layered deposits on Mars (*Kerber et al.*, 2011, 2012), including in the eastern Medusae Fossae Formation, which hosts polygonal ridges interpreted as filled fractures (*Kerber et al.*, 2017) that have similarities to those within the NE Syrtis layered sulfates. While Syrtis Major is mostly an effusive basaltic province (*Hiesinger and Head*, 2004), there is significant evidence that Nili Patera in its center hosted major pyroclastic eruptions (e.g. *Fawdon et al.*, 2015). *Ghent et al.* (2012) finds that the floor of Isidis Basin contains uniform, sub-kilometer sized cones on the basin floor, suggesting the devolatilization of a substantial amount of pyroclastic material within the basin. Perched layered deposits in Arabia Terra have been interpreted as ash fall deposits due to their lack of an apparent containing basin and proximity to Syrtis Major (*Fassett and Head*, 2007).

A pyroclastic origin for the dozens of conformable thin beds of similar size would imply airfall ash emplacement from consistently small or distant eruptions, regularly paced in time. While ash falls cannot be excluded based on the structural form of the layered sulfates, the regular thickness of bedding does not easily match a stochastic process such as volcanism (*Lewis et al.*, 2008; *Lewis and Aharonson*, 2014). Duststone deposition (*Bridges and Muhs*, 2012) also implies the fallout of suspended particles from the atmosphere, and climatic mediation can explain regular layering (*Lewis et al.*, 2008; *Lewis and Aharonson*, 2014). Both ash fall and dust settling would form draping bedding; however, the lack of similar deposits preserved elsewhere in the region, along with the single phase of volume loss implied by boxwork fracturing [Section 5.5.2], do not match airfall emplacement of volcanic ash or duststone deposition.

Niles and Michalski (2009) suggested that layered sulfates might occur as a sublimation residue of ice-rich airfall sediments; crudely layered mounds could be left over from progressive sublimation of these deposits, exhibiting shallow dips and potentially draping prior topography (*Michalski and Niles*, 2012). The consistent expression of successive layered beds within the sulfates [Figure 5.10] suggests that deposition did not include deflation in a style consistent with sublimation or melting alone, which would be required by this scenario.

Deep lacustrine sedimentation forms deposits with clear structural similarities to the NE Syrtis layered sulfates. Deepwater sedimentation is typically found at large scale on Earth along passive continental margins, environments with both a steady supply of terrestrial sediment and steep underwater topography (e.g. *Stuart and Caughey*, 1977). Deepwater sedimentary packages can dip relatively steeply (~5° depositional dips are common) while maintaining internally parallel geometries, and bedding can both onlap and dip concordantly with pre-existing topography. Depositional sequences are limited in thickness by the available accommodation space (i.e. the water depth). Prograding sedimentation allows accumulation of sediments outward from the basin margin, with deposits thinning and decreasing in elevation into the basin (*Mitchum et al.*, 1977). The geometry of pre-existing topography, along with relationships between individual stratal sequences, can lead to a diversity of bedding orientations with dominantly but not exclusively basinward dips (*Mitchum et al.*, 1977). Deepwater sedimentation operated on Mars in crater lakes (*Grotzinger et al.*, 2015) and deepwater deposition without regional topographic confinement has been proposed to explain larger-scale sedimentary features observed from orbit in Valles Marineris (e.g. *Dromart et al.*, 2007) and in the Northern Plains (*Oehler and Allen*, 2012).

The NE Syrtis layered sulfates exhibit internal features typical of deepwater sediments, such as variable bedding dips (up to 7-10°) and parallel-oriented bedding packages. Regionally, the extent, lack of confinement to localized basins, and onlapping and embayment of pre-existing highs also conform to this type of sedimentation. Both the preserved thickness and overall elevation of the layered sulfates decrease eastward into Isidis Basin [Figure 5.8d], although the original thickness may be masked by erosion. Collectively, the structural characteristics of the layered sulfates are typical of deposits at the margin of a deep water-filled basin.

5.5.2 Post-depositional alteration of the layered sulfates

Interpretation of boxwork fractures The large scale and continuity, throughgoing nature, and positive relief of boxwork polygonal ridges are typical of injective dikes; however, the detailed morphology, mineralogy, and structural form of these ridges [see Section 5.4.2] instead suggests a two-stage formation history: fracturing of the layered sulfates in a polygonal pattern followed by later mineralization channelized along fracture surfaces.

The lack of preferred orientation in the boxwork fractures suggests that these features were not formed in a regional stress field. This lack of tectonic fracture control is notable in contrast with the NE-SW regional trend of ridges in the phyllosilicate-bearing Noachian basement, which correspond to the circum-Isidis pattern of the Nili Fossae (*Saper and Mustard*, 2013). Our orientation measurements of the fracture sets within the layered sulfates show that they are fundamentally different in structural form than the basement-cutting ridges, which were mapped by *Saper and Mustard* (2013) and classified as "Nili-type" ridges more generally by *Kerber et al.* (2017). The absence of directional bias in the fractures within the layered sulfate unit suggests that the fractures formed in an isotropic regional stress field. This type of stress field typically arises under volume loss and contraction.

Several mechanisms are known to generate polygonal fractures through volume loss in sedimentary material. Melting is a common process forming polygonal "patterned ground" on Earth (e.g. *Kocurek and Hunter*, 1986) and on Mars (*El-Maarry et al.*, 2010). However, it generally occurs at near the free surface and involves sagging and large volumetric reductions that can disrupt or destroy internal layering (*Soare et al.*, 2017). Typical dessication polygons such as mud cracks are also generally vertical and tied to the free surface. Such fractures tend to form hexagonal patterns due to progressive annealing. By contrast, fractures in the sulfate unit (1) have 90° preferred intersection angles, (2) penetrate the full exposed thickness of the layered sulfates, and (3) are steeply-dipping as well as vertical [Figure 5.13]. These characteristics, along with the curvilinear nature of the fractures suggest that they were not formed at the free surface.

One type of fracture that fits all of these criteria are three-dimensional "polyg-

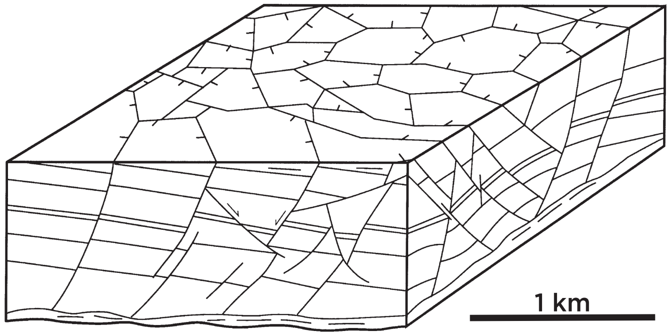

Figure 5.22: Schematic view of boxwork fracturing compiled from seismic well logs in the North Sea after *Cartwright and Lonergan* (1996). The polygonal geometry forms in the subsurface due to compaction during diagenesis, and is found at similar scales in offshore basins on Earth as the exposures in Syrtis Major.

onal faults" (*Goulty*, 2008) which are formed during diagenesis and dewatering of cohesive, clay-rich or chalk-rich sediments. These features are found often in shallow offshore sedimentary basins on Earth (*Cartwright and Lonergan*, 1996). Most examples of polygonal faulting on Earth are at similar scales to that examined in this study, with 500 m polygon domains typical [Figure 5.22]. The scale of boxwork domains is controlled by the strength and cohesion of sediments undergoing diagenesis (*Cartwright and Lonergan*, 1996; *Goulty*, 2008). Most examples of polygonal fractures occur a few hundred meters below the seafloor in continental-margin sedimentary basins, and have been investigated solely with seismic imaging (e.g. *Gay et al.*, 2004). A surface-exposed region of polygonal faults in Egypt was investigated by *Tewksbury et al.* (2014).

We interpret the boxwork polygonal ridges within the layered sulfates as fractures formed by polygonal faulting, followed by mineralization by fracture-following fluids (e.g. *Siebach and Grotzinger*, 2014). This interpretation supports the formation of the layered sulfates as fine-grained, water-lain sediments that experienced significant diagenetic volume loss.

Key to polygonal faulting is that during compaction-driven dewatering and diagenesis, volume loss creates localized extensional stresses. The exact mechanism causing the initiation of polygonal faults is unclear, but synaresis (e.g. *Siebach et al.*, 2014), overburden, and density inversion are several possibilities. It is also unclear how deeply sediments need to be buried before faulting initiates, but depths of 100 m or more are typical (*Goulty*, 2008; *Cartwright*, 2011). Once faults are initiated, the numerous "T-junction" and right-angle crossing fractures characteristic of this mechanism are due to a preference for linear defect propagation as dewatering progresses. Additionally, three-dimensional material shrinkage is converted to one-dimensional compaction by small-magnitude slip along fault surfaces. This suggests small bedding offsets and dip changes between boxwork domains, matching the character of boxwork in the layered sulfates.

On Mars, *Oehler and Allen* (2012) proposed polygonal faulting as a mechanism to explain ~2-10 km polygons expressed on the surface of Acidalia and Utopia Planitia, using this to argue for their formation in a subaqueous setting. Similar features have also been attributed to periglacial processes (e.g. *Haltigin et al.*, 2014). Unlike these examples, the northeast Syrtis layered sulfates show the full 3D geometry of the fault network, which allows a much clearer identification of polygonal faulting to be made, since the ridge characteristics match the scale, morphology, and penetrative nature of the fractures.

Implications for sediment size and amount of burial Based on the character of Earth analogs, polygonal faulting has a particular set of implications for sediment characteristics and diagenetic environment. Polygonal faults dependably involve dewatering of fine grained (silt/clay), water-rich sediments under three-dimensional compaction in the subsurface. Dewatering solely by compaction might require a few hundred meters of sediment above presently exposed ridges in the layered sulfates. However, dewatering may require less overburden in cases where drying conditions are favored by thermal/climatic factors (e.g. arid, evaporative conditions). Boxwork fracturing is chiefly found in the western part of the study area, and most areas of boxwork cluster in basin lows, which could easily be buried to the levels required based on projection of current exposures [Figure 5.8]. A clear exception is the boxwork fractures in `nf4`, which occur within some of the highest-elevation exposures of the sulfates in the study area [Figure 5.6c]. The presence of boxwork at these high elevations requires either significant overburden at levels above the sulfates currently exposed in the study area or volume-loss without substantial burial.

The chief factor governing the sediment-size constraint is the low internal friction angle of mud-sized sediments, which sets the stress threshold to initiate fracturing. In sediments with low internal friction, defects form and propagate under small, localized stresses (*Cartwright and Lonergan*, 1996; *Goulty*, 2008). Polyhydrated sulfates often have >10 wt. % water, and fine-grained polyhydrated sulfate sediments would have characteristics conducive to polygonal faulting. Fracture mineralization is also indicative of fine-grained sediments: channelization of altering fluids on boxwork fractures suggests that the bulk of the unit has low permeability. In contrast, sand-sized sediments have open pore spaces and easily permit fluid migration.

The formation of boxwork polygonal ridges by the mechanism outlined above requires thick, initially water-saturated, fine grained sediments. These features would not be found in ash and ice-residue deposits, and their presence within the layered sulfates aligns with the unit's structural geometry and layer orientations to imply a deep lacustrine sedimentary origin.

Mineralization of fractures and implications for water volume The parallel-sided, or isopachous, geometry of boxwork fractures, their current existence as resistant ridges, and a mineralogy distinct from the rest of the unit suggests the mineralization of pre-existing fractures. The diffuse "halo" around some fractures [Figure 5.11] represents an interaction between the fracture-filling material and its surroundings. These morphologies can be linked to either fracture-filling cements that close an open fracture inwards or an outward-propagating zone of alteration around a channel carrying a reactive fluid (e.g. *Nelson et al.*, 1999). Such a fluid would either chemically alter the groundmass of the unit or fill pores with light-toned cement. Both of these cases imply fluid channelization along pre-existing fractures, which must be hosted in relatively impermeable (likely fine-grained) sediments.

The margin of Isidis basin is modeled as an area of pervasive groundwater upwelling (*Andrews-Hanna and Lewis*, 2011) and the deep basins in in NE Syrtis would have the strongest topographic gradient in the region. These features suggest the focusing of abundant groundwater into the base of the layered sulfates to drive fracture mineralization. The presence of jarosite mineral detections on the ridges indicates additional infiltration of pH<4 fluids (e.g. *Ehlmann and Mustard*, 2012; *McCollom et al.*, 2013). Fluid leaching combined with induration has been proposed as a mechanism to develop haloed fractures in Candor Chasma (*Okubo and McEwen*, 2007). Double-walled fractures similar to those seen here have been identified from orbit in smaller (decameter-scale) boxwork fractures in the upper Gale Crater mound (*Siebach and Grotzinger*, 2014). For the Gale Crater system, a mass-balance given plausible limits on pore-water volume suggested that the formation of 1.75×10^6 m^3 of cemented fractures required the evaporation of at least ~0.4 km^3 of water (*Siebach and Grotzinger*, 2014). Using the same 30% porosity and mineral-precipitation assumptions and a fracture volume of 0.86 km^3 (860 km of fractures mapped, an average vertical penetration of 200 m, and a fracture width of 5 m), we estimate that ~515 km^3 of water were required to mineralize the fractures within the layered sulfates.

In a few locations, localized, pervasive jarosite mineralization within the groundmass of the sulfate unit is unchannelized and at the high end of alteration intensity observed [Figure 5.14]. Intricately patterned exposures in the *Erosional Window* could be driven by surface water as well as groundwater, with mineralization occurring in an transient, evaporitive lake fed by periodic outflow-channel inundation (*Mangold et al.*, 2008).

5.5.3 Containing basin for the layered sulfates

A key question for deep subaqueous sedimentation is the geometry and confinement of the containing basin. Deposition of the sulfates in a deep subaqueous setting would require a basin filled to about −1600 m, the maximum elevation of the layered sulfates in the region [Figure 5.8d]. Given the location at the edge of Isidis Basin, the basin is not confined by current topography. Two possible mechanisms to inundate the NE Syrtis region deeply enough to deposit the layered sulfates include a global ocean or a ice-dammed lake marginal to an ice sheet within Isidis basin.

A basin at the margin of a global ocean would provide a straightforward analog to Earth. However, evidence for a global ocean is uncertain (e.g. *Ghatan and Zimbelman*, 2006), and the required topographic level is higher than putative ocean deposits (*Perron et al.*, 2007; *DiBiase et al.*, 2013). An alternative is confinement of a large lake by a basin-filling ice sheet, which could provide the regional topographic confinement and be a source of abundant meltwater. *Ivanov et al.* (2012) suggested that ice sheets covered parts of the basin rim and floor during the early to late Hesperian (~3.5-3.1 Ga) and eroded previously-existing layered sediments, based on morphologic similarities of sinuous ridges to terrestrial, subglacially-formed eskers. *Souček et al.* (2015) modeled the potential extent of a crater-filling ice sheet given expected precipitation and climate, finding that an ice sheet would preferentially mantle the NE Syrtis region relative to other parts of the Isidis rim (and would actually overtop the entire study area at its maximum modeled extent). If slightly smaller, such an ice sheet could dam a regional lake including NE Syrtis, creating the conditions for deposition of the layered sulfates. A crucial question associated with the ice-dam hypothesis is whether an ice sheet could exist with surface temperatures clement enough to allow an adjacent water-filled basin of sufficient cumulative lifetime to produce the observed sedimentation.

The hemispheric ocean or Isidis-filling ice sheet required to bound this depositional basin raises a key question of preservation: why are the layered sulfates only found at NE Syrtis? No comparable deposits have been found elsewhere on the rim of Isidis Basin, though the Libya Montes to the south is otherwise similar (*Bishop et al.*, 2013). Erosion clearly played a major role: the layered sulfates are preserved only where capped or buttressed. The overriding of the sulfates by the Syrtis Major lavas is a fortuitous local relationship, but the mineralized boxwork fractures and smooth capping surface may owe their formation to localized groundwater interaction in this region. If these features only formed at NE Syrtis, any sulfates aggraded elsewhere could be easily stripped away by wind erosion or later fluvial incision.

5.5.4 Modification by fluvial erosion, lavas, and late lake deposits

Another key finding of this study is continued erosion and fluvial activity postdating the layered sulfates. The long sedimentary history after sedimentary deposition of the layered sulfates in a deepwater basin includes several phases of erosion, cap unit emplacement, further fluvial erosion, lava emplacement, and then still-later fluvial-lacustrine erosion and deposition. No matter how the layered sulfates formed, the smooth capping unit, Syrtis Major lavas, and late fluvial features formed significantly afterwards. This history implies substantial episodic interaction with surface water significantly postdating the formation of the layered sulfates.

Angular differences between the smooth capping surfaces and the underlying sulfates indicate erosional truncation of the underlying sulfates \Figure 5.6. This paleotopographic relief suggests an unconformity and thus the erosion of a significant volume of sulfates prior to cap unit formation. The observed smooth, featureless surface, low thermal inertia, and low crater retentivity are typical features of uncohesive material and are at odds with the observed resistant nature of the cap surface. A partly cemented sandstone, welded or later-indurated ash fall, highly degraded lava flow, or capping "duststone" (*Malin and Edgett*, 2000; *Bridges and Muhs*, 2012) could potentially generate the characteristics of the deposit. The jarosite-containing, light-toned "halo" extending up to 30 m beneath the capping unit [Figure 5.6a] may indicate interaction with the underlying sulfates during cementation of the capping surface.

Valley A in the center of the study area is cut between *Mesas A* and *B*, which are both topped by the smooth capping surface. *Valley A* and its upstream extension may be remnants of a major fluvial system that flowed from the northern margins of the Syrtis Major volcanic province [Figure 5.2b]. Beginning in the early Hesperian, effusive Syrtis Major lava flows flowed through these pre-existing fluvial channels and embayed the partially eroded layered sulfates at their southern margin in multiple locations, notably *Valleys A* and *B* [Figure 5.18b]. Cap unit formation, paleovalley erosion, and embayment by lava flows did not occur as a single event, and these processes may have been interleaved and closely spaced in time during a geologically active late Noachian to Hesperian transition.

The latest fluvial systems within the study area start atop the Syrtis Major flows and erode the capped sulfates and Noachian basement, forming deltas and inverted channels. The preserved fluvial and lacustrine deposits are relatively small, with sedimentary deposits at most ~20 m thick atop the basement and layered sulfates, and ampitheater canyons cut back at most 1 km into the Syrtis Major lavas. The basin-fill and associated layered scarps in *North Basin* and *Deep Basin* show lacustrine deposition and indicate inundation of substantial portions of the study area after erosion of the layered sulfates.

The alignment of deltas, basin-filling deposits, and the draping valley fill at similar topographic levels within the study area suggests, possibly, a single base level for deposition. This open-contour alignment of late sedimentary deposits suggests that they formed marginal to a open-basin lacustrine system not bounded within the study area. The −2300 m elevation of these features is nearly the same as that of the Jezero delta [Figure 5.2] and is near the elevation of the various deltas and coastline features making up the proposed coastline of a hemisphere-spanning ocean (*Di Achille and Hynek*, 2010). The presence of phyllosilicates in layered scarps of the late sedimentary deposits at NE Syrtis [Figure 5.20] suggests that these deposits contain detrital material similar to that in the Jezero delta (*Ehlmann et al.*, 2008b; *Goudge et al.*, 2015).

The final resolvable phase of lacustrine activity in the area built a series of lakes in interconnected topographic lows within *North Basin*. The outlet channel leading eastward from *North Basin* emphasizes that a lake filled this basin to −2400 m and drained to the east. That this outlet channel does not exit the basin at its current lowest-elevation location (-2550 m in `nf1`) is consistent with a prior blockage of this exit (*Skok and Mustard*, 2014). We propose that the current lowest exit in `nf1` was blocked by layered sulfates prior to Amazonian wind-driven erosion of the layered sulfates.

Outflow features continuous with those mapped across the Syrtis Major plains to the south of the study area by *Mangold et al.* (2008) suggest episodic, powerfully erosive flows across the Syrtis Major lava plains. Flow across the lava plains may have also caused episodic inundation of the *Erosional window* in the southwest part of the study area, driving the intense and localized acid-sulfate alteration seen solely in this basin [Figure 5.14].

5.6 Summary, Conclusions, and Future Work

The layered sulfates at NE Syrtis Major form a thick (up to 600 m) sedimentary package unconformable with the underlying Noachian basement and olivine-carbonate melt sheet. The deposit contains parallel meter-scale beds that dip up to 7-10° with no preferred direction, and boxwork polygonal fractures that were formed by diagenetic volume loss and mineralized by jarosite-containing fluids to form raised ridges. The layered sulfates thin against and embay basement highs, to a maximum elevation of −1600 m. The thin bedding, relatively steep depositional dips, and volume-loss fractures in the layered sulfates all suggest deposition within a deep, water-filled basin.

Overall, the upper stratigraphy of NE Syrtis Major was built by a multistage history of aqueous interaction [Figure 5.23]: The water-lain sulfates record (1) deposition in a subaqueous setting, (2) diagenetic volume-loss and fracturing, (3) partial erosion to form paleotopography, (4) mineralization of fractures and capping of partially-eroded sulfates with the "smooth capping surface." The extended erosional history of these deposits then includes later (5) paleovalley incision, (6) embayment by Syrtis Major lavas, (7) differential erosion of sulfates to uncover adjacent deep basins, and (8) the construction of small fluvial and lacustrine features in these basins.

Deposition was open to Isidis Basin to the east, and there is no evidence of either local confinement or the existence of higher-elevation sulfates on the adjacent *Nili Fossae Plains*. The layered sulfates were likely deposited as detrital sediments in a deepwater setting in a lake system confined by an Isidis Basin-filling ice sheet or at the margin an unconfined northern hemisphere ocean. Such an environment requires large volumes of surface water, and subsequent filling of volume-loss fractures requires abundant sulfate-containing groundwater. Both of these aqueous phases occurred during the Noachian-Hesperian transition, well after clay and carbonate formation in the Noachian highlands. Additionally, extensive erosion and superposed fluvial features on the Syrtis Major lavas demonstrate that surface water was at least episodically present into the Late Hesperian and Early Amazonian. The pattern seen at NE Syrtis, of aggradation of thick layered deposits during the Noachian–Hesperian transition, followed by significant erosion and superposed fluvial deposits from the Late Hesperian–Early Amazonian, is the result of a Martian surface water cycle at least episodically active for much of the planet's history.

This study used the maximum available resolution across a wide area and integrated new techniques for DEM creation, error analysis and visualization, and the level of detail presented here will be difficult to surpass using orbital data. The key unsolved questions of this study are most productively assessed at rover scale. Outcrop observation of sedimentary bedforms and grainsize within the layered sulfates will confirm or refute the deep-basin sedimentation hypothesis we propose for the unit based on its regional layering style and macrostructural form. The scales of variation in sedimentary deposition from sequence stratigraphy, given sub-centimeter sedimentary textures, may constrain the size of the basin (ice-sheet confined vs. open-ocean). Similar close-range observations of the

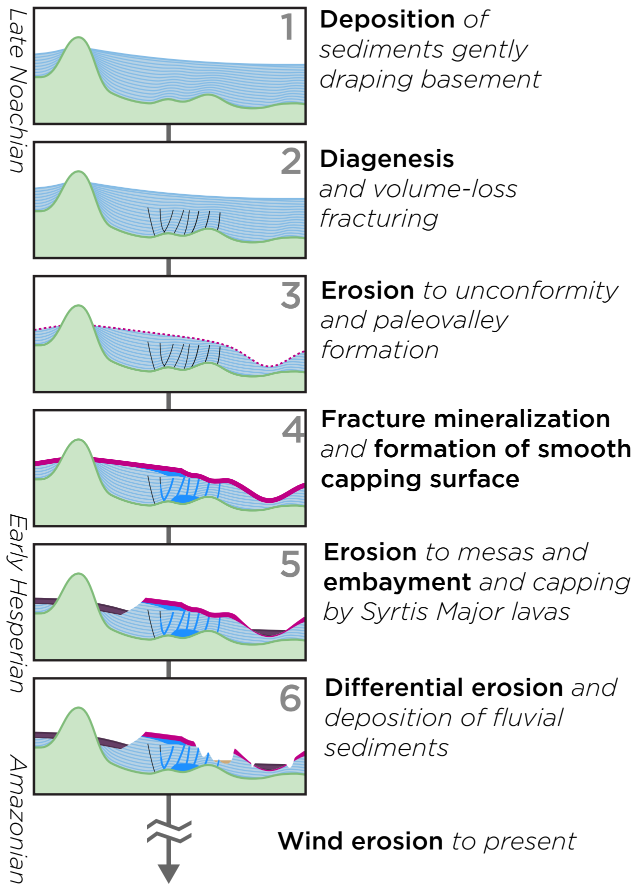

Figure 5.23: Model emplacement and alteration history of the layered sulfates. The relative timing of steps 3 and 4 are uncertain, and the genesis of the smooth capping surface is unknown.

smooth capping surface will clearly define its mechanism of deposition and test our finding of an unconformity with the sulfates. Detailed chemical analysis of the filled volume-loss fractures can confirm an upwelling groundwater source of fracture-filling fluids, and place firm bounds on the type and scale of groundwater interaction within the layered sulfates. Sufficient potassium might be present to place K-Ar dates to constrain absolute timing of alteration by isotopic analysis of the jarosite-filled fractures.

Additionally, examination of ambiguous relationships between the well-defined units described in this study will substantially clarify the sequence of geologic events affecting NE Syrtis. For instance, the contact between the draping valley fill and the Syrtis Major lavas, both of which overlie the layered sulfates in *Valley A*, may capture the interaction of lavas with water-lain sedimentary deposits, and investigation of both of these units will clarify the timing and interplay of sulfate erosion, lava embayment, and the late fluvial-lacustrine history and a potential Late Hesperian or Early Amazonian inundation of the region. These key features of the layered sulfates and their context can be evaluated *in situ*, within a 5 km-wide area in `nf3`, near the point in the layered sulfates closest to the Mars 2020 landing ellipse (as of early 2018). Such a 30-km traverse with observation and sampling campaign has the potential to greatly illuminate the multistage history of aqueous activity captured in the upper stratigraphy of northern Syrtis Major and provide new insights into the Mars surface environment, its climate, and its habitability over periods spanning the Noachian to Amazonian.

5.7 Acknowledgements

We would like to acknowledge NASA for the NASA Earth and Space Science Fellowship (to D.P. Quinn) that funded this work. HiRISE elevation datasets created during this study are archived with the Planetary Data Systems (*DOI not yet assigned*), and the geologic map database underlying the geologic map and cross-sections is archived with CaltechDATA (*DOI not yet assigned*).

Bibliography

Andrews-Hanna, J. C., and K. W. Lewis (2011), Early Mars hydrology: 2. Hydrological evolution in the Noachian and Hesperian epochs, *Journal of Geophysical Research*, *116*(E2), E02,007, doi:10.1029/2010JE003709.

Baratoux, D., P. Pinet, A. Gendrin, L. Kanner, J. Mustard, Y. Daydou, J. Vaucher, and J. P. Bibring (2007), Mineralogical structure of the subsurface of Syrtis Major from OMEGA observations of lobate ejecta blankets, *Journal of Geophysical Research E: Planets*, *112*(8), 1–30, doi:10.1029/2007JE002890.

Baratoux, D., M. J. Toplis, M. Monnereau, and V. Sautter (2013), The petrological expression of early Mars volcanism, *Journal of Geophysical Research E: Planets*, *118*(1), 59–64, doi:10.1029/2012JE004234.

Bibring, J.-P., Y. Langevin, J. F. Mustard, F. Poulet, R. Arvidson, A. Gendrin, B. Gondet, N. Mangold, P. Pinet, F. Forget, M. Berthé, C. Gomez, D. Jouglet, A. Soufflot, M. Vincendon, M. Combes, P. Drossart, T. Encrenaz, T. Fouchet, R. Merchiorri, G. Belluci, F. Altieri, V. Formisano, F. Capaccioni, P. Cerroni, A. Coradini, S. Fonti, O. Korablev, V. Kottsov, N. Ignatiev, V. Moroz, D. Titov, L. Zasova, D. Loiseau, P. Pinet, S. Douté, B. Schmitt, C. Sotin, E. Hauber, H. Hoffmann, R. Jaumann, U. Keller, R. Arvidson, T. Duxbury, F. Forget, and G. Neukum (2006), Global mineralogical and aqueous Mars history derived from OMEGA/Mars Express data., *Science*, *312*(5772), 400–4, doi:10.1126/science.1122659.

Bishop, J. L., D. Tirsch, L. L. Tornabene, R. Jaumann, A. S. McEwen, P. C. McGuire, A. Ody, F. Poulet, R. N. Clark, M. Parente, N. K. McKeown, J. F. Mustard, S. L. Murchie, J. Voigt, Z. Aydin, M. Bamberg, A. Petau, G. Michael, F. P. Seelos, C. D. Hash, G. a. Swayze, and G. Neukum (2013), Mineralogy and morphology of geologic units at Libya Montes, Mars: Ancient aqueously derived outcrops, mafic flows, fluvial features, and impacts, *Journal of Geophysical Research E: Planets*, *118*(3), 487–513, doi:10.1029/2012JE004151.

Bondre, N. R., R. a. Duraiswami, and G. Dole (2004), A brief comparison of lava flows from the Deccan Volcanic Province and the Columbia-Oregon Plateau Flood Basalts: Implications for models of flood basalt emplacement, *Journal of Earth System Science*, *113*(4), 809–817, doi:10.1007/BF02704039.

Bramble, M. S., J. F. Mustard, and M. R. Salvatore (2017), The geological history of Northeast Syrtis Major, Mars, *Icarus*, *293*, 66–93, doi:10.1016/j.icarus.2017.03.030.

Bridges, N. T., and D. R. Muhs (2012), Duststones on Mars: Source, transport, deposition, and erosion, in *Sedimentary Geology of Mars*, edited by J. P. Grotzinger and R. E. Milliken, 102, pp. 169–182, SEPM, doi:10.2110/pec.12.102.0169.

Brož, P., and E. Hauber (2012), A unique volcanic field in Tharsis, Mars: Pyroclastic cones as evidence for explosive eruptions, *Icarus*, *218*(1), 88–99, doi:10.1016/j.icarus.2011.11.030.

Cartwright, J. (2011), Diagenetically induced shear failure of fine-grained sediments and the development of polygonal fault systems, *Marine and Petroleum Geology*, *28*(9), 1593–1610, doi:10.1016/j.marpetgeo.2011.06.004.

Cartwright, J. A., and L. Lonergan (1996), Volumetric contraction during the compaction of mudrocks: A mechanism for the development of regional-scale polygonal fault systems, *Basin Research*, *8*(2), 183–193, doi:10.1046/j.1365-2117.1996.01536.x.

Caumon, G., P. Collon-Drouaillet, C. Le Carlier De Veslud, S. Viseur, and J. Sausse (2009), Surface-based 3D modeling of geological structures, *Mathematical Geosciences*, *41*(8), 927–945, doi:10.1007/s11004-009-9244-2.

Clenet, H., P. Pinet, Georges, Ceuleneer, Daydou, Yves, Heuripeau, Frédérick, Rosemberg Christine, Bibring Jean-Pierre, Bellucci Giancarlo, Altieri Francesca, and Gondet Brigitte (2013), A systematic mapping procedure based on the Modified Gaussian Model to characterize magmatic units from olivine/pyroxenes mixtures: Application to the Syrtis Major volcanic shield on Mars, *Journal of Geophysical Research: Planets*, *118*(8), 1632–1655, doi:10.1002/jgre.20112.

Di Achille, G., and B. M. Hynek (2010), Ancient ocean on Mars supported by global distribution of deltas and valleys, *Nature Geoscience*, *3*(7), 459–463, doi:10.1038/ngeo891.

DiBiase, R. A., A. B. Limaye, J. S. Scheingross, W. W. Fischer, and M. P. Lamb (2013), Deltaic deposits at Aeolis Dorsa: Sedimentary evidence for a standing body of water on the northern plains of Mars, *Journal of Geophysical Research: Planets*, *118*(6), 1285–1302, doi:10.1002/jgre.20100.

Dromart, G., C. Quantin, and B. Olivier (2007), Stratigraphic architectures spotted in southern Melas Chasma, Valles Marineris, Mars, *Geology*, *35*(4), 363–366, doi:10.1130/G23350A.1.

Ehlmann, B., J. Mustard, and S. Murchie (2008a), Orbital identification of carbonate-bearing rocks on Mars, *Science*, *322*(December), 1828–1832.

Ehlmann, B. L., and C. S. Edwards (2014), Mineralogy of the Martian Surface, *Annu. Rev. Earth Planet. Sci*, *42*, 291–315, doi:10.1146/annurev-earth-060313-055024.

Ehlmann, B. L., and J. F. Mustard (2012), An in-situ record of major environmental transitions on early Mars at Northeast Syrtis Major, *Geophysical Research Letters*, *39*(11), 1–7, doi:10.1029/2012GL051594.

Ehlmann, B. L., J. F. Mustard, C. I. Fassett, S. C. Schon, J. W. Head III, D. J. Des Marais, J. a. Grant, and S. L. Murchie (2008b), Clay minerals in delta deposits and organic preservation potential on Mars, *Nature Geoscience*, *1*(6), 355–358, doi:10.1038/ngeo207.

Ehlmann, B. L., J. F. Mustard, G. A. Swayze, R. N. Clark, J. L. Bishop, F. Poulet, D. J. Des Marais,

L. H. Roach, R. E. Milliken, J. J. Wray, O. Barnouin-Jha, and S. L. Murchie (2009), Identification of hydrated silicate minerals on Mars using MRO-CRISM: Geologic context near Nili Fossae and implications for aqueous alteration, *Journal of Geophysical Research*, *114*(10), 1–33, doi:10.1029/2009JE003339.

Ehlmann, B. L., J. F. Mustard, S. L. Murchie, J.-P. Bibring, A. Meunier, A. A. Fraeman, and Y. Langevin (2011), Subsurface water and clay mineral formation during the early history of Mars., *Nature*, *479*(7371), 53–60, doi:10.1038/nature10582.

El-Maarry, M. R., W. J. Markiewicz, M. T. Mellon, W. Goetz, J. M. Dohm, and A. Pack (2010), Crater floor polygons: Desiccation patterns of ancient lakes on Mars?, *Journal of Geophysical Research*, *115*(E10), E10,006, doi:10.1029/2010JE003609.

Fassett, C. I., and J. W. Head (2005), Fluvial sedimentary deposits on Mars: Ancient deltas in a crater lake in the Nili Fossae region, *Geophysical Research Letters*, *32*(14), 1–5, doi:10.1029/2005GL023456.

Fassett, C. I., and J. W. Head (2007), Layered mantling deposits in northeast Arabia Terra, Mars: Noachian-Hesperian sedimentation, erosion, and terrain inversion, *Journal of Geophysical Research E: Planets*, *112*(8), 1–19, doi:10.1029/2006JE002875.

Fassett, C. I., and J. W. Head (2008), The timing of martian valley network activity: Constraints from buffered crater counting, *Icarus*, *195*(1), 61–89, doi:10.1016/j.icarus.2007.12.009.

Fawdon, P., J. R. Skok, M. R. Balme, C. L. Vye-Brown, D. A. Rothery, and C. J. Jordan (2015), The geological history of Nili Patera, Mars, *120*(5), 951–977, doi:10.1002/2015JE004795.

Frey, H. (2008), Ages of very large impact basins on Mars: Implications for the late heavy bombardment in the inner solar system, *Geophysical Research Letters*, *35*(13), 1–4, doi:10.1029/2008GL033515.

Fueten, F., J. Flahaut, L. Le Deit, R. Stesky, E. Hauber, and K. Gwinner (2011), Interior layered deposits within a perched basin, southern Coprates Chasma, Mars: Evidence for their formation, alteration, and erosion, *Journal of Geophysical Research E: Planets*, *116*(2), 1–18, doi:10.1029/2010JE003695.

Gay, A., M. Lopez, P. Cochonat, and G. Sermondadaz (2004), Polygonal faults-furrows system related to early stages of compaction–upper Miocene to recent sediments of the Lower Congo Basin, *Basin Research*, *16*(1), 101–116.

Gendrin, A., N. Mangold, J.-P. Bibring, Y. Langevin, B. Gondet, F. Poulet, G. Bonello, C. Quantin, J. Mustard, R. Arvidson, and S. LeMouélic (2005), Sulfates in Martian layered terrains: The OMEGA/Mars Express view., *Science (New York, N.Y.)*, *307*(5715), 1587–91, doi:10.1126/science.1109087.

Ghatan, G. J., and J. R. Zimbelman (2006), Paucity of candidate coastal constructional landforms along proposed shorelines on Mars: Implications for a northern lowlands-filling ocean, *Icarus*, *185*(1), 171–196, doi:10.1016/j.icarus.2006.06.007.

Ghent, R. R., S. W. Anderson, and T. M. Pithawala (2012), The formation of small cones in Isidis Planitia, Mars through mobilization of pyroclastic surge deposits, *Icarus*, *217*(1), 169–183, doi:10.1016/j.icarus.2011.10.018.

Goudge, T. A., J. F. Mustard, J. W. Head, C. I. Fassett, and S. M. Wiseman (2015), Assessing the mineralogy of the watershed and fan deposits of the Jezero crater paleolake system, Mars, doi:10.1002/2014JE004782.Received.

Goudge, T. A., R. E. Milliken, J. W. Head, J. F. Mustard, and C. I. Fassett (2017), Sedimentological evidence for a deltaic origin of the western fan deposit in Jezero crater , Mars and implications for future exploration, *Earth and Planetary Science Letters*, *458*, 357–365, doi:10.1016/j.epsl.2016.10.056.

Goulty, N. R. (2008), Geomechanics of polygonal fault systems: A review, *Petroleum Geoscience*, *14*(4), 389–397, doi:10.1144/1354-079308-781.

Grotzinger, J. P., and R. E. Milliken (2012), Sedimentary Geology of Mars.

Grotzinger, J. P., R. E. Arvidson, J. F. Bell, W. Calvin, B. C. Clark, D. A. Fike, M. Golombek,

R. Greeley, A. Haldemann, K. E. Herkenhoff, B. L. Jolliff, A. H. Knoll, M. Malin, S. M. McLennan, T. Parker, L. Soderblom, J. N. Sohl-Dickstein, S. W. Squyres, N. J. Tosca, and W. A. Watters (2005), Stratigraphy and sedimentology of a dry to wet eolian depositional system, Burns formation, Meridiani Planum, Mars, *Earth and Planetary Science Letters*, *240*(1), 11–72, doi: 10.1016/j.epsl.2005.09.039.

Grotzinger, J. P., J. Crisp, A. R. Vasavada, R. C. Anderson, C. J. Baker, R. Barry, D. F. Blake, P. Conrad, K. S. Edgett, B. Ferdowski, R. Gellert, J. B. Gilbert, M. Golombek, J. Gómez-Elvira, D. M. Hassler, L. Jandura, M. Litvak, P. Mahaffy, J. Maki, M. Meyer, M. C. Malin, I. Mitrofanov, J. J. Simmonds, D. Vaniman, R. V. Welch, and R. C. Wiens (2012), *Mars Science Laboratory Mission and Science Investigation*, vol. 170, doi:10.1007/s11214-012-9892-2.

Grotzinger, J. P., D. Y. Sumner, L. C. Kah, K. Stack, S. Gupta, L. Edgar, D. Rubin, and K. Lewis (2013), A habitable fluvio-lacustrine environment at Yellowknife Bay, Gale Crater, Mars, *Science*, *342*, 1–18.

Grotzinger, J. P., S. Gupta, M. C. Malin, D. M. Rubin, J. Schieber, K. Siebach, D. Y. Sumner, K. M. Stack, A. R. Vasavada, R. E. Arvidson, F. Calef, L. Edgar, W. F. Fischer, J. A. Grant, J. Griffes, L. C. Kah, M. P. Lamb, K. W. Lewis, N. Mangold, M. E. Minitti, M. Palucis, M. Rice, R. M. E. Williams, R. A. Yingst, D. Blake, D. Blaney, P. Conrad, J. Crisp, W. E. Dietrich, G. Dromart, K. S. Edgett, R. C. Ewing, R. Gellert, J. A. Hurowitz, G. Kocurek, P. Mahaffy, M. J. McBride, S. M. McLennan, M. Mischna, D. Ming, R. Milliken, H. Newsom, D. Oehler, T. J. Parker, D. Vaniman, R. C. Wiens, and S. A. Wilson (2015), Deposition, exhumation, and paleoclimate of an ancient lake deposit, Gale crater, Mars, *Science*, *350*(6257), aac7575–aac7575, doi:10.1126/science.aac7575.

Haltigin, T., W. Pollard, P. Dutilleul, G. Osinski, and L. Koponen (2014), Co-evolution of polygonal and scalloped terrains, southwestern Utopia Planitia, Mars, *Earth and Planetary Science Letters*, *387*, 44–54, doi:10.1016/j.epsl.2013.11.005.

Hamilton, V. E., and P. R. Christensen (2005), Evidence for extensive, olivine-rich bedrock on Mars, *Geology*, *33*(6), 433, doi:10.1130/G21258.1.

Harvey, R. P., and J. Griswold (2010), Burial, exhumation, metamorphism and other dastardly deeds exposed at the Hesperian/Noachian boundary in the southern Nili Fossae region, in *Lunar and Planetary Science Conference*, vol. 41, p. 2045.

Hayes, A. G., Grotzinger J. P., Edgar L. A., Squyres S. W., Watters W. A., and Sohl-Dickstein J. (2011), Reconstruction of eolian bed forms and paleocurrents from cross-bedded strata at Victoria Crater, Meridiani Planum, Mars, *Journal of Geophysical Research: Planets*, *116*(E7), doi: 10.1029/2010JE003688.

Hiesinger, H., and J. W. Head (2004), The Syrtis Major volcanic province, Mars: Synthesis from Mars Global Surveyor data, *Journal of Geophysical Research*, *109*(E1), E01,004, doi:10.1029/2003JE002143.

Hoefen, T. M., R. N. Clark, J. L. Bandfield, M. D. Smith, J. C. Pearl, and P. R. Christensen (2003), Discovery of olivine in the Nili Fossae region of Mars., *Science (New York, N.Y.)*, *302*(5645), 627–30, doi:10.1126/science.1089647.

Howard, A. D., J. M. Moore, and R. P. Irwin (2005), An intense terminal epoch of widespread fluvial activity on early Mars: 1. Valley network incision and associated deposits, *Journal of Geophysical Research*, *110*(E12), E12S14, doi:10.1029/2005JE002459.

Hurowitz, J. A., W. W. Fischer, N. J. Tosca, and R. E. Milliken (2010), Origin of acidic surface waters and the evolution of atmospheric chemistry on early Mars, *Nature Geoscience*, *3*(5), 323–326, doi:10.1038/ngeo831.

Irwin, R. P., A. D. Howard, R. A. Craddock, and J. M. Moore (2005), An intense terminal epoch of widespread fluvial activity on early Mars: 2. Increased runoff and paleolake development, *Journal of Geophysical Research*, *110*(E12), E12S15, doi:10.1029/2005JE002460.

Ivanov, M. A., and J. Head (2003), Syrtis Major and Isidis Basin contact: Morphological and topographic characteristics of Syrtis Major lava flows and material of the Vastitas Borealis Formation, *Journal of Geophysical Research*, *108*(E6), 5063, doi:10.1029/2002JE001994.

Ivanov, M. A., H. Hiesinger, G. Erkeling, F. J. Hielscher, and D. Reiss (2012), Major episodes of geologic history of Isidis Planitia on Mars, *Icarus*, *218*(1), 24–46, doi:10.1016/j.icarus.2011.11.029.

Kaasalainen, H., and A. Stefánsson (2011), Sulfur speciation in natural hydrothermal waters, Iceland, *Geochimica et Cosmochimica Acta*, *75*(10), 2777–2791, doi:10.1016/j.gca.2011.02.036.

Kerber, L., J. W. Head, J. B. Madeleine, F. Forget, and L. Wilson (2011), The dispersal of pyroclasts from Apollinaris Patera, Mars: Implications for the origin of the Medusae Fossae Formation, *Icarus*, *216*(1), 212–220, doi:10.1016/j.icarus.2011.07.035.

Kerber, L., J. W. Head, J.-B. Madeleine, F. Forget, and L. Wilson (2012), The dispersal of pyroclasts from ancient explosive volcanoes on Mars: Implications for the friable layered deposits, *Icarus*, *219*(1), 358–381, doi:10.1016/j.icarus.2012.03.016.

Kerber, L., J. L. Dickson, J. W. Head, and E. B. Grosfils (2017), Polygonal ridge networks on Mars: Diversity of morphologies and the special case of the Eastern Medusae Fossae Formation, *Icarus*, *281*, 200–219, doi:10.1016/j.icarus.2016.08.020.

Kirk, R. L., E. Howington-Kraus, B. Redding, D. Galuszka, T. M. Hare, B. A. Archinal, L. A. Soderblom, and J. M. Barrett (2003), High-resolution topomapping of candidate MER landing sites with Mars Orbiter Camera narrow-angle images, *Journal of Geophysical Research-Planets*, *108*(E12), doi:10.1029/2003je002131.

Kirk, R. L., E. Howington-Kraus, M. R. Rosiek, J. a. Anderson, B. a. Archinal, K. J. Becker, D. a. Cook, D. M. Galuszka, P. E. Geissler, T. M. Hare, I. M. Holmberg, L. P. Keszthelyi, B. L. Redding, W. a. Delamere, D. Gallagher, J. D. Chapel, E. M. Eliason, R. King, and a. S. McEwen (2008), Ultrahigh resolution topographic mapping of Mars with MRO HiRISE stereo images: Meter-scale slopes of candidate Phoenix landing sites, *Journal of Geophysical Research*, *113*, E00A24, doi:10.1029/2007JE003000.

Kocurek, G., and R. E. Hunter (1986), Origin of polygonal fractures in sand, uppermost Navajo and Page sandstones, Page, Arizona, *Journal of Sedimentary Research*, *56*(6), doi:10.1306/212F8A7B-2B24-11D7-8648000102C1865D.

Koeppen, W. C., and V. E. Hamilton (2008), Global distribution, composition, and abundance of olivine on the surface of Mars from thermal infrared data, *Journal of Geophysical Research: Planets*, *113*(E5).

Lewis, K., O. Aharonson, and J. Grotzinger (2008), Quasi-Periodic Bedding in the Sedimentary Rock Record of Mars, *Science*, *1532*(2008), doi:10.1126/science.1161870.

Lewis, K. W., and O. Aharonson (2006), Stratigraphic analysis of the distributary fan in Eberswalde crater using stereo imagery, *Journal of Geophysical Research*, *111*(E6), 1–7, doi:10.1029/2005JE002558.

Lewis, K. W., and O. Aharonson (2014), Occurrence and origin of rhythmic sedimentary rocks on Mars, *Journal of Geophysical Research: Planets*, *119*(6), 1432–1457, doi:10.1002/2013JE004404.

Malin, M. C., and K. S. Edgett (2000), Sedimentary Rocks of Early Mars, *Science*, *290*(5498), 1927–1937, doi:10.1126/science.290.5498.1927.

Mangold, N., F. Poulet, J. F. Mustard, J.-P. Bibring, B. Gondet, Y. Langevin, V. Ansan, P. Masson, C. Fassett, J. W. Head, H. Hoffmann, and G. Neukum (2007), Mineralogy of the Nili Fossae region with OMEGA/Mars Express data: 2. Aqueous alteration of the crust, *Journal of Geophysical Research*, *112*(E8), E08S04, doi:10.1029/2006JE002835.

Mangold, N., V. Ansan, D. Baratoux, F. Costard, L. Dupeyrat, H. Hiesinger, P. Masson, G. Neukum, and P. Pinet (2008), Identification of a new outflow channel on Mars in Syrtis Major Planum using HRSC/MEx data, *Planetary and Space Science*, *56*(7), 1030–1042, doi:10.1016/j.pss.2008.01.011.

McCollom, T. M., M. Robbins, B. Moskowitz, T. S. Berquó, N. Jöns, and B. M. Hynek (2013), Experimental study of acid-sulfate alteration of basalt and implications for sulfate deposits on Mars, *Journal of Geophysical Research: Planets*, *118*(4), 577–614, doi:10.1002/jgre.20044.

McEwen, A. S., E. M. Eliason, J. W. Bergstrom, N. T. Bridges, C. J. Hansen, W. A. Delamere,

J. a. Grant, V. C. Gulick, K. E. Herkenhoff, L. Keszthelyi, R. L. Kirk, M. T. Mellon, S. W. Squyres, N. Thomas, and C. M. Weitz (2007), Mars Reconnaissance Orbiter's High Resolution Imaging Science Experiment (HiRISE), *Journal of Geophysical Research*, *112*(E5), E05S02, doi: 10.1029/2005JE002605.

McLennan, S., J. Bell, W. Calvin, P. Christensen, B. Clark, P. de Souza, J. Farmer, W. Farrand, D. Fike, R. Gellert, a. Ghosh, T. Glotch, J. Grotzinger, B. Hahn, K. Herkenhoff, J. Hurowitz, J. Johnson, S. Johnson, B. Jolliff, G. Klingelhöfer, a. Knoll, Z. Learner, M. Malin, H. McSween, J. Pocock, S. Ruff, L. Soderblom, S. Squyres, N. Tosca, W. Watters, M. Wyatt, and a. Yen (2005), Provenance and diagenesis of the evaporite-bearing Burns formation, Meridiani Planum, Mars, *Earth and Planetary Science Letters*, *240*(1), 95–121, doi:10.1016/j.epsl.2005.09.041.

Michalski, J., and P. B. Niles (2012), Atmospheric origin of Martian interior layered deposits: Links to climate change and the global sulfur cycle, *Geology*, *40*(5), 419–422, doi:10.1130/G32971.1.

Michalski, J., F. Poulet, J. P. Bibring, and N. Mangold (2010), Analysis of phyllosilicate deposits in the Nili Fossae region of Mars: Comparison of TES and OMEGA data, *Icarus*, *206*(1), 269–289, doi:10.1016/j.icarus.2009.09.006.

Milliken, R. E., J. P. Grotzinger, and B. J. Thomson (2010), Paleoclimate of Mars as captured by the stratigraphic record in Gale Crater, *Geophysical Research Letters*, *37*(4), 1–6, doi:10.1029/2009GL041870.

Milliken, R. E., R. C. Ewing, W. W. Fischer, and J. A. Hurowitz (2014), Wind-blown sandstones cemented by sulfate and clay minerals in Gale Crater, Mars, *Geophysical Research Letters*, *41*(May), 1149–1154, doi:10.1002/2014GL060535.Received.

Mitchum, R. M., P. R. Vail, and S. Thompson (1977), Seismic Stratigraphy and Global Changes of Sea Level, Part 2: The Depositional Sequence as a Basic Unit for Stratigraphic Analysis: Section 2. Application of Seismic Reflection Configuration to Stratigraphic Interpretation, *Seismic Stratigraphy: Applications to Hydrocarbon Exploration AAPG Memoir 26*, pp. 53–62.

Murchie, S., R. Arvidson, P. Bedini, K. Beisser, J.-P. Bibring, J. Bishop, J. Boldt, P. Cavender, T. Choo, R. T. Clancy, E. H. Darlington, D. Des Marais, R. Espiritu, D. Fort, R. Green, E. Guinness, J. Hayes, C. Hash, K. Heffernan, J. Hemmler, G. Heyler, D. Humm, J. Hutcheson, N. Izenberg, R. Lee, J. Lees, D. Lohr, E. Malaret, T. Martin, J. A. McGovern, P. McGuire, R. Morris, J. Mustard, S. Pelkey, E. Rhodes, M. Robinson, T. Roush, E. Schaefer, G. Seagrave, F. Seelos, P. Silverglate, S. Slavney, M. Smith, W.-J. Shyong, K. Strohbehn, H. Taylor, P. Thompson, B. Tossman, M. Wirzburger, and M. Wolff (2007), Compact Reconnaissance Imaging Spectrometer for Mars (CRISM) on Mars Reconnaissance Orbiter (MRO), *Journal of Geophysical Research*, *112*(E5), doi: 10.1029/2006JE002682.

Murchie, S. L., J. F. Mustard, B. L. Ehlmann, R. E. Milliken, J. L. Bishop, N. K. McKeown, E. Z. Noe Dobrea, F. P. Seelos, D. L. Buczkowski, S. M. Wiseman, R. E. Arvidson, J. J. Wray, G. Swayze, R. N. Clark, D. J. Des Marais, A. S. McEwen, and J.-P. Bibring (2009), A synthesis of Martian aqueous mineralogy after 1 Mars year of observations from the Mars Reconnaissance Orbiter, *Journal of Geophysical Research*, *114*, E00D06, doi:10.1029/2009JE003342.

Mustard, J. F., F. Poulet, A. Gendrin, J. P. Bibring, Y. Langevin, B. Gondet, N. Mangold, G. Bellucci, and F. Altieri (2005), Olivine and pyroxene diversity in the crust of Mars, *Science*, *307*(5715), 1594–1597, doi:10.1126/science.1109098.

Mustard, J. F., F. Poulet, J. W. Head, N. Mangold, J.-P. Bibring, S. M. Pelkey, C. I. Fassett, Y. Langevin, and G. Neukum (2007), Mineralogy of the Nili Fossae region with OMEGA/Mars Express data: 1. Ancient impact melt in the Isidis Basin and implications for the transition from the Noachian to Hesperian, *Journal of Geophysical Research*, *112*(E8), E08S03, doi:10.1029/2006JE002834.

Mustard, J. F., B. L. Ehlmann, S. L. Murchie, F. Poulet, N. Mangold, J. W. Head, J.-P. Bibring, and L. H. Roach (2009), Composition, Morphology, and Stratigraphy of Noachian Crust around the Isidis basin, *Journal of Geophysical Research*, *114*, E00D12, doi:10.1029/2009JE003349.

Nelson, E. P., A. J. Kullman, M. H. Gardner, and M. Batzle (1999), Fault-Fracture Networks and Related Fluid Flow and Sealing, Brushy Canyon Formation, West Texas, *Faults and subsurface fluid flow in the shallow crust*, pp. 69–81.

Niles, P. B., and J. Michalski (2009), Meridiani Planum sediments on Mars formed through weathering in massive ice deposits, *Nature Geoscience*, *2*(3), 215–220, doi:10.1038/ngeo438.

Oehler, D. Z., and C. C. Allen (2012), Giant polygons and mounds in the lowlands of Mars: Signatures of an ancient ocean?, *Astrobiology*, *12*(6), 601–15, doi:10.1089/ast.2011.0803.

Okubo, C. H., and A. S. McEwen (2007), Fracture-Controlled Paleo-Fluid Flow in Candor Chasma, Mars, *Science*, *315*(5814), 983–985, doi:10.1126/science.1136855.

Oliver, M. A., and R. Webster (1990), Kriging : A method of interpolation for geographical information systems, *International Journal of Geographical Information Systems*, *4*(3), 313–332, doi:10.1080/02693799008941549.

Papike, J., J. Karner, and C. Shearer (2006), Comparative planetary mineralogy: Implications of martian and terrestrial jarosite. A crystal chemical perspective, *Geochimica et Cosmochimica Acta*, *70*(5), 1309–1321, doi:10.1016/j.gca.2005.11.004.

Perron, J. T., J. X. Mitrovica, M. Manga, I. Matsuyama, and M. A. Richards (2007), Evidence for an ancient martian ocean in the topography of deformed shorelines, *Nature*, *447*(7146), 840–843, doi:10.1038/nature05873.

Quinn, D., and B. L. Ehlmann (2018), Statistical analysis and software workflow for remotely-sensed bedding attitudes, *Journal of Geophysical Research: Planets*, (submitted).

Quinn, D. P., and B. L. Ehlmann (2017), A method for error analysis and orientation statistics of best-fitting planes from remote-sensing data, in *Lunar and Planetary Science Conference*, vol. 48, p. 2980.

Ritzer, J. A., and S. A. Hauck (2009), Lithospheric structure and tectonics at Isidis Planitia, Mars, *Icarus*, *201*(2), 528–539, doi:10.1016/j.icarus.2009.01.025.

Saper, L., and J. F. Mustard (2013), Extensive linear ridge networks in Nili Fossae and Nilosyrtis, Mars: Implications for fluid flow in the ancient crust, *Geophysical Research Letters*, *40*(2), 245–249.

Schon, S. C., J. W. Head, and C. I. Fassett (2012), An overfilled lacustrine system and progradational delta in Jezero crater, Mars: Implications for Noachian climate, *Planetary and Space Science*, *67*(1), 28–45, doi:10.1016/j.pss.2012.02.003.

Shorlin, K. A., J. R. De Bruyn, M. Graham, and S. W. Morris (2000), Development and geometry of isotropic and directional shrinkage-crack patterns, *Physical Review E - Statistical Physics, Plasmas, Fluids, and Related Interdisciplinary Topics*, *61*(6 B), 6950–6957, doi:10.1103/PhysRevE.61.6950.

Siebach, K. L., and J. P. Grotzinger (2014), Volumetric estimates of ancient water on Mount Sharp based on boxwork deposits, Gale Crater, Mars, *Journal of Geophysical Research: Planets*, *119*, 189–198, doi:10.1002/2013JE004482.Received.

Siebach, K. L., J. P. Grotzinger, L. C. Kah, K. M. Stack, M. Malin, R. Léveillé, and D. Y. Sumner (2014), Subaqueous shrinkage cracks in the Sheepbed mudstone: Implications for early fluid diagenesis, Gale crater, Mars, *Journal of Geophysical Research: Planets*, *119*, 1597–1613, doi:10.1002/2014JE004623.Received.

Skok, J., and J. Mustard (2014), Glaciation and volcanic interaction to form the modern Northeast Syrtis region of Mars, in *Lunar and Planetary Science Conference*, vol. 45, p. 1924, doi:10.1002/jgre.20118.

Skok, J., J. Mustard, and B. Ehlmann (2010), Silica deposits in the Nili Patera caldera on the Syrtis Major volcanic complex on Mars, *Nature Geoscience*, *3*.

Soare, R. J., S. J. Conway, C. Gallagher, and J. M. Dohm (2017), Ice-rich (periglacial) vs icy (glacial) depressions in the Argyre region, Mars: A proposed cold-climate dichotomy of landforms, *Icarus*, *282*, 70–83, doi:10.1016/j.icarus.2016.09.009.

Souček, O., O. Bourgeois, S. Pochat, and T. Guidat (2015), A 3 Ga old polythermal ice sheet in Isidis Planitia, Mars: Dynamics and thermal regime inferred from numerical modeling, *Earth and Planetary Science Letters*, *426*(August), 176–190, doi:10.1016/j.epsl.2015.06.038.

Squyres, S. W., J. P. Grotzinger, R. E. Arvidson, J. F. Bell, W. Calvin, P. R. Christensen, B. C. Clark, J. a Crisp, W. H. Farrand, K. E. Herkenhoff, J. R. Johnson, G. Klingelhöfer, a. H. Knoll, S. M.

McLennan, H. Y. McSween, R. V. Morris, J. W. Rice, R. Rieder, and L. a Soderblom (2004), In situ evidence for an ancient aqueous environment at Meridiani Planum, Mars., *Science (New York, N.Y.)*, *306*(5702), 1709–14, doi:10.1126/science.1104559.

Stuart, C. J., and C. A. Caughey (1977), Seismic facies and sedimentology of terrigenous Pleistocene deposits in northwest and central Gulf of Mexico, *AAPG Memoir*, *26*, 249–275.

Tewksbury, B. J., J. P. Hogan, S. A. Kattenhorn, C. J. Mehrtens, and E. A. Tarabees (2014), Polygonal faults in chalk : Insights from extensive exposures of the Khoman Formation , Western Desert , Egypt, pp. 479–483, doi:10.1130/G35362.1.

Viviano-Beck, C. E., F. P. Seelos, S. L. Murchie, E. G. Kahn, K. D. Seelos, H. W. Taylor, K. Taylor, B. L. Ehlmann, S. M. Wisemann, J. F. Mustard, and M. F. Morgan (2014), Revised CRISM spectral parameters and summary products based on the currently detected mineral diversity on Mars, *Journal of Geophysical Research E: Planets*, *119*(6), 1403–1431, doi:10.1002/2014JE004627.

Werner, S. C. (2008), The early martian evolution-Constraints from basin formation ages, *Icarus*, *195*(1), 45–60, doi:10.1016/j.icarus.2007.12.008.

Wichman, R., and P. Schultz (1989), Sequence and mechanisms of deformation around the Hellas and Isidis impact basins on Mars, *Journal of Geophysical Research*, *94*(B12), 17,133–17,357.

6 Conclusion

Continental margins on Earth are the locations where the continents are added to by both sedimentary and tectonic accretion, forming first-order features such as the Earth's freeboard (*Wise*, 1974), which sets the basic conditions for much of the Earth surface system, such as its climate, sedimentation patters, and modes of biogeochemical cycling (e.g. *Hyde et al.*, 2000). Understanding the fundamental architecture of these systems provides information into the Earth and Mars system.

In Chapter 2, we outline an example of how a substantial fragment of the lithospheric underpinnings of the continental margin (the entire substrate of the Mojave Desert block in California) was replaced by new lithospheric material. The emplacement of a large mass of lithospheric mantle of oceanic origin beneath the crust suggests an isostatic reason that the Mojave block remained near sea level for much of Cenozoic time. This mantle lithosphere seems to have shielded the base of the crust from the major effects of the Neogene slab window.

Whether continental crust was fundamentally created through time or generated early in Earth history is debated in the literature (*Wise*, 1974; *Schubert and Reymer*, 1985; *Hynes*, 2001). It is unclear what effects this accretion had on the volume of North America — this tectonic addition could have been balanced by erosion as is well-documented in the Late Cretaceous by *Kidder and Ducea* (2006), *Chapman et al.* (2012), and others in specific locales of the southern Sierra Nevada and Coast Ranges. However, this mode of addition at the base a continent has not been so well documented before.

In Chapter 3, we document the re-mapping of the Zebra Nappe of the Naukluft Nappe Complex (NNC). We substantially simplify the tectonic dynamics and stratigraphic architecture envisioned by previous workers (*Korn and Martin*, 1959; *Hartnady*, 1980). This project is a clear example of the augmented power of modern mapping studies supported by technologies such as satellite and UAV imagery, digital methods of data display, and modern tectonostratigraphic interpretive frameworks. The success of this project provides a clear endorsement of the continued relevance of mapping-based geologic studies and the desirability of replicating techniques for extracting regional meaning from datasets in contexts with less ideal data availability.

In Chapters 4 and 5, we apply structural mapping techniques to a stratigraphy on Mars. Chapter 4 improves the toolset available for structural mapping with remote-sensing data: we create a statistical method that allows significant improvement in the amount of bedding-orientation information that can be extracted from a remotely-sensed dataset. This method is coupled with new visualization approaches and software pipelines that provide new ways to work with structural data collected remotely. This method is valuable for planetary science, but also in terrestrial studies using unmanned aerial vehicles and structure-from-motion techniques.

In Chapter 5, we apply the methodology constructed in Chapter 4 to map and describe a globally significant stratigraphy at northeast Syrtis Major. We discover that the sequence records a varied and multistage history of sedimentary deposition from the Noachian into the Amazonian. The layered sulfates that anchor this sequence were likely formed by deep basinal deposition at the margin of Isidis Basin. The architecture of a bounding basin required to contain such deposition is unclear, but may either be unconfined (i.e. an ocean) or confined by a previously-existing ice sheet in Isidis Basin (*Souček et al.*, 2015). We construct a geologic map based on a much more thorough characterization of units and their geologic meaning than current morphologic mapping studies (*Bramble et al.*, 2017).

This thesis has demonstrated the application of structural geologic methods to regional systems on Earth, in one case using stratigraphy and structural mapping, and in another using geochemistry and modeling. Additionally, we cover the extension of these methods to Mars science, building tools and describing the environmental signals contained in a key stratigraphy. These studies illuminate several directions of future study in Earth and Mars science.

Our terrestrial study of the deep lithosphere in Chapter 2 was enabled by geologic mapping of crustal-level exposures throughout California, seismic data, tectonic reconstructions, and geophysical modeling. This integrated approach led to a to a new conceptual framework for understanding the "slab window" beneath the California coast and Mojave Plateau. How does this new understanding relate to the geology and petrology of Miocene volcanism in the region? Testing against this refined framework will improve our process-based understanding of the formation and tectonic modification of the coast of North America.

Chapter 2 also suggests new avenues for Mars science. On Mars, the structure of the deep lithosphere and the processes by which it formed remain fundamentally unknown. Was the lithosphere created during planetary formation and mostly altered in place? Or was there an early epoch of resurfacing of the planet? Extensive lava flows have been documented to cover much of the planet (e.g. *McEwen et al.*, 1999) and to fill the northern plains of the planet to significant depth (*Pan et al.*, 2017). Regionally extensive, laterally continuous middle-crustal mafic layers suggest formation at the surface (*Edwards et al.*, 2008). Still, studies of surface–interior coupling are based on poorly constrained compositional models (e.g. *Wade et al.*, 2017). New geophysical data [e.g. from the InSIGHT mission, *Banerdt et al.* (2013)] will substantially improve this situation, and mapping middle crustal exposures from orbit using structural tools developed in this thesis can build complementary constraints. These new tools will ultimately lead to a new understanding of the deep structure of Mars.

In Chapter 3, our study of the Zebra Nappe of the NNC is the first detailed description of a thick passive-margin stratigraphy on the Kalahari Craton. This sedimentary sequence contains environmental proxies relevant to Neoproterozoic Earth history and builds out a tectonic sequence of events that can be used to test the history of the Damara orogen and Pan-African assembly of Gondwana (e.g. *Gray et al.*, 2008). There are several more nappe units in the NNC, and future study will continue to place nappe segments in age context, building a new record of Neoproterozoic Earth history that can be compared to existing systems. Late-Neoproterozoic Earth is understood from relatively few stratigraphies, and new proxies from the NNC will provide data to assess regional variability and potential drivers for the evolution of animal life on Earth.

Where the NNC represents a set of fragmentary windows in the Neoproterozoic stratigraphy and the paleoenvironment of Earth during the Cryogenian – Ediacaran periods, Northeast Syrtis Major on Mars represents an in-place, relatively complete record of early Mars history, analogous to Neoproterozoic reference sections in northern Namibia (*Hoffmann and Prave*, 1996; *Hoffman*, 1998) and Death Valley, California (e.g. *Corsetti and Kaufman*, 2005; *Petterson et al.*, 2011). We hope that Chapter 5 of this thesis will serve as a similar guide to the history of the Mars surface environment over a period of global change. However, many more fragmentary records of Mars surface geological history exist. These sometimes capture higher levels of detail than the Syrtis Major stratigraphy, as with delta deposits and their context at Aeolis Dorsa (*DiBiase et al.*, 2013; *Kite et al.*, 2015). Other areas capture regionally-differentiated systems, such as at Uzboi Vallis (*Grant et al.*, 2011) or Gale Crater (e.g. *Milliken et al.*, 2010). Further understanding of Mars history can put the environments captured by of these regions in the context of the Noachian–Amazonian history recorded at Northeast Syrtis. As in Earth science, such an approach allows the best chance of capturing regional variation and a detailed, time-ordered history of the Mars environment.

The methods developed in Chapter 4 were created to enable Chapter 5 but are broadly applicable to terrestrial and planetary geoscience, and potentially to surface-fitting and remote-sensing applications in other domains. The developed method relies on both detailed statistics and new visualization approaches, and its supporting software provides a user interface to easily interact with the statistical tools. Such integrated approaches with custom data pipelines and user interfaces are becoming increasingly valuable for the capture and distillation of complex data in the geosciences. So too are rigorous standards for data archival and reporting. Moving forward, similarly deep analyses of the structure of data will be crucial for methods development across the geosciences.

Bibliography

Banerdt, W. B., S. Smrekar, P. Lognonné, T. Spohn, S. W. Asmar, D. Banfield, L. Boschi, U. Christensen, V. Dehant, and W. Folkner (2013), InSight: A discovery mission to explore the interior of Mars, in *Lunar and Planetary Science Conference*, vol. 44, p. 1915.

Bramble, M. S., J. F. Mustard, and M. R. Salvatore (2017), The geological history of Northeast Syrtis Major, Mars, *Icarus*, *293*, 66–93, doi:10.1016/j.icarus.2017.03.030.

Chapman, A., J. Saleeby, D. Wood, A. Piasecki, S. Kidder, M. Ducea, and K. Farley (2012), Late Cretaceous gravitational collapse of the southern Sierra Nevada batholith, California, *Geosphere*, *8*(2), 314–341, doi:10.1130/GES00740.1.

Corsetti, F. A., and A. J. Kaufman (2005), The relationship between the Neoproterozoic Noonday Dolomite and the Ibex Formation: New observations and their bearing on 'snowball Earth', *Earth-Science Reviews*, *73*(1-4), 63–78.

DiBiase, R. A., A. B. Limaye, J. S. Scheingross, W. W. Fischer, and M. P. Lamb (2013), Deltaic deposits at Aeolis Dorsa: Sedimentary evidence for a standing body of water on the northern plains of Mars, *Journal of Geophysical Research: Planets*, *118*(6), 1285–1302, doi:10.1002/jgre.20100.

Edwards, C. S., P. R. Christensen, and V. E. Hamilton (2008), Evidence for extensive olivine-rich basalt bedrock outcrops in Ganges and Eos chasmas, Mars, *Journal of Geophysical Research: Planets*, *113*(E11), doi:10.1029/2008JE003091.

Grant, J., R. Irwin, S. Wilson, D. Buczkowski, and K. Siebach (2011), A lake in Uzboi Vallis and implications for Late Noachian–Early Hesperian climate on Mars, *Icarus*, *212*(1), 110–122, doi: 10.1016/j.icarus.2010.11.024.

Gray, W., a. F. Glazner, D. S. Coleman, and J. M. Bartley (2008), Long-term geochemical variability of the Late Cretaceous Tuolumne Intrusive Suite, central Sierra Nevada, California, *Geological Society, London, Special Publications*, *304*, 183–201, doi:10.1144/SP304.10.

Hartnady, C. J. (1980), Geological map of the Naukluft area, *Precambrian Research Unit, University of Cape Town*.

Hoffman, P. F. (1998), A Neoproterozoic Snowball Earth, *Science*, *281*(5381), 1342–1346, doi:10.1126/science.281.5381.1342.

Hoffmann, K. H., and A. R. Prave (1996), A preliminary note on a revised subdivision and regional correlation of the Otavi Group based on glaciogenic diamictites and associated cap dolostones, *Communications of the geological survey of Namibia*, *11*, 77–82.

Hyde, W. T., T. J. Crowley, S. K. Baum, and W. R. Peltier (2000), Neoproterozoic 'snowball Earth'simulations with a coupled climate/ice-sheet model, *Nature*, *405*(6785), 425.

Hynes, A. (2001), Freeboard revisited: Continental growth, crustal thickness change and Earth's thermal efficiency, *Earth and Planetary Science Letters*, *185*(1-2), 161–172.

Kidder, S., and M. N. Ducea (2006), High temperatures and inverted metamorphism in the schist of Sierra de Salinas, California, *Earth and Planetary Science Letters*, *241*(3-4), 422–437.

Kite, E. S., A. D. Howard, A. S. Lucas, J. C. Armstrong, O. Aharonson, and M. P. Lamb (2015), Stratigraphy of Aeolis Dorsa, Mars: Stratigraphic context of the great river deposits, *Icarus*, *253*, 223–242, doi:10.1016/j.icarus.2015.03.007.

Korn, H., and H. Martin (1959), Gravity tectonics in the Naukluft Mountains of South West Africa, *Geological Society of America Bulletin*, *70*(8), 1047, doi:10.1130/0016-7606(1959)70[1047:GTITNM]2.0.CO;2.

McEwen, A. S., M. C. Malin, M. H. Carr, and W. K. Hartmann (1999), Voluminous volcanism on early Mars revealed in Valles Marineris, *Nature*, *397*(6720), 584–586, doi:10.1038/17539.

Milliken, R. E., J. P. Grotzinger, and B. J. Thomson (2010), Paleoclimate of Mars as captured by the stratigraphic record in Gale Crater, *Geophysical Research Letters*, *37*(4), 1–6, doi:10.1029/2009GL041870.

Pan, L., B. L. Ehlmann, J. Carter, and C. M. Ernst (2017), The stratigraphy and history of Mars' northern lowlands through mineralogy of impact craters: A comprehensive survey, *Journal of Geophysical Research: Planets*, pp. 1824–1854, doi:10.1002/2017JE005276.

Petterson, R., A. R. Prave, B. P. Wernicke, and A. E. Fallick (2011), The Neoproterozoic Noonday Formation, Death Valley region, California, *GSA Bulletin*, *123*(7-8), 1317–1336.

Schubert, G., and A. P. S. Reymer (1985), Continental volume and freeboard through geological time, *Nature*, *316*(6026), 336.

Souček, O., O. Bourgeois, S. Pochat, and T. Guidat (2015), A 3 Ga old polythermal ice sheet in Isidis Planitia, Mars: Dynamics and thermal regime inferred from numerical modeling, *Earth and Planetary Science Letters*, *426*(August), 176–190, doi:10.1016/j.epsl.2015.06.038.

Wade, J., B. Dyck, R. M. Palin, J. D. P. Moore, and A. J. Smye (2017), The divergent fates of primitive hydrospheric water on Earth and Mars, *Nature*, *552*(7685), 391–394, doi:10.1038/

nature25031.

Wise, D. U. (1974), Continental margins, freeboard and the volumes of continents and oceans through time, in *The Geology of Continental Margins*, pp. 45–58, Springer.